Petroleum and Coal

Article **Open Access**

EFFECT OF NON-IONIC POLYMERS ON YIELD STRESS AND KINETIC STRUCTURE OF ALGERIAN BENTONITE USED IN DRILLING FLUIDS

*Hocine Ouaer**, *Mourad Gareche*

Laboratoire Génie Physique des Hydrocarbures, Faculté des Hydrocarbures et de la Chimie, Université M'Hamed Bougara de Boumerdes, Avenue de l'indépendance 35000 Boumerdes, Algérie

Received February 1, 2019; Accepted March 26, 2019

Abstract

This paper reports the effect of two polymers on the rheological behavior of Algerian bentonite. This latter was sourced from Mostaganem –M'zila- and was used as drilling fluid in Algerian oil and gas wells. The two evaluated polymers were hydroxyethyl cellulose with a molecular weight of 9.5×10^5g/mol and polyethylene glycol with molecular weight of 6×10^3g/mol and 1×10^4g/mol. Steady-state and dynamic shear rheology measurements were performed on a controlled stress rotational rheometer at a controlled temperature of 25±0.1°C. It was found that all mixtures 'water-bentonite-HEC' and 'water-bentonite-PEG' exhibit shear-thinning behavior and the flow curves could be described by the Herschel-Bulkley (H-B) model. The obtained results show that (HEC) increased the rheological properties of bentonite dispersion such as yield stress and consistency index and deleted the gel time of this dispersion contrary to (PEG), which decreased these rheological properties and increased the gel time. It was also noticed that the rheological behavior of bentonite dispersion enhanced with increasing (PEG) molecular weight.

Keywords*: non-ionic polymers; drilling fluids; Algerian bentonite; rheological behavior; hydroxyethyl cellulose; polyethylene glycol.*

1. Introduction

Bentonite represents a very important clay material for a multitude of processes due to the exceptional properties of its dispersions in water [1]. Water-bentonite dispersions are used in different industries including oil and gas industry where these dispersions are used as drilling fluids [2-3]. These drilling fluids are designed to carry out several functions such as to transport cuttings to the surface, to prevent cuttings from sedimentation, to cool and lubricate bits and drill pipes, to minimize friction between formation and drilling equipment, to stabilize walls of the wellbore and to control formation pressure [4-6]. It is true that bentonite-water based drilling fluids are performant, but the high bentonite contents can have detrimental effects on drilling operations such as the reduction of the drilling operation productivity, thick filter cake, potential pipe sticking, and formation damage [7-8]. To overcome these problems, polymer-clay based drilling fluids are normally used [9]. These polymers have low cost, good rheological properties, and scant environmental impact.

In the last decade, it is found that non-ionic polymers can inhibit shale dispersion or clay swelling [10-11]. These non-ionic polymers are used in drilling fluids for different purposes, including building viscosity, reducing fluid loss, stabilizing bentonite dispersions and modifying drilling fluids rheology. Among the non-ionic polymers used in the drilling of oil and gas wells, hydroxyethyl cellulose (HEC), is used primarily for viscosity and fluid-loss-control in drilling and completion fluids [12-13] and polyethylene glycol (PEG), which has good performance concerning shale and gas-hydrate inhibition [14-15]. The addition of these polymers to water-bentonite dispersions affects the rheological behavior of these dispersions. Consequently, it is more important for rheological behavior to control the mixture water-clay-polymer.

Alemdar and Güngör [16], Tunç and Duman [17] and Ebagninin *et al.* [18], have studied the influence of polyethylene glycol of different molecular weight on the rheological behavior of bentonite dispersions. All these studies showed that the kinetic structure of the mixture 'bentonite-PEG', which is a significant property of drilling fluids, did not receive any attention. In addition, those previous studies did not make relationships between the obtained results and their application in the field.

The aim of this article is to investigate the effect of adding different non-ionic polymers to drilling mud sample containing Algerian bentonite followed by a comparison of different changes caused by these polymers. For this purpose, an experimental data from steady state shear rheology are obtained and fitted to the Herschel-Bulkley (H-B) model to study the non-Newtonian behavior of the drilling fluids formulated based on bentonite, (HEC) or (PEG) of different molecular weight over wide shear rate range, from 10^{-3} to 10^{3} s^{-1}. The knowledge of the (H-B) model rheological parameters is important. (H-B) yield stress data allows mud engineers to predict the minimum force required to initiate fluid flow. Meanwhile, the knowledge of the fluid consistency (k) and index flow (n), gives drilling engineers information on the type of fluid. The effect of the two non-ionic polymers on the bentonite dispersions kinetic structure is also investigated by measuring the viscoelastic moduli evolution as a function of time, which grants field engineer idea about the gelation time of the mixture bentonite-polymers. To our knowledge, it is the first time that the rheological behavior of the drilling fluid, 'water-bentonite-HEC' is studied.

2. Experimental study

2.1 Materials

A bentonite sample obtained from an Algerian field (Mostaganem, M'zila) was the constitute material of this study. This bentonite had this chemical composition, which was supplied by ENOF (Algerian Public Company of the Mining Products non-ferrous and useful Substances): 55-65 % SiO_2, 12-19 % Al_2O_3, 0.20 % TiO_2, 1-3.4 % Fe_2O_3, 1-3 % Na_2O, 1-2 % CaO, 0.5-1.18 % K_2O and 2-3.4 % MgO. It was confirmed by X-ray fluorescence (XRF) analysis that the major components of the studied bentonite were 60.49 % SiO_2, 13.87 % Al_2O_3, 3.14 % Fe_2O_3, 3.95 % CaO, 2.37 % MgO, 0.24 % SO_3, 1.69 % K_2O, 3.54 % Na_2O, 0.08 % P_2O_5 and 0.29 % TiO_2.

To the base bentonite dispersion (3 wt%), two non-ionic polymers were added separately:

- The first polymer was hydroxyethyl cellulose (HEC), a water-soluble polymer considered as cellulose derivatives. Its molecular weight was 9.5×10^5g/mol [19], and it was used as an additive to the bentonite dispersions for controlling the rheological behavior of these dispersions. This polymer was supplied from UK Ltd. It was a cellulose ether, which was essentially non-ionic in nature and was widely used as a rheology modifier or stabilizer in drilling, completion and work-over fluids with good environmental acceptability [20]. For drilling fluids application, this linear polymer was used as a viscosifier especially to reduce filtrate volume [13].

-Polyethylene glycol (PEG), a water-soluble polymer of the polyether family, was supplied by Acros Organics. The molecular weight of the studied (PEGs) was 6×10^3g/mol and 1×10^4g/mol. This polymer was also non-ionic in nature, used principally for inhibiting shale and gas-hydrate in drilling fluids applications [14-15].

2.2. Samples preparation

Drilling fluids were formulated as follows: in the first step, a 3 wt% of bentonite powder was immersed slowly in distilled water under magnetic stirring conditions to achieve the best swelling of bentonite and to well disperse these particles of clay in water. After four hours of agitation, (HEC) powder of different concentrations ranged from 0.02 to 0.1 wt% or (PEG) powder of different molecular weight was added to the mixture. The obtained mixture (water-bentonite-HEC or water-bentonite-PEG) was left under magnetic agitation for twenty hours.

2.3. Rheological measurements

The rheological measurements were performed on a controlled-stress rheometer (Anton Paar-Physica MCR-301) equipped with coaxial cylinders geometry (R_e=14.464 mm, R_i=13.325 mm, R_e/ R_i=1.088, h=39.997 mm) at a controlled temperature of 25±0.1°C.

Before each test, the samples were gently stirred for twenty min; afterward, the samples were carefully loaded to the measuring geometry of the rheometer. In the measurement geometry, samples were subjected also to a preshear of 1000 s^{-1}, then left to rest time prior to the measurements because the domain structure of bentonite dispersions is quite sensitive to shear deformation history. In dynamic rheological tests, a thin layer of low-viscosity paraffin oil was used to prevent sample evaporation via covering the free surface of the sample.

The flow curves were obtained by applying an increasing shear stress ramp at 20 s for each stage and were measured at a shear rate ranging from 10^{-3} to 10^{3} s^{-1}.

The linear viscoelastic properties of the mixture 'water-bentonite-HEC' and 'water-bentonite-PEG' were studied by measuring the evolution of storage (G') and loss (G'') moduli as a function of time for five hours. This time sweep was measured by applying a chosen stress and frequency values equal to 0.15 Pa and 10 rad/s respectively, allowing measurements within the linear viscoelastic region.

3. Results and discussion

3.1 Steady-state shear rheology of water-bentonite-polymers dispersions

Flow curves extracted from shear stress-shear rate measurements for the bentonite dispersions in the presence of non-ionic polymers are shown in Figure 1 (a and b). On the one hand, it was noticed, that shear stress enhanced with the increase in (HEC) concentration, indicating that higher force was required to start the flow of the fluids.

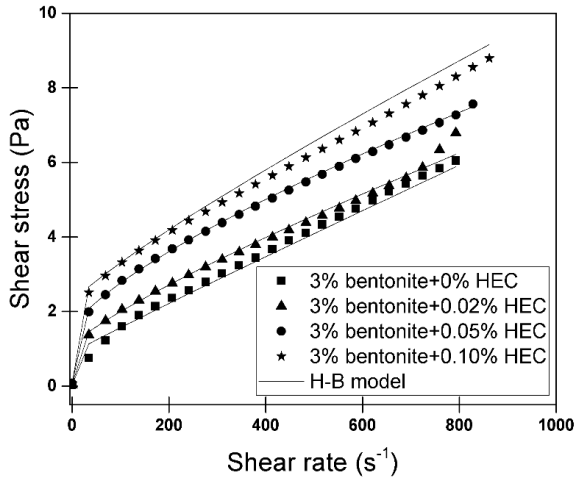

Figure 1. Flow curves of water-bentonite-polymers dispersions predicted by the Herschel-Bulkley model: (a) water-bentonite-HEC

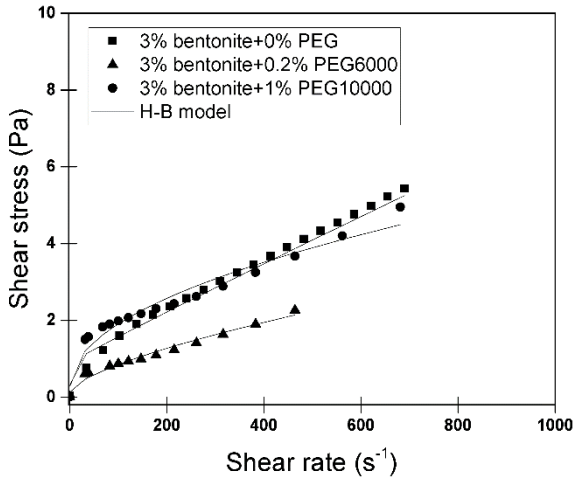

(b) water-bentonite-PEG6000 and water-bentonite-PEG10000

This enhancement in shear stress was attributed to the highly entangled (HEC), which could hold bentonite particles and consequently a flexible three-dimensional network was formed throughout the fluid system. On the other hand, it was also noticed that (PEG6000) addition to the bentonite dispersion decreased the shear stress, due to the fact that (PEG) reduced the interactions particle-particle and favored the interactions particle-additive [21]. In the case of (PEG10000), it can be observed that shear stress increased at low shear rate and decreased at a high shear rate, this effect is attributed to the fact that (PEG) acts inversely with increasing its molecular weight. The latter result was in good agreement with that of Ebagninin *et al.* [18],

who studied the effect of different molecular weight (PEG) on the rheological behavior of bentonite dispersions and found that the rheological properties of the mixture increased with increasing (PEG) molecular weight.

Experimental data are analyzed and fitted to the (H-B) model, which has already used to describe the drilling fluids rheological behavior [22-24]. It can be expressed as follows:

$$\tau = \tau c + k\,\dot{\gamma}^{n} \quad (1)$$

where (τ) is the shear stress (Pa), (τc) is the yield stress (Pa), (k) is the consistency index (Pa.s^n), ($\dot{\gamma}$) is the shear rate (s^{-1}) and (n) is the flow index.

From Table 1, which represents the (H-B) model rheological parameters of the mixture 'water-bentonite-HEC' and 'water-bentonite-PEG', it is clear that all mixtures have shear-thinning behavior with yield stress. In the case of mixtures obtained with (HEC), it was found that yield stress and consistency index increased with increasing in (HEC) concentration inversely to the flow index, which decreased. The increase in yield stress and consistency index was due to entanglements of polymer macromolecules, which were adsorbed onto the clay surface. This adsorption favored either flocculation or steric stabilization of the system 'water-bentonite-HEC' [17]. However, according to Güngör and Ece [25], bridging flocculation was induced at very low polymer concentration.

Table 1. The Herschel-Bulkley model rheological parameters of water-bentonite-HEC and water-bentonite-PEG mixtures

	The Herschel-Bulkley model rheological parameters			
Drilling fluid formulation	τ_c (Pa)	k (Pa.s^n)	n (-)	R^2
3% Bentonite	0.892	0.008	0.964	0.996
3% Bent+ 0.02% HEC	1.080	0.02	0.831	0.996
3% Bent+ 0.05% HEC	1.510	0.042	0.738	0.997
3% Bent+ 0.10% HEC	2.238	0.02	0.865	0.994
3% Bent+ 0.2% PEG6000	0.129	0.033	0.669	0.995
3% Bent+ 1.0% PEG10000	0.272	0.167	0.495	0.993

For 'water-bentonite-PEG' dispersions, the results showed that this polymer induced a decrease in yield stress, which can be explained by the fact that the presence of (PEG) decreased the interactions between clay particles, which were rigid and benefited the interactions particle-additive, which were less rigid [26]. This decrease in yield stress was significant in the case of (PEG6000) in despite that the concentration used for (PEG6000) was lower than that used in the case of (PEG10000). This was mainly due to the reinforcement of the bonds between bentonite particles with the increase in polymer molecular weight [18]. Otherwise, the polymer molecules were adsorbed simultaneously on two or more particle surfaces. This phenomenon is accentuated, with the molecular weight where the length of the polymer chains allows the adsorption on more than one particle. This forms what is known as "polymer bridge flocculation", causing an increase in the rheological properties of the colloidal system [27-28].

3.2. Dynamic rheology of water-bentonite-polymers dispersions (kinetic structure)

To highlight the effect of (HEC and PEG) polymers on the gelation mechanism of the mixture 'water-bentonite-HEC' and 'water-bentonite-PEG', the evolution of the storage and loss moduli as a function of time for five hours was followed. On the one hand, the results (Fig. 2) showed that (HEC) addition to the basic bentonite dispersion allowed accelerating the mixture gel time, i.e., for the basic bentonite dispersion, it was found that the gel time closed to 109 s (determined by the crossing of modulus, G'=G'' according to Tung and Dynes [29]), whereas this transition from liquid to solid state did not exist for all 'water-bentonite-HEC' mixtures, these mixtures behaved like a gel from the beginning. One can say that (HEC) accelerates the kinetics of aggregation of clay particles. Focusing on these results, it can be concluded that the gel time disappearance by adding (HEC) to the basic bentonite dispersion (gel behavior in

the beginning) was due to the bridging of clay particles, this phenomenon favored the flocculation of the system while increasing (HEC) concentration and consequently mixture rigidity was reinforced.

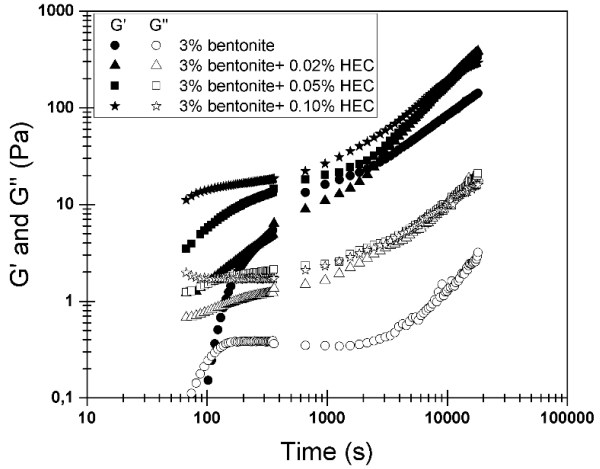

Figure 2. Kinetic structure of the basic bentonite dispersion and the mixture water-bentonite-HEC

On the other hand, the gel time (T_{gel}) evolution according to (PEG) molecular weight presented in Table 2 confirmed that (PEG) addition to the bentonite dispersion increased the gel time, which means that the basic dispersion gel time was always inferior to that of the mixture 'water-bentonite-PEG'. Therefore, (PEG) acts inversely to (HEC), it slows down the kinetics of aggregation of clay particles. This result can be explained by the way that (PEG) is adsorbed between one or several clay particles, but this adsorption is done without bridging phenomenon [26]. It can also be noticed that the gel time with (PEG1000) was inferior to that obtained with (PEG6000), which means that increasing (PEG) molecular weight decreased the gel time. Consequently, one can think that the increase in (PEG) molecular weight allowed the appearance of bridging phenomenon between the clay particles and thereafter flocculation of the system would occur. Indeed, these results are in good agreement with the results obtained in steady state shear rheology

Table 2. Gel time of water-bentonite-PEG mixtures

Drilling fluid formulation	3% Bentonite	3% Bent+ 0.2% PEG6000	3% Bent+ 1.0% PEG10000
T_{gel} (s)	109	123	116

In summary, non-ionic polymers can act with different mechanisms on the clay particles such as: adsorbing onto the clay surface, intercalate the clay interlayer.

4. Conclusions

The rheological properties of water-bentonite-polymer dispersions were investigated using two different non-ionic polymers. The results revealed that (HEC) and (PEG) addition to Mostaganem bentonite dispersions resulted in different changes in the rheological behavior of these dispersions. On the one hand, the presence of (HEC) in drilling fluids formulation allowed yield stress and consistency index to be increased whereas it decreased the flow index. In addition, (HEC) accelerated the kinetics of aggregation of clay particles by favoring system flocculation. Consequently, a small (HEC) amount can replace high bentonite quantity, which avoids high solid content drilling-fluids. On the other hand, (PEG) addition to drilling fluids containing Mostaganem bentonite resulted in decreasing the yield stress and increasing the gel time. Furthermore, an increase in (PEG) molecular weight allowed an increase in the yield stress and a decrease in the gel time. As a consequence, low molecular weight (PEG) are recommended to be added to the drilling fluids when drilling operation is stopped, which allowed decreasing yield stress because this parameter increased significantly in this case due to a gelation mechanism. However, high molecular weight (PEG) is recommended to stabilize or increase slightly drilling fluids rheological properties.

Symbols

H-B	*Herschel-Bulkley*	*K*	*Consistency index (Pa. s^n)*
HEC	*Hydroxyethyl cellulose*	*N*	*Flow index*
PEG	*Polyethylene glycol*	*$\dot{\gamma}$*	*Shear rate (s^{-1})*

G′	*Storage modulus (Pa)*	*T*	*Shear stress (Pa)*
G″	*Loss modulus (Pa)*	τ_c	*Yield stress (Pa)*

Acknowledgment

The authors wish to extend a special thanks to Ms. Sabrina BOUCHAMA and Mr. Mohamed El Amine BEN SEGHIER for their help.

References

[1] Vryzas Z. Kelessidis VC. Nalbantian L. Zaspalis V. Gerogiorgis DI. Wubulikasimu Y. Effect of temperature on the rheological properties of neat aqueous Wyoming sodium bentonite dispersions. Appl. Clay Sci. 2017; 136: 26 –36.

[2] Kok MV. Rheological and thermal analysis of bentonites for water base drilling fluids. Energy Sources A: Recovery, Utilization, and Environmental Effects. 2004; 26 (2):145-151.

[3] Kok MV. A rheological characterization and parametric analysis of a bentonite sample. Energy Sources A: Recovery, Utilization and Environmental Effects. 2011; 33(4): 344-348.

[4] Baba Hamed S. Belhadri M. Rheological properties of biopolymers drilling fluids. J. Pet. Sci. Eng. 2009; 67: 84–90.

[5] Kelessidis VC. Poulakakis E. Chatzistamou V. Use of carbopol 980 and carboxymethyl cellulose polymers as rheology modifiers of sodium-bentonite water dispersions. Appl. Clay Sci. 2011; 54: 63–69.

[6] Kosynkin DV. Ceriotti G. Wilson KC. Lomeda JR. Scorsone JT. Patel AD. Friedheim JE. Tour JM. graphene oxide as a high-performance fluid-loss-control additive in water-based drilling fluids. ACS Appl. Mater. Interfaces. 2011; 4: 222–227.

[7] Anyanwu C. Mustapha Unubi M. Experimental evaluation of particle sizing in drilling fluid to minimize filtrate losses and formation damage. SPE-184303-MS, presented at SPE Nigeria international conference and exhibition held in Lagos, 2016; https://doi.org/10.2118/184303-MS.

[8] Song K. Wu Q. Li M. et al. Water-based bentonite drilling fluids modified by novel biopolymer for minimizing fluid loss and formation damage. Colloids and Surfaces A: Physicochemical and Engineering Aspects. 2016; 507: 58-66.

[9] Luo Z. Pei J. Wang L. Yu P. Chen Z. Influence of an ionic liquid on rheological and filtration properties of water-based drilling fluids at high temperatures. Appl. Clay Sci. 2017; 136: 96-102.

[10] Aston MS. Elliot GP. Water-based glycol drilling muds: Shale inhibition mechanisms. SPE -28818- Europ. Petr. Conf., London, 1994; 107-113, https://doi.org/10.2118/28818-MS.

[11] Downs JD. Van Oort E. Redman DI. Ripley D. Rothman B. A new concept in water-based drilling fluids for shales. SPE -26699- Offshore European Conference, Aberdeen, 1993, 239-253, https://doi.org/10.2118/26699-MS.

[12] Arisz PWF. Lusvardi KM. water-soluble, low substitution hydroxyethyl cellulose, derivatives thereof, process of making, and uses thereof. US patent 0199742 A1, 2006.

[13] Raines RH. Use of low M.S. (molar substitution) hydroxyethyl cellulose for fluid loss control in oil well applications. U.S. patent 4629573, 1986.

[14] Hao S-q. A study to optimize drilling fluids to improve borehole stability in natural gas hydrate frozen ground. J. Pet. Sci. Eng. 2011; 76: 109–115.

[15] Jiang G. Liu T. Ning F. Tu Y. Zhang L. Yu Y. Kuang L. Polyethylene glycol drilling fluid for drilling in marine gas hydrates-bearing sediments: An experimental study. Energies. 2011; 4: 140-150.

[16] Almedar A. Güngör N. The rheological properties characterization of bentonite dispersions in the presence of nonionic polymer PEG. J. Mat. Sci. 2005; 40: 171–177.

[17] Tunç S. Duman O. The effect of different molecular weight of poly (ethylene glycol) on the electrokinetic and rheological properties of Na-bentonite suspensions, Colloids surf. A. 2008; 317: 93–99.

[18] Ebagninin KW. Benchabane A. Bekkour K. Influence du polyéthylène oxyde (PEO) de différentes masses moléculaires sur les propriétés rhéologiques des suspensions d'argile. Int. J. Biol. Chem. Sci. 2012; 6 (6): 7027-7047.

[19] Ouaer H. Gareche M. the rheological behaviour of a water-soluble polymer (HEC) used in drilling fluids. J. Brazilian Soci. Mech. Sci. Eng. 40: 380, DOI: 10.1007/s40430-018-1301-7.

[20] Zhang L-M. Sun B-W. Inhibition of water-soluble cationic cellulosic polymers to clay hydration. J. Appl. Polm. Sci. 1999; 74: 3088–3093.

[21] Rossi S. luckham PF. Tadros ThF. Influence of non-ionic polymers on the rheological behaviour of Na^+-montmorillonite suspensions- I Nonylphenol-polypropylene oxide- polyethylene oxide copolymers. Colloids surf. A. 2002; 201: 85-100.
[22] Abu-Jdayil B. Ghannam M. The modification of rheological properties of sodium bentonite-water dispersions with low viscosity CMC polymer effect. Energy Sources, Part A. 2014; 36 (10): 1037-1048.
[23] Alderman NJ. Gavignet A. Guillot D. Maitland GC. High-temperature, high-pressure rheology of water based muds. SPE -18035- 63rd ANN. Tech. Conf. Houston, 1988; 187-195.
[24] Benyounes K. Mellak A. Benchabane A. The effect of carboxymethyl cellulose and xanthan on the rheology of bentonite suspensions. Energy Sources, Part A. 2010; 32: 1634–1643.
[25] Güngör N. Ece OI. Effect of the adsorption of non-ionic polymer polyvinyl/pyrolidone on the rheological properties of Na-activated bentonite. Mater. Lett. 1999; 39: 1–5.
[26] Gareche M. Zeraibi N. Allal A. Amoura M. The influence of low molecular weight polymer on the rheological behavior of bentonite suspensions. Petrol. Sci. Techn. 2012; 30: 1981–1989.
[27] Isci S. Günister E. Ece ÖI. Güngör N. The modification of rheologic properties of clays with PVA effect. Mater. Lett. 2004; 58: 1975-1978.
[28] Luckham PF. Rossi S. The colloidal and rheological properties of bentonite suspensions. Adv. Coll. Interf. Sci. 1999; 82(1-3): 43-92.
[29] Tung CYM. Dynes PJ. Relationship between viscoelastic systems. J. Appl. Polym. Sci. 1982; 27: 569-574.

To whom correspondence should be addressed: Dr. Hocine Ouaer, Laboratoire Génie Physique des Hydrocarbures, Faculté des Hydrocarbures et de la Chimie, Université M'Hamed Bougara de Boumerdes, Avenue de l'indépendance 35000 Boumerdes, Algérie

Petroleum and Coal

Article **Open Access**

COAL PYROLYSIS PRODUCTS UTILISATION FOR SYNTHESIS OF CARBON NANOTUBES

Lina Kieush

National Metallurgical Academy of Ukraine, Faculty of Metallurgy, Dnipro, Ukraine

Received February 3, 2019; Accepted April 3, 2019

Abstract

Coal pyrolysis products are to be a good substitute for existing carbon sources. They are applied in carbon nanotubes synthesis in the role of the raw materials due to their abundance and cheapness. This publication reveals the possibility of using coal pyrolysis products to produce various carbon nanomaterials such as carbon nanotubes and carbon whiskers via the plasma arc method. The obtained carbon nanomaterials have been investigated by means of SEM and TEM. As the global recent approach to the application problem for carbon nanotubes derived from coal pyrolysis products is in their use as the anode material in lithium-ion batteries, the currently reported studies has targeted this problem. They have evidenced that the carbon nanotubes vs. conventional anode materials can increase the reversible capacity, the rate capability, and improve cyclability.

Keywords: *Carbon nanomaterials; Carbon nanotubes; Plasma-arc method; Coal pyrolysis products; Lithium-ion battery.*

1. Introduction

Nanotechnology is a rapidly growing industry of a global economy value, it includes the development and production of nanoscale engineering particles, fibres and coatings, generally often called nanomaterials. The nanomaterials belong to the type of those materials, which have at least one dimension less than 100 nanometers. In particular, for the particles, it is the size characteristics that is the principle one to attribute a particle to the class of nanomaterials and to name it as a nanoparticle. With their unique properties, nanomaterials are used for the industrial and the consumer applications. Their various types have found their place in a multitude of sectors: agriculture, energy, aerospace, cosmetics, food, medicine, construction, transport, electronics, etc. Most of the nanomaterials, promised for the production in large volumes or for significant volumes on the nanomarket of the nearest future, will consist specifically of the following main materials: soot in the amount of 9.6 million tons, silicon dioxide (amorphous and crystalline) - 1.5 million tons, aluminium oxide - 200 000 tons, barium titanate - 15 000 tons, titanium dioxide - 10 000 tons, cerium oxide - 10 000 tons, zinc oxide - 8 000 tons, carbon nanotubes and carbon nanofibers - 100-3000 tons and silver nanoparticles - 20 tons [1].

The precursors for synthesis can play a pivotal role for the viability of nanotechnology. Most conventional methods use expensive carbon materials, for instance, graphite and hydrocarbons (methane, acetylene, etc.). Coal and its pyrolysis products have a great potential as a substitute for all the named, as shown in the review article [2]. This review article reveals the recent developments in the production of a large number of carbon-based nanomaterials from different types of coal (lignite, bituminous, anthracite) with the purpose to apply them as the synthesis precursors and to outlines their potential applications in the energy engineering, the environmental spheres and the biomedicine. Moreover, the thereof publication highlights the results of the coal pyrolysis products application, namely, those with coal tar to obtain quantum dots via the chemical oxidation method.

Generally, among the synthesis approaches, the plasma-arc method has shown advantages in the mass production of high-quality carbon-based nanomaterials such as single-walled carbon nanotubes (SWCNTs), multi-walled carbon nanotubes (MWCNTs) [3], double-walled carbon nanotubes [4], branched carbon nanotubes [5], bamboo shaped carbon tubes [6], graphene [7], carbon nanofibers [8], and carbon dots [9].

One of the instances how a plasma-arc method can serve with a conventional carbon precursor for nanomaterials obtaining has been shown in the paper [10]. It reports on obtaining carbon nanomaterials, including fullerene, graphene and nanorods from the inside of the chamber using different gaseous atmospheres, namely, argon, nitrogen and hydrogen at a constant electric current. They also write concerning both anode and cathode, which were the graphite rods with the diameter of 10 mm and the purity of 99.999%.

The feasibility to obtain carbon nanomaterials from coal was first demonstrated by the synthesis of C_{60} and C_{70} [11]. It is important to note here that coal has limitations in its application, since it is not possible to obtain a conductive material directly from coal and to enjoy the characteristics suitable for electrodes. Therefore, all works related to the nanomaterials production include the step of coal carbonisation with the objective to prepare semi-coke or coke. Further, the electrode preparation is carried out in the temperature range of 400-500°C from non-caking coal (for example, anthracite) or, alternatively, semi-coke can be manufactured from the mixture of coal and binder (for instance, pitch or coal tar) or from a caking coal without any additives. Then, the carbonisation process is carried out and it takes several hours in a stream of an inert gas at the temperatures of 1000-1200°C to obtain the conductive electrode. In some cases, they apply a hollow graphite high purity anode filled in certain techniques with powders of coal, or carbon black, or coal plus catalyst [5]. The coal pyrolysis products are usually used as a binder in the preparation of the anodes for further use in the arc discharge.

The report by Iijima and Ichihashi [12] was the first to demonstrate the feasible for the fabrication of SWCNTs in catalytic arc synthesis with graphite electrodes in the helium atmosphere. Their anode had a cavity, which was filled with a catalyst (Fe, Co, Ni). In order to generate the arc on the electrodes, the current of 200 A was supplied with the voltage of 20 V. As a result of the arc synthesis, SWCNTs with the diameters in the range of 0.7-1.65 nm were obtained.

As the another instance can serve Williams *et al.* [13] who used bituminous coal with a carbon content of 73.25%, subjected to hot pressing along with the binder. Further, the anodes obtained were subjected to carbonisation in the stream of N_2 at 1200°C. The resulting electrodes were characterised with the diameter of 8 mm, the length of 75 mm and the electrical resistance of 1 Ohm. The graphite was used as the cathode. The arc was formed at the current of 100 A and the voltage of 30 V in an atmosphere of helium at the pressure of 66 kPa. These researchers concluded that from the web-like material, the output of SWCNTs was higher than that of a more dense material from the walls of the chamber.

Additionally, Qiu *et al.* [4] conducted the studies with one of the types of Chinese anthracite. Firstly, the samples of coal were crushed and were screened to the value of less than 150 μm. Secondly, the carbon powder was mixed with Fe catalyst (less than 200 μm) and binder (coal tar) in the ratio of 3:1:1 by weight. Finally, the obtained mixture was subjected to the pressure and the subsequent carbonisation at the temperature of 800°C for two hours to form carbon rods. Obtained after the synthesis, the double-walled carbon nanotubes had the outer diameters of 1.0-5.0 nm and the interlayer spacing in the walls of nanotubes about 0.41 nm.

Recently, Li *et al.* [14] reported on the synthesis of bamboo-structure carbon nanotubes from Bitumite by arc discharge in the presence of a Ni-Sm_2O_3 catalyst. The results showed that the nanotubes obtained had a surface area of 23 m^2g^{-1} and consisted of empty compartments that were separated at a distance of 50-100 nm with graphite layers.

The coke utilisation as a carbon precursor is much less commonly used to fabricate carbon nanotubes. However, Mathur *et al.* [15] made the research with the mixture of graphite, coke,

coal tar pitch and catalyst Ni+Co (8.6 % by weight) and obtained sufficiently long and flexible SWCNTs and MWCNTs.

In addition, Pang *et al.* [16] described the production of fullerenes from the laboratory coke and the industrial coke. In this study, using the laboratory coke, the maximum yield of fullerene structures was obtained as much as 8.6 % compared to 3.3 % from the industrial coke.

The carbon nanotubes prepared from coal or the products of its pyrolysis are generally equal by their characteristics to those carbon nanotubes, which are produced by means of the conventional approaches and raw materials. One of the advanced carbon nanotubes applications that has recently gained momentum is their use in the role of an anode material for lithium-ion batteries [17-19]. Indeed, some of the most interesting innovations at improving lithium-ion cell anodes have come from the attempts to combine carbon nanotubes with various deposits. It is reported that carbon nanotubes are characterized by high conductivity of 10^6 S/m and 10^5 S/m for SWCNTs and MWCNTs, respectively, and high tensile strength up to 60 GPa. For instance, SWCNTs can have reversible capacities from 300 $mAhg^{-1}$ to 600 $mAhg^{-1}$. This means SWCNTs capacity can be significantly higher than the capacity of graphite (320 $mAhg^{-1}$), a widely used battery electrode material. Furthermore, mechanical and chemical treatments to the SWCNTs can further increase the reversible capacities up to 1000 $mAhg^{-1}$ [20].

Eventually, it can be evidenced that the carbon nanotubes utilisation as the anode material for lithium-ion batteries is a promising prospect to improve energy storage.

2. Experimental

In order to obtain carbon nanomaterials in the arc discharge, the anodes have been prepared using coal pyrolysis products. For this purpose, pitch coke, coal tar, pitch and NiO (II)-Fe catalyst were pressed at the pressure of 69 kPa in the matrix. The resulting rods were placed in the oven and were heated with the step of 10°C/min up to 500°C. After reaching the required temperature, the heat treatment was further performed for 1 hour. Then the electrodes were carbonised up to 900°C. After reaching the final temperature, the anode was subjected to further heat treatment for 6 hours.

For the production of carbon nanomaterials, a plasma arc reactor was used and it was operated in the following way. Two electrodes, the anode and the cathode, placed in the plasma arc reactor, were connected to an external energy source of 80-90 A DC and the voltage of 20-25 V. When the distance between the electrodes reached 1-2 mm, the arc was formed in the argon atmosphere under the pressure of 69 kPa. The apparatus walls cooling was carried out through the circulation of water through the pipes. The durations of the experiments in the set were approximately 20-30 minutes, resulting in soot on the chamber walls, as well as the solid deposit on the cathode, and the carbon "web" was also formed.

The obtained carbon nanotubes were examined by a scanning electron microscope (Jeol JSM 840) and by a transmission electron microscope (TEM 125K), equipped with a digital output system for the image of SEO-SCAN.

3. Result and discussion

As a result of arcing evaporation for the carbon black, the carbon "web" and the carbon deposit have been obtained. The examination of the carbon black has revealed the presence of C_{60} and C_{70}. Subsequently, the samples of carbon "web" were subjected to burning soot and acid wash (HCl). Further, the carbon nanotubes have been found both in the treated carbon "web" and in the treated carbon deposit.

The developed composition was worked to shape the anodes and it has produced the SWCNTs with the diameters ranging within 35-40 nm and lengths of 2.1-2.3 μm (refer to Fig. 1 a, b).

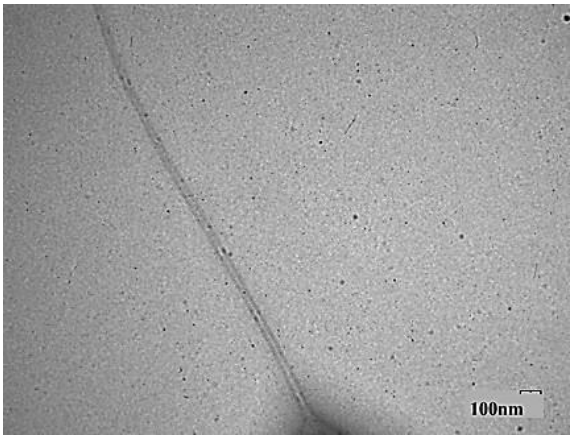

Figure 1a. TEM images of SWCNTs (x10000)

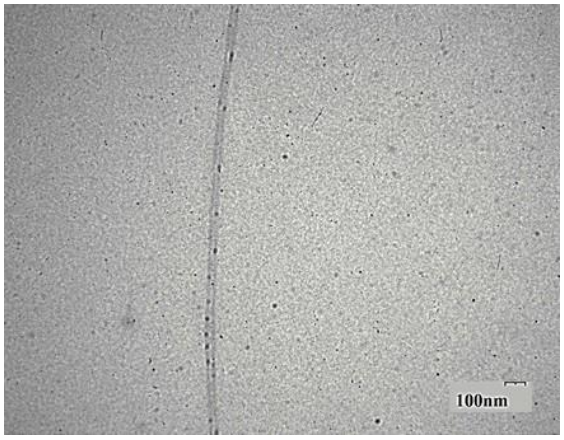

Fig. 1b.

Fig. 2 shows the SWCNTs obtained by the electric arc method. Their lengths are within 3.4-3.5 μm while their diameters are 15 nm on average.

The TEM image evidences that the obtained MWCNTs consist of several concentric cylindrical layers of graphene (refer to Fig. 3): the length of 345-504 nm, the outer diameters of 28-50 nm and the inner diameters of 6.2-8.5 nm. For these MWCNTs with a rather rigid structure, the greater tensile strength is inherent.

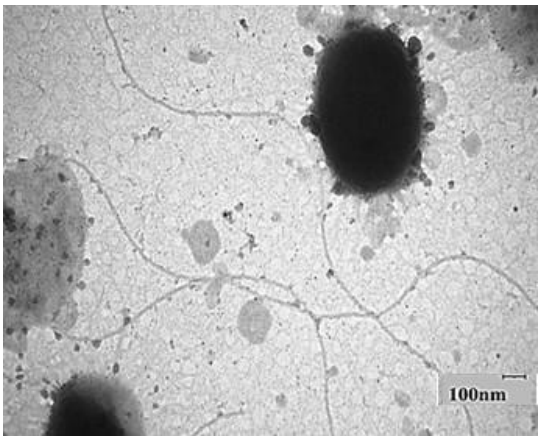

Figure 2. TEM image of SWCNTs (x10000)

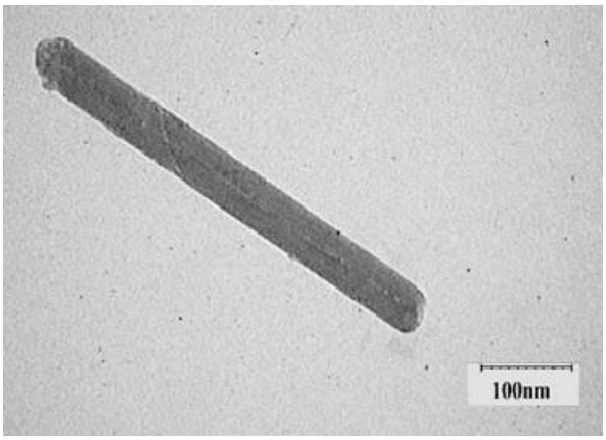

Figure 3. TEM image of MWCNTs (x40000)

In the arc discharge, whiskers have been also obtained (Fig. 4) and selected from the carbon "web" as shiny, rather rigid threads.

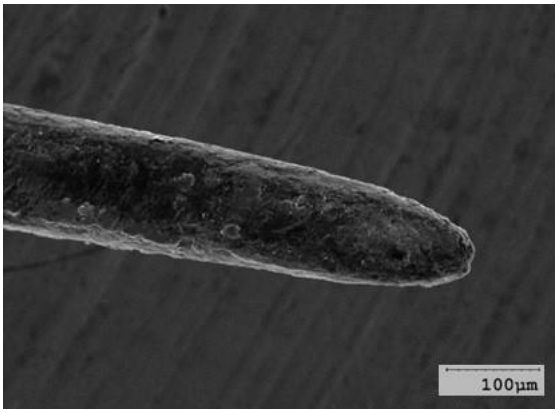

Figure 4. SEM image of carbon whiskers (x200)

The lengths of some whiskers reach 12 mm, and the diameters are about 135-200 μm. By zooming x200, it can be seen that the structure of whiskers is formed from a continuously twisted carbon structure in the form of a scroll.

The resulting carbon nanotubes with the above mentioned characteristics can increase the specific power of lithium-ion batteries to 187.4 mAh/g at a charge-discharge rate of 50 mA/g and good cyclability, they can also enhance the Coulomb efficiency up to 101.9% after 50 cycles, as shown in the work [21].

4. Conclusions

Coal pyrolysis products are a unique source of raw materials for obtaining various types of carbon nanomaterials, for example, carbon nanoparticles, quantum dots, graphene, graphene oxides, SWCNTs, MWCNTs and other types of nanotubes. The results of the reported research make it possible to conclude that for the production of carbon nanomaterials in electric arc synthesis it is possible to use the anodes made from coal pyrolysis products instead of expensive conventional materials. This has the potential to reduce the cost of the final product and to expand the possibilities of practical application of various coal processing products.

Carbon nanotubes derived from coal pyrolysis products have excellent prospects for being used in lithium-ion batteries as anode material. The carbon nanotubes utilisation in lithium-ion batteries allows increasing the reversible capacity, increasing the rate capability, and improving cyclability. Eventually, the carbon nanotubes can greatly enhance the lithium storage capacity of the composites electrode as a surface template and a conductive frame with the high specific capacity.

Acknowledgments

The publication is produced within the framework of the project entitled "The Development of Techniques to Apply the Carbon Materials Produced from Renewable Raw Materials in the Metallurgy", 0117U003919. The author would like to acknowledge Dr. Volodymyr Shmalko for his kind support in carrying out this work.

References

[1] World Health Organization. Guidelines on protecting workers from potential risks of manufactured nanomaterials. Geneva: World Health Organization; Licence: CC BY-NC-SA 3.0 IGO. 2017.
[2] Hoang VC, Hassan M, Gomes VG. Coal derived carbon nanomaterials – Recent advances in synthesis and applications. Appl. Mater. Today, 2018; 12: 342-358.
[3] Moothi K, Iyuke SE, Meyyappan M, Falcon R. Coal as a carbon source for carbon nanotube synthesis. Carbon, 2012; 50: 2679–2690.
[4] Qiu J, Wang Z, Zhao Z, Wang T. Synthesis of double-walled carbon nanotubes from coal in hydrogen-free atmosphere. Fuel, 2007; 86:282–286.
[5] Wang Z, Zhao Z, Qiu J. Synthesis of branched carbon nanotubes from coal. Letters to the Editor. Carbon, 2006; 44:1298–1352.
[6] Li YF, Qiu JS, Zhao ZB, Wang TH, Wang YP, Li W. Bamboo shaped carbon tubes from coal. Chem. Phys. Lett., 2002; 366(5-6): 544–550.
[7] Awasthi S, Awasthi K, Ghosh AK, Srivastava SK, Srivastava ON. Formation of single and multi-walled carbon nanotubes and graphene from Indian bituminous coal. Fuel, 2015; 147:35–42.
[8] Zhao H, Wang L, Jia D, Xia W, Li J, Guo Z. Coal based activated carbon nanofibers prepared by electrospinning. J. Mater. Chem. A., 2014; 2: 9338–9344.
[9] Hu S, Wei Z, Chang Q, Trinchi A, Yang J. A facile and green method towards coal-based fluorescent carbon dots with photocatalytic activity. Appl. Surf. Sci., 2016; 378: 402–407.
[10] Zhang D, Ye K, Yao Y, Liang F, Qu T, Ma W, Yang B, Y Dai, Watanabe T. Controllable synthesis of carbon nanomaterials by direct current arc discharge from the inner wall of the chamber. Carbon, 2019; 142: 278-284.
[11] Pang LSK, Vassallo AM, Wilson MA. Fullerenes from coal. Nature. 1991; 352:480.
[12] Iijima S, Ichihashi T. Single-shell carbon nanotubes of 1-nm diameter. Nature. 1993; 363:603-605.
[13] Williams KA, Tachibana M, Allen JL, Grigorian L, Cheng S-C, Fang SL, Sumanasekera GU, Loper AL, Williams JH, Eklund PC. Single-wall carbon nanotubes from coal. Chem. Phys. Lett., 1999; 310: 31–37.
[14] Li J, Cao Y, Wang L, Jia D. Cost-effective synthesis of bamboo-structure carbon nanotubes from coal for reversible lithium storage. RSC Adv., 2017; 7: 34770-34775.
[15] Mathur RB, Seth S, Lal C, Rao R, Singh BP, Dhami TL, Rao AM. Co-synthesis, purification and characterization of single- and multi-walled carbon nanotubes using the electric arc method. Carbon, 2007; 45: 132–140.
[16] Pang LSK, Vassallo AM, Wilson MA. Coal as feedstock for fullerene production and purification. ACS Division of Fuel Chemistry preprints. 1992; 37: 564-567.

[17] Fang S, Shen L, Zhang X. Application of carbon nanotubes in lithium-ion batteries. Industrial applications of carbon nanotubes; Peng, H., Li, Q., Chen, T. Eds.; Elsevier, 2017; Chapter 9; p. 251-276.
[18] Sehrawat P, Julien C, Islam SS. Carbon nanotubes in Li-ion batteries: A review. Mater. Sci. Eng. B Solid State Mater. Adv. Technol., 2016; 213: 12–40.
[19] Yan Y, Li C, Liu C, Mutlu Z, Dong B, Liu J, Ozkan CS, Ozkan M. Bundled and dispersed carbon nanotube assemblies on graphite superstructures as free-standing lithium-ion battery anodes. Carbon. 2019; 142:238-244.
[20] de las Casas C, Li W. A review of application of carbon nanotubes for lithium ion battery anode material. J. Power Sources., 2012; 208: 74-85.
[21] Zhang YP, Chen TQ, Wang J, Min G, Pan L, Song Z, Sun Z, Zhou W, Zhang J. The study of multi-walled carbon nanotubes with different diameter as anodes for Lithium-ion batteries. Appl. Surf. Sci., 2012; 258: 4729-4732.

To whom correspondence should be addressed: Dr. Lina Kieush, National Metallurgical Academy of Ukraine, 49600, Gagarina av., 4, Dnipro, Ukraine, linakeush@gmail.com

Petroleum and Coal

Article **Open Access**

ENHANCING LUBRICITY OF DRILLING FLUID USING NANOMATERIAL ADDITIVES

Asawer A. Alwasitti[1], Nada S. Al-Zubaidi[2] and Massara Salam[1]*

[1] *Petroleum Technology Department, University of Technology, Iraq*
[2] *Department of Petroleum Engineering, College of Engineering, University of Baghdad, Iraq*

Received January 30, 2019; Accepted March 26, 2019

Abstract

Poor lubricity and high friction between the drill string and wellbore/casing in directional and horizontal wells causes excessive torque and drag which is one of the most important issues in the drilling stage of oil wells. An important function of drilling fluids is the reduction of frictional forces between the drill string and wellbore/casing. In this research, the enhancement of the lubrication behaviour of a KCl polymer mud is fundamentally examined by adding different amounts of xanthan gum nanoparticles (XC polymer NPs), barite NPs, and lignite NPs.

The lubricity, rheology and filtration properties of the KCl polymer mud are measured at room temperature. KCl polymer mud with the best concentration, that yielded good results in improving coefficient of friction (COF), of XC polymer NPs, barite NPs, and lignite NPs was tested at two different temperatures 75°C, 100°C, and for 6 hours to investigate the effect of aging at high temperature towards KCl polymer mud with nanomaterials.

The nanomaterials show a reasonable reduction in the coefficient of friction. The coefficient of friction reduction percentage is increased with increasing nanomaterial weight, and the maximum value of the coefficient of friction reduction (more than 60%) is attained by adding 4 gm XC polymer NPs. Also, adding 4gm lignite NPs to KCl polymer mud caused 51.49% reduction in COF. While barite NPs has a limited friction reduction. Also, the results show an increase in the rheological properties (average viscosity, yield point, plastic viscosity, and gel strength) with increasing nanomaterial amounts except for the lignite NPs (mud thinner). By adding the best concentration of XC polymer NPs, and lignite NPs to KCl polymer mud, lubrication behavior was maintained unchanged after aging at 100°C, and for 6 hours.

Keywords: *KCl drilling fluid; lubricity; nanomaterials; thermal agent.*

1. Introduction

In the process of drilling, the friction, high torque, and drag, which result from the drill string and wellbore/casing interactions, causes over pullsin trip-outs, pipe stuck and even well loss. Furthermore, inside the casing, the energy that is formed from metal-metal surface contact between the drill string and casing causes casing wear [1].

When the contact surfaces have been immersed in a fluid, such as the drilling fluid, the force required to move the surfaces is usually reduced. Thus, the drilling fluid lubricates the drill string.

The coefficient of friction (CoF) provides a measure of the frictional forces encountered during the drilling stage of a well; a reduction in the CoF obtained by the drilling fluid is a function of the fluid composition [2].

Oil-based and synthetic-based drilling fluids generally produce lower friction and torque values than do water-based drilling fluids. However, these oil-based and synthetic-based drilling fluids are severely limited because of high costs and environmental concerns. As a solution, it appears that it would be advantageous to identify a water-based drilling fluid system with added lubricants that are environmentally friendly, cost-effective and lubricious similar to oil-based and synthetic-based drilling fluids [1].

Researchers have shown that using nanomaterials in drilling fluids enhanced the lubricity of the water-based drilling fluid system. Jahns investigated titanium and silica nanoparticles, which effectively reduced the friction factor of drilling fluids [3]. Taha & Lee studied the improvement in drilling fluid performance by using nanographene, and they reported an 80% torque reduction using 5% by volume of an engineered nano graphene product [4]. Krishnan *et al*. improved the lubricity of water-based drilling fluid by using a boron-based-nanomaterial-enhanced additive (PQCB), and they showed that the addition of 5% by volume of this additive resulted in an 80% torque reduction [5]. Caldarola *et al*. studied the effect of barite nanoparticles on the lubricity of a water-based drilling fluid, and they indicated a reduction in the coefficient of friction of more than 34 % with a concentration of 3% by weight of the chemically generated barite nanoparticles and a reduction of more than 15% with the mechanically generated nanoparticles [6]. Abdo & Al-Sharji showed the effect of using nano-sepiolite (NSP) on the lubricity of drilling fluids, and they determined that the friction was reduced by approximately 34 % at high-temperature high-pressure HTHP when a concentration of 4% by weight of NSP was used in a water-based lignosulfonate drilling fluid [7]. Al-Ogaili & Suripis evaluated the effect of the addition of TiO_2 nanoparticles on the rheology, filtration and lubricity characteristics of drilling fluid, and they reported an average torque reduction of 24% for amounts lower than 1g of TiO_2 in water-based mud [8]. Dhiman investigated the impact of different nanoparticles on various drilling fluid properties, including rheology, filtration, and lubricity [9]. Belayneh *et al*. showed the effect of titanium nitride (TiN), MoS_2 and graphene nanoparticles on the properties and performance of water-based drilling fluid [10-11].

A few researchers investigated the effect of nanoparticles on the lubricity behaviour of drilling fluid and more study should be conducted in this field. In this paper, experimental work has been conducted to minimize the lubricity coefficient of a KCl polymer mud using XC polymer nanoparticles, barite nanoparticles, and lignite nanoparticles.

2. Experimental work

2.1. Materials

2.1.1. Raw materials

The materials used in the preparation of the KCl polymer mud are bentonite, potassium chloride (KCl), caustic potash (KOH), low viscous polyanionic cellulose (PAC-LV), xanthan gum (XC-polymer), and barite. All the above materials were supplied from Oren Hydrocarbons Middle East Inc.

2.1.2. Nanomaterials

The nanomaterials used in this study are XC polymer, barite, and lignite with particle size 10-400, 112 and 63 nm, respectively.

2.2. Experiments

The effects of nanomaterials of different types and different amounts are explored in the KCl polymer mud, and the formulation of the KCl polymer mud is shown in Table 1.

Table 1. Formulation of drilling fluids

Material	Concentration	Primary function
Distilled water, mL	350	Liquid phase
Bentonite, gm/350 mL	8	Viscosity and filter cake
KCl, gm/350 mL	10	Potassium source
KOH, gm/350 mL	0.5	pH and potassium
PAC polymer, gm/350 mL	2	Fluid-loss control and encapsulation
XC polymer, gm/350 mL	1	Low-shear viscosity
Barite, gm/350 mL	100	Density

A blank sample of the KCl polymer mud is prepared by mixing the bentonite with distilled water for 20 minutes, and the suspension is aged in a sealed container for 16 hours. Then, the KCl, KOH, PAC polymer, XC polymer, and barite are added to the bentonite suspension, and each material is left to mix with the suspension for 2 minutes to ensure the dispersion of particles into the drilling fluid matrix. Finally, the whole mixture is mixed for 10 minutes. The nanomaterials with amounts of (0.2, 0.5, 1, 2 and 4 gm) are added to the blank sample of the KCl polymer mud and mixed for 10 minutes using a Hamilton Beach mixer. Then, the samples are further mixed using an ultrasonic bath for 10 minutes to ensure good dispersion of nanomaterials in the drilling fluid samples.
Before any testing, the drilling fluid samples are remixed for a period ranging from 5 to 15 minutes. The lubricating and rheological properties of the drilling fluid samples are determined at room temperature using an OFITE EP lubricity tester and Model 900 viscometer, respectively. The filtration properties are measured under conditions of 100 psi and room temperature using an OFITE filter press.

Finally, the stability of the KCl polymer mud under the conditions of temperature and circulation with the optimum amount of each type of nanomaterial is investigated using an OFITE roller oven. All experiments were repeated three times, and the average had been taken to ensure the accuracy of the results

3. Results and discussion

3.1. Clay characterization analysis

3.1.1. X-Ray Fluorescence (XRF)

The X-Ray fluorescence (XRF) analysis of the bentonite that is used in the preparation of KCl polymer mud is shown in Table 2. The XRF analysis of bentonite showed a significant percentage of silicon oxide (SiO_2) and aluminum oxide (Al_2O_3), and a low percentage of potassium oxide (K_2O) which means that bentonite is composed of mostly montmorillonite.

Table 2. XRF analysis of bentonite

SiO_2 %	Fe_2O_3 %	Al_2O_3 %	CaO %	MgO %	SO3 %	LOI %	P_2O_5 %	Na_2O %	K_2O %
49.98	10	17.5	4.4	4.9	0.16	8.49	0.62	2.24	0.12

3.1.2. X-Ray diffraction (XRD)

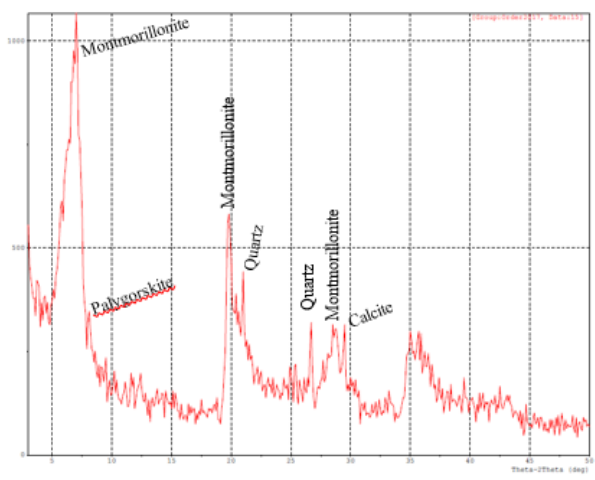

The X-Ray diffraction (XRD) analysis of the commercial bentonite is shown in Figure 1. As discussed in the previous section, the major component of bentonite is montmorillonite and quartz. The minor components are palygorskite and calcite.

Figure 1. XRD Analysis of bentonite

3.1.3. Particle size distribution

The particle size distribution of bentonite, lignite NPs and barite NPs are shown in Figures 2-5. The results of particle size distribution analysis show that the average size of bentonite is 238

nm, lignite NPs is 63 nm, and barite NPs is 112 nm. While the size of XC polymer NPs ranging from 10.6 to 5. The 8 nm to 339.68 nm.

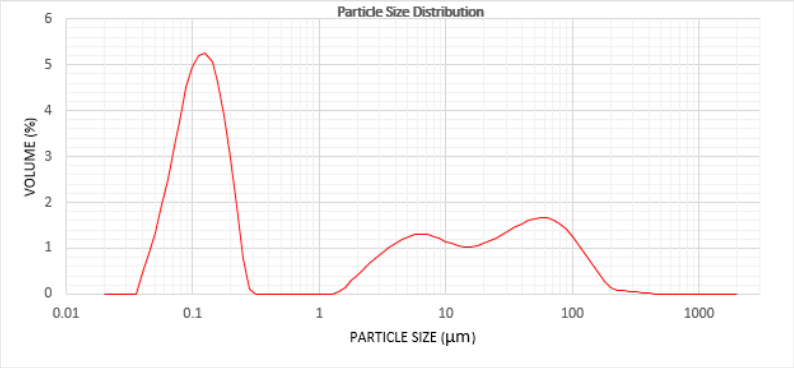

Figure 2. Particle size distribution of bentonite

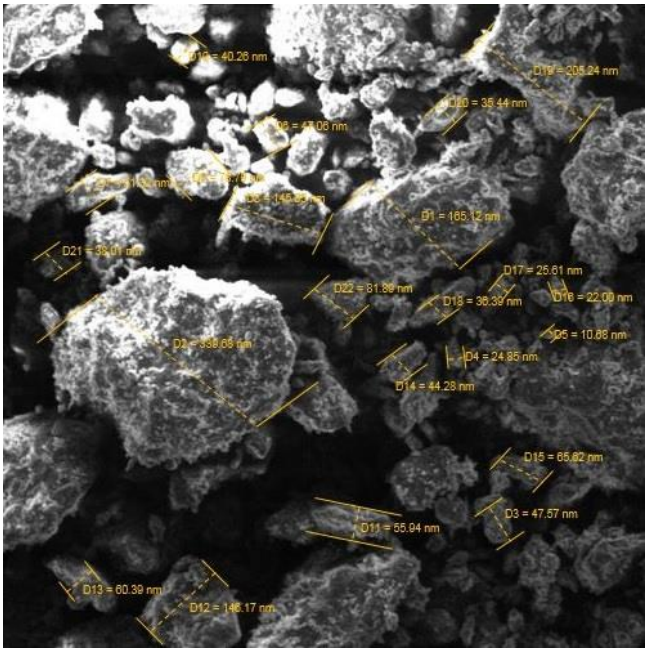

Figure 3. SEM image of XC polymer NPs

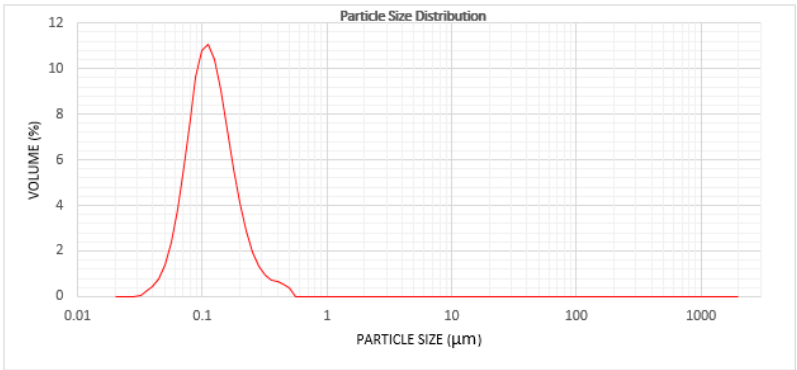

Figure 4. Particle size distribution of barite NPs

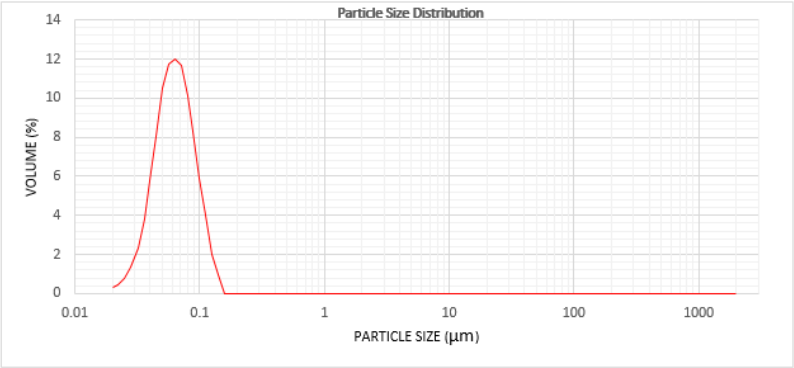

Figure 5. Particle size distribution of lignite NPs

3.2. Lubrication behaviour

To study the effects of nanomaterials on the lubricating properties of a water-based drilling fluid system, XC polymer NPs, barite NPs, and lignite NPs are added at different amounts to blank samples of the KCl polymer mud. The results are presented in Table 3.

Table 3. CoF and CoF reduction % of KCl polymer mud with nanomaterials

W_t, g	$\%W_t$	CoF	CoF reduction %	W_t, g	$\%W_t$	CoF	CoF reduction %
Blank	-	0.367	-	Blank	-	0.367	-
Blank + XC Polymer NPs				Blank + Barite NPs			
0.2	0.04	0.349	4.9	0.2	0.04	0.323	11.98
0.5	0.1	0.312	14.98	0.5	0.1	0.315	14.16
1	0.2	0.329	10.35	1	0.2	0.308	16.07
2	0.4	0.268	26.97	2	0.4	0.332	9.53
4	0.8	0.139	62.12	4	0.8	0.357	2.72
Blank + Lignite NPs				0.2	0.04	0.323	11.98
0.2	0.04	0.288	21.52				
0.5	0.1	0.226	38.41				
1	0.2	0.215	41.41				
2	0.4	0.185	49.59				
4	0.8	0.178	51.49				

3.2.1. Effect of XC polymer nanoparticles

The Table 3 visualize the obtained CoF values of KCl polymer muds with different amounts of the XC polymer NPs .-The highest CoF reduction (62.12 %) is generated with a weight of 4 gm. As the amount of the XC polymer NPs increases, the CoF value of the KCl polymer mud decreases.

XC polymer NPs show a mixed lubrication regime [13], which means it acts as a boundary lubricant and establishes a high-strength thin film at the contacting surfaces when the speed is too low, and the load is too high. When the load is decreased, and the speed is increased, the XC polymer NPs act as a hydrodynamic or elastohydrodynamic lubricant and form a wedge-shaped film between the contacting surfaces. In both situations, the result is a complete separation of the contacting surfaces, reducing the frictional forces between them.

3.2.2. Effect of barite nanoparticles

Table 3 show that the addition of barite NPs to the KCl polymer mud causes a reduction in the CoF value, and better lubrication results are observed with low amounts (≤ 1gm), where the maximum reduction in the CoF (16 %) is gained using the weight of 1 gm. At high amounts (more than 1 gm), the general trend is inverted, where the CoF is increased with increasing barite NP amount. However, this value remains less than the CoF value of the blank sample.

Barite is a soft, lamellar, crystalline material and as a result of these properties and structure, it can act as a lubricant due to its ability to form a low shear strength film on the contacting surfaces and thus reducing the CoF [14-15].

At an amount of 1 gm, a maximum reduction in the CoF is observed due to the formation of a complete low shear strength film, which explains why the CoF increases with an increasing barite NP amount above the amount of 1 gm.

3.2.3. Effect of lignite nanoparticles

The CoF values of the KCl polymer mud with different amounts of lignite NPs are illustrated in Table 3. The CoF values of the KCl polymer mud with different amounts of lignite NPs are illustrated in Table 4. According to the results, the KCl polymer mud with an amount of 4 gm shows a 51.49 % reduction in the CoF. As the amount of lignite NPs increases, the CoF value of the KCl polymer mud decreases. According to the XRD study, lignite has a random layer lattice structure (graphite-like structure) [16]. For this reason, lignite may act as graphite (self-lubricating solid material) and form a film between the contacting surfaces. As a result of the film formation, the friction between the contacting surfaces could be reduced.

3.3. Rheological properties

After the addition of nanomaterials to the drilling fluids, the rheological properties may change. Therefore, it is essential to investigate the effects of these nanomaterials on rheological behaviour. The rheological properties (including PV, YP, AV, gel strength), KCl polymer mud with different concentrations of nanomaterials, are illustrated in Table 4.

Table 4. Rheological properties of KCl polymer mud with different concentrations of nanomaterials

Wt (g)	% Wt	PV (cP)	YP (lb/100 ft²)	AV (cP)	YP/PV (lb/100 ft²/cP)	10 sec gel	10 min gel
Blank	----	14.6	27.9	27.85	1.91	6.4	19.2
Blank + XC Polymer NPs							
0.2	0.04	17	48.7	39.95	2.864	17.4	38.3
0.5	0.1	18.8	60.5	49.05	3.218	33.1	42.4
1	0.2	18.2	68.2	50.3	3.747	39	44.7
2	0.4	22.6	82.7	61.45	3.659	35.8	57.4
4	0.8	27.4	125.7	86.4	4.587	71.4	87.8
Blank + Barite NPs							
0.2	0.04	17.7	27.2	31.3	1.536	6.6	24.4
0.5	0.1	17.8	30.3	32.05	1.702	8.1	24.2
1	0.2	17.8	30.9	32.1	1.735	8.1	23.5
2	0.4	16.9	32.5	32.25	1.923	8.2	22.3
4	0.8	16.8	34.1	32.9	2.029	8.6	24
Blank + Lignite NPs							
0.2	0.04	17.5	35.1	35.05	2.005	11.5	38.7
0.5	0.1	20.4	34.3	36.55	1.681	8.8	24.8
1	0.2	22.2	33	37.4	1.486	6.8	17.6
2	0.4	25.6	27.4	38.4	1.070	6.7	17
4	0.8	22.4	26.8	34.5	1.196	5.8	16.6

3.3.1. Effect of nanomaterials on plastic viscosity

The results in Table 4 show that the addition of nanomaterials causes an increase in plastic viscosity compared with that of the blank sample. However, the plastic viscosity increases as XC polymer NPs amount increase while increasing amounts of the barite NPs above the amount of 0.2 gm do not show any effects on the plastic viscosity value.

Plastic viscosity is part of the resistance to flow caused by mechanical friction. An increase in the number of solids, a reduction in the size of the solid particles, and an increase in the total surface area of solids exposed will all increase the plastic viscosity. Nanomaterials have

a large surface area per volume, which increases the interaction of nanomaterials with the drilling fluid matrix. The nanomaterials may then link or bond directly, through an intermediate chemical linkage, with the drilling fluid matrix, causing an increase in plastic viscosity. On the other hand, the reduction of the plastic viscosity is due to a repulsive force between nanomaterials and the drilling fluid matrix.

3.3.2. Effect of nanomaterials on the yield point

The yield point of the KCl polymer mud with different amounts of nanomaterials. The results show that the addition of nanomaterials causes an increase in the yield point compared with the blank sample, and the greatest increase in yield point value is obtained using the XC polymer NPs (125.7 lb/100 ft² at an amount of 4 gm).

The yield point is a measurement of the attractive forces (resulting from negative and positive charges located on or near the particle surfaces) in a drilling fluid under flow conditions. The yield point is increased with the addition of nanomaterials (as that with the addition of XC polymer NPs and barite NPs), and this may be due to the more effective dispersion ability of nanomaterials on the surface of bentonite, increasing the attractive force between them. Sometimes, the yield point decreases upon the addition of nanomaterials (as that with the addition of lignite NPs with high amounts), and this may be due to a repulsive force that occurs between the nanomaterials, water molecules, and bentonite particles [19].

3.3.3. Effect of nanomaterials on apparent viscosity

The results in Table 4 show that the addition of nanomaterials causes an increase in the apparent viscosity compared with that of the blank sample, and the greatest increase in apparent viscosity is recorded using the XC polymer NPs (86.4 cP ft² at a weight of 4 gm).

While the trends of the barite NPs and lignite NPs slightly increase with the increasing amount, an exception is that of the lignite NPs with an amount of 4 gm, causing a decrease in the apparent viscosity.

3.4. Filtration properties

The filtration properties of the KCl polymer mud with different amounts of nanomaterials are presented in Table 5.

Table 5. Filtration properties of KCl polymer mud with different concentrations of nanomaterials

Wt (g)	% Wt	Density (ppg)	PH meter	PH paper	Stability %	V7.5 (ml)	V30 (ml)	Mud cake thickness, (mm)
Blank	----	10	10.75	12	100	4	8	0.622
Blank + XC Polymer NPs								
0.2	0.04	10	10.17	12	100	4.2	8.4	0.488
0.5	0.1	10	10.06	10	100	4.4	8.8	0.488
1	0.2	10.1	9.89	10	100	3.8	7.6	0.586
2	0.4	10.12	9.74	10	100	3.4	6.8	0.672
4	0.8	10.15	8.94	9	100	3.6	7.2	0.572
Blank + Barite NPs								
0.2	0.04	10	10.65	12	100	3.8	7.6	0.368
0.5	0.1	10.1	10.58	12	100	4	8	0.448
1	0.2	10.12	10.55	12	100	4.2	8.4	0.458
2	0.4	10.15	10.53	12	100	4.2	8.4	0.554
4	0.8	10.2	10.42	12	100	4.2	8.4	0.778
Blank + Lignite NPs								
0.2	0.04	10	9.69	10	100	3.4	6.8	0.49
0.5	0.1	10.2	9.34	10	100	3.4	6.8	0.478
1	0.2	9.9	9.18	10	100	3.4	6.8	0.444
2	0.4	8.6	9.20	10	99	3.6	7.2	0.396
4	0.8	8.3	9.16	10	98	4	8	0.356

The Table 5 shows–barite NPs have no effect on the filtrate loss volume. The XC polymer NPs at low amounts (≤ 0.5 gm) cause a slight increase in the filtrate loss volume, while high amounts (≥ 1 gm) cause slight decreases in filtrate loss volume. The lignite NPs cause slight decreases in filtrate loss volume, and this trend increases with increasing the amount. The lowest value of filtrate loss volume (3.4 ml, 51% reduction in filtrate loss volume) is generated by using 2 gm XC polymer NPs and 0.2 to 1 gm lignite NPs.

The Table 6 shows that a decrease in mud cake thickness is obtained with the use of the XC polymer NPs, barite NPs, and lignite NPs.

Additionally, the XC Polymer NPs shows irregular increasing and decreasing behaviours in mud cake thickness as the weight increases, while increasing the barite NP weight increases the mud cake thickness. This thickness decreases with increasing lignite NP amounts, and the lowest value of mud cake thickness (0.356 mm, 42.76% reduction in mud cake thickness) is obtained with the use of 4 gm lignite NPs.

The addition of nanomaterials to the drilling fluid causes an increase in the filtrate loss volume, and this may be explained due to the solid accumulation that makes the mud less stable; this means an impermeable and low porosity mud cake cannot be obtained, and more filtrate can pass through the mud cake. On the other hand, nanomaterials may cause a decrease in the filtrate loss volume, and this may be explained due to the ability of nanomaterials to seal the nanopore throats of the wellbore formation and prevent water infiltration [20-21]. The results indicate that the role of nanomaterials in improving the drilling fluid performance is dependent on the type and the amount of nonmaterial used.

3.5. Effect of temperature on lubrication behaviour and rheological properties of KCl polymer mud with nanomaterials

The effect of temperature and circulation on KCl polymer mud with an optimum concentration of each type of nanomaterials is shown in Table 6.

Table 6. Effect of temperature and aging on KCl polymer mud with nanomaterials

T (°C)	CoF	PV (cP)	YP (lb/100 ft²)	AV (cP)	YP/PV (lb/100 ft²/cP)	10 sec gel	10 min gel
Blank							
35	0.367	14.6	27.9	27.85	1.91	6.4	19.2
75	0.399	33.7	63.5	63.4	1.88	27.1	28.5
100	0.279	22.7	61.7	51.8	2.71	28.8	39.5
Blank+ 4 gm XC Polymer NPs							
35	0.139	27.4	125.7	86.4	4.587	71.4	87.8
75	0.148	25.1	148.7	95	5.924	88.2	100.8
100	0.138	20.9	126.7	80.3	6.06	73.3	81.9
Blank+ 1 gm Barite NPs							
35	0.308	17.8	30.9	32.1	1.735	8.1	23.5
75	0.288	17.2	69.3	50	4.029	32.4	37.4
100	0.172	17.5	79	54.7	4.51	37.8	43.5
Blank + 4 gm Lignite NPs							
35	0.178	22.4	26.8	34.5	1.196	5.8	16.6
75	0.179	24.3	24.5	36.05	1.01	6.4	17.5
100	0.18	23.7	33.9	39.85	1.43	7.9	24

The increasing the temperature to 75°C causes an increase in the CoF values of the blank sample and with XC polymer NPs. At a temperature of 100°C, the CoF values of these samples are either equal to or less than their values at 35°C, while the CoF values of the barite NP samples decrease with increasing temperature. Increasing the temperature has no effect on the CoF values of the KCl polymer mud with the lignite NPs.

The increasing the temperature to 75°C causes an increase in the PV, YP and AV values of the blank sample and the sample with lignite NPs; at a temperature of 100°C, the PV values

of these samples are less than the values at 75°C. These values slightly decrease with increasing temperatures of the XC polymer NPs. Increasing the temperature has no effect on the PV value of the KCl polymer mud with the barite NPs.

4. Conclusions

Nanomaterials promise a reduction in the coefficient of friction of KCl polymer drilling fluid. The addition of barite NPs, with amounts up to 1 gm, to the KCl polymer drilling fluid, can reduce the CoF up to 16%. XC polymer NPs with amounts up to 4 gm can reduce the CoF up to 60%in the KCl polymer mud.

Generally, nanomaterials (XC polymer NPs and barite NPs) increased rheological properties (PV, YP, AV, and gel strength), except lignite NPs which is a mud thinner. XC Polymer NPs with the best concentration (weight of 4gm) improved filtration properties of KCl polymer mud. The reduction percentages in filtrate volume and mud cake thickness were 10% and 8% respectively. Nanomaterials (XC polymer NPs and lignite NPs) with the best concentration-maintained lubrication behavior of KCl polymer mud after aging at 100°C for 6 hours.

References

[1] Sönmez A, Kök MV and, Özel R. Performance analysis of drilling fluid liquid lubricants. Journal of Petroleum Science and Engineering, 2013; 108: 64-73.

[2] Redburn M, Dearing H and, Growcock F. Field Lubricity Measurements Correlate with Improved Performance of Novel Water-Based Drilling Fluid. in the 11th Offshore Mediterranean Conference and Exhibition, Ravenna, 2013.

[3] Jahns C. Friction Reduction by using Nano-Fluids in Drilling, Master of Science Thesis, Trondheim: Norwegian University of Science and Technology/Department of Petroleum Engineering and Applied Geophysics, 2014.

[4] Taha NM and, Lee S. Nano Graphene Application Improving Drilling Fluids Performance. in International Petroleum Technology Conference, Doha, 2015.

[5] Krishnan S, Abyat Z, and Chok C. Characterization of Boron-Based Nanomaterial Enhanced Additive in Water-Based Drilling Fluids: A study on Lubricity, Drag, ROP, and Fluid Loss Improvement," in SPE/IADC Middle East Drilling Technology Conference and Exhibition, Abu Dhabi, 2016.

[6] Caldarola V, Akhtarmanesh S, Cedola A, Qader R and, Hareland G. Potential Directional Drilling Benefits of Barite Nanoparticles in Weighted Water-Based Drilling Fluids. in the 50th US Rock Mechanics/Geomechanics Symposium, Houston, 2016.

[7] Abdo J and, Al-Sharji H. ffect of Nano-Clays on The Lubricity of Drilling Fluids. in the ASME 2016 International Design Engineering Technical Conferences and Computers and Information in Engineering Conference IDETC/CIE 2016, Charlotte, 2016.

[8] Al-Ogaili FHA and Suripis N. Evaluation of Nanoparticles in Enhancing Drilling Fluid Properties. International Journal of Scientific & Engineering Research, 2016; 7(10): 1489-1497.

[9] Dhiman P. Experimental Investigation of The Influence of Various Nanoparticles on Water-Based Mud. Master's Project, Fairbanks: University of Alaska Fairbanks/Department of Petroleum Engineering, 2016.

[10] Vegard B and. Belayneh M. The Effect of Titanium Nitride (TiN) Nanoparticle on The Properties & Performance Bentonite Drilling Fluid. International Journal of NanoScience and Nanotechnology, 2017; 8(1): 25-35.

[11] Wrobel S and, Belayneh M. The Effect of MoS_2 and Graphene Nanoparticles on The Properties and Performance of Polymer/Salt Treated Bentonite Drilling Fluid. International Journal of NanoScience and Nanotechnology, 2017; 8(1): 59-71.

[12] Guo D, Xie G and, Luo J. Mechanical properties of nanoparticles: basics and applications. Journal of Physics D: Applied Physics, 2014; 47(1): 013001.

[13] de Vicente J, Stokes J and, Spikes H. Lubrication properties of non-adsorbing polymer solutions in soft elastohydrodynamic (EHD) contacts. Tribology International, 2005; 38(5): 515–526.

[14] NASA, Lubrication, Friction, and Wear, 1971.

[15] Kogel JE, Trivedi NC, Barker JM and, Krukowski ST. Industrial Minerals & Rocks: Commodities, Markets, and Uses, 7th ed., vol. 14, Colorado: Society for Mining, Metallurgy, and Exploration, Inc., 2006, pp. 1192-1197.

[16] Msagati T, Mamba B, Sivasankar V and, Omine K. Surface restructuring of lignite by biochar Cuminum cyminum – Exploring the prospects in de-fluoridation followed by fuel applications. Applied Surface Science, 2014; 301: 235-243.
[17] AR Ismail, TC Seong, NA Buang and WRW. Sulaiman Improve Performance of Water-based Drilling Fluids Using Nanoparticles. in 5th Sriwijaya International Seminar on Energy and Environmental Science & Technology, Palembang, 2014.
[18] Salih AH, Elshehabi TA and Bilgesu HI. Impact of Nanomaterials on the Rheology and Filtration Properties of Water-Based Drilling Fluids. in the SPE Eastern Regional Meeting, Canton, 2016.
[19] Amarfio EM and, Abdulkadir M. Effect of Fe_4O_3 Nanoparticles on the Rheological Properties of Water-Based Mud, Journal of Physical Science and Application, 2015; 5(6): 415-422.
[20] Ismail AR, Rashid NM, Jaafar MZ, Sulaiman WRW, and. Buang NA Effect of Nanomaterial on the Rheology of Drilling Fluids. Journal of Applied Sciences, 2014; 14(11): 1192-1197.
[21] Aftab A, Ismail A and Ibupoto Z. Enhancing the rheological properties and shale inhibition behaviour of water-based mud using nano silica, multi-walled carbon nanotube, and graphene nanoplatelet. Egyptian Journal of Petroleum, 2017; 26(2): 291–299.

To whom correspondence should be addressed: Dr. Asawer A. Alwasitti, Petroleum Technology Department, University of Technology, Iraq, e-mail: 150003@uotechnology.edu.iq

Petroleum and Coal

Article **Open Access**

METHOD OF CALCULATION OF OIL-WATER MIXTURE DENSITY AT THE BOTTOM-HOLE WITH THE PRESSURE EXCEEDING GAS SATURATION PRESSURE OF OIL

Valeriy A. Kostilevsky

Lukoil Zapadnaya Sibir LLC, Kogalym, Russian Federation

Received February 9, 2019; Accepted April 4, 2019

Abstract

Based on the analysis of the vertical drift flow structure, we propose the experimental method for calculating the density of oil-water mixture at the bottomhole of the wellbore which considers well gross rate, water cut, diameter of production string, as well as density of oil and water. This formula is applicable for calculations of the pressure from the fluid column at the bottomhole section of the lower reservoir under condition of applying dual pump production technology for calculation of the well operation modes.

Keywords: *Oil-water mixtures; Dual pump production technology.*

1. Introduction

One of the key issues in performing well studies and obtaining required information during the dual production is measuring bottomhole and formation pressure of the reservoirs [1]. In the West Siberian region of Russia, a dual production technology using dual electric submersible pumps with common downhole motor drive, has become very widespread [2-3]. With that the most important parameter for calculation of bottomhole pressure and well operation modes is average fluid density at the bottomhole of the wellbore. This problem is severed in dual oil production technologies applied for stacked reservoirs, especially for the lowest reservoir with restricted measurement capabilities. This raises the necessity to improve the calculation methods applied. Presently, the process of pressure measurement and calculation in the perforation interval is significantly complicated by water cut, especially when suction pressure becomes less than gas saturation pressure of oil. The difficulty in pressure measurement in the perforation interval is caused by inability to run the downhole gauge to the perforation interval. The top of the upper pay zone is located much lower of the ESP intake, and it is impossible to run a pressure gauge to the top of the upper reservoir, also due to the presence of sliding slot in the intake nozzle of the dual pump lower section.

In this work, we report an innovative approach towards the calculation of the density of oil-water mixture at the bottomhole, considering all key parameters, and discuss its applicability on the data obtained on Arlan oilfield (Bashkortostan, Russia).

2. Methods and theoretical background

Pressure measurement at the bottomhole is performed with maximum proximity of the gauges to the tops of both reservoirs, and the bottomhole and formation pressure is determined through empirical dependence. For the upper reservoir the pressure gauge is installed inside the ESP telemetry system (TMS), and for the lower- at the level of sliding slot in the intake nozzle of the lower pump. In this case the gauge is installed in the lower tubing at the intake nozzle of the lower reservoir pump.

Earlier studies were carried out on the density of water-oil mixture in the bottomhole section from the pump intake to the reservoir top using gamma-density meter, which allows to

obtain the parameters of the dual-phase flow, which include fluid density at the bottomhole and the actual phases content in the production string. The tool provides registration of gamma rays, which are absorbed proportionally to the density of the fluid under study (Arlan Oilfield) [4].

When processing the results of the study the average fluid density was taken into account between the reservoir top and the level corresponding to the gas saturation pressure of oil ($\rho_{sat} \approx 8$ MPa). Having the value of the actual density of the oil-water mixture ρ_l at depth, water density ρ_w and oil density ρ_o, the actual water content of the mixture was determined by the formula (1)

$$\varphi = \frac{\rho_l - \rho_{sat}}{\rho_w - \rho_o} \quad (1)$$

It is known that the actual water content φ varies from 0 to 1, i.e. from complete filling of the string with oil to complete filling with water. The value (1-φ) characterizes the actual oil content at the bottomhole. Direct measurement of the actual fluid density combined with measurements of water cut, BHA performance and density of oil and water in the surface conditions allows for determination of almost all flow parameters. These include the actual and the relative phase velocity, density of oil drift flow, the actual content of oil and water, maximum oil flow rate through a fixed water column and flooding conditions for the drift flow.

Cross-sectional areas Ω_o and Ω_w relate to the volumes occupied by oil and water in the string.

Therefore $\varphi = \Omega_o/\Omega_w$, Qo=$Q_{well}$-$Q_w$ and B= Q_w/Q_{well}.

It results in obvious ratio for calculation of relative oil flow speed "u" (Formula 2)

$$u = \frac{(\varphi - B)}{\varphi(1-\varphi)}\,\omega_c \quad (2)$$

where $\omega_s = Q_{well}/\Omega$; Ω – string cross section.

The author analyzed the data of earlier studies of fluid density performed in Arlan field wells. The measurements were made by lowering the subsurface pressure gauge through the annulus past the pump to the bottom hole [4]. Experimental records of density values in almost all cases demonstrated a spike in fluid density at the transition point from oil to water column (Fig. 1).

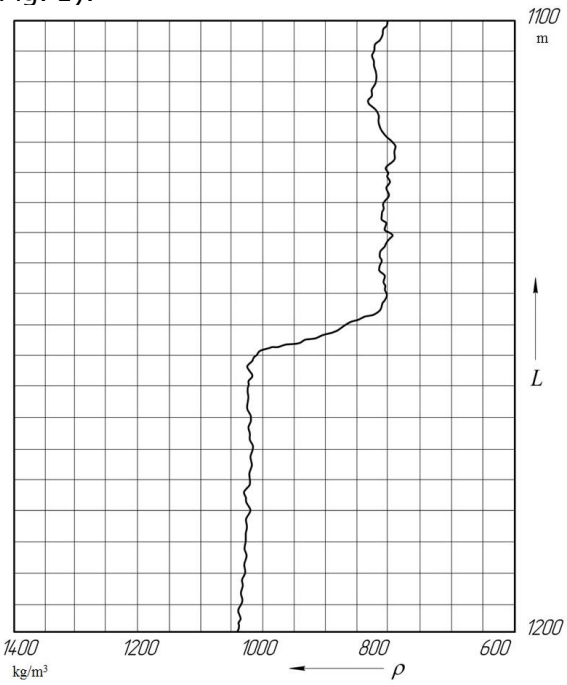

Right above the pump intake in the annulus there was oil column with 830-870 kg/m^3 density. Under the pump the fluid density increased abruptly up to 1080-1150 kg/m^3. This spike in density tells about the phase inversion at the level of the pump intake.

Additionally empirical dependence of the average oil and water emulsion speed on the parameter $\frac{1-\varphi}{1-B}$ obtained during the Arlan field studies. The nature of vertical drift flow illustrated by the dots on the graph showed linear interrelation between the parameters, described by the formula 3:

$$\frac{1-\varphi}{1-B} = 0{,}136\ \omega_c \quad (3)$$

Figure 1. Change in fluid density in well 3426 at the level of pump intake

3. Results and discussion

Based on the data reported in [4], by substituting φ with its expression in (3), and ω_s with Q_{well}/Ω, the authors obtained the expression for calculation of fluid density at the bottomhole section of the wellbore (Formula 4):

$$\rho_f = \rho_o + [1 - 0{,}173\ Qwell(1 - B)/D_c^2](\rho_w - \rho_o) \quad (4)$$

where D_C is the inside diameter of production string.

The resulting experimental formula (4) allows for high precision calculation of pressure at the formation top with known values of Q_{well}, D_c, B, ρ_w, ρ_o and gas absence using the already used formula:

$$P_{bth} = \rho_f g H \quad (5)$$

where H is the height of the fluid column between the formation top and the downhole gauge in the production string.

It should be noted that the formula (5) can be used with bottomhole values not exceeding the respective values of gas saturation pressure of oil P_{sat}. Beyond this level, the release of gas begins, i.e. the fluid density will start changing along the wellbore, and the bottomhole pressure $P_t < P_{sat}$ will be determined by a different value.

Conclusion

We suggest that the calculation based on the experimental formula should be applied for the cases when it is impossible to perform pressure measurement in the perforated interval using downhole pressure gauges.

References

1. Muslimov EYa. Overview of TNK-BP experience in dual production technologies/SPE Moscow Section Meeting. January 17. – 2012 – p38.
2. Valeev MD, Kostilevsky VA, Gorbatov VN, Minnahmedov TM, Sadrutdinov RR, Kan TV. Electrical submersible pump assembly for dual oil production. Patent RU No120461 U1. Application number No2012114038. Submitted on 10.04.2012. Published on 20.09.2012. Bul.26.
3. Kostilevsky VA. Analysis of dual oil production technologies applied in Western Siberia. Scientific-technical journal "Oilfield engineering", JSC "VNIIOENG". 2017; (8): 16 -20.
4. Valeev MD, Khasanov MM. Bottomhole pumping of viscous oil.–Ufa.: Bashknigoizdat._1992: 144.

To whom correspondence should be addressed: Dr. Valeriy A. Kostilevsky, Lukoil Zapadnaya Sibir LLC, Kogalym, Russian Federation

Petroleum and Coal

Article **Open Access**

FULL FIELD PRODUCTION OPTIMIZATION STUDY USING NODAL ANALYSIS TECHNIQUE

Reda Abdel Azim

Future University in Egypt Petroleum Engineering Department, Egypt

Received February 7, 2019; Revised April 4, 2019, Accepted April 24, 2019

Abstract

To better understand the well performance and forecast its future response, a PIPESIM model was built for each tested intervals of the currents wells excluding the intervals which are tested by swapping due to the high uncertainty of getting conclusive results from these types of test. These PIPESIM models simulate the actual inflow and outflow performance of the tested intervals with the same completion used during the DST results and depends on the initial condition of each well (initial reservoir pressure, well head pressure, and water cut value). Sensitivity Analysis is done for the different parameters (water cut, wellhead pressure, reservoir pressure, tubing diameter) produced from each reservoir. The field contains 10 wells, two of them exist in north area (J-1, and J-2), one in the central area (JC-1) and the others located at the south area (JS-1, JS-2, JS-3, JS-4, JS-5, JS-6, and JS-7).

Keywords: *Production Optimization; Nodal Analysis; Artificial Lift.*

1. Introduction

The studied field planned to produce from Bentiu and Abu Gabra formation. DST data are available from most of the existing wells testing each interval separately using natural flow completion. For the tight interval, the interval is tested by swabbing.

The objectives from the production technology study of the existing wells are summarized in the following points:

- Simulate the well performance using PIPESIM and forecast its performance by making sensitivity analysis on parameters affecting the well performance (i.e. well head pressure, reservoir pressure, water cut, tubing size).
- Choose the optimum completion for the producing wells.
- Screen the different Artificial lift (AL) methods to select the best candidate to produce all the wells.

2. Production technology workflow

Fig.1 shows the production technology workflow used to achieve the above-mentioned objectives. The next section details all the steps used in the nodal analysis sensitivity and the Artificial lift screening.

3. Vertical flow correlation selection

After building PIPESIM models for each perforation interval, a correlation match module is used to choose vertical flow model that simulates the well flow performance. Fig. 2 shows the behavior of the different vertical flow correlations for well JS-1 with the tested interval (2452–2457 m) that is used to select the best vertical flow correlation based on the surface production rate. Table 1 summarizes the matched correlations for well JS-1 for both Bentiu and Abu Gabra reservoirs for each tested interval. From this analysis, it was found that HAGEDORN & BROWN

(HBR) [2] correlation is the best model to simulate the liquid vertical flow for the wells producing from Bentiu & Abu Gabra, while ANSRI correlation [3] is the best model to simulate the gas flow for the wells tested in the gas zone of Abu Gabra.

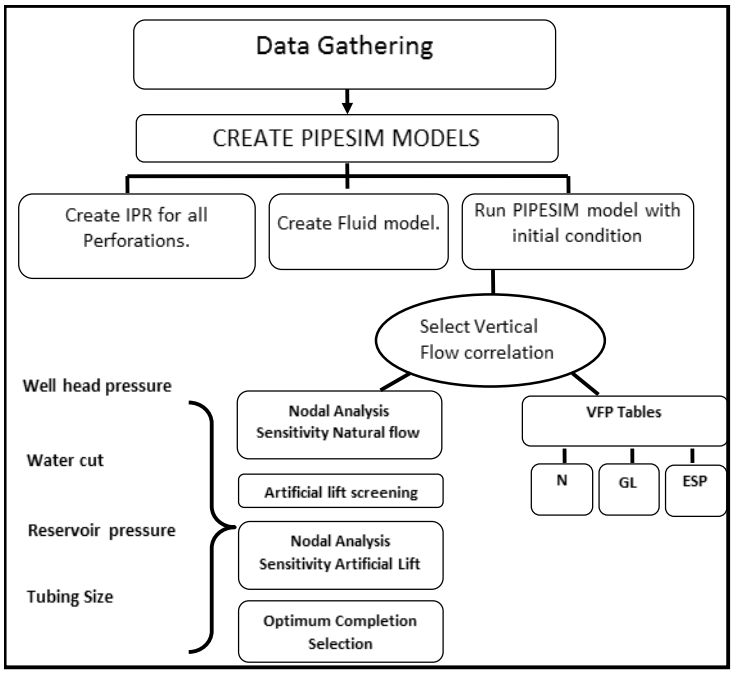

Fig. 1. Production technology workflow for the studied field

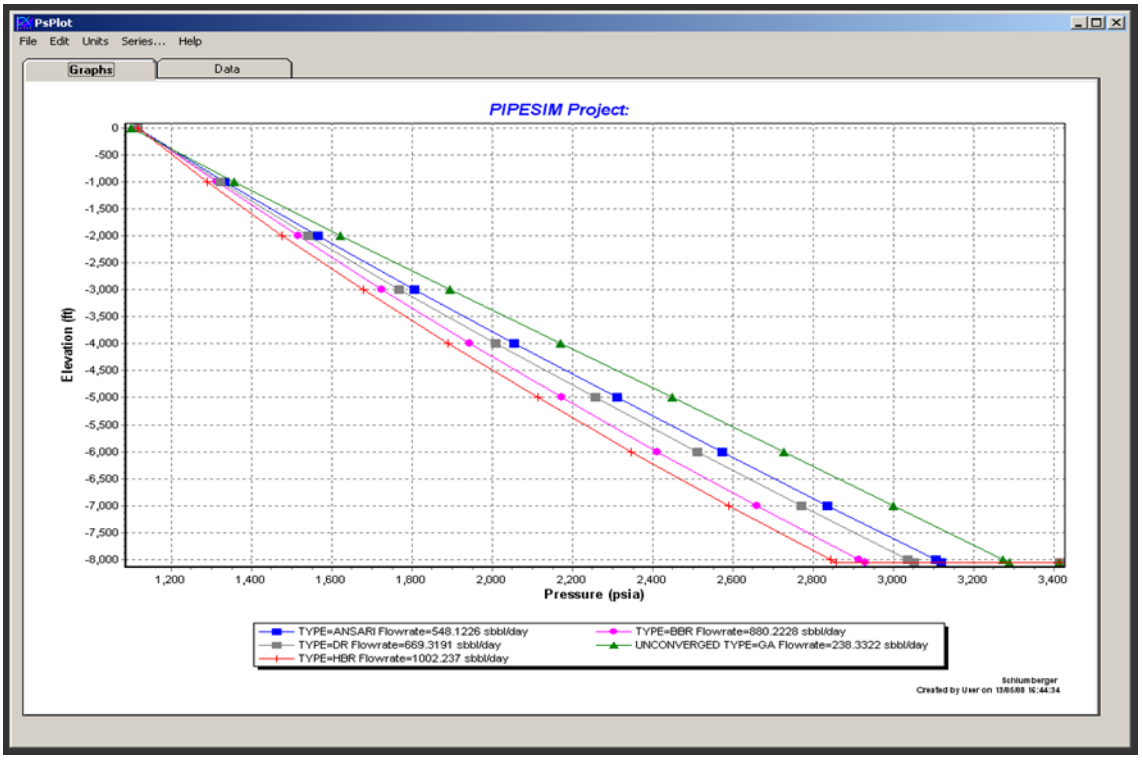

Fig. 2. Different vertical flow correlations for well JS-1 (interval 2452-2457m)

Table 1. Vertical flow correlation selection based on JS-1 test

Depth (m)	Formation	Correlation matched	Rate actual	Rate PIPESIM model	Status	Flowing pressure psi	PI DST, Bbl/d/psi	Reservoir Pressure psi
3038-3043	AG	--------	Traces	No model	swabbed		--	
2771-2775	AG	--------	Traces	No model	swabbed		--	
2566-2573	AG	ANSRI	8.9 MMscf/d	8.8 MMcf/d	Flowing naturally	3219	--	3550
2452-2457	AG	HBR	1011 bbl/d	990 bbl/d	Flowing naturally	3017	1.9	3400
1476-1483	Bentiu	HBR	603 bbl/d	612 bbl/d	Flowing naturally	1790	3.02	2033
1381-1384	Bentiu	HBR	491.2 bbl/d	512 bbl/d	Flowing naturally	1812	3.9	1916

4. Sensitivity scenarios for Bentiu Formation

This section gives detailed overview of the different sensitivity runs performed on one selected zone in Bentiu from well JS-1 as a sample.

4.1. Sensitivity scenarios for Bentiu Reservoir

The selected zone for Bentiu is from well JS-1 in the tested interval (1381 – 1384 m). The well parameters used to construct the PIPESIM model for this zone are as follows:

Tubing size = 2.441 inch (ID);
Flowing pressure = 1686 Psi (from DST data);
GOR= 100 SCf/Stb (from DST data);
WHP = 220 psi (from DST data)
Water cut = 0 % (from DST data);
Reservoir pressure= 1916 Psi (from RFT/DST data);
Gross rate = 512 BLPD (from DST data);

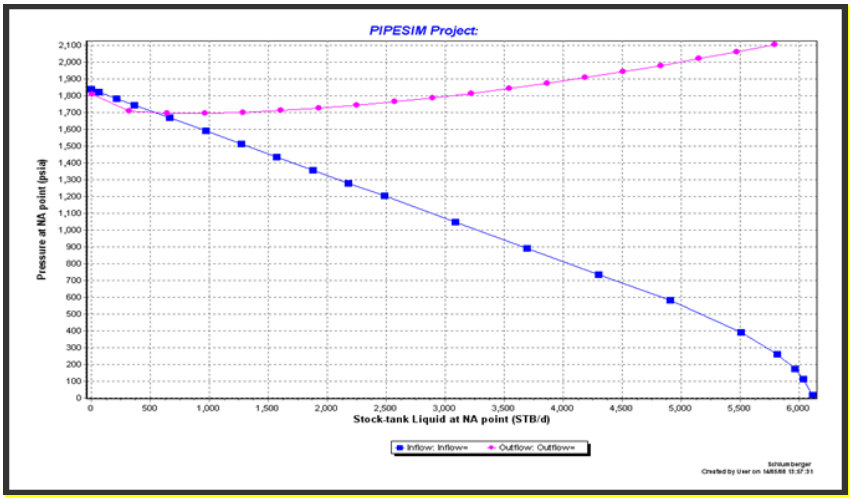

Fig.3. Nodal analysis model for the selected zone in Bentiu formation

Figure 3 gives the nodal analysis performance (inflow and outflow performance) with a schematic diagram showing the tested zone in well JS-1. The nodal analysis model parameters that match the current situation of the selected perforation interval in Bentiu are summarized in the following points:

- The Qmax (AOF) for this well = 6200 BBl /day, with current PI = 3.9 bbl/day /psi.

- Well producing 500 bbl/day during the test which considers 10 % from maximum potential for this well.
- The intersect between inflow and outflow performance is showing unstable flowing condition (may lead to well stop flowing at early stage of production).

Different sensitivity analysis runs are performed on the current base case of the selected zone. These runs are summarized in the following sections.

4.2. Sensitivity on Well head pressure

The well head sensitivity runs are performed from the current well head condition of 220 to drop to 50 psi. Figure 4 shows the inflow and outflow performance for these sensitivity runs. As shown in Fig. 4, the well showed improve in its performance as results to a drop in the well head pressure. However, this improvement is very limited due to the limited reduction in well head pressure (minimum of 50 psi). Table 2 gives the expected gross rate per each drop in well head pressure.

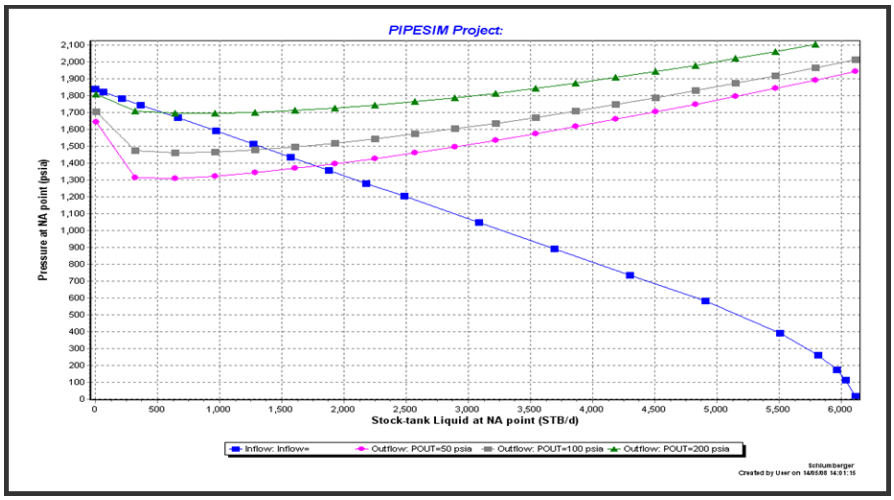

Fig. 4. Nodal analysis models for the well head sensitivity

Table 2. Well head sensitivity analysis results

WHP, psi	Gross rate BLPD
220	500
100	1400
50	1800

4.3. Sensitivity on reservoir pressure

The reservoir pressure sensitivity runs are performed on changing the reservoir pressure from current condition to 1840, 1700 & 1500 psi. Figure 5 shows the inflow and outflow performance for these sensitivity runs. As shown from Fig. 5, the well stops flowing as a result to a drop-in reservoir pressure from the initial test condition. Table 3 gives the expected gross rate for each reservoir pressure.

Table 3. Reservoir pressure sensitivity analysis results

Reservoir pressure, psi	Gross rate, BLPD
1840	500
1700	No flow
1500	No flow

4.4. Sensitivity on reservoir pressure vs. well head pressure

The sensitivity analysis is performed on change reservoir pressure from 1840, 1700, 1500 psi vs. change in WHP of 220, 100 and 50 psi. As shown from results even at very low well

head pressure, the well stops flowing at 1300 psi. Thus, the current operating condition for the well is very risky.

4.5. Sensitivity on water cut

The sensitivity runs are performed on different values of water cut of 0, 10 and 20 % at the current condition of the well head pressure of 220 psi. As shown from the results in Table 4, the well performance is highly affected with increasing in the water cut. The well will stop flowing at water cut of 20 %.

Table 4. Water cut sensitivity analysis results

W.C., %	Gross rate, BLPD
0	500
10	280 (unstable condition)
20	No flow

4.6. Sensitivity on different tubing diameter

The sensitivity runs are performed at well head pressure of 50 psi with different tubing diameter of 2", 3 1/2 "& 4 ½". From Table. 5, it can be easily noticed a significant change in well performance when using 3 ½" tubing diameter compared to the 2 7/8", and there is no much different between 3 ½" & 4 ½". Thus, the 3 ½" is recommended over the 4 ½".

Table 5. Tubing size sensitivity analysis results

Tubing diameters, inch	Gross rate, BLPD
2 7/8"	1600
3 ½ "	2100
4 ½"	2350

5. Artificial Lift Screening for Bentiu formation

As from the natural flowing analysis for both Bentiu and Abu Gabra, it was realized the importance of using artificial lift method especially for Bentiu wells from the starting of production. The next sections summarize the artificial lift screening performed for Bentiu reservoir based on the reservoir rock and fluid characteristic of each reservoir separately.

5.1. Artificial Lift Screening for Bentiu

Artificial lift (AL) screening software [4] is used to select the best artificial lift candidate for Bentiu reservoir based on its rock and fluid characteristics. Table 6 gives the main Bentiu reservoir characteristics that are used in selecting the best AL method. Based on the parameters shown in Table 6 gives the weight percent of the selected AL method compared to the others. As shown from the results, the best AL candidates for Bentiu are ESP, PCP and Gas lift.

Table 6. Artificial lift screening parameters for Bentiu

Parameters	Value	Parameters	Value
API gravity	30 API	Dogleg	0 deg/100ft
Production rate	500-2000 bbl/D	Water cut (%)	0 – 100 %
Flowing bottom hole pressure	1600 psi	Electricity available	Yes
Deviation	0 deg	Height restriction	No
Gas available	Yes	Casing size	7"
Depth	5000 ft	H_2S content	0
Gas liquid ratio	100 scf/bbl	Subsurface safety valve	Yes
Solid content (%)	0	Stuffing box	No
Bottom hole temperature	150 F	CO_2 content	0
Gas well dewatering	No		

5.2. Artificial lift analysis (ESP vs Gas Lift)

In this section, two artificial lift methods were studied to describe their performance over the FDP time period and how each artificial lift type acts during the well life. All the artificial lift analysis had been conducted for well SP-21 as a pilot well reflect the field higher cumulative liquid production during the primary depletion scenario obtained from the simulation model.

The objective is to perform a nodal analysis for the above mentioned well at different time spots over the well life for three different FDP scenarios which are the primary depletion, the water injection, and the gas injection. The input data used to build the nodal analysis model for the selected well is taken from the dynamic modeling. These data are: reservoir pressure, flowing bottom hole pressure, water cut, gas oil ratio at each time spot. The results from this analysis are to choose the ESP pump and the proper Gas lift design which can achieve the dynamic model liquid rate at surface and to check if this pump or the gas lift design can work properly along the well life time.

Accordingly, the next sections give the ESP and Gas Lift analysis for each FDP scenario separately.

5.3. Artificial lift analysis for primary depletion scenario

Fig. 5 gives the selected well performance based on the dynamic modeling with the different points selected along the life of the well to perform the nodal analysis to select the optimum ESP and Gas lift design for the selected well. PIPSIM model had been built for the three selected points along the life of the well based on the reservoir pressure, bottom hole flowing pressure, water cut, and gas oil ratio available from the dynamic modeling.

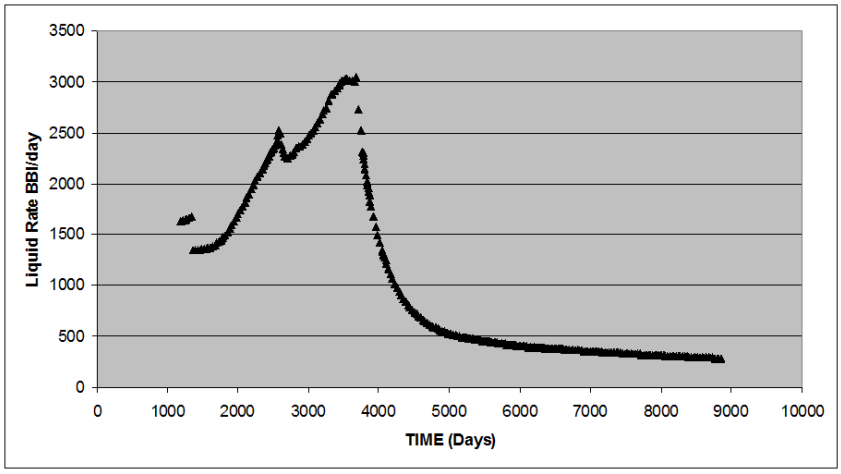

Fig.5. Liquid rate performance of the selected well from the dynamic modeling

Table 7 gives the selected ESP pump along with the well head pressure for this pump for the three selected points.

Table 7. Summary of the ESP design for the primary depletion scenario

Time	P_R, psi	W.C. %	GOR scf/stb	Q_L stb/d	No. of stages	WHP, psi	H.P.	Pump type
2127	1008	16	61	1855	102	850	97	GN2500
3284	398	26	109	2818	250	600	178	GN3200
6584	160	90	430	374	350	400	36	DN1000

General charts (Fig. 6a, b, c) have been generated to show the behavior of well head pressure versus No. of stages per each ESP pump based on the change in reservoir pressure, water cut, GOR and liquid rates. The importance of these charts is that it can be used to select the proper ESP pump based on the well conditions and the required well head pressure (WHP)

based on the surface facilities design. From the ESP analysis for the pilot well (Table 7 and Fig. 6), it can be easily concluded that the ESP design to obtain the predicted performance of the wells requires changing the ESP during the life time of the well. This is a very important factor that should be taken into consideration in designing the proper artificial lift for the new proposed wells. Similarly for the gas lift design, Table 8 gives the gas lift design parameter which is the point of injection, the gas injection rate, and the surface injection pressure along with the well head pressure at each selected time during the life of the well.

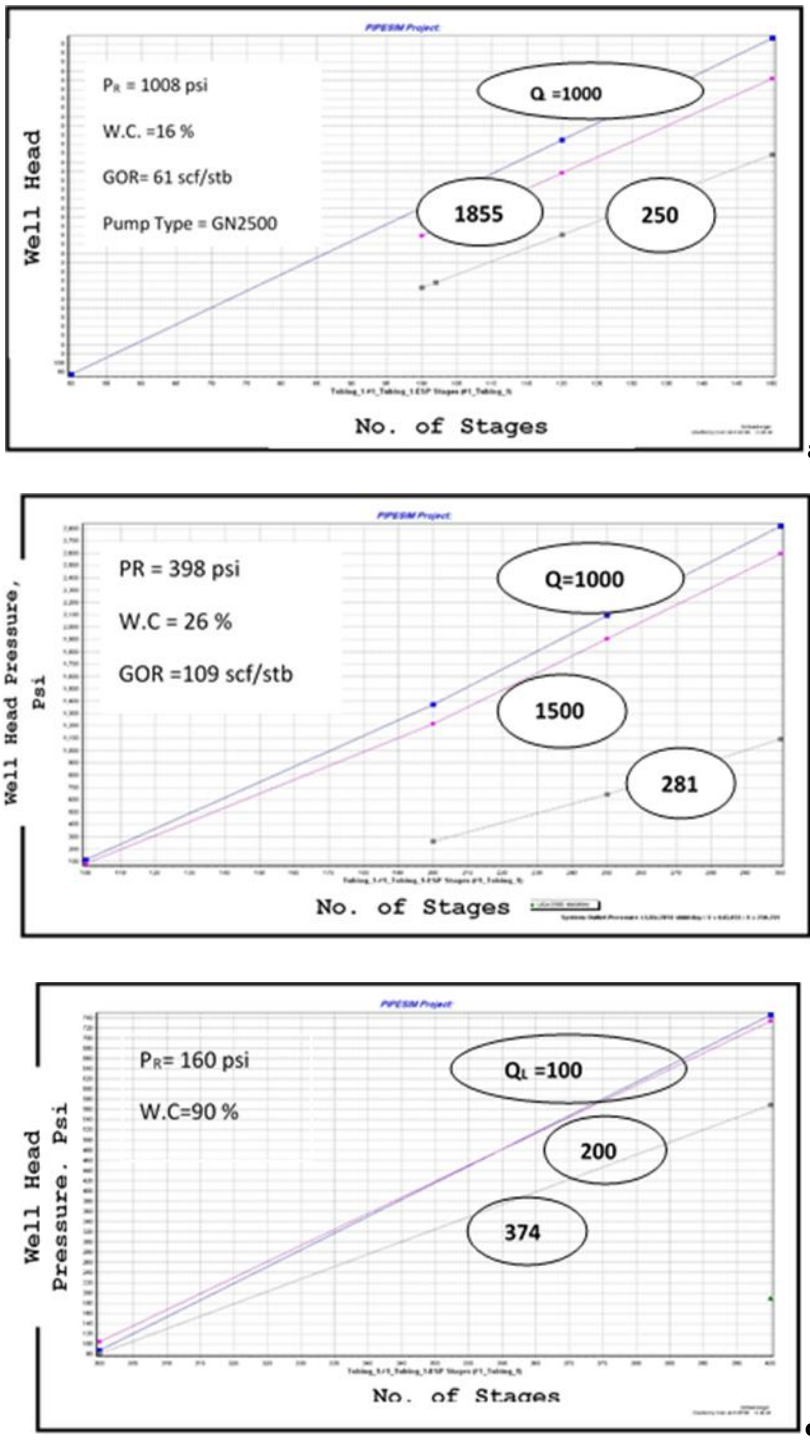

Fig. 6. General charts for ESP design for primary depletion scenario

Table 8. Gas lift design summary for the primary depletion case

Time	P_R psi	W.C. %	GOR scf/stb	Q_L, stb/d	P_{inj}, psi	Q_{inj} optimum	Point of injection	WHP, psi
2127	1008	16	61	1855	1000	4 MMscf/d	5100 ft	350
3284	398	26	109	2818	-	-	-	-
6584	160	90	430	374	-	-	-	-

From Table 8, it can be easily concluded that the gas lift was able to operate at the initial time with surface injection pressure of 1000 psi and injection rate of 4 MMSCF/D with well head pressure of 350 psi. However, for the rest of the points, gas lift cannot get the rate obtained from the dynamic model at these conditions.

5.4. Artificial lift analysis for water injection scenario

Similarly, as discussed before for the primary depletion case, the same selected pilot well is used to analyze the performance of both ESP and Gas lift during the life time of the well. Figure 7 gives the liquid rate performance for the water injection case obtained from the dynamic modeling along with the selected time spots for the nodal analysis work.

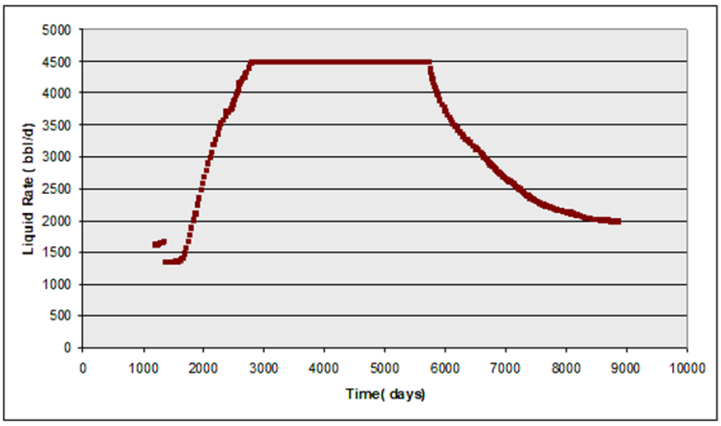

Fig. 7. Liquid performance for the water injection scenario of the selected well

A PIPSIM model had been built for the three selected points along the life of the well based on the reservoir pressure, bottom hole flowing pressure, water cut, and gas oil ratio available from the dynamic modeling for the water injection scenario. Table 9 gives the selected ESP pump along with the well head pressure for this pump for the three selected points. General charts (Fig. 8 a, b, c) have been generated for each pump to describe the change in well head pressure due to the change in the number of stages for the used pump under different conditions. For the ESP analysis in case of water injection, it is easily noticed that the ESP pump needs to be changed along the life of the well similar to the case of primary depletion. Similarly, for the gas lift analysis, Table 10 gives the gas lift design parameters for the pilot well selected for the water injection scenario. Similarly, as the primary depletion case, the gas lift cannot operate at high rate (4500 STB/D) and low reservoir pressure as shown from the last two points in Table 9. This indicates that the gas lift cannot be selected as a good candidate to achieve the production rates predicted from the dynamic modeling phase for field wells.

Table 9. Summary of the ESP design for the water injection scenario

Time	P_R psi	W.C. %	GOR scf/stb	Q_L, stb/d	No. of stages	WHP, psi	H.P.	Pump type
2036	1393	53	60	2791	80	600	102	GN3200
4196	506	87	58	4500	201	600	285	GN4000
8306	172	97	360	2053	174	600	174	GN3200

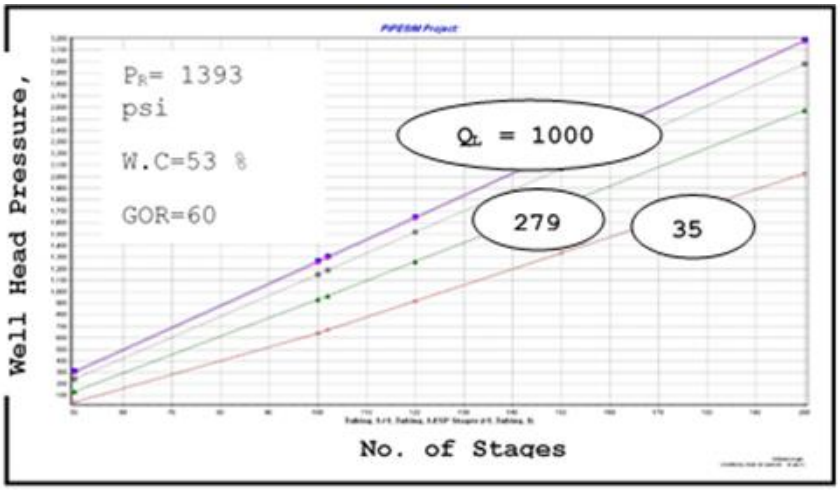

(a)

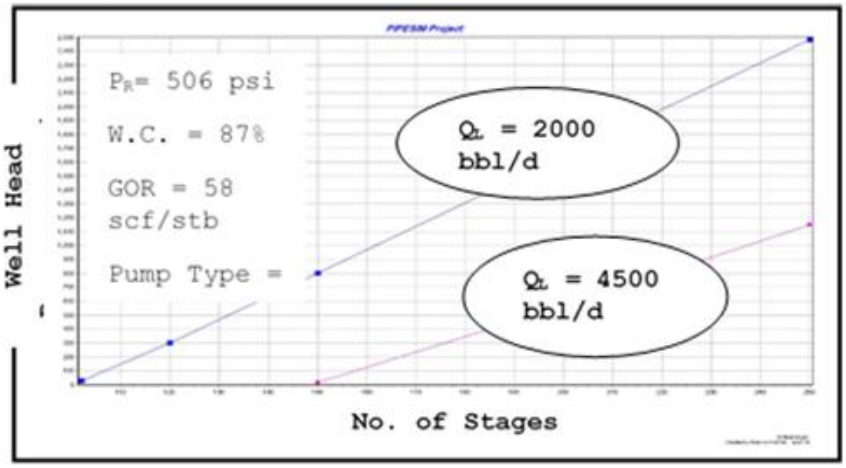

(b)

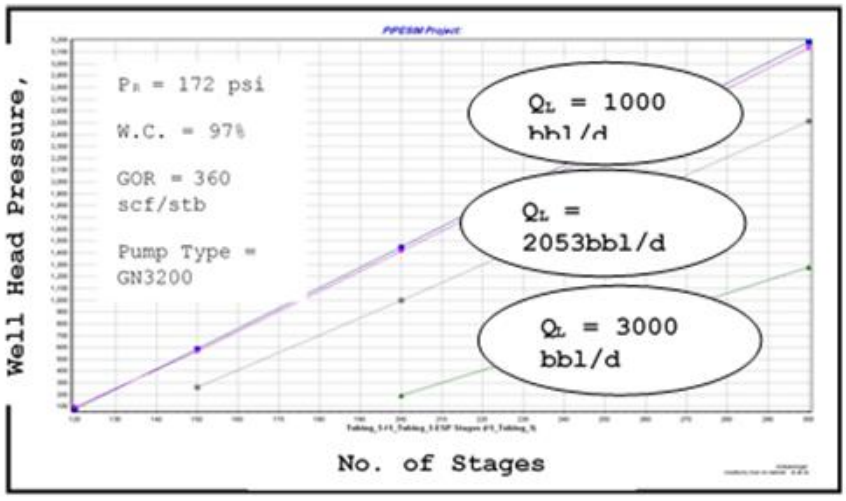

(c)

Fig. 8. General ESP design charts for water injection scenario

Table 10. Gas lift design summary for the water injection scenario

Time	P_R psi	W.C. %	GOR scf/stb	Q_L stb/d	P_{inj}, psi	Q_{inj} optimum	Point of injection	WHP psi
2036	1393	53	60	2791	2000	4 MMSCF/d	5100 ft	450
4196	506	87	58	4500	-	-	-	-
8306	172	97	360	2053	-	-	-	-

6. Conclusion

For Bentiu Reservoir all the sensitivity runs showed that the wells stop flowing (Natural flowing) when water cut reached 20 %. Sensitivity on well head pressure showed that the decreasing in WHP can improve well performance. The average WHP for the current wells are around 200-300 psi so there is no room to change WHP.

The sensitivity on reservoir pressure showed that the well performance is very sensitive to the reservoir pressure. Based on these analyses, it is recommended to run the completion equipped with artificial lift from the starting of production to avoid any future work over to change the completion. The Artificial Lift screening showed that ESP, Gas Lift (GL), and PCP are candidates to produce Bentiu wells.

The drawback of the gas lift is that the well production is highly sensitive to the change in reservoir pressure. Both ESP & GL wells showed stable performance at increasing of WC.

The tubing diameter of 3.5" is recommended to produce Bentiu wells. A detailed analysis for both ESP and Gas Lift was performed to examine the efficiency of the both methods in producing the recommended production rates for a pilot well obtained from the dynamic modeling for three different recommended scenarios which are the primary depletion, water injection and gas injection. The results show that ESP can produce the predicted well performance, but it needs to be changed during the life time of the well by changing its number of stages to handle the changes in the liquid rates and reservoir pressures anticipated from the three tested scenarios.

References

[1] PIPESIM User Guide-Version 2007.2, Schlumberger, 2005

[2] Khasanov MM, Krasnov V, Khabibullin R, Pashali A, and Guk V. A Simple Mechanistic Model for Void-Fraction and Pressure-Gradient Prediction in Vertical and Inclined Gas/Liquid Flow. SPE Production & Operations 24(1):165-170.

[3] Su H-J and Oliver DS. Smart Well Production Optimization Using An Ensemble-Based Method. SPE Reserv. Eval. Eng., 2010, 13: 884–892.

[4] Abdul Majeed GH, Al-Soof NBA, and Alassal JR. An improved revision to the Hagedorn and Brown liquid holdup correlation. J. Can. Pet. Technol., 1989; 28(6).

To whom correspondence should be addressed: Dr. Reda Abdel Azim, Future University in Egypt Petroleum Engineering Department, Egypt

Petroleum and Coal

Article **Open Access**

EOCENE–MIOCENE STRATIGRAPHY OF THE SURMA TROUGH, BENGAL BASIN: A SEQUENCE STRATIGRAPHIC APPROACH

AKM Eahsanul Haque[1], *W.S. Downey*[2], *M. Mustafa Alam*[3], *Md. Aminul Islam*[4], *Md. Omar Faruk*[5], *Riyadul Islam*[5]

[1] *Dimension Strata Sdn Bhd, Ground Floor, Unit 5, Bgn. Zainuddin & Azizah, Spg 501, Jln Tutong, Kg Telanai, Bandar Seri Begawan, BA 2312, Brunei Darussalam*
[2] *Department of Petroleum Engineering, Curtin University, Sarawak Campus CDT 250, Miri, Sarawak, Malaysia*
[3] *Department of Geology, Faculty of Earth & Environmental Sciences, University of Dhaka, Bangladesh*
[4] *Department of Physical & Geological Sciences, Faculty of Science, Universiti Brunei Darussalam, Brunei Darussalam*
[5] *Geological Survey of Bangladesh (GSB), 153 Pioneer Road, Segunbagicha 1000, Bangladesh*

Received January 3, 2019; Accepted February 28, 2019

Abstract

The Bengal Basin is the thickest sedimentary basin in the world; however, little work has been carried out on establishing sequence stratigraphic boundaries within the basin. The stratigraphic framework of the exposed Eocene to Miocene sediments in the Jaintiapur and surrounding areas, northeastern Sylhet, Bangladesh, was constructed from surface sedimentological studies together with sequence stratigraphic modeling of the Sylhet trough. In this study, the exposed Eocene to Miocene sediments having conventional names like Jaintia, Barail and Surma Group have been reinterpreted and renamed as of Dauki Allogroup, Tamabil Alloformation, and Surma Allogroup. The Tamabil Allogroup has been regarded as an undifferentiated unit. Both the Jaintiapur Alloformation and the Afifanagar Alloformation are well developed in the study area. In this work, the parasequences, systems tracts, bounding surfaces and sedimentary sequences of the exposed Eocene to Miocene sedimentary deposits of the study area have been redefined and are recognized as representing responses to changes in relative sea level, sediment influx, and paleogeography.

Keywords: *Sylhet trough; parasequences; system tracts; sequences; depositional environment.*

1. Introduction

Sequence stratigraphy has been defined as the "study of the rock relationships within a chronostratigraphic framework of repetitive, genetically related strata bounded by surfaces of erosion or non-deposition, or their correlative conformities" [1]. The key attributes of the sequence stratigraphic approach have been a delineation of discontinuity surfaces and the relation of these surfaces with relative sea-level changes [2-3]. Bengal Basin is one of the largest basins in the world; however, little work has been carried out to establish sequence stratigraphic boundaries in the basin as a whole. The Paleogene and Neogene sequence of the Sylhet Trough and the surrounding area was studied by several authors [4-6], but there is currently a lack of detailed sedimentological and sequence stratigraphic information on the Sylhet Trough.

Analysis of facies and facies associations is an appropriate technique for understanding depositional environments. This method was used in the present study for environmental interpretation using the available sedimentological data. The sequence stratigraphy of the exposed Eocene to Miocene sediments of Jaintiapur and surrounding areas of northeastern

Sylhet, Bangladesh, was assessed to obtain a sequence stratigraphic framework for the area. The results of this study will aid future academic and exploration activities in the basin.

2. Study area

The selected study region is the Jaintiapur–Tamabil–Jaflong area in the northeastern part of Sylhet district, northeastern Bangladesh. The northern border of the area forms the international border between Bangladesh to the south and the Indian State of Meghalaya to the north. The study area (Fig. 1) is a hilly region with low hillocks in the west and high hills in the east. The boundary between the two countries in this region is marked by a fault zone, the Dauki Fault zone. This fault zone is filled by the flood plains and channels of many hilly rivers issuing from the Shillong Plateau of Meghalaya. The southern part of the study area is also plain-land, forming the large flood plains of the Meghalayan and Jaintia rivers [7].

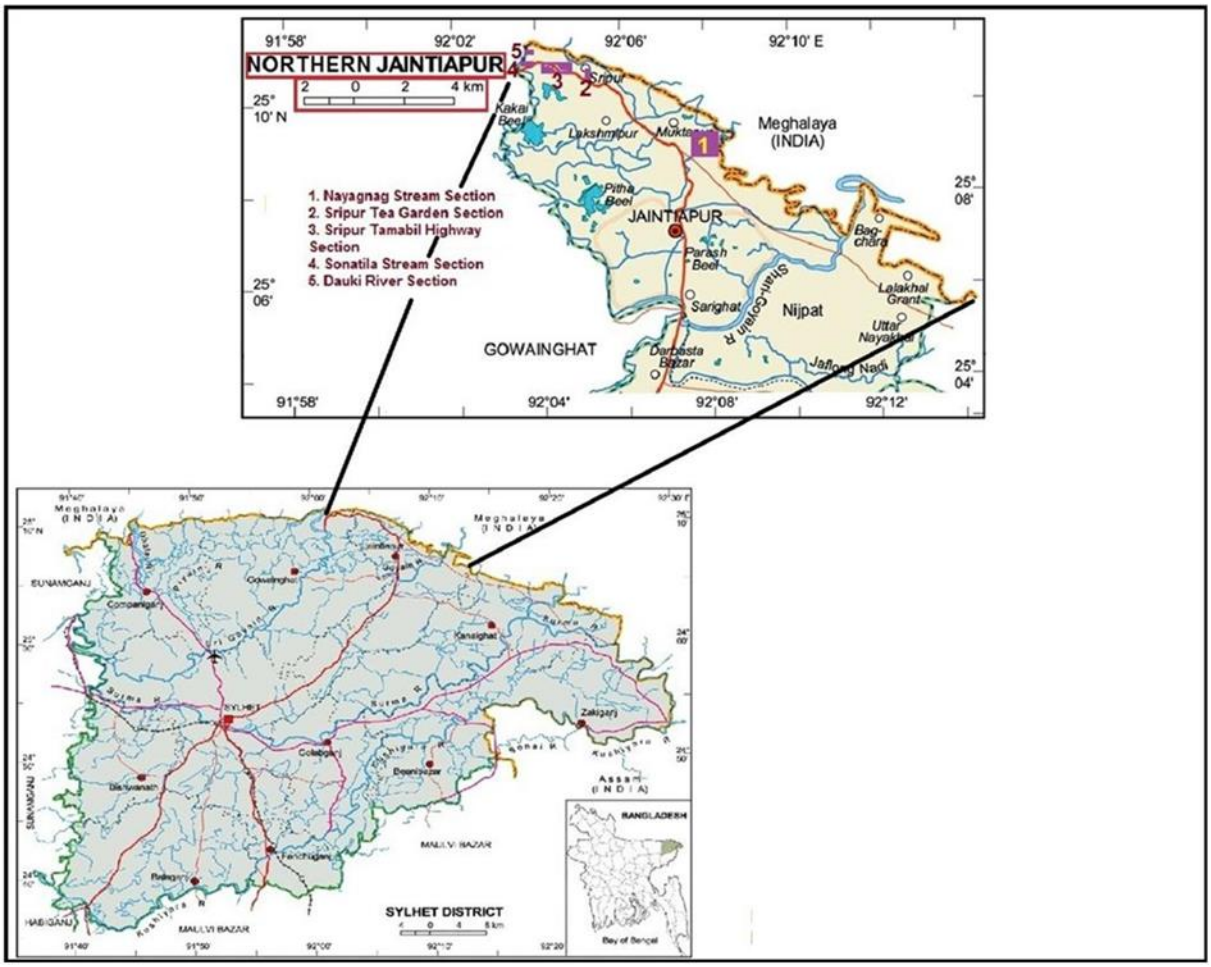

Fig.1. Local map of the study area in Sylhet *(Modified after Khan FH. [20])*

The most important stream within this country is Sonatila Chara in Jaflong. This area was selected for study because good exposures of the Dauki Allogroup (conventional Jaintia Group), Tamabil Allogroup (conventional Barail Group) and Surma Allogroup (conventional Surma Group) are available; unique Allogroup names have been proposed in this study that are all taken from local type sections based on local stratigraphic boundaries and available lithofacies; earlier formation names being taken from Indian type sections. Another important reason is that little work has been carried out using the sequence stratigraphic approach in the area, although the Surma Allogroup has been well studied [8].

3. Geological setting of the Bengal Basin

The Sylhet Trough is located in the northeastern part of the Bengal Basin, which in turn is adjacent to the northern part of the southeastern corner of the Indian Shield where the shield narrows, and can be considered to be the horn of the Indian Shield. The Indian Shield continues toward the northeast as far as the Mishmi Hills. In terms of paleotectonics and paleoenvironment, the Bengal Basin can be regarded as the southwestern continuation of the Assam Basin [9]. As a result, there are many similarities between these two geographically separated basins, and so the stratigraphic nomenclature of the Assam Basin has been applied to the Bengal Basin. Thus, the stratigraphy used has been highly generalized and oversimplified in the Bengal Basin region, at least for the Miocene rocks [8].

The northeastern horn of the Indian Shield is very important in the tectonic history of this region. It has got some pop up blocks such as the Mishmi Hills in the northeast [4], the Shillog and Mikir massifs in the southwest. In the northern half of the Indoburman Range, the orogenic cycle is complete, and the basin is now undergoing thrusting instead of folding. In the southern side of the range, the orogenic cycle is continuing to the west in the Bengal Basin [10].

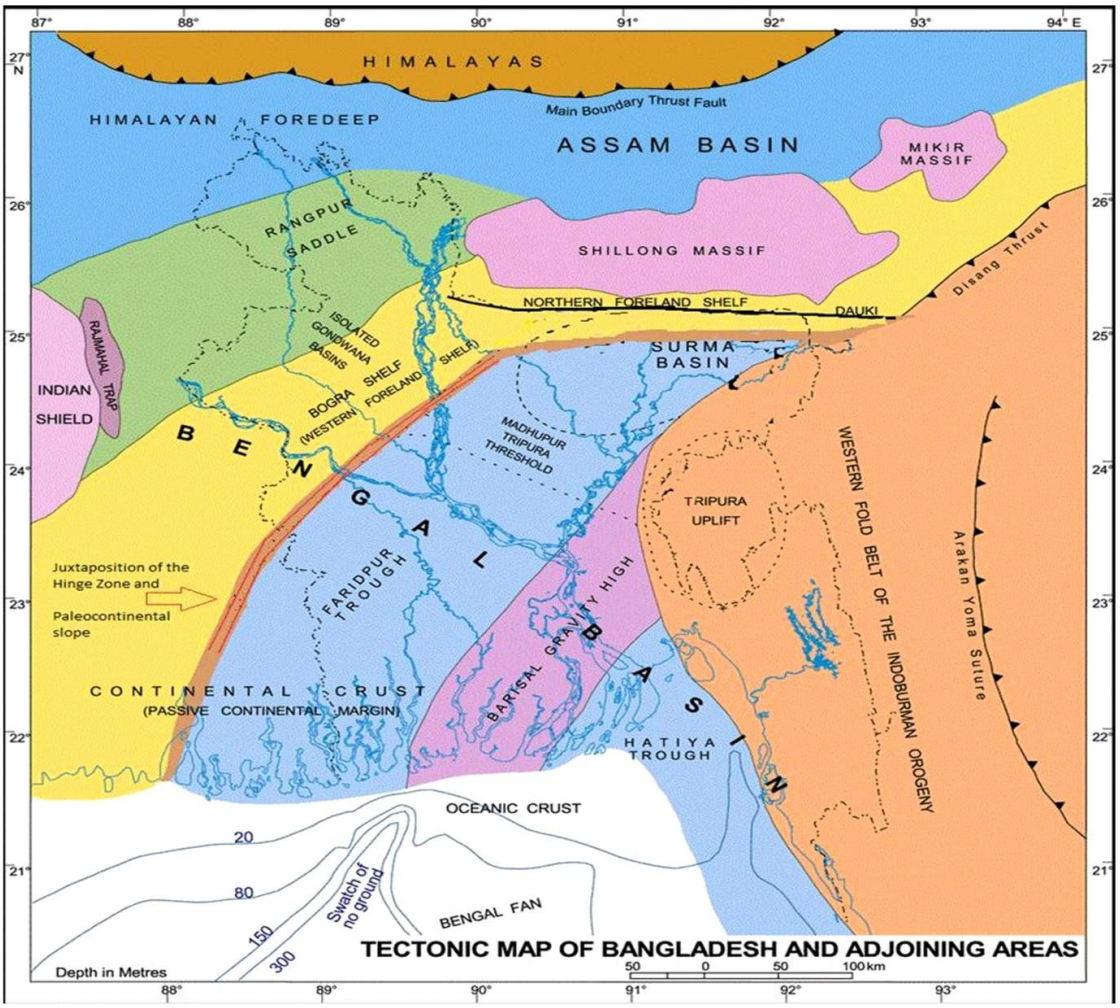

Fig.2. Tectonics map of Bengal Basin to show the juxtaposition of the Hinge Zone and paleo-continental slope

Knowledge of the geology of the Bengal Basin and its basin-fill history has been based to a large extent on seismic evidence from the subsurface, because basin-fill sediments are exposed in only a small part of the country [9, 11]. Two important tectonic elements are located

on the western margin of the Bengal Basin. The first tectonic element is the hinge zone, i.e., the close spacing of 300 to 700 m NE–SW contours in the middle of the basin, indicating a sharp slope toward the basin: this zone is a geological structure but is tectonically important. The other tectonic element is the continent–ocean crust boundary. The basin configuration has been studied using gravity and magnetic anomaly data, in which the hinge zone (Fig. 2), the continental shelf, the continental rise, and the continent–ocean boundary are not well demarcated. The hinge zone is normally thought to terminate at the Shillong Plateau in the north; however, the contours are more widely spaced in the north, and the slope is gentler. Movement along the hinge zone has caused the Bengal Basin to undergo a tremendous amount of subsidence, allowing a great thickness of sediments to be accumulated. In the Sylhet Trough, the subsidence was initiated after the Miocene as a result of uplift of the Shillong Plateau by isostatic compensation and subduction of Indian oceanic crust beneath the Burmese Plate.

The Bengal Basin has experienced a series of evolutionary phases since the Permian. The basin did not exist prior to the Cretaceous Period. Instead its current position was occupied by the continental blocks (Fig. 3) of Gondwanaland.

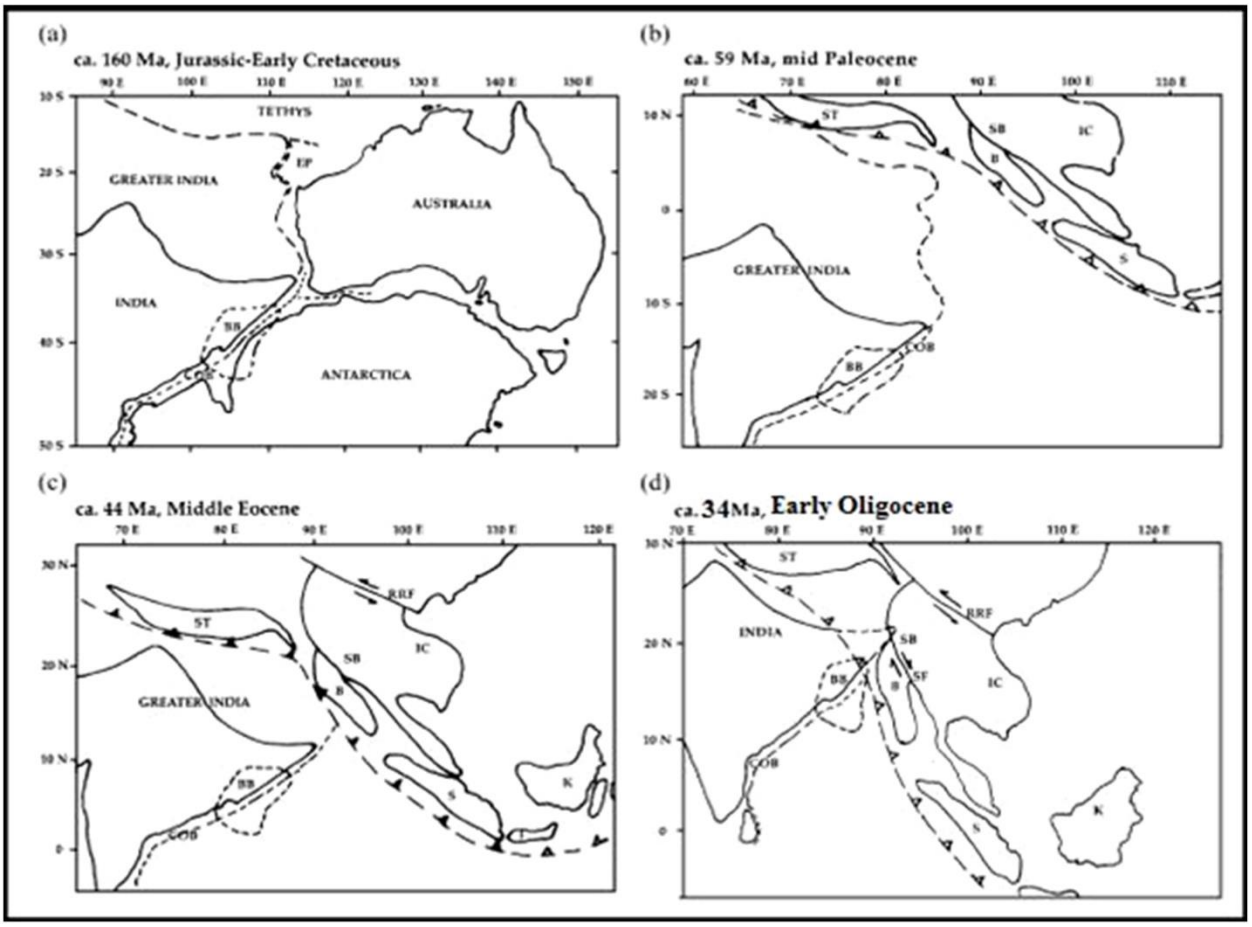

Fig.3. Plate reconstructions of the regional tectonic areas. EP= Exmouth Plateau; COB= continent ocean boundary; ST = South Tibet; B = Burma Block or IBA (Indo, Burma, Andaman); SB = SIBUMASU (Siam, Burma, Malaysia, Sumatra); IC = Indochina; S = Sumatra; BB = Bengal Basin; K= Kalimantan; J = Java; RRF = Red River Fault; SF = Sagaing Fault. (a) Eastern Gondwana fit of the margins of ''Greater India'', Australia and Antarctica. (b) Plate reconstruction at about 59 Ma, Mid-Paleocene, the start of ''soft collision'' between India and Southeast Asia. (c) About 44 Ma, Middle Eocene, the start of ''hard collision'' between India and South Asia. (d) About 34 Ma, Early Oligocene, a time of major collision between India and South Tibet in the north and India and Burma in the east *(Modified from Alam [6])*

The breakup of Gondwanaland began with rifting along the edges of continental India, Australia, Africa, and South America. This is rifting allowed development of the Bengal Basin along the northeastern border of the Indian continental plate margin. Thus the Bengal Basin started off as a rift basin: the rifting is marked by Permian Gondwanan half-grabens on the Precambrian basement. After separation from Gondwanaland, India drifted northward, and the southwestern fringe of the Bengal Basin was a pericratonic basin on a stable shelf over a passive continental margin. An oceanic basin occupied the place of the present Bengal Basin and existed until the Paleogene Himalayan orogeny when the eastern half of the basin was destroyed as a result of subduction of the Indian Oceanic Plate beneath the Burmese Plate during the Neogene [7]. As a result, the basin was left in the very early Neogene as a remnant ocean basin [6] and continued with this status until the end of the Miocene Epoch. The stratigraphic development of the region south of the horn of the Indian Shield began as early as the onset of the breakup of Gondwanaland when the Australian, South American, African, and the Indian Plates separated from the Antarctic Plate, as discussed in detail by previous authors [6, 9].

4. Sedimentological and sequence stratigraphic analyses

4.1. Dauki Allogroup (Jaintia Group)

4.1.1. Sylhet Limestone Formation

The Sylhet Limestone Formation is well exposed along the eastern flank of the Dauki River near Jaflong town; however, the base of this unit is not exposed in Jaflong area but is found in Takerghat to the west of the studied area along Bangladesh-Maghalaya border. The formation is overlain by the Jaflong Shale Alloformation (Fig. 4). The total thickness of the Sylhet Limestone Formation is still unknown, but the few exposed sections are approximately 15–17 m thick. This unit is mainly composed of fossiliferous and non-fossiliferous limestone. Common fossils present in the formation include *Nummulites*, *Discocyclina* and *Alveolina*.

Fig.4. Contact between Sylhet Limestone and Jaflong Shale

Sedimentary facies analysis is one of the initial stages of understanding the sequence stratigraphy of a formation. Appraisal of the bounding surfaces allows reconstruction of the physical extent and time duration of the sedimentation patterns.

Two distinct facies have been recognized in the study area of the Sylhet Limestone Formation.

a. Crystalline limestone facies (Lc)

b. Fossiliferous limestone facies (Lf)

Based on sequence stratigraphic analyses, two parasequences were found in the section, forming a Shelf Margin Systems Tract (SMST). The SMST was formed at a time when sea level was falling relatively slowly, and the location of deposition remained at the edge of the continental shelf. This SMST consists of fossiliferous and crystalline shelf carbonates in an aggradational stacking pattern. The abundance of foraminifera indicates a shallow, warm-water shelf environment. The Sylhet Limestone Formation appears in outcrop as a complete sequence (Fig. 5). The upper boundary of the formation is its contact with the Jaflong Shale (Kopili), which is a type II sequence boundary. This is unconformable with the Tura Formation; this contact is also a Type II sequence boundary.

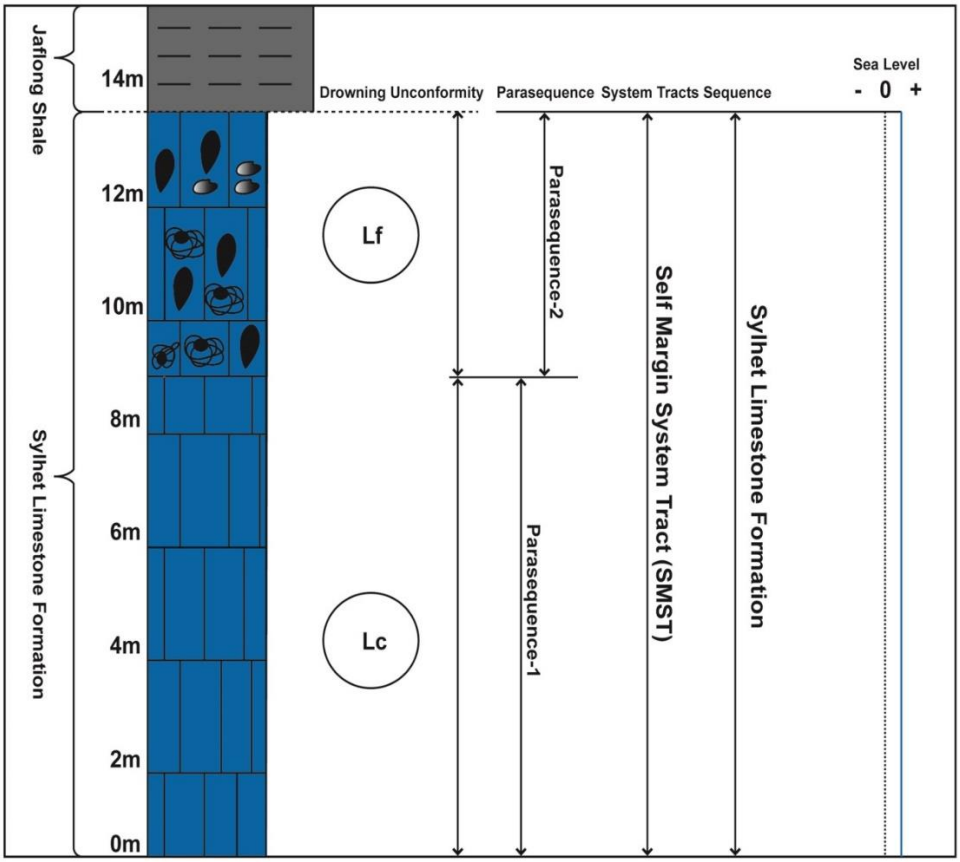

Fig.5. Sequence Stratigraphy of Sylhet Limestone

The Sylhet Limestone Formation was clearly formed in a carbonate depositional setting. In terms of carbonate buildup, the carbonate production (carbonate factory) is controlled by climatic variations, water circulation, nutrient supply, and water depth. Carbonate sediment was precipitated and produced from organic skeletal remains. The sediments were formed by the build-up of more rigid resistant features, such as coral reefs or sandy shoals. The carbonate sediments that have been accumulated display a wide range of platform morphologies often with slopes exceeding the angle of repose [12]. The epeiric carbonate platform was subsequently transformed into a rimmed shelf as a result of relative sea-level rise during the carbonate build-up in the upper part of the Sylhet Limestone Formation. A rimmed shelf with high carbonate production typically develops ramps, which may have a localized distribution around the edge of the platform [13].

4.1.2. Jaflong Shale Alloformation (Kopili Shale)

The Jaflong Shale Alloformation, which conformably overlies the Sylhet Limestone Formation, has been identified as late Eocene in age. This formation is exposed in the same section of the Dauki River as described above. That outcrop and the Tamabil Road section are the only exposures of the Jaflong Shale Formation within Bangladesh. This exposure is composed of dark gray to black shales. The lower contact of the formation is conformable and apparently fault-bounded. The contact between Jaflong Shale Alloformation and the Tamabil Allogroup (Barail) is unconformable.

The Jaflong Shale Alloformation contains the following lithofacies.

a. *Parallel-laminated siltstone (Sh)*
b. *Gypsum facies (Fg)*
c. *Laminated black shale (Fb)*
d. *Red shale (FRc)*
e. *Limestone (Lsc)*

The Jaflong Shale Alloformation contains three parasequences that form a Highstand Systems Tract (HST). The base is a Maximum Flooding Surface (MFS) that unconformably overlies the Sylhet Limestone Formation. The formation of the HST is associated with the creation of accommodation space at a lower rate than that of sediment supply. This accommodation space was created by a rapid sea level rise during deposition of the Jaflong sediments. The sediment supply was negligible in comparison to the much larger accommodation space closer to the coastal area, where sediment was abundant. The black shale and interbedded turbidites indicate a deep-water marine environment of deposition for the HST with an aggradational stacking pattern. The sediments forming the turbidite-related sandstone and siltstones were transported from an eroded orogenic provenance under sub-humid climatic condition [14].

The Jaflong Shale Formation is a siliciclastic sequence. The sediment dispersal system appears to have included submarine turbidity currents that generated small channels in the distal fan area, as well as hemipelagic to pelagic sediment suspension in abyssal to bathyal plains (Fig. 6). The presence of minerals such as glauconite and chert within the interlaminated sandstone and siltstones is typical of this type of depositional setting [13].

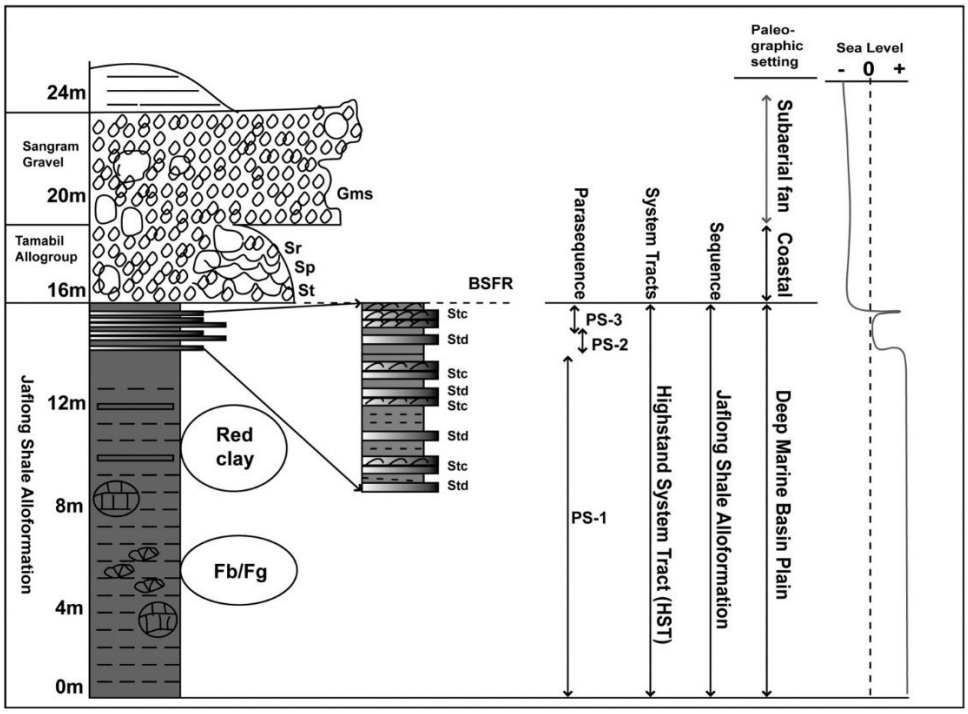

Fig.6. Sequence Stratigraphic Settings of the Jaflong Shale Allo formation

4.2. Tamabil Allogroup (Undifferentiated Barail)

The Tamabil Allogroup is the new name for the Barail Group. This unit largely represents the Oligocene sediments of the Sylhet Trough and the adjacent Assam Basin. The Tamabil Allogroup occupies a large area of the northeast of the Haflong–Disang Thrust that covers areas in Eastern Sylhet and Southwest Assam. The unit is well developed in the Surma Valley, North Kachar and the Garo–Khasia–Jaintia Hills [9-10]. The Tamabil sandstone is light gray, light brown and pink in color and very-fine- to fine-grained with thin- to medium-sized beds. Although the Tamabil Allogroup consists of three formations, it is considered to be "undifferentiated" in the present study in the exposures within the Sylhet Trough. The rocks of the Tamabil Allogroup show lateral and vertical lithological variations.

Alam [5, 8] suggested that the Tamabil Allogroup (Barail) succession in the Jaintiapur–Tamabil–Sangram bazaar areas of the northeastern Sylhet trough consists of shallow-marine deposits. However, the group has also been interpreted as a sequence of coastal, deltaic to shallow marine deposits [7]. The predominant lithology includes conglomerates, sandstones, siltstones, shales and mudstones. Channels, cross-bedding, intercalations, carbonaceous shale and lenses of coal indicate a probable swampy deltaic environment of deposition under tropical climatic conditions.

On the basis of the lithology and facies association, the Tamabil Sandstone Allogroup has been divided into three units as described below.

The lowermost member (130 m in thickness) of the formation is dominated by sandstone with minor amounts of shale. The sandstones are pink and brick-red in color, medium- to coarse-grained and cross-bedded with evidence of ripple cross-lamination. The beds are not well compacted and friable but in some places are very hard because of the presence of ferruginous cement. Splintery, black to grayish-black shales and yellowish-brown siltstones are also present in minor quantities. Intraformational conglomerates occur within the sandstone: these are well exposed along a road-cut and the tributary section from Tamabil through Sonatila Stream (Fig. 7).

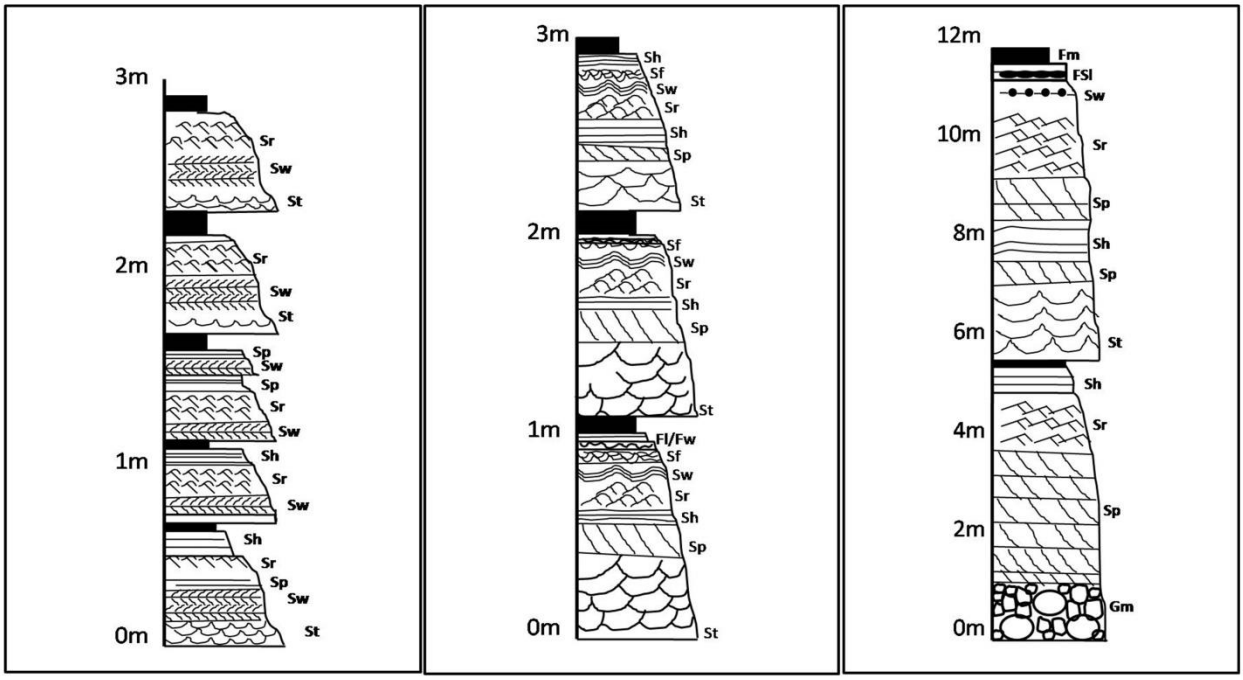

Fig.7. Litho-stratigraphic Log Model of the Tamabil Allogroup

The middle member (65 m in thickness) of the formation is a pink to yellowish-brown sandstone. The rock is fine- to medium-grained, ripple-laminated to ripple cross-laminated and planar cross-bedded with bidirectional cross-bedding. Thinly bedded shales are also present within sandstone beds. The sandstones are lenticular, wavy and sometimes flaser-laminated with abundant mud clasts in the lower part. Several channels are identifiable in this subunit with widths of several centimeters. The middle part of the allogroup is best exposed in the section from Tamabil BGB camp to Noljhuri camp.

The uppermost and thickest member (450 m thick) of the formation is dominantly sandstone with minor amounts of shale and siltstone. The sandstones are pink to brick-red in color and are unconsolidated showing massive, trough-cross-bedded and planar cross-bedded sandstones.

The best-developed sections are located between the Sripur Tea Garden and the Nayagang BGB Camp and in the Assampara–Rangapani river section. All deposits are exposed as channel and over-bank deposits on relatively flat terraces.

The facies and facies associations are classified according to their origin and sedimentological structures.

a. Clast-supported conglomerate facies (Ccg)
b. Trough cross-stratified sandstone facies (St)
c. Planar cross-stratified sandstone facies (Sp)
d. Horizontal-laminated sandstone–siltstone facies (Sh)
e. Ripple cross-laminated sandstone–siltstone facies (Sr)
f. Wavy-laminated very-fine-grained sandstone facies (Sw)
g. Flaser-bedded and laminated sandstone–siltstone facies (Sf)
h. Lenticular-laminated sandstone–siltstone facies (Fsl)
i. Mudstone facies (Fm)

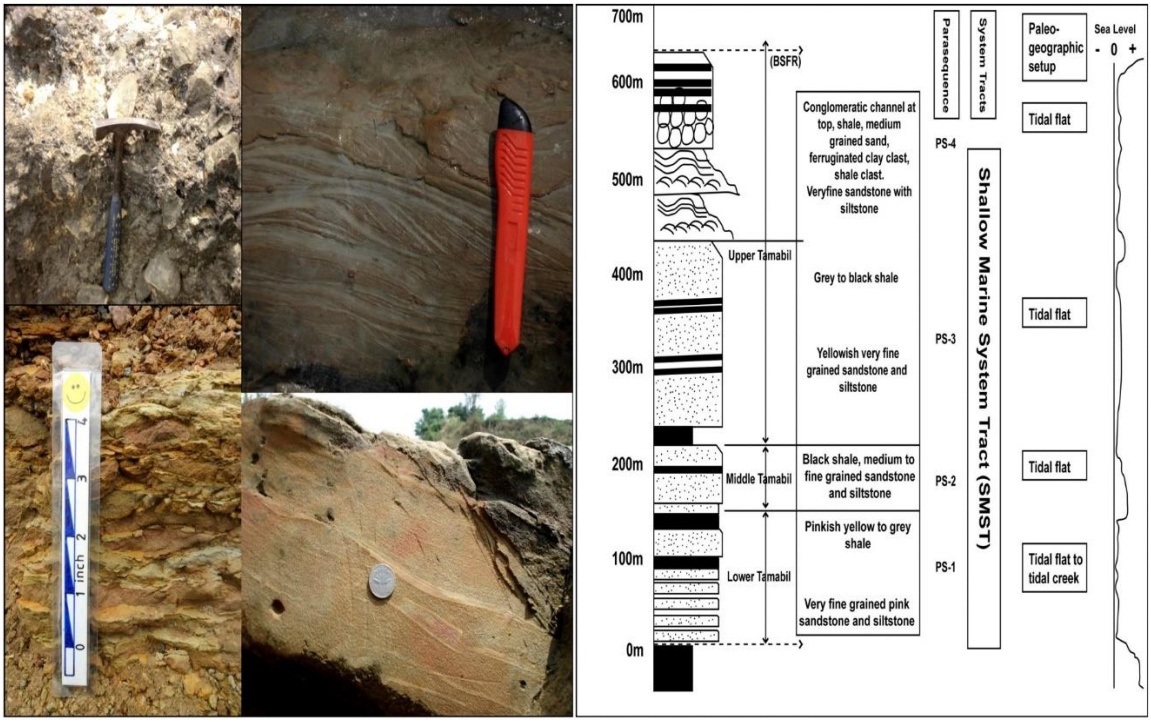

Fig.8. Clast-supported conglomeratic bed, trough cross-stratified sandstone facies, heterolithics of the Tamabil Allogroup, mud interclasts within the Tamabil Sandstone Allogroup and the sequence stratigraphic setting of the Tamabil Allogroup

The undifferentiated Tamabil Allogroup as exposed in the study area is mostly arenaceous and consists of approximately 650 m of thick sandstone, siltstone, silty shale, shale, and mudstones. This indicates a tidal flat–estuarine environment in a marginal-marine setting. The depositional environments are interpreted as tidal channels, tidal creeks, and intertidal flats. From the sequence stratigraphic point of view, the depositional site remained stationary relative to sea level and basin floor movement. These conditions were created after the retreat of the deep-marine conditions of the Jaflong Shale Formation that was encased in a HST. The boundary between the Jaflong Shale Formation and the Tamabil Allogroup is considered to be a Type I sequence boundary. Subsequently, during the marine regression at the beginning of the Oligocene, the Tamabil Allogroup was deposited in a marginal-marine to the estuarine–tidal flat environment [15]. Thus the Tamabil Allogroup can be interpreted as an SMST that was repeated several times (Fig. 8).

4.3. Surma Allogroup

4.3.1. Jaintiapur Alloformation (Bhuban)

The Jaintiapur Alloformation of the Surma Allogroup, which is of Miocene age, contains three sequences deposited in tide-dominated (nearshore), storm-dominated (shelf) and continental slope environments. Tide-dominated facies are exposed in the Jalhas–Guabaria area, storm-dominated shelf facies occur in the Nayagang section, and marine facies are exposed along the Hari River. The general interpretation of the Jaintiapur Alloformation suggests that the unit is of marine origin [16-17].

The Jaintiapur Alloformation has been measured as approximately 1000 m thick. The unit is characterized by bluish to black shale with subordinate light yellow to green sandstone, grayish-white siltstone, dark gray mudstone and conglomerate. Pebbly sandstone and medium-grained massive sandstone and conglomerate are present only in the lower part of the formation. The exposed lower boundary of the formation with the Tamabil (Undifferentiated) Group is represented by a marked unconformity and consists of conglomeratic laterite. The upper contact with the Afifanagar Alloformation of the Surma Allogroup is also unconformable but not distinct and is exposed at the Lalakhal Tea Garden section.

Fifteen lithofacies were identified within the Jaintiapur Alloformation. Each of these is characterized by a unique combination of lithology, texture and sedimentary structures and represent deposition in a specific subenvironment within a submarine fan complex.

a. Conglomerate facies (Gm)
b. Pebbly sandstone facies (Ps)
c. Massive sandstone facies (Sm)
d. Fine-grained sandstone facies (ST)
e. Planar c-stratified sandstone facies (Sp)
f. Hummocky cross-stratified sandstone (SH)
g. Swaley cross-stratified sandstone (Ss)
h. Parallel-bedded sandstone–siltstone facies (Sh)
i. Rippled and ripple cross-laminated sandstone–siltstone facies (Sr)
j. Flaser-laminated sandstone–siltstone facies (Sf)
k. Laminated sandstone–siltstone and silty claystone facies (Sl)
l. Lenticular-laminated sandstone–siltstone facies (Sll)
m. Wavy laminated silty shale to shale (Fw)
n. Bluish-black to black shale facies (Fl)
o. Massive mudstone facies (Fm)

Analysis of the vertical distribution of facies is based on grain size, bed thickness and facies changes that appear to be characteristic of specific morphological elements. The facies model for the Jaintiapur Alloformation was determined on the basis of the facies, depositional environments and fluid flow movement. Facies models of the Jaintiapur Alloformation are illustrated in Fig. 9.

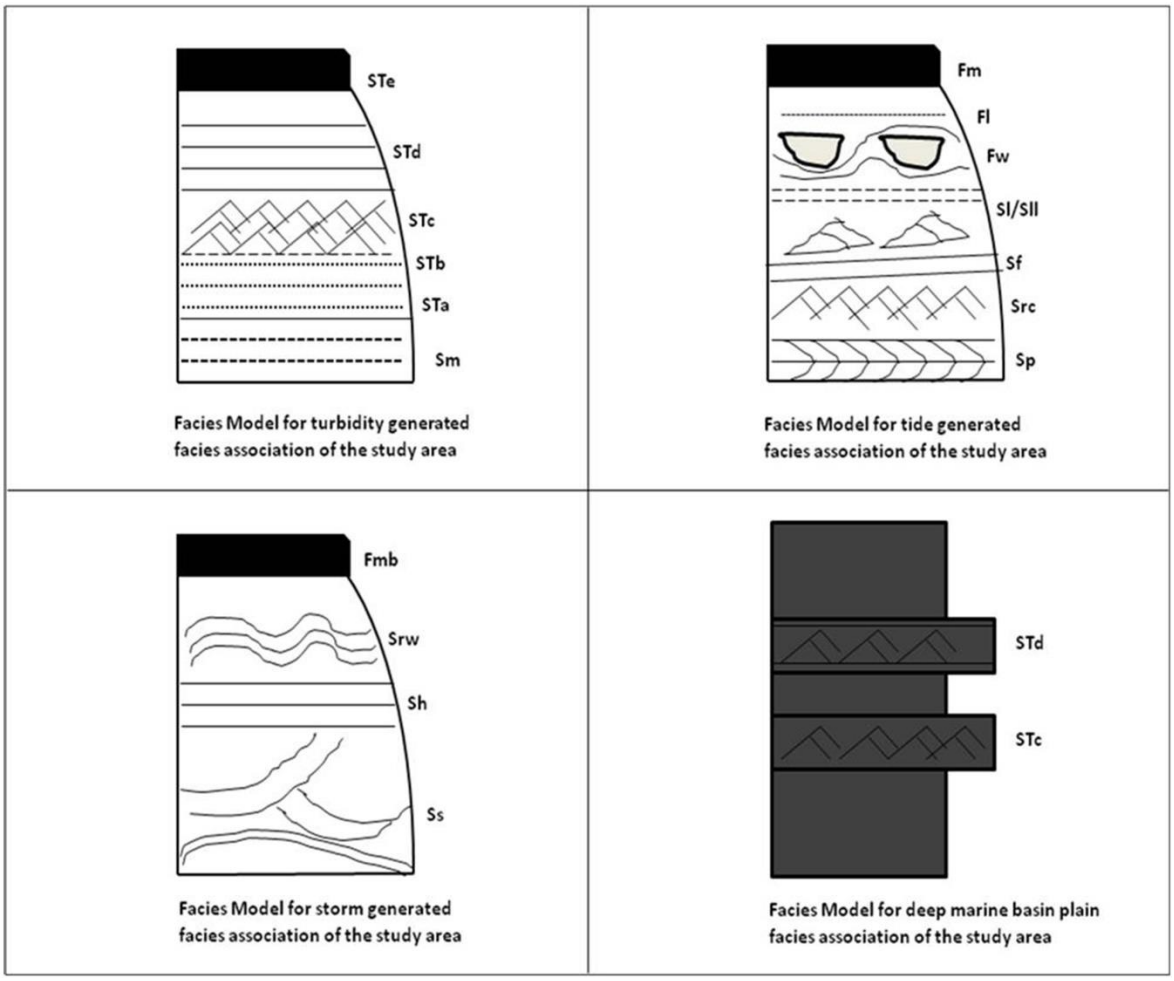

Fig.9. Facies models of the different studied sections in the Jaintiapur Alloformation

From the study of facies analysis and lithology of the Jaintiapur Alloformation (Fig. 10), fifteen parasequences with at least three distinct systems tracts were identified in the Jaintiapur area of the Sylhet Trough. Sedimentation in the Jaintiapur Alloformation began on the exposed coastal areas of the upper Tamabil Allogroup. This exposed surface is an unconformity filled by conglomerate that may have been an incised valley fill. The sedimentary sequence began with a Lowstand Systems Tract (LST). Faulting during a later period changed the environment into a deep-marine basinal plain forming an HST as a result of rapid sea level rise. The overall depositional pattern of the Jaintiapur Alloformation contains repeated HSTs and SMSTs ending with a basal surface of forced regression (BSFR) formed in a shallow environment. Thus, the upper bounding surface is also an unconformity. The entire lithological succession of the Jaintiapur Alloformation represents a sequence. Sea level changes have resulted in a stacking pattern of the systems tracts related to third- to fourth-order cycles of sea level change.

In the Jaintiapur Alloformation, the siliciclastic depositional systems of tides, storms and turbidity currents below the continental slope and deep-marine pelagic to hemipelagic suspension contain definite areas of sediment accumulation. The paleogeographic setting of the formation varies from the estuary to tidal flat and tidally dominated shallow-marine shelf through storm-dominated deeper shelf and submarine proximal distal fan with turbidity currents. The sequence is also indicative of a deep-marine anoxic basin plain with pelagic sedimentation caused by relative sea level change (Fig. 11) and tectonic settings.

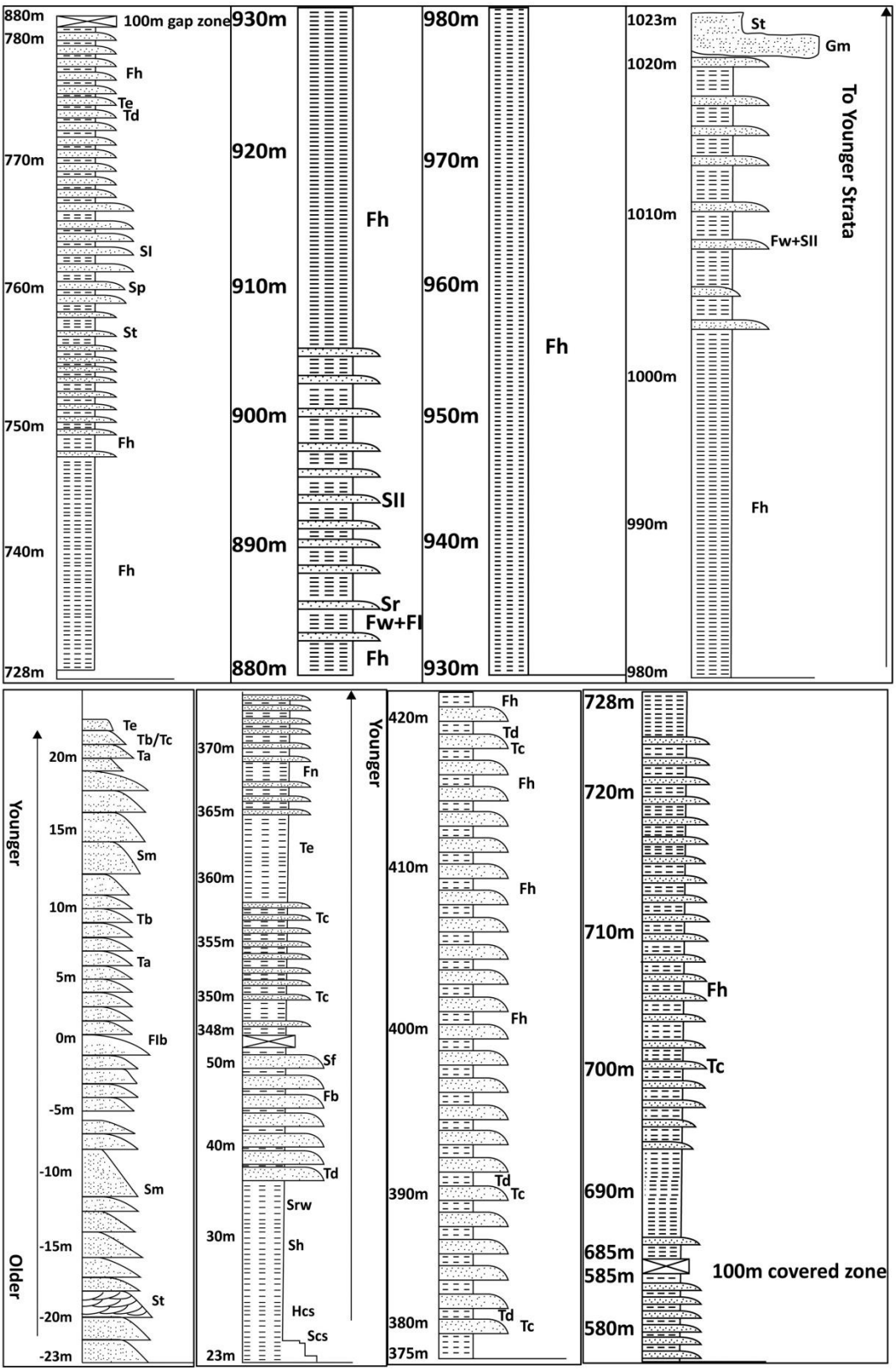

Fig.10. Sedimentary litholog of the Jaintiapur Alloformation

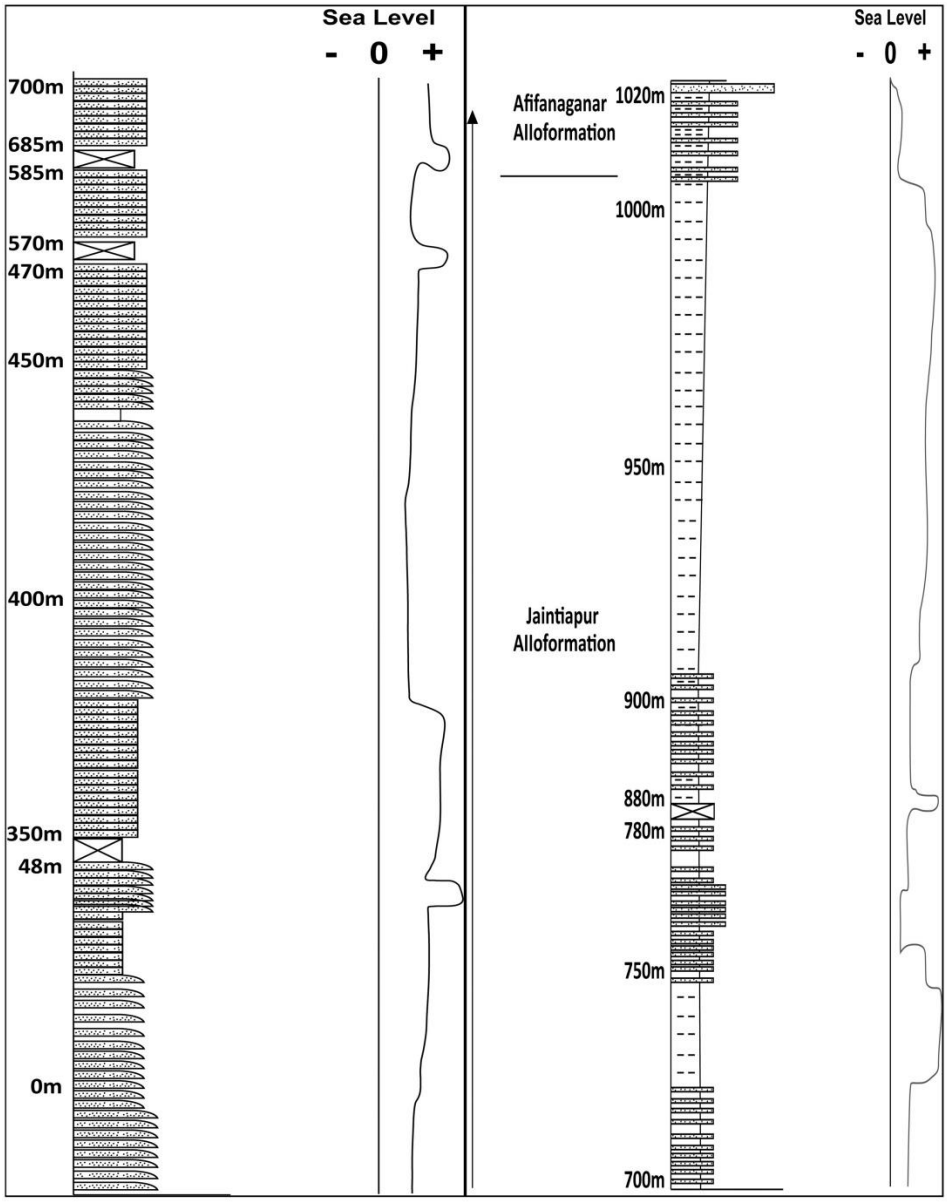

Fig.11. Interpreted sea level curve for the Jaintiapur Alloformation, Sylhet

4.3.2. Afifanagar Alloformation (Bokabil)

The Afifanagar Alloformation is the youngest unit of the Surma Allogroup and is well exposed along the banks of the Hari River, in the Lalakhal area and in the Tetulghat area of Jaintiapur, Sylhet. The objective of the study of Afifanagar Alloformation is to delineate better the facies and facies associations to generate a depositional model for the paleoenvironmental interpretation during deposition of the unit in the Miocene Epoch, which will ultimately help to obtain a sequence stratigraphic model of the formation.

The Miocene Afifanagar Alloformation unconformably overlies the Jaintiapur Alloformation and is overlain by the Mio–Pliocene Lalakhal Sandstone Alloformation with an erosional unconformity. The unit is mainly composed of silty shale, shale, siltstone, and sandstone. The silty shale is gray to bluish-gray in color, laminated to thinly bedded, moderately compact and highly jointed. The shale is greenish-gray, very-fine-grained, thinly to thickly laminated and

intercalated with silty shale. The sandstone is light gray, medium- to very-fine-grained, moderately compacted and contains trough, planar and ripple cross-stratification and parallel to flaser and lenticular lamination.

In total, eleven lithofacies were identified within the Afifanagar Alloformation.

a. *Clast-supported conglomerate facies (Gm)*
b. *Trough cross-stratified facies (St)*
c. *Planar cross-stratified sandstone facies (Sp)*
d. *Fine-grained sandstone–siltstone facies (STc–STd)*
e. *Parallel-laminated sandstone–siltstone facies (Sl)*
f. *Ripple cross-laminated sandstone–siltstone facies (Sr)*
g. *Flaser-laminated sandstone–siltstone facies (Sf)*
h. *Lenticular-laminated sandstone–siltstone facies (Sll)*
i. *Wavy-laminated shale facies (Flw)*
j. *Parallel-laminated shale facies (Fl)*
k. *Mudstone facies (Fm)*

A vertical facies model is defined as a general summary of a specific sedimentary environment; the relationships of the facies in a stratigraphic sense can be understood by the construction of a facies model. Facies models for the lower, middle and upper parts of the Afifanagar Alloformation are illustrated in Fig. 12. An overall facies model of the Afifanagar Alloformation exposed along the Hari River section is also described below.

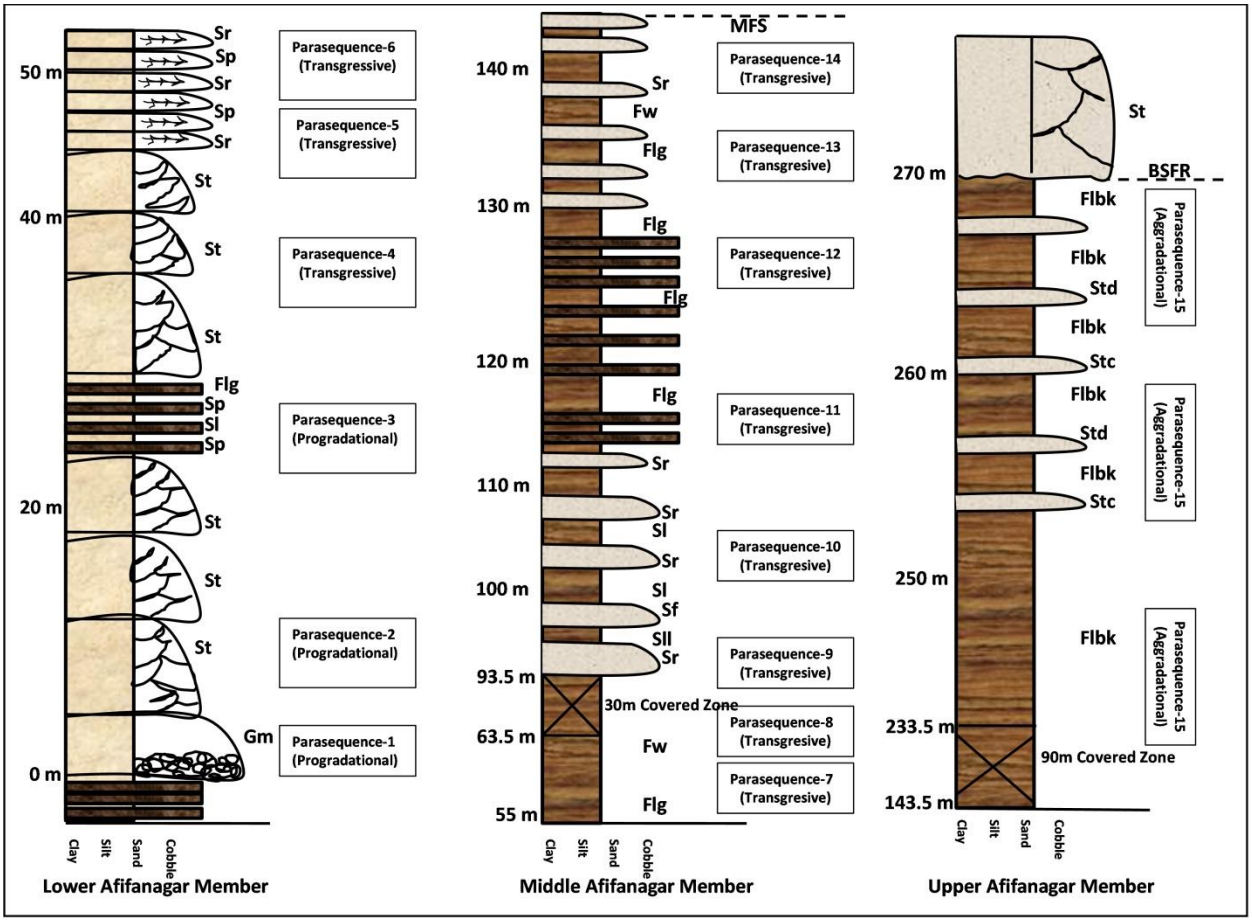

Fig.12. Sedimentary log and sequence stratigraphy of the Afifanagar Alloformation

The Afifanagar Alloformation can be grouped into three facies associations on the basis of paleoenvironments. The fluvial facies association (FFA) represents incised valley, braided

channel and overbank deposition, the tidal facies association (TFA) was formed in the estuary, tidal creek and tidal flat environments, and the marine facies association (MFA) was the result of deep marine hemipelagic sedimentation some distal turbidite progradation. The FFA consists of facies Gm and Stf, Spf, Slf, Flg subfacies and the Lower Afifanagar Member is composed of Fmf facies, the TFA is constituted by facies and subfacies of Stt, Spt, Slt, Sr, Sll, Sf Flb and Fmt forming the Middle Afifanagar Member. MFA is constituted of facies and subfacies of STc, STd, Flb, and Flbk represent the Upper Afifanagar Member.

From the analysis of the facies, facies association, and lithological succession, a total of seventeen parasequences were identified within the Afifanagar Alloformation from base to the top within the studied area. These parasequences can be classified into three types of system tracts on the basis of the stratigraphy, facies associations, and depositional environments.

The basal deposit of the studied area is a conglomerate, which is located above the shelf deposit of the uppermost part of the Jaintiapur Alloformation. The conglomerate represents sedimentation in an incised valley and is included in Parasequence 1. Such incised valleys were formed as a result of rapid sea-level fall or local tectonic uplift. The incised valley over the exposed Upper Jaintiapur shelf and the clasts within the conglomerates are mainly composed of shale from the shelf. This conglomerate is followed by a comparatively large thickness of Parasequence 2, i.e., channelized areneous deposits. The sediments are coarse-grained trough-cross-stratified sandstone (St) of braided fluvial origin. Parasequence 3 contains very fine sandstone to siltstone alternating with parallel-laminated gray shale. These rocks are moderately hard and sometimes calcareous. The parasequences in this systems tract are usually stacked to form a progradational pattern. The progradational geometry was formed by lateral building out to form a gently sloping depositional surface. This type of geometry is generated in conditions of stable sea level with a high sediment supply.

The parasequences in this system tract were deposited during a rapid sea level regression from the depositional site of the Upper Jantiapur shelf, and the earlier depositional site was exposed and eroded. Formation of the falling stage system tract (FSST) was associated with progressive destruction of accommodation space caused by a fall in relative sea level [1, 18]. The low sea level caused subaerial exposure of the shelf, and rivers become incised and bypassed the shelf to deposit sediments directly on the slope and basin floor. The incised valley between the Upper Jaintiapur Alloformation and the Lower Afifanagar Alloformation marks the sequence boundary and is termed the BSFR. The top of this systems tract is bounded by a conformable transgressive surface (CTS).

In the Hari River section, the TST includes about half of the total lithological succession of the Afifanagar Alloformation. PS 4 to PS 8 constitute the transgressive systems tract. These parasequences are related to each other, and the environment of deposition varied because of slight variations in sea level and tectonic activity. The basal part of this systems tract consists of Parasequence 4, which is approximately 15 m thick and contains trough-cross-stratified, medium- to fine-grained, moderately sorted sandstone bodies that are channelized. Shale shingles are occasionally present within the sandstone (St) of the channels. The presence of mud and occasional bidirectional paleocurrents in the St facies of the channels indicate tidal action within estuarine channels. This was followed by a transgression in the depositional area after waning of fluvial activity.

Above PS 4, silty tidal flat deposits of PS 5 are present, followed by medium- to fine-grained, planar cross-stratified to ripple-laminated small channel-fill sandstone deposits. These channel features constitute PS 6 and contain bidirectional paleocurrent patterns indicative of tidal action. These are small estuarine channel fills. PS 5 and PS 6 alternate with each other and the thickness of this zone is about 10 m.

Parasequence 7 overlies this zone and consists of parallel- to wavy-laminated grayish shale. This parasequence alternates with PS 8. The ripples of these two parasequences are bidirectional, indicating a small tidal flat deposit. The parallel- to wavy-laminated shale together with the presence of the lenticular-laminated siltstone suggest a tidal flat environment. The depth of the tidal channel deepens and the grain size changes from very-fine-grained sandstone–

siltstone to shale in the upper part of the succession, i.e., mud-dominated deposition. Tidal creek siltstone indicates high-energy conditions, i.e., probably spring tide and a fluctuating energy level in the shale-dominated zone. After the 10-m-thick alternating zone of muddy tidal flats with small tidal creek deposits, an approximately 30-m covered zone is present in the lithological succession. After this, 18 m thickness of small estuarine sediments of PS 9 alternate with the tidal-flat sediments of PS 10. There is a possibility that a slight fall in sea level occurred at this time. Another 15-m-thick alternating zone of PS 11 and PS 12 is present above the comparatively coarser-grained lower horizon of PS 9 and PS 10. The final zone of this systems tract consists of alternations of two parasequences, PS 13 (muddy tidal flat deposits) and PS 14 (tidal creek deposits).

The overall deposition of this transgressive tract occurred in conditions with fluctuating energy levels. As a result, a marginal marine depositional environment was formed. Thick channel fills indicating high-energy conditions later diminished to form a sandy–silty–muddy tidal flat that characterizes the basal part of the systems tract. The thicknesses of the sand, silt, and shale units are variable throughout the whole system tract, which also indicates negligible fluctuations in sea level. The parasequences of this tract show a retrogradational geometry characterized by back-stepping over the basal incised valley. The formation of the transgressive system tract was associated with the creation of accommodation space at a rate faster than the rate of sediment supply. Consequently, a retrogradational parasequence set was developed.

The boundary between the TST and the HST of the Upper Afifanagar Member is marked by a fault in the field area, which might be syndepositional in nature. As a result, abrupt alterations in the environment of deposition were observed, i.e., coastal deposits overlain by deep-marine basin plain deposits. This is the uppermost part of the Afifanagar Alloformation, which is about 116 m thick. At the base of the deposit, an approximately 90-m covered zone (superficial cover) is marked by the presence of a tributary of the Hari River, which is oriented at a right-angle to the Hari River and parallel to the strike of the strata.

After the 90-m gap in the succession, there is a unit of dark blue shale that is highly splintered, weathered and occasionally convoluted. These shales are deep-marine pelagites and make up Parasequence 15. These shales are occasionally embedded within ripple-laminated, very-fine-grained turbiditic sandstone–siltstone (Tc) and parallel-laminated (Td) sandstone, the bases of which have channel-like morphologies. These are small distal turbidite channels. The presence of dark blue shale containing calcium carbonate suggests that this unit was formed above the carbonate compensation depth. Above this, PS 17 occurs, which consists of black shale and contains occasional pyrite.

The contact between the Afifanagar Alloformation and the overlying Lalakhal Sandstone Alloformation is erosional and unconformable and acts as a type I sequence boundary. This boundary is identified as the BSFR, which may have formed as a result of rapid sea-level fall enhanced by uplift of the depositional surface. The parasequences of this system show aggradational to progradational geometry characterized by uniform progradation of sediments from shelf to slope to deep marine basin plain. Instead of rapid sea level rise caused by downfaulting of the depositional site, the sediment supply was low because the depositional site was far away from the shore. The faulted surface acts as a maximum flooding surface and the upper boundary, which is with the Lalakhal Sandstone Alloformation, is forced-regressive. Hence the HST of the Upper Afifanagar Member lies below the forced regression surface and above the maximum flooding surface.

The Afifanagar Alloformation as a whole contains a FSST in the lower part, a TST in the middle part and an HST in the upper part. The formation as a whole is bounded at the base by a type I sequence boundary with the Jaintiapur Alloformation and at the top by a type I sequence boundary with the Lalakhal Sandstone Alloformation.

The paleogeography of an ancient sedimentary basin at a particular time can be reconstructed from the sedimentary succession by studying the set of depositional systems tracts that existed contemporaneously in the basin [18]. The lithological succession of the Afifanagar

Alloformation in the study area contains siliciclastic deposits. The Afifanagar Alloformation in the study area contains fluvial, marginal-marine, shallow–marine and deep-marine sedimentary systems.

5. Proposed stratigraphy of the Sylhet Trough

The stratigraphic nomenclature used currently to describe the Sylhet Trough and the overall Bengal Basin has its roots in the famous work by Evans [19]. The complete stratigraphic column with the type sections (in Assam, India) has been mostly obtained from that work. After Evans, many other sedimentologists have worked on the Sylhet Trough: of these, the works of Alam [4-6, 8] are the most notable.

On the basis of previous studies and on the field data collected in this study, a new stratigraphic nomenclature is proposed for the Eocene–Miocene sediments of the Sylhet Trough. A detailed sequence stratigraphic model is constructed, which includes a renewed sea-level model based on the global sea level curve, demarcation of each of the sequence stratigraphic surfaces identified and an overall model of the Sylhet Trough (Fig. 13).

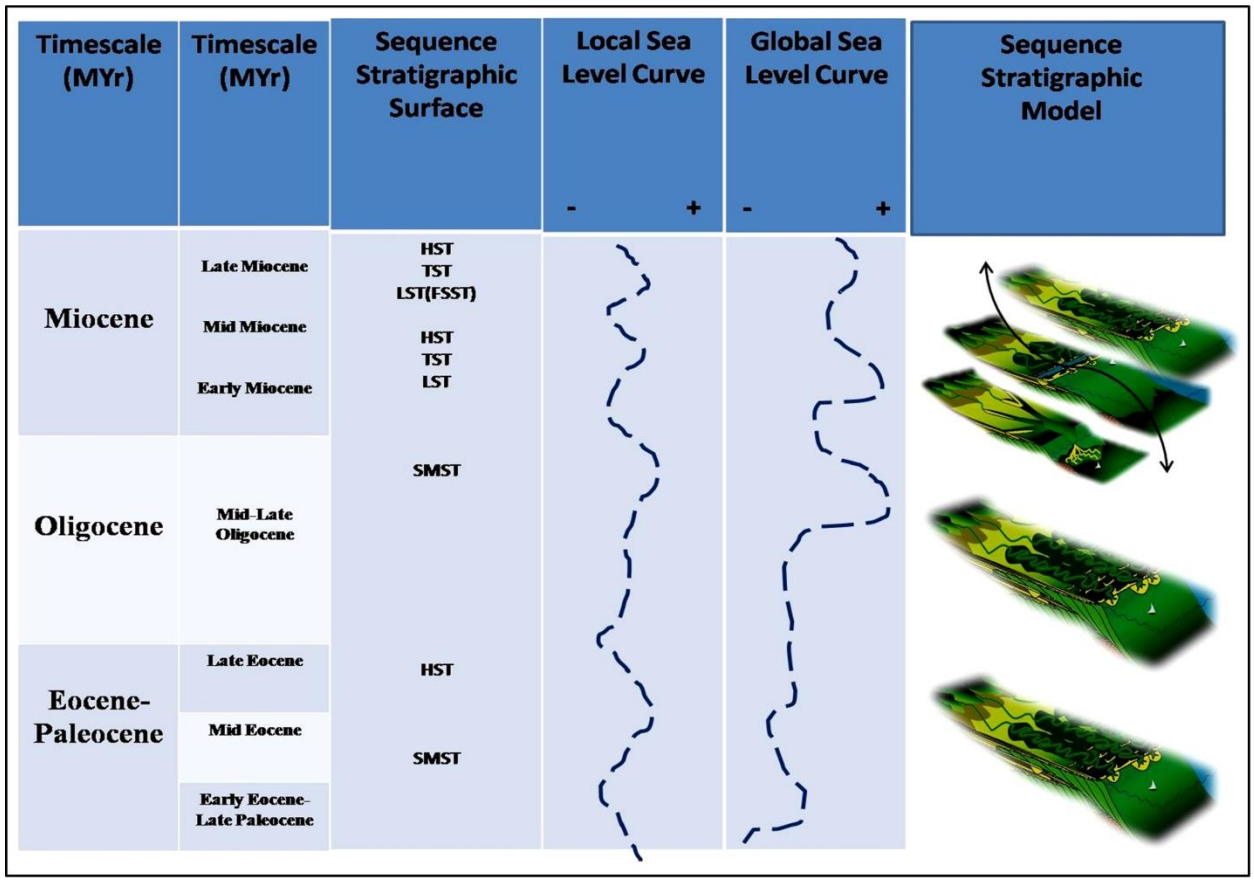

Fig.13. Stratigraphic model of the Sylhet Trough, Exxon-Vail Curve (modified)

6. Conclusions

Observations on the surface exposures of the formations from the Sylhet Limestone to the Afifanagar Alloformation of the Surma Allogroup (Eocene to Miocene periods) have revealed new sequence boundaries based on the broad sequence stratigraphic characteristics of the study area and local type section names replaced with previous stratigraphic nomenclatures. By using classical sequence stratigraphic approaches, the stacking patterns of the parasequences have been well understood and interpreted. The results of this study will aid future

surface and subsurface studies on the Sylhet Trough from the sequence stratigraphic point of view.

6. Acknowledgements

The first author would like to express his deepest gratitude to the Govt. of Brunei and UBD for supporting the research. The authors would also like to thank Phua Eng Siong for his technical support with the drawings. The authors are also thankful to Dr. Badrul Imam for his critical suggestions on the paper.

References

[1] Posamentier HW, Vail PR. Eustatic controls on clastic deposition II—Sequence and systems tract models. In: Wilgus, C.K., et al. (Eds.), Sea-level changes: An integrated approach. Society of Economic Paleontologists and Mineralogists Special Publication, 1988; 42: 125–154.

[2] Boyd R, Suter J, Penland S. Implications of modern sedimentary environments for sequence stratigraphy. In: James, D.P., Leckie, D.A. (Eds.), Sequences, stratigraphy, sedimentology: Surface and subsurface. Canadian Society of Petroleum Geologists Memoir, 1988; 15: 33–36.

[3] Hallam A. 1984. Pre-Quaternary sea-level changes. Annual Reviews, Earth and Planetary Sciences, 1984; 12: 205–243.

[4] Johnson SY, Alam MM. Sedimentation and tectonics of the Sylhettrough, Bangladesh. Geological Society of America Bulletin, 1991; 103: 1513–1527.

[5] Alam MM. 1993. Sedimentology and depositional environment of subsurface Neogene sediments in the Sylhet Trough, Bengal Basin: case study of the Fenchuganj and Beanibazar structures, northeastern Bangladesh. Unpublished Report, Bangladesh Petroleum Institute, 1993; 5: 1–82.

[6] Alam MM, Curray JR, Chowdhury MLR, Gani MR. An overview of the sedimentary geology of the Bengal Basin in relation to the regional tectonic framework and basin-fill history. Sedimentary Geology, 2003; 155: 179–208.

[7] Holtrop JF, Keizer J. Some aspects of the stratigraphy and correlation of the Surma Basin wells, East Pakistan. ECAFE Miner Resource Development Series, 1970; 36: 143–154.

[8] Alam MM. Tide-dominated sedimentation in the upper Tertiary succession of the Sitpaar anticline, Bangladesh. International Association of Sedimentologists Special Publication, 1995; 24: 329–341.

[9] Curray JR. Geological history of the Bengal Geosyncline. Journal of Association of Exploration Geophysics, 1991; 12: 209–219.

[10] Rahman MJJ. 1999. Sedimentology of the subsurface Neogene Surma Group of the Sylhet Trough, Bengal Basin, Bangladesh. M.Sc Dissertation (Unpublished), University of Vienna, Vienna, 1999: 1–173.

[11] Salt CA, Alam MM, Hossain MM. Bengal Basin-Current exploration of the hinge zone of southwestern Bangladesh. Proceed. 6th Offshore Southeast Asia Conf. 1986, Singapore, pp. 55–67.

[12] Coleman JM, Prior DB. Deltaic sand bodies. American Association of Petroleum Geologists Continuing Education Course Note Series 1980; 15: 1–171.

[13] Ingersoll RN, Graham SA, Dickinson WR. Remnant ocean basins. In: Busby, C.J., Ingersoll, R.V. (Eds.), Tectonics of sedimentary basins. Blackwell, Oxford 1995, pp. 363–391.

[14] Mutti E. Turbidite systems and their relations to depositional sequences. In: Zuffa, G.G. (Ed.), Provenance of arenites. NATOASI series. Reidel Publishing Company 1985, pp. 65–93.

[15] Haq BU, Hardenbol J, Vail PR. Chronology of fluctuating sea levels since the Triassic. Science, 1987; 235: 1156–1167.

[16] Boersma JR, Terwindt JH. Neap-spring tide sequences of intertidal shoal deposits in a mesotidal estuary. Sedimentology, 1981; 28: 151–170.

[17] Einsele G. Sedimentary Basins. Springer 1992, Berlin, pp. 1–628.

[18] Vail PR, Mitchum RM, Thompson S. Seismic stratigraphy and global changes of sea level, part 3: Relative changes of sea level from coastal onlap. In: Payton, C.W. (Ed.), Seismic stratigraphy—Applications to hydrocarbon exploration. AAPG Memoir, 1977; 26: 63–97.

[19] Evans P. Tertiary succession in Assam. Trans. Min. Geol. Inst. India, 1932; 27: 155 – 260.

To whom correspondence should be addressed: Dr. AKM Eahsanul Haque, Dimension Strata Sdn Bhd, Ground Floor, Unit 5, Bgn. Zainuddin & Azizah, Spg 501, Jln Tutong, Kg Telanai, Bandar Seri Begawan, BA 2312, Brunei Darussalam, E-mail akmeahsan@yahoo.com

Petroleum and Coal

Article **Open Access**

IN SITU TRANSESTERIFICATION OF MICROALGAE OVER KOH SUPPORTED ON MESOPOROUS CeO_2 CATALYST

Jing Zhang[1,2], Rui Wang[1,2] and Marcelo M Pereira[3]*

[1] *School of Environmental Science and Engineering, Shandong University, No. 72 Seaside Road, Jimo, Qingdao 266237, P.R.China*
[2] *Suzhou Research Institute of Shandong University, No. 388 Ruoshui Road, Suzhou, P.R.China*
[3] *Federal University of Rio de Janeiro, Technology Center, Inorganic Chemistry Department, Athos da Silveira Ramos Avenue, Rio de Janeiro, RJ, Brazil*

Received February 10, 2019; Accepted April 24, 2019

Abstract

In this study, a mesoporous CeO_2 with large surface area and uniform pore size distribution was synthesized using Brij35 as a surfactant. The solid base catalyst KOH/CeO_2 prepared by impregnation method was used to produce biodiesel from *Chlorella vulgaris* biomass by *in situ* transesterification. The characteristics of the catalysts were analysed by the X-ray diffraction (XRD), Brunauer-Emmett-Teller (BET) surface area analyzer and Fourier Transform infrared spectroscopy (FT-IR). The effects on biodiesel yield of catalyst preparation conditions and transesterification parameters were investigated. The optimum preparation conditions of solid base catalyst KOH/CeO_2 were as follows: 50 wt% loading of KOH, 350 °C of calcination temperature and 3 h of calcination time. At the optimal transesterification conditions of catalyst content of 14% wt%, methanol to biomass ratio of 6 mL/g, reaction temperature of 60 °C and reaction time of 8 h, the highest biodiesel yield could achieve 92.9%.

Keywords: *Microalgae; Biodiesel; KOH/CeO_2; Solid base catalyst.*

1. Introduction

With the rapid development of industry and the increasing demand for transportation, traditional sources of energy such as petroleum and coal have been excessively consumed, resulting in the serious environment destruction. Biodiesel has aroused great interest as an alternative energy source to nonrenewable fuels [1-2] .Biodiesel is defined as the fatty acid methyl esters (FAME) produced by transesterification, the feedstock for biodiesel can be vegetable oils, animal fats, waste cooking oil and microalgae oil [3-5]. Compared to traditional fuels, biodiesel has better property such as bio-degradable, no-toxic, and low carbon emission [6]. Therefore, biodiesel is an ideal clean energy for the replacement of traditional energy.

The range of raw materials to prepare the biodiesel is wide. Due to the edible oil clashes with the food, this feedstock has caused heated argument [7].Compared with terrestrial plants, there are some advantages for microalgae as the raw materials. As a lower phytoplankton, microalgae have high photosynthetic efficiency, causing a rapid grow and a high biomass production [8]. Moreover, microalgae have a high oil content. The lipid content of some microalgae is up to 20%~70% [9]. Since the cultivation process of microalgae is not restricted by region and season, microalgae can grow everywhere, avoiding the occupation of crops land [10]. Based on the above features, microalgae are recognized as promising feedstock for biodiesel. Microalgae biodiesel technology covers a number of sport technique segments, including the screening, cultivation and harvesting of microalgae, the extraction and transesterification of microalgae lipid [11]. The lipid in microalgae is usually extracted by organic solvents, such as methanol, chloroform [12-14]. Due to the volatility and toxicity of organic solvents, this method causes the high cost for biodiesel production as well as environment pollution. Recently, in

situ transesterification (direct transesterification) method has been developed, as it combines lipid extraction and transesterification into a one step process [15].Compared to the conventional two-step method, the in situ transesterification simplifies the process of biodiesel production. In addition, it reduces the use of organic solvents and consumption of energy, giving an environment-friendly economic routine [16].

In the process of the transesterification reaction, catalysts play an important role. The homogenous catalysts such as H_2SO_4 and NaOH have been applied in the transesterification reaction so far [17-18]. However, the homogenous catalysts are difficult to be separated from the product. The purification of the product requires a large amount of water, resulting in the emission of waste water. In addition, the homogenous catalyst has high requirement for the quality of raw materials and it causes serious corrosion of equipment [19]]. Since heterogeneous catalyst is easier to be recycled and reused, it simplifies the biodiesel production process and reduces the production cost. The application of heterogeneous catalyst in the preparation of biodiesel is widely studied [20]. Liu et al. synthesized a nano-solid base catalyst ($K/ZrO_2/\gamma$-Fe_2O_3) with weak magnetism and used it for transesterification of soybean oil to produce biodiesel, the biodiesel yield reached above 93.6 wt% and the magnetic catalyst was reused in six cycles without remarkable loss in catalytic activity [21]. Saba *et al.* prepared KOH/ZSM5 for transesterification of sunflower oil, the FAME yield could reach 95.1% under optimal conditions and the catalyst remained high catalytic activity after four times' reuse [22].

As an inexpensive rare earth oxide, CeO_2 is commonly used in catalytic systems as a catalyst or as a carrier for catalyst. For instance, CeO_2 and modified CeO_2 were used as catalysts by Venkatesh for the transesterification of *Pongamia pinnata* oil [23]. Farias *et al.* reported that CeO_2 supported on bentonite was used for ethylic transesterification [24] CeO_2 was also mixed with other metal oxides such as CaO, MgO for transesterification of different oils [25-26]. However, the studies on mesoporous CeO_2 used as catalyst carrier for transesterification have never been reported.

In this study, a mesoporous CeO_2 with large surface area and uniform pore size distribution was synthesized using Brij35 as a surfactant. The solid base catalyst KOH/CeO_2 prepared by impregnation method was used to produce biodiesel from *Chlorella vulgaris* biomass by *in situ* transesterification. The purpose of this study was to investigate the characteristics of the CeO_2 carrier. The optimal synthesis condition of the catalyst for the transesterification reaction was investigated. Furthermore, the optimal transesterification reaction conditions were studied and the effect of the reaction parameters was evaluated.

2. Materials and methods

2.1. Materials

C. vulgaris powder was purchased by Shandong WudiLvqi Biological Engineering Company (Binzhou, China). Heptadecanoic acid methyl ester and FAME standards were obtained from J&K Scientific (Beijing, China).Polyoxyethylene ether (Brij35) was procured from Macklin (Shanghai, China). ($Ce(NH_4)_2(NO_3)_6$), ethanol, ammonia solution (25wt%), potassium hydroxide (KOH), methanol and n-hexane were obtained from Sinopharm (Shanghai, China).All reagents used were of analytical grade. The water used in the experiment was deionized water.

2.2. Catalyst preparation

Firstly, mesoporous CeO_2 carrier was synthesized through the soft-templating approach using polyoxyethylene ether (Brij35) as a surfactant [27]. 20.0 g of Brij35 was dissolved in 50% ethanol, then 10.97 g of $Ce(NH_4)_2(NO_3)_6$ was added by stirring to form a homogeneous solution with the molar composition of Birj35/ $Ce(NH_4)_2(NO_3)_6$ of 2:1. Ammonia of 25wt% was added drop-wise to the solution until the final pH value of the aqueous solution was maintained at 9.0~10.0. The mixture was stirred for 3 h and aged for 2 d. The yellow precipitate was recovered by suction filtration, followed by washing thrice with deionized water and ethanol, respectively. The precipitate was then heated in an oven at 80°C under vacuum. Finally, the dried material was calcined at 350°Cfor 4 h in a muffle furnace to obtain mesoporous CeO_2carrier.

The KOH/CeO_2 catalysts with different KOH loadings (35, 40, 45, 50, 55wt%) were prepared by impregnation of the CeO_2 with an aqueous solution of KOH. The mixture was stirred for 2h and then dried at 100°C for 12 h. The impregnated precursor was calcined in a muffle furnace to obtain the KOH/CeO_2 solid catalyst.

2.3. In situ transesterification

The transesterification reactions were carried out in a 250mL three neck round-bottom flask with a condenser. 5 g of dry microalgae, 20 mL of hexane, a certain proportion of methanol (4-12 mL/g) and amounts of the catalyst KOH/CeO_2(12-20 wt%) were added to the neck flask. The neck flask was put in a water bath with vigorous stirring to a preset temperature (50-70°C) for a preset time (2-10 h).After the completion of the reaction, the mixture was cooled to room temperature and filtered to remove the residues. 20 mL of hexane was added to the filtrate to extract the FAME product, this step was repeated three times. The obtained hexane layer was transferred to a clean flask and evaporated to obtain the biodiesel. The FAME content in the sample was directly analyzed by gas chromatography. The conversion efficiency of lipid to FAME was expressed as weight of FAMEs compared with weight of total convertible lipids [28].

2.4. Biodiesel sample analysis

The composition of biodiesel was analyzed using a gas chromatography-mass spectrometer (Shimadzu, Japan) equipped with a flame-ionization detector (FID) and a Rxi-Wax capillary column (30m × Φ 0.25 mm × 0.25 μm). The injector temperature was 250°C, the oven temperature was set at 160°C and held for 1 min, and then it was increased to 200°C at the rate of 5°C/min before the temperature increase to 230°C at rate of 2°C/min and held for 5 min. The detector temperature was set at 260°C. Helium was used as carrier gas at a flow rate of 1.0mL/min.

2.5. Catalyst characterization

Fourier transform infrared (FT-IR) spectra of the samples were performed using ALPHA-T Fourier Transform Infrared Spectrometer (BRUKER Corp, Germany) from 400 cm^{-1} to 4000 cm^{-1}. X-ray diffraction (XRD) was carried out on D/MAX-rA instrument (Rigaku Corp., Japan).Nitrogen adsorption and desorption isotherms of CeO_2 were studied using the ASAP2020 analytical system (USA). The specific surface area was calculated by the Brunauer-Emmett-Teller (BET) method and the mesopores volume and pore size distribution were calculated by the Barrett-Joyner-Halenda (BJH) method from the desorption curve of the isotherm.

3. Results and discussion

3.1. Catalyst characterization

3.1.1. BET and N_2 adsorption-desorption isotherm

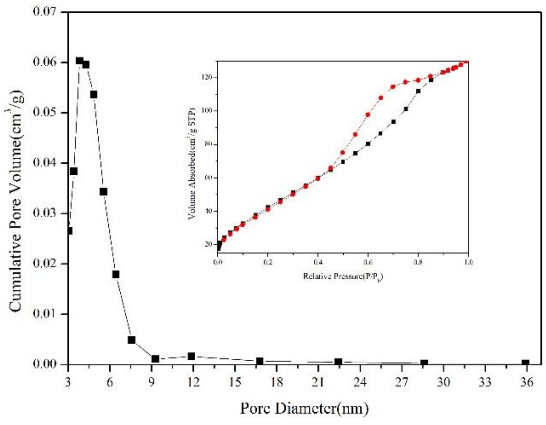

Fig.1. (a) Pore size distribution curve and (b) Nitrogen adsorption-desorption isotherm of CeO_2

The BET result of the CeO_2showed that the carrier had a surface area of 160.04 m^2/g, a pore volume of 0.187 m^3/g and an average pore diameter of 3.817nm. Fig.1 shows the N_2 adsorption/desorption isotherm and pore diameter distribution of CeO_2.The pore diameter distribution indicated the CeO_2 carrier possessed mesoporous pore with a pore size that mainly distributed in 3-9 nm. According to the IUPAC classification, the N_2 adsorption/desorption isotherm of the CeO_2 belonged to type IV with a notable H_2 hysteresis loop, revealed that the carrier was typical of mesoporous materials.

3.1.2. FT-IR

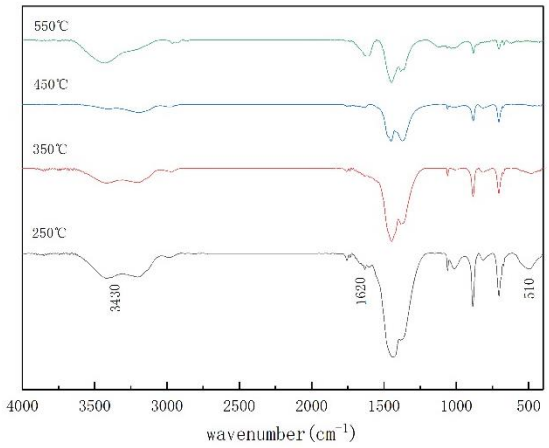

Fig.2.The FT-IR absorption spectra of KOH/CeO_2 calcinated in different temperatures

The FT-IR absorption spectra of KOH/ CeO_2 calcinated in different temperatures was represented in Fig.2. The broad band at 3430 cm^{-1} attributed to the presence of the O-H stretching vibration. The peak appeared at 1603 cm^{-1}can be assigned to the bending vibration of O-H. The peaks appeared at 700-1500$cm^{-1}$was due to the presence of C-H, -CH_2- and C-O-C vibration in the polyoxyethylene ether (Brij35) structure. The peak at 510 cm^{-1}corresponded to the characteristic stretching of Ce-O bond [29]. As can be seen in Fig.2, the intensity of absorption peak decreased with the calcination temperature increases, which indicated that the calcination temperature had influence on the structure of catalyst.

3.1.3. XRD

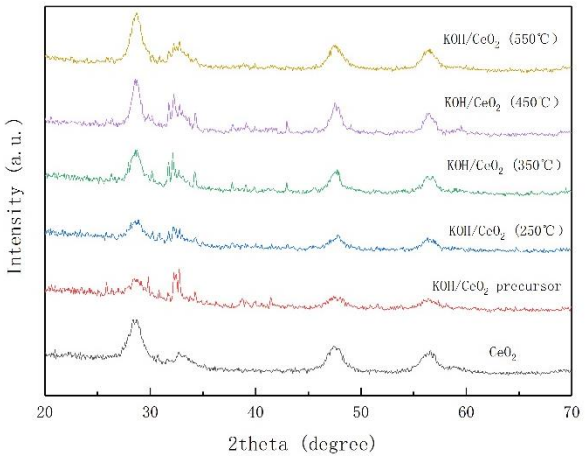

Fig.3. XRD patterns of CeO_2, uncalcinated KOH/ CeO_2 precursor and calcined KOH/ CeO_2 at different temperatures

Fig. 3 shows that the XRD patterns of CeO_2, uncalcinated KOH/ CeO_2 precursor and calcined KOH/CeO_2at different temperatures. All samples showed diffraction peaks at 2θ =28.5˚, 33.1˚, 47.5˚and 56.4˚, which corresponded to the characteristic cubic fluorite structure of CeO_2. After loading with KOH, the diffraction peaks of CeO_2 almost disappeared, which proved that KOH had been loaded on the CeO_2 surface successfully. As can be seen, the diffraction peak related to the KOH phase has not been found, which might be due to high dispersion of K^+ species. With increasing calcination temperature from 250°C to 550°C, the intensities of diffraction peaks of CeO_2 gradually increased, indicating that the calcination temperature had influence in the distribution of KOH on the surface of CeO_2.

3.2. Catalytic performance for biodiesel production

3.2.1 Effect of preparation conditions on the FAME yield

The effects of various preparation conditions include KOH loading amount, calcination time and calcination temperature on catalytic performance were investigated in the microalgae transesterification. The transesterification reactions were carried out at a catalyst content of 14 wt.%, a methanol to biomass ratio of 6 mL/g, a temperature of 60°C and a reaction time of 8 h.

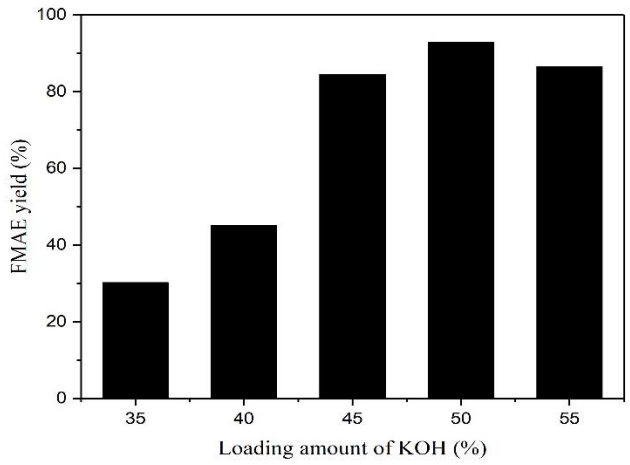

Fig.4. Effects of KOH loading amount on FAME yield (%)

A series of KOH/CeO_2 catalysts with KOH loading from 35 to 55 wt% calcined at 350°C for 3 h were prepared. As shown in Fig.4, as the KOH loading increased from 10 wt% to 30 wt%, the biodiesel yield increased from 30.2% to 92.9%. However, the biodiesel yield decreased as the KOH loading exceeded 50wt %.The increase of biodiesel yield was attributed to the formation of active sites with the increase of KOH loading. As the KOH loading continued to increase, the active sites on the surface of the carrier gradually approach saturated and agglomerated on the carrier partially, resulting in the decrease in catalyst activity , which caused the reduce of biodiesel yield. Therefore, the optimum loading amount of KOH was 50wt%.

The influence of calcination temperature of the KOH/CeO_2 catalyst was studied with the calcination temperature ranging from 250°C to 650°C.

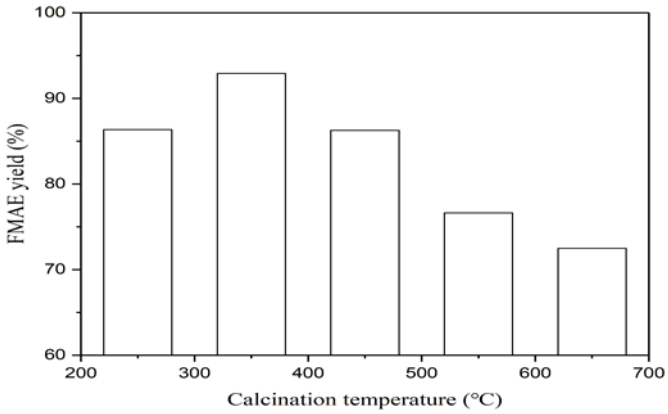

Fig.5. Effects of calcination temperature on FAME yield (%)

Fig.5 shows that the biodiesel yield increased from 86.3% to 92.9% as the calcination temperature of the catalyst increased from 250°C to 350°C. However, the biodiesel decreased after the calcination temperature exceeded 350°C. Previous research had documented that, K_2O formed by decomposition of KOH as calcination temperature exceed 600°C, which contributed to the strong basic activity in transesterification reaction [30]. In this study, the FT-IR and XRD results indicated that the calcination temperature had influence on the structure of mesoporous CeO_2. When the calcination temperature exceeded 350°C, it may lead to the sintering of catalyst surface, resulting in the reduction of the specific surface area. Therefore, the appropriate calcination temperature was 350°C.

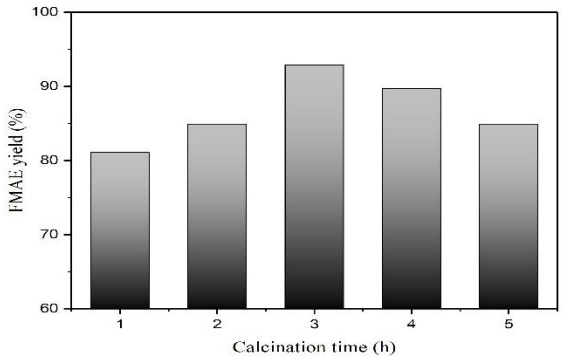

Fig.6. Effects of calcination time on FAME yield (%)

In order to determine the effect of calcination time for the catalyst preparation, the calcination time was varied within the range of 1 – 5 h. Fig.6 shows that the biodiesel yield increased from 81.1% to 92.9% as the calcination temperature of the catalyst increased from 1 h to 3h. However, the biodiesel decreased after the calcination temperature exceeded 3 h. Excessive time would result in the catalyst surface sintering. Thus, the best calcination time for catalyst preparation was 3h.

3.2.2. Effect of transesterification conditions on the FAME yield

The optimum preparation conditions of solid base catalyst KOH/CeO_2 were as follows: 50 wt% loading of KOH, 350°C of calcination temperature and 3 h of calcination time. The KOH/CeO_2 prepared in the optimum conditions was applied to research the influence of reaction conditions on the biodiesel yield.

3.2.2.1. Effect of catalyst content

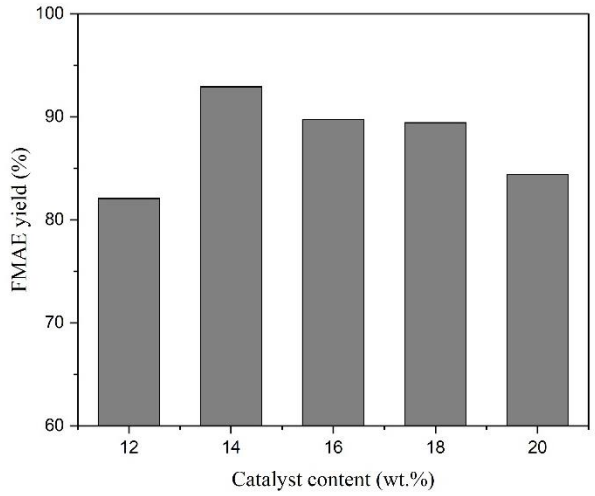

Fig.7. Effects of catalyst content on FAME yield (%)

To study the effect of catalyst content, transesterification reactions were performed with different amounts of the catalyst (12-20wt%) at a methanol to biomass ratio of 6 mL/g, a temperature of 60°C and a reaction time of 8 h. Fig.7 shows that the biodiesel yield increased from 44.0% to 92.9% as the catalyst amount increased from 10 wt% to 14 wt%. However, the biodiesel yield decreased slightly with the catalyst amount further prolonged to. It was probably because the excessive catalyst caused saponification. Therefore, the optimal mass ratio of the catalyst was 14wt%.

3.2.2.2. Effect of methanol/oil molar ratio

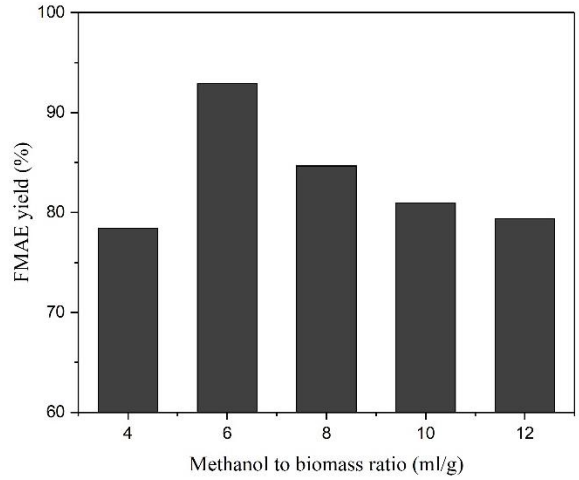

The biodiesel yield under various methanol to biomass ratios was showed in Fig.8 with catalyst content of 2wt% and the temperature of 60°C after reacting for 8h.The biodiesel yield increased from 78.4% to 92.9% as the methanol to biomass ratio increased from 4 mL/g to 6mL/g. The dilution of the oil and catalyst concentration caused by excess methanol explained the decrease of biodiesel yield. Therefore, the optimum methanol/oil molar ratio was 6:1.

Fig. 8. Effects of methanol to biomass ratio on FAME yield (%)

3.2.2.3. Effect of reaction temperature

To investigate the optimum reaction temperature, transesterification reactions were carried out with various reaction temperature (50, 55, 60, 65, 70°C) at a methanol to biomass ratio of 6 ml/g, a catalyst amount of 14 wt% and a reaction time of 8 h. As shown in Fig.9, the biodiesel yield increased from 75.1% to 92.9% with the reaction temperature increased from 50°C to 60°C. However, the biodiesel yield decreases to 82.0% as the catalyst amount increased to 70°C. Because the boiling point of methanol is 64.7°C, methanol would volatilize from the reaction system when the reaction temperature exceeded 64.7°C, resulting in the loss of methanol and a decrease in biodiesel yield. Thus, 60°C was considered as the appropriate reaction temperature.

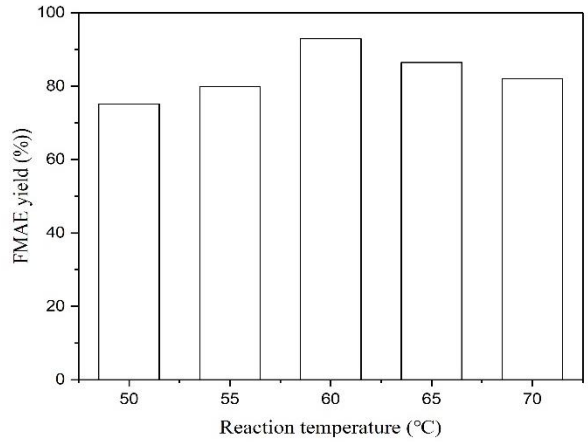

Fig.9. Effects of reaction temperature on FAME yield (%)

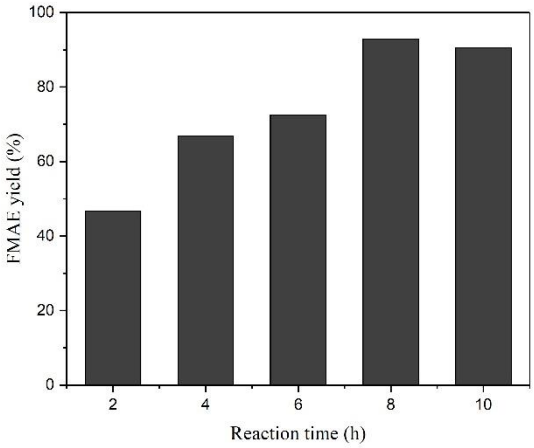

Fig.10. Effects of reaction time on FAME yield (%)

3.2.2.4. Effect of reaction time

The optimal reaction time was investigated with the reaction time ranging from 2 h to 10 h. Fig.10 presented that the biodiesel yield increased rapidly from 46.8% to 92.9%. However, when the reaction time increased to 10 h, the biodiesel yield was not significantly improved. The slightly decrease of the biodiesel yield may be due to the degradation of long-chain unsaturated fatty acids [28]. Therefore, 8h was chosen as the optimum reaction time.

4. Conclusion

In this paper, a mesoporous CeO_2 was successfully synthesized using Brij35 as a surfactant. The BET result showed that the mesoporous CeO_2 had the advantages of large surface area and uniform pore size distribution. The solid base catalyst KOH/CeO_2 was prepared by impregnation method and used to produce biodiesel from *Chlorella vulgaris* biomass by *in situ* transesterification. The optimum preparation conditions of solid base catalyst KOH/CeO_2 were as follows: 50 wt% loading of KOH, 350°C of calcination temperature and 3 h of calcination time. The highest yield of biodiesel of 92.9% was achieved at the optimal reaction condition of 14 wt% of catalyst content, 6 mL/g of methanol to biomass ratio and at 60°C for 8 h. KOH/CeO_2 catalyst is a promising solid base catalyst for the high catalytic activity and low cost.

Acknowledgements

Funding for this research was provided by the Science & Technology Development Program of Suzhou City, China (SYN201520).

References

[1] Faried M, Samer M, Abdelsalam E, Yousef R, Attia Y,Ali A. Biodiesel production from microalgae: Processes, technologies and recent advancements. Renew. Sust. Energ. Rev., 2017; 79: 893-913.

[2] Veillette M, Giroir-Fendler A, Faucheux N, Heitz M. Esterification of free fatty acids with methanol to biodiesel using heterogeneous catalysts: From model acid oil to microalgae lipids. Chem. Eng. J., 2017; 308: 101-109.

[3] Ullah Z, Bustam M A, Man Z, Khan A S, Muhammad N, Sarwono A. Preparation and kinetics study of biodiesel production from waste cooking oil using new functionalized ionic liquids as catalysts. Renew. Energy, 2017; 114: 755-765.

[4] Alajmi F S, Hairuddin A A, Adam N M, Abdullah L C. Recent trends in biodiesel production from commonly used animal fats. Int. J. Energy Res., 2018; 42 (3): 885-902.

[5] Chen C-L, Huang C-C, Ho K-C, Hsiao P-X, Wu M-S, Chang J-S. Biodiesel production from wet microalgae feedstock using sequential wet extraction/transesterification and direct transesterification processes. Bioresour. Technol., 2015; 194: 179-186.

[6] Nautiyal P, Subramanian K, Dastidar M. Production and characterization of biodiesel from algae. Fuel Process. Technol., 2014; 120: 79-88.
[7] Taparia T, MVSS M, Mehrotra R, Shukla P, Mehrotra S. Developments and challenges in biodiesel production from microalgae: A review. Biotechnol. Appl. Biochem., 2016; 63 (5): 715-726.
[8] Mohan S V, Rohit M, Chiranjeevi P, Chandra R, Navaneeth B. Heterotrophic microalgae cultivation to synergize biodiesel production with waste remediation: progress and perspectives. Bioresour. Technol., 2015; 184: 169-178.
[9] Milano J, Ong H C, Masjuki H, Chong W, Lam M K, Loh P K, Vellayan V. Microalgae biofuels as an alternative to fossil fuel for power generation. Renew. Sust. Energ. Rev., 2016; 58: 180-197.
[10] Zhu L, Nugroho Y, Shakeel S, Li Z, Martinkauppi B, Hiltunen E. Using microalgae to produce liquid transportation biodiesel: what is next? Renew. Sust. Energ. Rev., 2017; 78: 391-400.
[11] Dickinson S, Mientus M, Frey D, Amini-Hajibashi A, Ozturk S, Shaikh F, Sengupta D, El-Halwagi MM. A review of biodiesel production from microalgae. Clean Technol. Environ. Policy, 2017; 19 (3): 637-668.
[12] Guldhe A, Moura C V, Singh P, Rawat I, Moura E M, Sharma Y, Bux F. Conversion of microalgal lipids to biodiesel using chromium-aluminum mixed oxide as a heterogeneous solid acid catalyst. Renew. Energy, 2017; 105: 175-182.
[13] Syazwani O N, Rashid U, Yap Y H T. Low-cost solid catalyst derived from waste Cyrtopleura costata (Angel Wing Shell) for biodiesel production using microalgae oil. Energy Convers. Manage., 2015; 101: 749-756.
[14] Mubarak M, Shaija A, Suchithra T. A review on the extraction of lipid from microalgae for biodiesel production. Algal Res., 2015; 7: 117-123.
[15] Salam K A, Velasquez-Orta S B, Harvey A P. A sustainable integrated in situ transesterification of microalgae for biodiesel production and associated co-product-a review. Renew. Sust. Energ. Rev., 2016; 65: 1179-1198.
[16] Tangy A, Kumar V B, Pulidindi I N, Kinel-Tahan Y, Yehoshua Y, Gedanken A. In-situ transesterification of chlorella vulgaris using carbon-dot functionalized strontium oxide as a heterogeneous catalyst under microwave irradiation. Energy & Fuels, 2016; 30 (12): 10602-10610.
[17] Guzatto R, De Martini T L, Samios D. The use of a modified TDSP for biodiesel production from soybean, linseed and waste cooking oil. Fuel Process. Technol., 2011; 92 (10): 2083-2088.
[18] Hoda N. Optimization of biodiesel production from cottonseed oil by transesterification using NaOH and methanol. Energy Sources Part A-Recovery Util. Environ. Eff., 2010; 32 (5): 434-441.
[19] Mardhiah H H, Ong H C, Masjuki H, Lim S, Lee H. A review on latest developments and future prospects of heterogeneous catalyst in biodiesel production from non-edible oils. Renew. Sust. Energ. Rev., 2017; 67: 1225-1236.
[20] Semwal S, Arora A K, Badoni R P,Tuli D K. Biodiesel production using heterogeneous catalysts. Bioresour. Technol., 2011; 102 (3): 2151-2161.
[21] Liu K, Wang R, Yu M. Biodiesel production from soybean oils by a novel nano-magnetic solid base catalyst ($K/ZrO_2/\gamma$-Fe_2O_3). RSC Adv., 2017; 7 (82): 51814-51821.
[22] Saba T, Estephane J, El Khoury B, El Khoury M, Khazma M, El Zakhem H, Aouad S. Biodiesel production from refined sunflower vegetable oil over KOH/ZSM5 catalysts. Renew. Energy, 2016; 90: 301-306.
[23] Shamshuddin M, Zaheeruddin S, Shyamsundar M, Thammannigowda Vasanth V. Biodiesel synthesis from Pongamia pinnata oil over modified CeO_2 catalysts. J. Mex. Chem. Soc., 2014; 58 (4): 378-385.
[24] Farias A F F, Moura K F, Souza J K, Lima R O, Nascimento J D, Cutrim A A, Longo E, Araujo A S, Carvalho-Filho J R, Souza A G. Biodiesel obtained by ethylic transesterification using CuO, ZnO and CeO_2 supported on bentonite. Fuel, 2015; 160: 357-365.
[25] Wong Y, Tan Y, Taufiq-Yap Y, Ramli I, Tee H. Biodiesel production via transesterification of palm oil by using CaO–CeO_2 mixed oxide catalysts. Fuel, 2015; 162: 288-293.
[26] Manríquez-Ramírez M, Gómez R, Hernández-Cortez J, Zúñiga-Moreno A, Reza-San Germán C M, Flores-Valle S O. Advances in the transesterification of triglycerides to biodiesel using MgO–NaOH, MgO–KOH and MgO–CeO_2 as solid basic catalysts. Catal. Today, 2013; 212: 23-30.
[27] Zhao X, Luo L, Liu C, Li M. Synthesis and Characterization of Mesoporous Ceric Oxide. Materials Review, 2006: S2.

[28] Cheng J, Qiu Y, Huang R, Yang W, Zhou J, Cen K. Biodiesel production from wet microalgae by using graphene oxide as solid acid catalyst. Bioresour. Technol., 2016; 221: 344-349.
[29] Magdalane C M, Kaviyarasu K, Vijaya J J, Siddhardha B, Jeyaraj B. Photocatalytic activity of binary metal oxide nanocomposites of CeO_2/CdO nanospheres: Investigation of optical and antimicrobial activity. J. Photochem. Photobiol. B: Biol., 2016; 163: 77-86.
[30] Ma G, Hu W, Pei H, Jiang L, Ji Y, Mu R. Study of KOH/Al_2O_3 as heterogeneous catalyst for biodiesel production via in situ transesterification from microalgae. Environ. Technol., 2015; 36(5): 622-627.

To whom correspondence should be addressed: Professor Dr. Rui Wang, School of Environmental Science & Engineering Shandong University No.27, Shanda South Rd., Jinan 250100, P.R. China

Petroleum and Coal

Article **Open Access**

CHALLENGES AND SOLUTIONS OF GAS SWEETENING UNIT IN POLYPROPYLENE PLANT USING PROCESS SIMULATION: A CASE STUDY

Walaa M. Shehata[1,], Abeer M. Shoaib[1], Ahmed A. Bhran[1,2], Mohamed A. Gabr[1], Fatma K. Gad[1]*

[1] *Department of Petroleum Refining and Petrochemical Engineering, Faculty of Petroleum and Mining Engineering, Suez University, Suez, Egypt*
[2] *Chemical Engineering Department, College of Engineering, Al Imam Mohammad Ibn Saud Islamic University, Riyadh, Saudi Arabia*

Received February 5, 2019; Accepted April 4, 2019

Abstract

Gas sweetening units using amines are an important part of lots of industries. They provide clean burning fuels and valuable chemical feedstock. The integration of these units with petrochemical plants has increased their importance and complexity over the years. The advantages of computer simulation models as tools for designing and troubleshooting gas treating plants is increasingly obviously. This paper discusses the major problems faced in operation of the amine gas sweetening unit in polypropylene plant using a process simulation tool, HYSYS version 10. Several highlighted problems in such a plant have been investigated and discussed; then a number of proposed modifications have been suggested to overcome these problems and increase the productivity of the plant as designed. The results showed that the proposed modifications have a high impact on the amine sweetening unit efficiency. The modified procedures were applied, and the lab analysis showed good agreement with the simulation results.

Keywords: *Simulation; MDEA; Gas sweetening; Amine system; Troubleshooting.*

1. Introduction

Gas sweetening using amines is a key operation in gas processing facilities, refinery operations, petrochemical plants, and other industries; aiming to maintain efficient operation and meet sales specifications [1]. The amine system is designed as a closed-circuit system and directed primarily to remove hydrogen sulfide, carbon dioxide and other acidic components from gaseous hydrocarbon streams. It takes great attention due to high pressure for environmental compliance and high quality of acid gas removal [2]. However, many operational problems face the amine-based gas sweetening process; such as intense corrosion, capacity reduction, instability of operation, amine degradation, carryover and excessive foaming [3-4]. The occurrence of such problems in gas sweetening units will consequently result in a reduction in treating efficiency and hence, higher amounts of acid gases in the resulted gas stream. Some of these problems have taken great attention from the researchers over the years; for example, corrosion problems have been addressed by Mogul [5] who introduced thermoplastic coating to insulate process equipment from corrosion-inducing conditions. Further corrosion control methods have been introduced and discussed by other researchers [6-9]. On the other hand, the foaming problem has been discussed in details by Gondule *et al.* [10]; from the view point of causes, disadvantages and how to control it. They reported that foaming could be a result of contamination in the absorbing solvent or feed gas. Possible contaminants may be corrosion products, corrosion inhibitors, well treating fluids, liquid hydrocarbons, amine degradation products, organic acids, foam reducing agents or other finely divided solids. Foaming

results in many negative effects such as reduction in mass transfer area, efficiency and absorption capacity. Even more, carryover of amine solution to the downstream plant could be a result of foaming [11-13]. Sarker [14] has discussed the theoretical effect of various process variables on the performance of the gas sweetening process. The studied variables were amine circulation rate and concentration; temperature and pressure of single and mixed amine solvents; and sweetening stages. Over the years, some other research work has addressed the probable problems in amine based sweetening units and introduced the suggested solutions [2, 15-17]. However, most of the previous works were focused on the natural gas sweetening units. In this work, the research was focused on the challenges facing the gas sweetening unit in an existing petrochemical plant.

Process streams and feedstocks for polymerization units are needed to be of high purity, to avoid negative effects on catalyst activity and functionality. Furthermore, polymer quality and yield could also be affected negatively by improper treatment or sweetening of the monomer feedstock stream [18]. Therefore, the sweetening unit is an important purification unit for removing carbon dioxide and other acid gases.

In this work, the troubleshooting in the amine based sweetening unit, specially using methyl diethanolamine (MDEA) as a solvent, in a petrochemical plant was studied. Many solutions were suggested in order to overcome operational problems and increase the productivity of the plant to reach its designed value. HYSYS software version 10 was used in this work as the simulation tool. It is expected that the introduced solutions and modifications can handle huge amounts of CO_2 out of the feed gas stream.

2. Case study and process description

The case study taken in this research work is for the MDEA sweetening unit in polypropylene production plant located in Egypt. Propane is fed to the dehydrogenation unit for the production of propylene, which is the feedstock for the polypropylene production plant.

During propane dehydrogenation reaction, CO_2 is formed due to the hydrolysis reaction, and reconversion of coke lay down on the catalyst (caused by thermal cracking) with steam during the operation cycle. Propylene stream containing CO_2 should be purified to overcome the acid gas negative effects on catalyst activity and functionality as well as polymer quality and yield. Moreover, this gas stream will undergo liquefaction process that requires operation under a very low temperature (-90°C) and a low pressure reaching 3 bar. At these conditions, CO_2 can freeze on the exchanger surface (cold box), and cause plugging of the pipes and reduction in plant efficiency. So, the amine sweetening process is constructed prior to the liquefaction process. Figure1 shows a block diagram for the propane dehydrogenation plant (PDH).

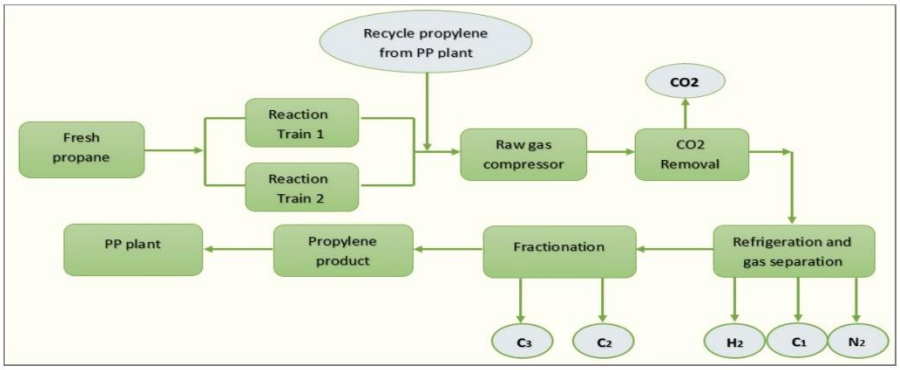

Figure 1. Block diagram of the main processes of PDH plant

As shown in Figure 1, PDH plant consists of reaction section and heat recovery, natural gas compression, a CO_2 removal unit, refrigeration and gas separation, and fractionation processes, in addition to polypropylene (PP) production plant.

2.1. Processes chemistry

The processes chemistry of this case study includes two parts. The first part describes how the CO_2 gas is produced from the propane dehydrogenation reaction section, while the second part describes how methyl diethanol amine solvent absorbs the CO_2 in the presence of piperazine as an activator in the CO_2 removal unit. The dehydrogenation of propane to propylene takes place in two series reactors; super heating reactor; called steam reformer, and an oxy-reactor. This is performed in two identical, parallel reaction trains, (train I and train II). Dehydrogenation is a strongly endothermic reaction, in which propane is converted to propylene and hydrogen according to the reaction described in Equation 1 [19-21].

$$C_3H_8 \rightleftharpoons C_3H_6 + H_2 \quad (1)$$

Within the reformer reactor, the heat required for the reaction is provided by super heating steam. Approximately 75% of overall propylene production is accomplished in this reactor. Side reactions like cracking and hydrolysis can lead to the formation of lower hydrocarbons like methane, ethane, and ethylene as addressed in Equations 2- 4 [19, 21].

$$C_3H_8 \rightarrow C_2H_4 + CH_4 \quad (2)$$

$$C_3H_8 + H_2 \rightarrow C_2H_6 + CH_4 \quad (3)$$

$$C_2H_4 + H_2 \rightarrow C_2H_6 \quad (4)$$

These cracking reactions are primary of thermal cracking type, which can result in the formation of small amounts of coke (Equation 5). Therefore, the platinum oxide catalyst used (PtO_2) should be regenerated regularly to burn off the coke. However, the presence of steam during reaction lowers coke lay down on the catalyst; allowing longer operation cycles as well as quick and simple regeneration.

$$CH_4 \rightarrow C + 2H_2 \quad (5)$$

The product gas emerged from the reformer reactor is admitted to the oxy-reactor for more conversion of propane to propylene by oxidative dehydrogenation. Within the oxy-reactor, selective conversion of hydrogen, as well as further conversion of propane, takes place. The oxygen is admitted to the oxy-reactor to provide the endothermic heat requirement for dehydrogenation of propane. However, the equilibrium can be shifted in forwarding direction by removal/conversion of hydrogen for the formation of H_2O as presented in Equation 6. The formation of H_2O is an exothermic reaction, which provides the heat of reaction for further endothermic conversion of paraffins to olefins; this consequently leads to an increase in propane conversion as presented in Equation 1.

$$H_2 + {}^1/_2 O_2 \rightarrow \quad H_2O \quad (6)$$

Combustion of propane and propylene may exist according to Equations 7, and 8.

$$C_3H_8 + 5\,O_2 \rightarrow 3\,CO_2 + 4\,H_2O \quad (7)$$

$$C_3H_6 + {}^9/_2\,O_2 \rightarrow 3\,CO_2 + 3\,H_2O \quad (8)$$

Besides the above reactions, carbon monoxide (CO) and carbon dioxide can be formed as described in Equations 9-12.

$$C + {}^1/_2\,O_2 \rightarrow CO \quad (9)$$

$$C + H_2O \rightarrow CO + H_2 \quad (10)$$

$$2CO \rightarrow C + CO_2 \quad (12)$$

The CO_2 produced with the propylene product (Equations 7,8, and 12) from the reaction section is removed in the CO_2 removal unit while the other side product gases are removed in the refrigeration and the fractionation units as shown in Figure 1.

In the CO_2 removal unit, CO_2 is absorbed in an absorption tower using piperazine-activated MDEA as a solvent. This solvent selectively absorbs CO_2 contained in the gas produced from the oxy-reactor. The main problem associated with MDEA usage without activator is the lower rate of the absorption process. Therefore, the activator is required to increase the absorption rate. Although MDEA can be activated through many ways like Mono-ethanol amine, but activating MDEA with piperazine (PZ) will increase the absorption process rate to be many times faster, compared to Mono-ethanol amine. The needed dose of piperazine to achieve the required purity of the process gas is small [9, 22].

Many reactions can take place during the CO_2 absorption process using activated MDEA solution in the sweetening unit. These reactions are presented by the following equations [4, 23-27].

$$CO_2 + \text{MDEA} + H_2O \leftrightharpoons \text{MDEA}H^+ + HCO_3^- \quad (13)$$
$$CO_2 + OH^- \leftrightharpoons HCO_3^- \quad (14)$$
$$CO_2 + \text{PZ} + H_2O \leftrightharpoons PZCOO^- + H_3O^+ \quad (15)$$
$$CO_2 + \text{MDEA} + PZ \leftrightharpoons \text{MDEA}H^+ + PZCOO^- \quad (16)$$
$$CO_2 + PZCOO^- + H_2O \leftrightharpoons PZ(COO^-)_2 + H_3O^+ \quad (17)$$
$$CO_2 + \text{MDEA} + PZCOO^- \leftrightharpoons \text{MDEA}H^+ + PZ(COO^-)_2 \quad (18)$$
$$HCO_3^- + H_2O \longrightarrow CO_3^{2-} + H_3O^+ \quad (19)$$
$$\text{MDEA} + H_3O^+ \longrightarrow \text{MDEA}H^+ + H_2O \quad (20)$$
$$2H_2O \longrightarrow H_3O^+ + OH^- \quad (21)$$
$$PZ + H_3O^+ \longrightarrow PZH^+ + H_2O \quad (22)$$
$$PZCOO^- + H_3O^+ \longrightarrow PZH^+COO^- + H_2O \quad (23)$$

where:

- Equation (13) is the basic catalyzed hydration reaction of MDEA solution
- Equation (14) is the formation reaction of bicarbonate
- Equation (15) represents the formation of mono-carbamate reaction by PZ
- Equation (16) is the reaction of formation of mono-carbamate by PZ/MDEA
- Equation (17) is the formation of di-carbamate reaction
- Equation (18) represents the formation reaction of di-carbamate by $PZCOO^-/MDEA$
- Equation (19) is the formation reaction of carbonate reaction
- Equation (20) represents the protonation reaction of MDEA
- Equation (21) is the dissociation of water reaction
- Equation (22) is the protonation reaction of piperazine
- Equation (23) represents the protonation reaction of mono-carbamate.

In the regeneration tower in the sweetening unit, the mono and di-carbamate are transformed into free piperazine and CO_2. In the presence of piperazine, the heat required to separate CO_2 from the carbamate (Equations 15-18) increases in the regeneration process according to carbamate stability (Equation 24). In case of absence of the piperazine, bicarbonate (HCO_3^-) and carbonate (CO_3^{2-}) are only formed with CO_2 in the absorber (Equations 13, 14, and 19) and are easily separated in the regenerator using a lower amount of heat according to Equations 25 and 26 [2, 28].

$$PZCOO^- + H_2O \rightleftharpoons CO_2 + PZ + OH^- \quad (24)$$
$$HCO_3^- \leftrightharpoons CO_2 + OH^- \quad (25)$$
$$CO_3^{2-} + H_2O \rightleftharpoons CO_2 + 2OH^- \quad (26)$$

2.2. CO_2 removal unit

As discussed previously, CO_2 gas must be removed to achieve the purity specification of the propylene product. For this purpose, the CO_2 removal unit is constructed. Traces of H_2S, which may present due to sulphur contained in the propane feed, could also be removed during the sweetening process. The flow diagram of this unit, which is the focus of the present work is illustrated in Figure 2.

The used MDEA solvent contains 20 to 40 mole percent of MDEA and 5 to 6 mole percent piperazine, while balance constitutes of water. The rich solvent is regenerated and then, stripped from CO_2/H_2S traces. However, it is noted that lean solvent is not fully free of CO_2/H_2S and contains some observable residual amount of them.

As shown in Figure 2, the sour compressed gas from the process gas compressor is admitted to the bottom of the absorber column and contacted counter currently with the lean MDEA solution which is admitted to the top of the absorber column, at a pressure of 3106 kPa and a temperature of 65°C. The treated gas from absorber top is routed to the fractionation unit after knocking out of potential liquid carry over in treated gas knock out the drum. In the absorber, a small quantity of water is added to the absorber to balance the loss of vapor leaving the system with the gas streams. The regeneration of the MDEA solution is carried out

at a low pressure of 348.1 kPa and an elevated temperature of 95°C in the stripper. The CO_2 content in the treated gas outlet from the absorber top is reduced to 1300 ppm. The rich solution is let down to a lower pressure across control valve rich MDEA (Rich aMDEA LV) and routed to the high-pressure flash drum (HP Flash Drum). This flash drum operates at a pressure in between the absorber and stripper operating pressures and normally higher than the partial pressure of CO_2 in the feed gas to the absorber. This ensures that CO_2 is not lost through the flash gas containing absorbed hydrocarbons which are routed back to the raw gas compressor unit for recompression. The bottom product of the high-pressure flash drum is heated in the solvent heat exchanger with the lean solution from the stripper bottom to a temperature of 95°C and fed to the stripper.

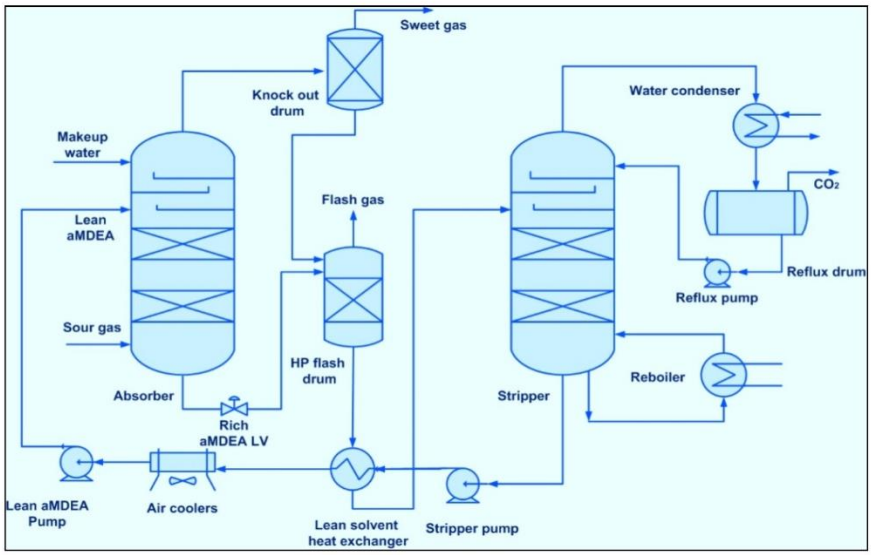

Figure 2. Process flow diagram of CO_2 removal unit

The stripper reboiler supplies the necessary heat required to strip off the CO_2 from the stripper top. The reboiler is heated with a stream of process gas at a temperature of 137°C. Overhead vapors from stripper are partially condensed, then received in a reflux drum. The condensed liquid is returned as reflux to the stripper while the vapor phase containing CO_2 is routed to the auxiliary boiler, where it is incinerated in the burners. Inflammable components in the vapors and C_3H_8 are to be burned in the boiler furnace. The regenerated solution from the stripper bottom shows a very low residual loading of CO_2. The heat from this hot stream is recovered in the solvent heat exchanger. The bottom product out from the stripper should be cooled to absorber operating temperature using air cooler. Anti-Foam agent is added as required to the absorber column and to the stripper column.

2.3. Refrigeration and gas separation unit

The refrigeration and gas separation unit include gas dryers and gas chilling processes. In the gas drying process, water is removed by molecular sieves and emerged from the CO_2 removal unit to prevent the hydrate formation in the process gas before cooling it in the cold box of the chilling process. Purpose of the cold box is to separate un-condensable process gas components like hydrogen, nitrogen, and methane from propane and propylene containing hydrocarbon phase by partial condensation. The hydrocarbon phase will be condensed while hydrogen, nitrogen, and methane remain in the gas phase. The temperature of the process gas is reduced to approximately -85°C. Due to refrigeration, more hydrocarbons will condense out of the process gas.

The CO_2 removal unit has some troubles that affect the sweetening and subsequent units. These troubles can lead to the isolation of the cold box in the refrigeration and gas separation units. This means much propane and propylene losses directed to the fuel gas network via cold box bypass. Additionally, the side products emerged from the reaction section can cause many problems. The main problems that affect the CO_2 removal process are the foaming and the solid compounds formation.

2.4. Amine sweetening unit operational issues

The different highlighted operational issues in the studied existing sweetening unit and in the subsequent units (Refrigeration and gas separation) are summarized as follows:

1. The fast rise of the level in the coolers of treated natural gas.
2. High amine losses and amine carryover into equipment downstream of the absorber in the forward refrigeration and gas separation unit.
3. Decrease of acid gas removal system efficiency and an increase of the CO_2 content in treated natural gas.
4. High differential pressure across the absorber.
5. Increase in the pressure drop across the drier in service.
6. Freezing out (hydrate formation) in the cold box.

Most of these problems (2, 3, and 6) are an indication of the inefficient removal of acid gases in the MDEA sweetening unit. This will lead also consequently to increase propane and propylene losses in the fuel gas network via cold box bypass in the refrigeration and gas separation unit. The remaining problems may happen due to the passage of liquid droplets (amine and water) at high gas velocities with the vapor from a packing section to the packing above (carryover), then, towards the equipment located downstream of the acid gas removal column. By this effect, lower volatile liquid is withdrawn to the packing above where liquid with higher volatility is present. It is detrimental that packing efficiency will be reduced. Carryover is also detrimental when nonvolatile impurities are carried upward to contaminate the overhead product from the column. There are many probable causes for inefficient acid gas removal as reported in the literature. Foaming, carryover, and amine degradation may lead to such problems [2, 5, 9].

The present study has discussed the problem of foam and amine carryover at the head of the acid gas absorber and showed that its origin comes from the stable foam in the columns. This phenomenon is primarily due to contaminants, under-sizing of the acid gas absorber, and the reaction of an amine with the side products of the oxy-reactor. Contaminants can be obtained from two sources. One of these sources is degradation products of the MDEA resulting from thermal decomposition, while the other source is degradation products of the MDEA by the formation of the non-regenerable products. The degradation of the MDEA by thermal decomposition is a problem when the MDEA is subjected to high temperatures. This problem occurs in the reboiler, where the high temperatures can cause localized overheating. Under the action of heat, the MDEA decomposes and gives in particular ethylene oxide which is extremely reactive. The ethylene oxide can be polymerized and react with the MDEA, and the anti-foam used. The products of these reactions, which are found in a solid or liquid form, deactivate the solution of MDEA and favor the effect of corrosion and foaming of the amine solution. In addition to the reaction of the MDEA with CO_2 where it forms regenerable products, the MDEA also reacts irreversibly with CO_2. The reactions are very slow and complex. Corrosion products settle on the column packing and cause an inflexibility of the valves which are constrained in their movement by a fibrous texture, that, limit the flow of the liquid and increase the speed of the gas, generating possible aerosols thus favoring the formation of stable foam. A bad filtration may cause activated carbon filter particles to deeply circulate with the system leading to a foaming problem. Any contaminants which may cause the surface tension of the solution to decrease will increase foaming possibility in the solution. Also, any contaminants which may cause the solution viscosity to increase will help in foam formation. Contaminants in addition to all of the above reasons can be formed from the reaction between the activated

MDEA solution specially piperazine and side reactions out from oxy-reactor plus free oxygen according to lab results.

Under-sizing of the acid gas absorber is achieved as the gas velocity starts to increase. That will carry more liquid droplets with the outlet vapor causing the carry-over problem. Many experimental studies of carry-over were conducted and showed that the dominant variable affecting carry-over is gas velocity through the two-phase zone on the packing. The carryover is a significant factor in determining the limits of flooding of a column. Therefore, to size a column and avoid its flooding, it is necessary to know the maximum flows of gas and liquid, which can be introduced into the column. The maximum gas flow rate and consequently the maximum gas speed correspond to the flooding of the column should be determined. For optimal value, the speed of gas must be below the value for which the flooding occurs. In general, it is recommended to operate at 80% of the conditions of the flooding. The column diameter is obtained then, by knowing the gas flow rate, the selected speed (at 0.80 the speed of vapor at flooding) and to the packing active section.

The reaction of an amine with the side products of the oxy-reactor (amine degradation) may exist directly or alternatively if H_2S is present in the feed. Oxygen can react with a sulfur species first, followed by a subsequent reaction with the amine. The product distribution of the various carboxylic acids depends on the oxygen concentration, the operating temperature and the amine used.

The temperature of the absorber may be an important indirect parameter causing foaming; if the absorber temperature is reduced to reach the dew point of heavy hydrocarbons in the feed gas, then condensable hydrocarbons may exist in the gas stream. These condensates result in foaming, which is responsible for the sweetening reduced efficiency.

The increased foaming tendency requires a lower circulation rate of the MDEA solvent and more antifoam doses. Normally the circulation rate of the solvent is 180 m^3/h, but when the foaming increases a decision of decreasing the circulation rate to around 100 m^3/h may be taken to control foaming problems. The lower circulation rate minimizes the MDEA carryover from sweet gas knockout drum to the downstream refrigeration and gas separation unit.

Foaming also makes liquid levels of columns and vessels unstable. When liquid levels become unstable, the reduction of the circulation rates saves the running pumps from being stopped. So, the reduction of the solvent circulation rate is better than having carryover or complete stop of the solvent circulation rate.

The presented troubleshooting results accordingly in some consequences in CO_2 removal unit and in the subsequent refrigeration and gas separation unit due to MDEA decreased concentration. These consequences on CO_2 removal unit are summarized in the following points:

- Reduction in the CO_2 removal unit capacity until 80% of the design capacity.
- Excess of MDEA consumption.
- Corrosion of the equipment included in the CO_2 removal unit

However, the problems consequences in the subsequent refrigeration and gas separation unit can be summarized in the following:

- Contamination of the molecular sieves contained in the drier's unit shutdown for the defrosting and the drying of cryogenic exchangers.
- Replacement and repairs of several cold box cores.
- Several interventions of maintenance.

Addition of more antifoam does not prevent the foam; it only stops the generation of the foam, while the cause of foam formation still exists. Many problems may be resulted by using antifoams with unlimited use; corrosion and pollution of the mechanical equipment are the main problems [13,29,30]. If corrosion inhibitors are added to the amine system, these inhibitors do not cause foaming, but stabilize the foam; these consequently increase the foaming tendency [13,31,32].

In this work, some modifications were proposed and studied to the sweetening unit to overcome the operational problems mentioned above.

2.5. Economic study formulations

HYSYS version 10, with Acid gas – chemical solvents as a fluid package was used as the simulation software in the present research work. It was applied to build the original and the modified sweetening unit. It is also used to consider the economic calculations needed to evaluate the introduced modifications. The effectiveness of the suggested modifications to the sweetening unit should be confirmed through an economic study. Thus, it is needed to evaluate the modifications via estimating of return on investment (ROI) and consequently the payback period. ROI is related directly to the total annual cost (TAC) which can be calculated according to the following Equation:

$$\text{Total costs} = C_{cap} . Af + C_{op} \quad (27)$$

where C_{cap} and C_{op} are the capital equipment and the operating costs of the process, respectively.

Af is an annualization factor used to annualize the capital equipment cost and calculated as presented in Equation 28:

$$Af = \frac{m\,(1+m)^n}{(1+m)^n - 1} \quad (28)$$

where m is fractional interest rate; n is a number of years.

The capital equipment cost includes columns, air coolers, pumps, heat exchangers and separators costs. Where the operational cost includes steam, power and cooling water costs [33]. The cost of power, cooling water, high pressure steam, and low-pressure steam are assumed by Hysis program to be \$0.078 per kWh, \$120 per million gallons, \$3.16 per million BTU and \$2.11 per million BTU, respectively.

Profitability that can be acquired from a company at a specified status is an important denominator for all business activities [34]. Return on investment (ROI) indicated in Equation 29 consists of two main terms; the first is the saving in the operating cost, which acquired in case of the modified plan. On the other hand, the second term is the increase in the total capital cost (C_{Cap}) which includes purchased equipment, installation and foundation costs.

$$\text{ROI} = \frac{\text{saving in operating cost}}{\text{increasing in } C_{Cap}} \quad (29)$$

Payback period is the period required to recover the sum of the paid investment; Payback period can be calculated by applying Equation 30.

$$\text{Payback period} = {}^{1}/_{\text{ROI}} \quad (30)$$

In this work, the capital cost is annualized in one year (n) with 5% fractional interest rate (m).

3. Results and discussion

The purpose of this study is to modify the investigated sweetening unit for overcoming its operational problems as well as to raise the plant throughput to be near the designed value. The following sections discuss the proposed modifications and their effectiveness and effects on the original plant.

3.1. Original plant simulation

To show the benefits of the proposed modifications, it is needed firstly to simulate the investigated original sweetening unit before modifications. This simulation is based on the design basis of the plant with taking into account the feed gas composition of the CO_2 removal unit and the real operational conditions of the current plant, which differs from the design basis data. The real composition of the plant feed gas was identified via lab analysis. Table 1 addresses the sour feed gas composition of the current CO_2 removal unit. The flowrate of this gas feed is 4356 kgmole/hr. The lean solvent solution which consists of 23.59 mole% methyl di-ethanol amine (MDEA), 5.42 mole% piperazine and 70.99 mole % water are applied with a flow rate of 180 m^3/hr. Aspen HYSYS version 10 was used as the simulation software, and the chosen fluid package for simulation is acid gas – chemical solvents package. The simulated plant under consideration is presented in Figure 3.

Table 1. CO_2 removal plant sour gas feed composition

Components	Mole fraction	Components	Mole fraction
Methane	0.028700	1-Butene	0.000099
Ethane	0.015000	1,3-Butadiene	0.000000
Ethylene	0.000999	M-Acetylene	0.000999
Propene	0.197422	Nitrogen	0.000699
Propane	0.476371	Oxygen	0.0000999
n-Butane	0.000300	CO_2	0.0359000
i-Butane	0.003300	CO	0.0006990
Propadiene	0.000000	Hydrogen	0.235188
i-Butene	0.004300	Total	1.0

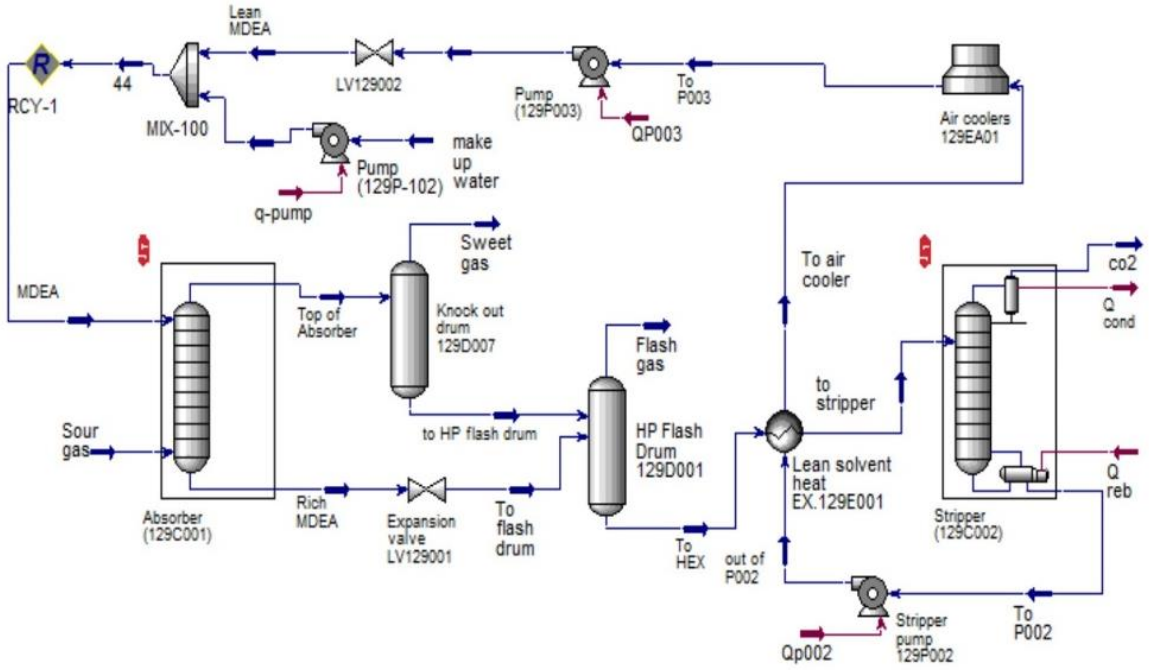

Figure 3. Simulation of original CO_2 removal unit

3.2. Proposed modifications

A modification for the sweetening unit was proposed in order to overcome operating problems and increase the productivity of the plant to reach its designed value. It was found that the CO_2 concentration out from the reaction section unit increased more than expected which lead to series problems in sweetening unit (carryover, foaming, and MDEA degradation). Therefore, modification included changes in process configuration and some operating conditions, was proposed, in order to achieve purity specification of the propylene product.

A comparative process simulation by HYSYS was done for the modified cases; design basis process and the modified process. The suggested modifications are as follows:

1) Using MDEA without an activator
2) Replacement of the old absorber with a larger one which contains three beds of structured packing
3) Increasing of MDEA circulation rate.
4) Addition of two pumps around equipped with two stages of side air coolers
5) Addition of a reclamation unit.

For improving the sweetening process, the operating parameters should be investigated, and the optimum condition should be identified. Depending on the feed gas composition, temperature and pressure along with the sweet gas requirements. The most sensitive operating parameters taken into consideration include rich amine temperature, amine circulation rate, gas/liquid contact time, and influence of MDEA activator.

3.2.1. Using MDEA without an activator

For alleviating the foaming problems or reducing their bad impacts, some operational practices were carried out in this study to investigate the causes of this problem. One of these trials was to cut oxygen feed to the reaction section of the PDH plant. The results showed that there is no foaming formed by avoiding oxygen to reach the reaction section. Therefore, it is confirmed that the main source of the foaming problem was the side products of MDEA reaction in the presence of oxygen outside the oxy-reactor. Accordingly, the action should be taken is using MDEA without piperazine activator. Since as declared in the reaction mechanism, piperazine activates MDEA and gives more amounts of activated MDEA ($MDEA^+$) as illustrated in Equations 16, 18, and 20. These activated amounts can react with the side products and produce solid compounds that can contribute to foaming formation. The MDEA is used in the modified suggested sweetening process model without activator using the Hysis program and the results showed that the foaming height is decreased from 680 mm to 180 mm as illustrated in Table 2. Also, the field results illustrated that using of MDEA without activator is a good idea to decrease the foaming. Thus, for the newly modified plant, MDEA should be used without activator with taking into account the possibility of increasing solvent circulation rate and volume of the absorber itself, which can be taken as alternatives for eliminating the foaming issues.

Table 2. Comparison between original and modified sweeting processes regarding sweet gas compositions, MDEA strength and foaming properties

Components	Simulation results of sweet gas composition, mole fraction	
	Original plant	Modified plant
Methane	0.02980	0.030342
Ethane	0.01560	0.015801
Ethylene	0.00100	0.000968
Propene	0.18880	0.183448
Propane	0.49380	0.503309
n-Butane	0.00030	0.000317
i-Butane	0.00340	0.003487
Propadiene	0.00001	0.000000
i-Butene	0.00380	0.003652
1 Butene	0.00009	0.000085
1,3 Butadiene	0.00010	0.000000
M-Acetylene	0.00000	0.000855
Nitrogen	0.00080	0.000742
Oxygen	0.00010	0.000083
CO2	0.00130	0.000106
CO	0.00070	0.000742
Hydrogen	0.24430	0.249196
MDEAmine	0.00000	0.000045
H2O	0.01610	0.006822
Lab MDEA strength, foaming		
MDEA strength (mole %)	23.59	24.1
Lab foam test height (millimeter)	680	180
Lab test breakdown (sec)	40	<30

3.2.2. Replacement of the current absorber with a larger one

Since the reaction of CO_2 with MDEA is slow in the absence of activator, the column diameter, and packing height must be adjusted to give sufficient time for the reaction to take place. By consulting certain experts in the gas industry field, it was confirmed that the replacement of the existing absorber by another large one more effective might bring a solution to the foaming problem and consequently, as well as the problem of amine carryover. For this study, the old absorber tower with two packing beds is replaced by a larger one with three structured packing beds in the modified sweetening process. The results of the simulation gave decreasing in the CO_2 concentration in the outlet sweet gas as described in Table 2

3.2.3. Increasing of MDEA circulation rate

Increasing the MDEA solvent circulation rate for a given absorber column will lead to an increase of the CO_2 pickup [14]. This usually holds true for MDEA in an absorber column of a fixed diameter, even though, the liquid residence time will decrease with increasing solvent circulation rate. In this research work, a new modification was proposed to increase the circulation rate from 180 to 220 m^3/h. This suggested modification cannot be achieved without increasing the length of the tower itself by adding a new packing in order to improve effectively the absorption process. The simulated results of the modified plant presented in Figure 4 display that CO_2 concentration in the treated gas decreases from 1200 ppm to 106 ppm by increasing the solvent circulation rate from 140 m^3/h to 220 m^3/h respectively. It is also noticed that increasing of MDEA rate above 220 m^3/h has no effect on the CO_2 concentration in the treated gas.

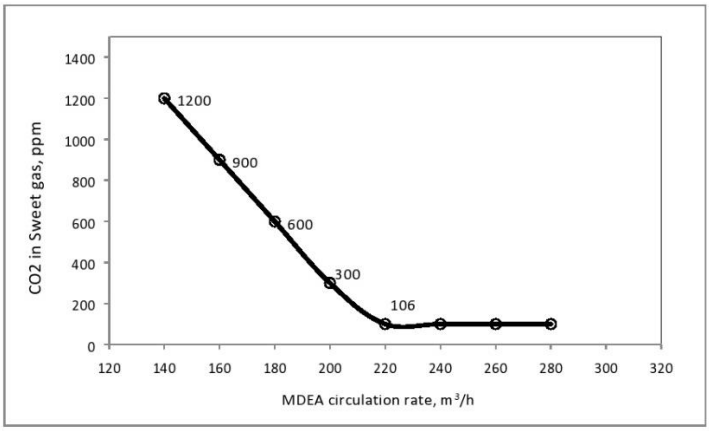

Figure 4. Relationship between MDEA circulation rate and CO2 concentration in sweet gas

3.2.4. Addition of two pumps around equipped with two stages of side air coolers

Usually, the only parameter available for controlling the absorber temperature is the lean amine temperature. Since the CO_2 reaction with MDEA is kinetically controlled; a hotter column increases the reaction rate. However, once the lean amine temperature reaches about 90°C at the operating pressure, the decrease in solubility of the CO_2 in the amine solution will usually become the overriding factor, and the net CO_2 pickup will begin to decrease.

To overcome the degradation problem of the solvent, it is required to control the temperature profile of the absorber.

In this work, it is suggested to add air cooler after each packing. This will help in controlling the temperature increase of the MDEA ascribed to the exothermic reaction between CO_2 and the amine. Therefore, the outlet MDEA temperature of the first packing section can return back to the desired operating feed condition. Then, the MDEA will be pumped again back to the second packing of the absorber as shown in the modified sweetening process shown in Figure 5. This procedure will be repeated with the same sequence for the three packing sections

of the absorber. For raising the absorption capacity of the MDEA solvent solution, the down flowing liquid is drawn off from absorber column below the 1st and 2rd absorber packing sections and cooled down in external air coolers. According to Figure 5, below the 2nd packing, the MDEA solution is drawn off and circulated by rich MDEA circulation pump (Pump 129P002) via rich MDEA air cooler (129EA02) back to the absorber column (MDEA recycle 1 in Figure 5). Below the 1st packing, the MDEA solution is drawn off and circulated by rich MDEA circulation pump (pump 129P003) via rich MDEA air cooler (129EA03) back to the absorber column (MDEA recycle 2 in Figure 5). Applying this suggested solution for controlling the temperature of the absorber increased the net CO_2 pickup as illustrated in Table 2.

3.2.5. Addition of a reclamation unit

As proposed before, the modified sweetening plant should include a Reclaimer vacuum distillation separation unit (Reclaimer 129D008). The function of this Reclaimer is to permit cleaning up of amine, which is contaminated with heat stable salts. This can be realized by converting the amine salts to sodium salts and boiling the amine away from the resulting salt solution. Figure 5 presents the simulated modified plant, which includes the new reclamation system. The simulated Reclaimer feed rate (stream 55 in figure 5) is taken as 25% of the out stream of the stripper pump 129P002. According to Figure 5, a slip amine stream from booster pump (129P002) is routed to the Reclaimer to fill it with the amine. The medium pressure (MP) steam is used for heating the contents to nearly 98°C. The Reclaimer is operating at a vacuum pressure -0.2 bar. This will help in evaporating the water and volatile MDEA while making up with lean MDEA to hold levels. The overhead vapor is cooled and partially condensed in condenser 129E004. The condensed liquid is separated in separator 129D009. The condensed liquid is pumped back to the stripper by condensate pump 129P017. When enough heavier components have accumulated in the Reclaimer, the inlet liquid feed of the Reclaimer is stopped, then, the sludge in the Reclaimer is dumped, and the cycle can be repeated. Figure 5 shows the simulation of the CO_2 removal unit after including all the proposed modifications for improving the sweetening process as well as solving some of the operational issues.

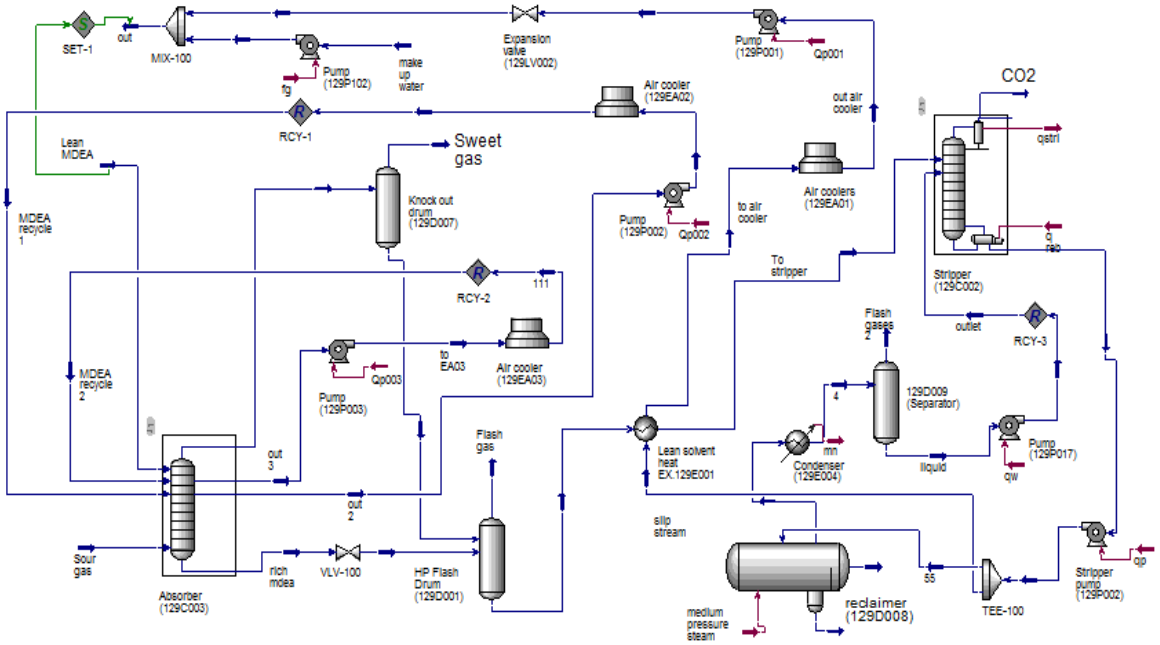

Figure 5. Simulated suggested modified CO_2 removal unit

In this work, by using the HYSYS program, it is found that the amount of sludge formed corresponds to the loss in the amount of MDEA. The actual concentration of MDEA used by

HYSYS is 23.59 mole% in the existing sweetening unit and 24.1 mol% in the modified unit. In the existing and the modified sweetening unit, the MDEA concentration is increased by an amount compensated by the sludge. This amount equals 14 mole% of the amine (loss in the amine).

3.3. Economic evaluation of the original and the modified sweetening unit

HYSYS program was used to calculate the total capital and operating costs of the original and the modified plants. The results showed that there is saving in operating costs in case of the modified plant. As shown in Table 3, according to the proposed modifications of using MDEA solution without activator, saving in operating cost is $ 2 919 802.23 per year.

Table 3. Capital and operating costs of the original and modified plats

Items	Operating cost	
	Original case	Modified case
Electricity (US$/year)	597 460.41	495 209.39
Cooling water (US$/year)	317 180.8	105 099.98
High pressure steam (US$/year)	5 456 825.57	
Medium pressure steam (US$/year)		2 851 355.18
Total operating cost (US$/year)	6371466.78	3 451 664.55
Saving in operating cost (US$/year)	2919802.23	
	Capital cost (US$)	
	Original case	Modified case
Knock out drum 129D007	188 700	188,700
Stripper pump 129P002	124 300	124,300
Lean solvent heat EX.129E001	531 800	531,800
Pump(129P003)	520 200	520,200
Pump (129P102)	165 800	165,800
Air coolers129EA01	585 700	585,700
HP Flash Drum 129D001	401 000	401,000
Stripper (129C002)	19 419 600	19 419 600
Main Tower_@Absorber (129C001)	194 600	
New Main Tower_@Absorber (129C003)		430 900
Reclaimer (129D008)		242 500
Separator (129D009)		161 000
Air cooler (129EA02)		159 000
Condenser (129E004)		118 200
Pump (129P002)		105 200
Pump (129P001)		427 300
Air cooler (129EA03)		163 600
Pump (129P017)		51 700
Total capital cost (US$)	22 131 700	23 796 500
Total capital cost (US$/year)	23 238 285	24 986 325
Total annual cost (US$/year)	29 609 751.78	28 437 989.55
Increasing in capital cost (US$)	1 664 800	
Return on Investment (ROI) ($year^{-1}$)	(2 919 802.23/1 664 800) =1.75	
Payback period (year)	(1/1.75) = 0.571	

This is because the heat required for the regeneration of MDEA in the case of amine-free activator is small compared with that required if amine is used with the activator [22]. Another example of a variation of operating cost is the steam type used in the reboiler of the stripper (Reboiler @ Stripper (129C002)). In the modified plant, the applied steam is of intermediate pressure type, which costs approximately the half value of the high-pressure steam used in the current plant as described in Table 3. This steam used to separate CO_2 from the rich solvent stream (MDEA+CO_2). Besides the reduction of operational costs, more benefits can be ascribed to the modified plants such as higher absorptive power of solvent that leads to removal of a high amount of CO_2 with lower energy consumption and higher stability [13]. Nevertheless, the lower

reaction time in the absence of the MDEA activator is the greatest disadvantage of the proposed modification. This drawback can be solved by increasing the absorber volume as well as the amine circulation rate.

As illustrated in Table 3, the capital cost of the modified plant is increased by 1 664 800 US$. This increment is attributed to the addition of new equipment such as an additional absorber, a separator, condenser, two air coolers, three pumps, and a Reclaimer vacuum unit. However, the calculated return on investment (ROI) and the payback period are 1.75 $year^{-1}$ and 0.571 years respectively (see the last two rows of Table 3). This very low value of payback period indicates that the modified plant with applying the amine solvent without activator is more profitable than the original plant.

3.4 Validation of the proposed modified sweetening unit

All the previous suggested modifications in the existing gas sweetening unit in this work are implemented in the plant. The results of the operation agree with the simulation results obtained in this work. A comparison is made between the results of the original and modified CO_2 removal unit from the viewpoint of the sweet gas composition, the strength of MDEA and foaming properties. The results illustrate that CO_2 concentration in the outlet sweet gas for the modified plant decreases from 1300 ppm to 106 ppm compared to the old plant. This consequently diminishes the potential formation of hydrate in cold box refrigeration system. Consequently, this leads to reducing the tendency towards foaming formation inside the absorber. These results are confirmed by lab tests which indicated the reduction of foam height from 680 millimeters at 40 sec in case of original unit to 180 millimeter at <30 sec for the absorber tower as illustrated in Table 2. Therefore, it is strongly recommended to apply the introduced modification of the investigated and similar plants to increase the plant profitability as well as to improve the plant performance.

4. Conclusion

The main objective of the present study is to enhance the sweetening unit owned to one of the biggest companies in the Middle East, particularly in the gas treatment sections. Additionally, this work investigates how to solve some encountered operational problems of this sweetening plant. Some experimental practices and analysis were undertaken to explore the sources of the solvent carry over the problem, and the obtained results showed that this problem is related primarily to the characteristics of MDEA solvent used for acid gas removal via absorption. Such characteristics are a tendency to foam, the presence of hydrocarbons and solid particles, in addition to the under-sizing of the acid gas removal columns.

The present study introduces some modifications in order to alleviate or eliminate effectively the problems in the acid gas removal section. These modifications include the following: Using MDEA without activator, replacing the current absorber with a larger one includes three structured packing instead of two packing bed, adding two pumps around with two stages of side air coolers, adding a reclamation unit, and increasing amine solvent circulation rate. The original and modified plants were simulated by using HYSYS software version 10. Compared to the original plant, results showed that the modified plant has a higher strength of lean MDEA and lower CO_2 concentration in the outlet sweet gas. This, in turn, increases the absorption capacity for CO_2, reduces the tendency towards foaming formation inside the absorber, and diminishes the potential formation of hydrate in the cold box. However, the proposed modification for the sweetening unit under consideration can solve effectively the encountered operational problems. The economic studies of the modified and original plants show that the modified plant is more profitable. Therefore, it is strongly recommended to apply the proposed modifications to the plant under investigation or similar plants in order to raise their economics and performances as well as to solve their operational problems.

References

[1] Abry RGF, DuPart MS. Amine plant troubleshooting and optimization. Laurance Reid Gas Conditioning Conference, Norman, Oklahoma; 1993.

[2] Bishnoi S, Rochelle GT. Thermodynamics of Piperazine/Methyldiethanolamine/Water/Carbon Dioxide. Industrial & Engineering Chemistry Research, 2002; 41 (3): 604-612.

[3] Bishnoi S, Rochelle GT. Absorption of carbon dioxide in aqueous piperazine/methyldiethanolamine. AIChE Journal, 2002; 48 (12): 2788–2799.

[4] Closmann FB. Oxidation and Thermal Degradation of Methyldiethanolamine/ Piperazine in CO2 Capture. Thesis. The University of Texas, USA; 2011.

[5] Cummings AL,Veatch FC, Keller AE. Corrosion and Corrosion Control Methods in Amine Systems Containing H_2S. Corrosion (NACE), Paper No. 341; 1997.

[6] Elvevoll IM. Experimental study of foaming in alkanolamine system. Thesis. Norwegian University of Science and Technology; 2013.

[7] Farjoo A, Khorasheh F, Niknaddaf S, Soltani M. Kinetic modeling of side reactions in propane dehydrogenation over Pt-Sn/γ-Al_2O_3 catalyst. Scientia Iranica Journal, 2011; 18 (3): 458-464

[8] Foral MJ, Alexander BD, Satek LC, Bahr BC. Purification of polyolefin feedstocks using multiple adsorbents. US Patent Application: WO 2003048087 A1; 2003.

[9] Ghalib L, Ali BS, Mazari S, Ashri WM, Saeed IM. Modeling the Effect of Piperazine on Carbon Steel Corrosion Rate in Carbonated Activated MDEA Solutions. International Journal of electrochemical science, 2016; 11: 4560 – 4585.

[10] Gondule YA, Dhenge SD, Motghare K. (2017) Control of Foam Formation in the Amine Gas Treating System. International Advanced Research Journal in Science (Engineering and Technology), 2017; Special Issue 3: 183-188

[11] Hajilary N, Ehsani AN, Sheikhaei S, Foroughipour H. Amine Gas Sweetening System Problems Arising from Amine Replacement and Solutions to Improve System Performance. Journal of Petroleum Science and Technology, 2011; 1(1): 24-30

[12] Herauville VMTh. Catalytic Dehydrogenation of Propane: Oxidative and Non Oxidative Dehydrogenation of Propane. Thesis. Norwegian University of Science and Technology; 2012.

[13] Kamps ÁP-S, Xia J, Maurer G. Solubility of CO_2 in (H_2O+piperazine) and in (H_2O+MDEA+piperazine). AICHE Journal, 2003; 49: 2662–2670

[14] Khan AA, Halder GN, Saha AK. Comparing CO_2 removal characteristics of aqueous solutions of monoethanolamine, 2-amino-2-methyl-1-propanol, methyldiethanolamine and piperazine through absorption process. International Journal of Greenhouse Gas Control, 2016; 50: 1179-189.

[15] Khan AA, Halder GN, Saha AK. Experimental investigation on efficient carbon dioxide capture using piperazine (PZ) activated aqueous methyldiethanolamine (MDEA) solution in a packed column. International Journal of Greenhouse Gas Control, 2017; 64: 163–173.

[16] Kittel J, Idem R, Gelowitz D, Tontiwachwuthikul P, Parrain G, Bonneau A. Corrosion in MEA units for CO2 capture: pilot plant studies. Energy Procedia, 2009; 1(1): 791–797.

[17] Kohl A, Nielsen R. Gas Purification. 5th Ed. Gulf Publishing Company, Houston, Texas; 1997.

[18] Loo S, Elk EPV, Versteeg GF. The removal of carbon dioxide with activated solutions of methyl-diethanol-amine. Journal of Petroleum Science and Engineering 2007; 55: 135–145.

[19] Mogul MG. Reduce corrosion in amine gas absorption columns. Hydrocarbon Processing, 1999; 78 (10): 47-56.

[20] Pauley CR. Ways to control amine unit foaming offered. Oil Gas J., 1989; 87 (50): 67–75

[21] Patil P, Malik Z, Jobson M. Retrofit design for gas sweetening processes. Institution of Chemical Engineers Symposium Series, 2006; 152: 460-468.

[22] Rooney PC, Bacon TR, DuPart MS. Effect of heat stable salts on MDEA solution corrosivity. Hydrocarbon Process, 1996; 75.

[23] Sarker NK. Theoretical effect of concentration, circulation rate, stages, pressure and temperature of single amine and amine mixture solvents on gas sweetening performance. Egyptian Journal of Petroleum, 2016; 25 (3): 343–354.

[24] Sahebdelfar S, Zangeneh FT. Dehydrogenation of Propane to Propylene Over Pt-Sn/Al_2O_3 Catalysts: The influence of operating conditions on product selectivity. Iranian Journal of Chemical Engineering, 2010; 7(2): 51-57.

[25] Samanta A, Bandyopadhyay SS. Absorption of carbon dioxide into piperazine activated aqueous N-methyldiethanolamine. Chemical Engineering Journal, 2011; 171(3): 734-741.

[26] Shao J, Lu G, Ye M. Removal of Heat Stable Salts-A Solution to Amine Plant Operational Problems. Chemical Engineering in Petroleum & Natural Gas Journal, Technical Paper 157; 2002.
[27] Shiveler G, Solis GS, Gonzalez LHP, Bueno ML. Retrofit of a H_2S Selective Amine Absorber Using Mellapak Plus Structured Packing. Asia-Pacific Journal of Chemical Engineering, 2007; 2: 232–244.
[28] Verma N,Verma A. Amine system problems arising from heat stable salts and solutions to improve system performance. Fuel Processing Technology, 2009; 90 (4):483-489.
[29] von Phul S, Stern L. Antifoam - What is it? How does it work? Why do they say to limit its use? In: Proceedings of the Laurance Reid Gas Conditioning Conference 2005; 231-240.
[30] von Phul SA. Sweetening process foaming and abatement. In: Proceedings of the Laurance Reid Gas Conditioning Conference, 2001; 251–280.
[31] Ying J, Raets S, Eimer D. The Activator Mechanism of Piperazine in Aqueous Methyldiethanol-amine Solutions. Energy Procedia, 2017; 114: 2078-2087.
[32] Zhao B, Sun Y, Yuan Y, Gao J, Wang S, Zhuo Y, Chen C. Study on Corrosion in CO_2 Chemical Absorption Process Using Amine Solution. Energy Procedia, 2011; 4: 93–100.
[33] Peters MS, Timmerhaus KD, West RE. Pant design and economics for Chemical Engineers, 5th ed, McGraw- Hill, New York; 2003.
[34] Rojey A, Jaffret C, Marchall N. Natural Gas: Production, Processing, Transport, Editions Technip, Paris; 1997.

To whom correspondence should be addressed: Dr. Walaa M. Shehata, Department of Petroleum Refining and Petrochemical Engineering, Faculty of Petroleum and Mining Engineering, Suez University, Suez, Egypt

Petroleum and Coal

Article **Open Access**

STUDIES THE EFFECT OF HYDRAZIDE DERIVATIVES AS FLOW IMPROVERS FOR WAXY CRUDE OIL

Omnia A. A. El-Shamy[1,], Taisir T. Khidr[1], and Entsar E. Badr[2,3]*

[1] *Egyptian Petroleum Research Institute (EPRI), Nasr City, 11727, Cairo, Egypt*
[2] *Chemistry Department, Faculty of Science, Qassim University, Qassim, KSA*
[3] *Chemistry Departments, Faculty of Science, Al Azher University, Nasr City. Cairo, Egypt*

Received February 19, 2019; Accepted May 3, 2019

Abstract

Adding pour point depressants (PPD) to lower the pour point of crude oil is a powerful and economical way of increasing the cold flow properties of the oils. The impact of two ethoxylated stearyl hydrazides (E10 = 10 ethylene oxide units (e.o.) and E20 = 20 e.o.) on the pour point, and rheological properties of crude oil examples were studied. The result with their structure on the surface activity as critical micelle concentration "cmc," a maximum surface excess concentration "Γ_{max}" and minimum area per molecule, "A_{min}". The standard free energy of micellization and adsorption were calculated and discussed. Efficiencies of the two hydrazides additives were influenced by number of the ethylene oxide units, the much longer group of ethoxylate (E20) was the better result in the reduction of pour point and obvious viscosity. From the results, it is found that E20 exhibited maximum pour point depression and improve the calorific values of crude oil.

Keywords: *Hydrazide derivatives; Surface activity; Crude oil; Flow improvers; Rheology.*

1. Introduction

One of the most actively traded commodities in the world is crude oil. The global demand for crude oil has been maintaining a stable gross annual growth rate. Crude oil with a higher wax content has a high pour point "PP" and low-temperature fluidity. In addition, the transportation and extraction of this oil became more complicated. Pour-point depressants "PPDs" are added in the industry for the wide transmission of this oil. Recently, several types of PPDs have been developed, which caused modification to the wax crystals forming a three-dimensional network, resulting in a decreased pour point of the crude oil [1-3].

Many polymeric molecules are used as flow improvers, which are chemical additives that can affect nucleation, adsorption or solubility of waxes. A copolymer of ethylene and vinyl acetate has widely used in the pipeline transportation of crude oil was studied as an excellent pour point depression efficiencies [4-5]. Another alternative method to reduce the viscosity of the oil is the utilization of flow improvers "FI" that can affect the wax properties. The modification of wax crystallization leads to depress both viscosity and PP of crude oil and give stress appreciably. Although crude oil treatment with chemical additives is not the only known methods, it remains the recommended methods comparing with pigging, heating, and biological treatments [6-8].

Pour point depressants, and movement improvers are additives that used to diminish the pour point and enhance the flow characteristics of crude oil, respectively. In doing that PPD's and movement improvers should have a lipophilic chain in addition to the lipophobic group, these requirements are achieved by surface active agents [9-11].

Because of the amphiphilic characters of surfactant molecules, they are widely used in several fields of applications. Surfactants have different kinds that differ based on the type of

headgroups. Non-ionic surfactants that possess long lipophilic alkyl chain and long lipophobic ethylene oxide chain were applied as PPDs and give higher efficiency [12-14].

In this paper, the surface activities, the standard free energy of micellization and adsorption are determined of two hydrazide molecules with different ethylene oxide units (E10 and E20). These compounds are examined as pour point depressants and rheology improvers for crude oil sample from Petroleum Company. The effect of the structure of surfactant additives used as crude oil movement improver additives on the pour point and rheological properties of crude oil samples examined. The relationship between the chemical structures of these well-prepared surfactants and their influence on the calorific value of crude oil are discussed.

2. Experimentals

2.1. Crude oil used

Crude oil with high wax content was obtained from Egypt (Qarun Petroleum Company). Their physicochemical properties are listed in Table 1. The n-paraffin circulation of the isolated waxes was determined by gas chromatography analysis according to American Society for Testing and Materials "ASTM" D 2887 standard.

Table 1. Physicochemical properties of the investigated crude oil

Test	Method	Result
Density@15ºC, kg/L	ASTM D1298	0.865
Pour point, ºC	ASTM D97	24
Flash point, ºC (PMC)	ASTM D93	200
Kinematic viscosity at 40ºC, cSt	ASTM D445	243.59
Kinematic viscosity at 100ºC, cSt		18.94
Wax content, wt%	UOP 46/64	11.01
n-paraffins, wt%	ASTM D2887	62.27
iso- paraffin, wt%	ASTM D2887	4.12
Total paraffins content, wt%	Urea adduct	66.39
Average carbon number (n)	calculated	28.56

2.2. Surfactants

The prepared ethoxylated stearyl hydrazide, E10, contains 10 ethylene oxide (e.o.) units, and E20 contain 20 e.o. units (Figure 1). The compounds were prepared in previous work through two steps and are being used after chemical structure confirmation [15].

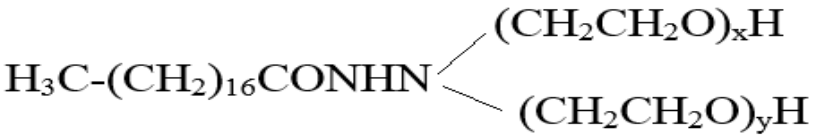

Figure1. Chemical structure of E10 and E20 where x+y =10 and 20, respectively

2.3. Sample preparation

Synthetic surfactants (E10 and E20) dissolved in a certain amount of toluene. A certain volume of the toluene solution of surfactant was added gradually into a required amount of the crude oil under stirring, and the mixture utilized to form a stable and homogeneous sample. The sample was taken for measurements.

a- As pour point depressants

The prepared compounds were examined as pour point depressants using crude oil through the pour point testing in line with the ASTM-97-93, respectively. The effect of additive concentration was investigated by using different concentrations ranging from (2.5–30.0)x10^3 ppm.

b- As rheology measurements

Brookfield DV-III programmable rheometer (M/97-164-D1000) is used to determine the dynamic viscosity at different temperatures above and below the pour point of the used crude oil (15ºC, 20ºC, and 30ºC). The viscosity is measured at different shear rates in the range of 1.0-200 sec^{-1}. The measurement was carried out at 0.5% g/100 mL and 2.5% g/100mL additive concentration.

c- As the calorific values

ASTM (D240) is used to determine the calorific values for the crude oil in the absence and presence of the additives.

2.4. Surface tension measurements

The surface activity of the E10 and E20 was examined via surface tension measurements using Kruss K6 tensiometer. The ring is oriented to the interface of various ranges of concentrations (0.05 - 0.03 x 10^{-3} mol/L) and the force exerted on it is measured. After each measurement, the ring was washed with ethanol then di-ionized water. The critical micelle concentration, cmc of the investigated molecules were evaluated from the surface tension concentration curve, and the data were listed in Table 2.

Table 2. Surface activity and standard free energy of micellization and adsorption

	cmc, 10^{-3} mol/L	Γ_{max}, 10^{10} mol/cm^2	A_{min} Å^2/molecule	π_{cmc}	ΔG^0_{mic} kJ/mol	ΔG^0_{ads} kJ/mol
E10	2.479	2.479	66.976	34.2	-16.01	-17.37
E20	1.456	1.456	114.052	30.2	-14.29	-16.37

3. Results and discussion

3.1. Surface properties

3.1.1. Maximum surface excess concentration "Γ_{max}"

The concentration of surfactant molecules at the user interface per unit area is defined as the Γ_{max}, and calculated from surface tension using Gibb's equation:

$$\Gamma_{max} = \left(\frac{1}{2.303RT}\right)\left(\frac{\delta\gamma}{\delta log C}\right) \quad (1)$$

where: γ is the surface tension; C is the concentration; R is the universal gas constant and T is the absolute temperature.

Concerning the data in Table 2, the increase in the ethylene oxide unit increase the excess surface concentration. This may explain by the coiling of the e. o. units in case of E20 which cause a decrease in the lipophobic properties. In addition, it prevents the formation of a meander type and decreases its hydrophilic character [16]

3.1.2. Minimum surface area "A_{min}"

The area occupied by each adsorbed molecule at the interface calculating from the following equation:

$$A_{min} = \frac{10^{16}}{\Gamma_{max} N} \quad (2)$$

where N is Avogadro's number.

Concerning the data in Table 2, the increase the e.o. units shift A_{min} to higher value due to the large surface area occupied by the coiling of the long e.o. chain.

3.2. Standard free energy of micellization and adsorption

The thermodynamic parameters of adsorption and micellization of the investigated surfactants are calculated according to Gibb's adsorption equations:

$$\Delta G^0_{mic} = RTlnC \quad (3)$$

$$\Delta G^0_{ads} = \Delta G^0_{mic} - 6.023 \times 10^{-2} \times \pi_{cmc} \times A_{min} \quad (4)$$

The data listed in Table 2 declare that, ΔG_{mic}^{0} have negative values, which decrease with increasing the hydrophilic moiety indicating spontaneous micellization process [17]. ΔG_{ads}^{0} for both additive (E10 and E20) were less negative value comparing with ΔG_{mic}^{0} for each one, which implies that both additive favor adsorption rather than micellization. The chemical structure of these additives is the controlling factor influencing their thermodynamic aspects.

3.3. Pour point depressants

The test results on pour point are shown in Table 3 as evidenced by pour point reductions with regards to the pour point of the crude oil minus the pour point of crude oil with additives. Table 3 show that E10 and E20 were quite effective in lowering the pour point of crude oil. The effectiveness of the investigated compounds as a pour point depressants depended on both the concentrations and the number of e.o. units of the investigated surfactants. The performance increased with the increase in the number of the ethylene oxide units of the investigated compounds. The reason why was that the surfactants functioned by adsorption onto the crystals being developed to redirect their crystal development and by co-crystallization to create much smaller isotropic crystals and higher solubility wax in the combined crystals providing as the move improver [18]. Under the same conditions, the long ethylene oxide chain could increase the compatibility of the additives in the crude oil and could destroy the established interlocking network of the waxes.

Table 3. The effect of surfactants on pour point of crude oil

Sample, conc. g/100mL	Pour point reduction, °C			
	E10		E20	
	PP	Δ PP	PP	Δ PP
0.25%	21	3	15	9
0.50%	18	6	15	9
1.00%	18	6	12	12
2.00%	12	12	6	18
2.50%	9	15	3	21

3.4. Influence of surfactants on the viscosity of crude oil

The effects of concentration of E10 and E20 on the viscosity of crude oil are shown in Table 4. The presence of additives caused a strongly reduced amount of apparent viscosity of crude oil.

Table 4. Influence of temperature on DVR of the crude oil with addition of surfactant

Temperature,ºC	DVR,%			
	0.5 %g/100mL E10	2.5%g/100mL E20	0.5 %g/100mL E10	2.5 %g/100mL E20
15	10.3	20.91	32.21	44.33
21	12.88	28.66	41.70	60.55
30	18.33	30.91	48.22	72.61

The obvious viscosity reduced with an increasing concentration amount of ethylene oxide unit. This could appear because the molecules getting together with the high-molecular compounds in crude oil increased with a growing concentration of the additives and the effect could prevent wax and asphaltene from developing hydrogen bonds. The degree of viscosity reduction (DVR) is created to gain access to the degree of the viscosity decrease, , and it could be determined by the following equation:

$$DVR = \frac{(\eta_0 - \eta_c)}{\eta_0} \times 100 \quad (5)$$

where: η_0 : the apparent viscosity (Pa·s) of the crude oil at a shear rate of 1.0-200 sec^{-1} and a certain temperature and η_c (Pa·s): the equivalent obvious viscosity of the crude oil after addition of the additives (E10 and E20) at shear rate of 1.0-200 sec^{-1} and the equivalent temperature [19].

The DVR of the crude oil with addition of hydrazide derivatives above the temperature range of 15- 30ºC at a shear rate of 1.0-200 sec^{-1} is detailed in Table 4. It is noted that there is a significant increase in DVR with increasing temperature. This may be related to two reasons. The first reason was that the temperature had a strong influence on the obvious viscosity of heavy components in crude oil such as wax and asphalting. The second reason was that high temperature had an effect on the chemical composition of heavy components that could lead to destroying the ordered structures of heavy components in the crude oil [19-20].The effects of e. o. unit on the DVR of crude oil are shown in Figure 2.

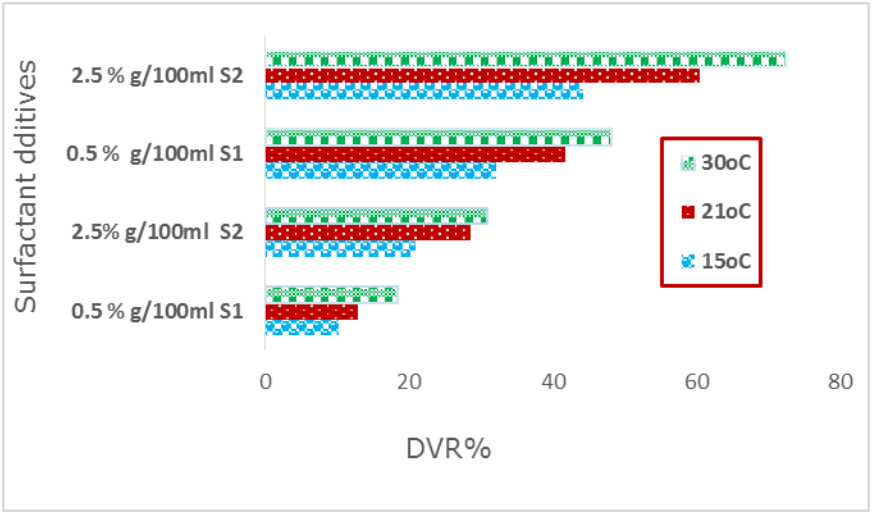

Figure 2. Variation of the temperature of DVR of the crude oil with S1(E10) and S2(E20)

It could be seen that the DVR increased with a growing hydrophilic group, which show the formation of the comb-like polymer, and the dispersion of the additives (E10 and E20) in the crude oil could be improved. Asphaltenes have hydrogen bonded phenolic OH species and nitrogen bases which can provide go up to proton transfer complexes, and the complexes are responsible for the rise in the viscosity of oil crude [21]. The heteroatom of the investigated additives "oxygen and nitrogen," may cause changes in the orientation of the aliphatic part of asphaltene and don't connect to the polar groups that can be found in asphaltene complexes to avoid the polar groups of asphaltene from developing hydrogen bonds that could destroy their ordered structures. The lipophilic chain is crystallized with the wax and the polar end groups which are responsible for disrupting the crystal composition of wax. This technique inhibits the crystals for agglomerating developing a gel-like composition to deposit on the pipeline surface. Because the efficiency of additives as move improver is influenced by their surface activities, the changes of the hydrophobic and hydrophilic groups are required [22].

Moreover, the tendency of the looked into surfactants to adsorption facilitate the well adsorption of the polar groups in the crude oil. The polar groups of the investigated surfactant are distributed into the ordered composition of the wax and asphaltene and may destroy their space network composition.

3.5. Effect calorific value of the additives on the calorific values of crude oil

The calorific values (dependent on Mohler Bomb and Boy's calorimeter) are discovered for crude in lack and occurrence of E10 and E20 and complete in Table 5. Which complete mounting brackets (Table 5) were given as gross calorific values in different commercial applications, however, the merchandise of combustion leave the place at temperature amounts will more than 25°C, which means normal water produced remains in the vapour talk about. The calorific regarding water remains as vapour is specified as net calorific value. There will vary methods could be used to calculate the calorific value of crude essential oil [23-24]. The amount of the radicals increase by incorporation of ethylene oxide group surfactants, which coupled with

hydrogen as normal water and hence improved the calorific value of the analyzed crude. The incorporation of nitrogen in the applied additive escalates the calorific value for all people tested crude oil one of the set of other additives.

Table 5. Calorific values of the crude oil with and without surfactants

Additives	Crude oil
Blank	42.770
E10	42.949
E20	43.612

4. Conclusion

The surface activities of ethoxylated stearyl hydrazide E10 and E20 are affected by their structure. The value of the free energies of micellization and adsorption give an indication about their spontaneous behaviors. E10 and E20 have a good effect on reducing pour point a good effect on reducing viscosity.

The efficiency of these additives as pour point reduction increases by increasing their concentrations and by decreasing their molecular weight. The maximum pour point reduction was obtained when the crude oil was treated by the E20 additive (Δpp=21°C, at 2.5% g/100mL), and the minimum pour point reduction was obtained for the crude oil treated by the E10 additive (Δpp=15°C, at 2.5% g/100mL).

The longer the ethylene oxide units of E20 apparently blended with the paraffin chains existing in the crude oil, the better the effect on preventing their facile crystallization. The surfactant additives increase the calorific values of the tested crude oil.

References

[1] Al-Sabagh AM, El-Hamouly SH, Khidr TT, El-Ghazawy RA, Higazy SA. Preparation the Esters of Oleic Acid-Maleic Anhydride Copolymer and Their Evaluation as Flow Improvers for Waxy Crude Oil. Journal of Dispersion Science and Technology, 2013; 34: 1585–1596.

[2] El-Ghazawy RA, Atta AM, Kabel KI. Modified maleic anhydride-co-octadecene copolymers as flow improver for waxy Egyptian crude oil. Journal of Petroleum Science and Engineering, 2014; 122: 411–419.

[3] Khidr TT, Azzam EMS, Mutawaa SS, Omar AMA. Study of some anionic surfactants as pour point depressants additives for a waxy gas oil. Industrial Lubrication and Tribology, 2007; 59: 64–68.

[4] Deshmukh S, Bharambe DP. 2014. The improvement of low temperature flow characteristics of waxy crude oil using multifunctional polymeric additives. Petroleum Science and Technology, 2014; 32: 1333–1339.

[5] Khidr TT, El-Shamy OAA. Synergistic effect between ethoxylated surfactants and commercial additive on the decrease pour point for distillate fuel oil. Pet Coal, 2018; 60(1): 99-105.

[6] Khidr TT, Omar AMA. Anionic/nonionic mixture of surfactants for pour point depression of gas oil. Egyptian Journal of Petroleum, 2003; 12: 21–26.

[7] Martínez-Palou R, Mosqueira ML, Zapata-Rendón B, Mar-Juárez E, Bernal-Huicochea C, Clavel-López, JC., Aburto J. Transportation of heavy and extra-heavy crude oil by pipeline: A review. Journal of Petroleum Science and Engineering, 2011; 75: 274–282.

[8] Yang F, Zhao Y, Sjöblom J, Li C, Paso KG. Polymeric wax inhibitors and pour point depressants for waxy crude oils: a critical review. Journal of Dispersion Science and Technology, 2015; 36: 213–225.

[9] Khidr TT. Pour point depressant additives for waxy gas oil. Petroleum Science and Technology, 2011; 29: 19–28.

[10] Semikhina LP, Nelyubov DV, Vazhenin DA. Effect of the structure of pour-point depressant additives on the deposition of solid petroleum hydrocarbons. Petroleum Chemistry, 2015; 55: 575–577.

[11] Wang SL, Flamberg A, Kikabhai T. Select the optimum pour point depressant. Hydrocarbon processing, 1999; 78: 59–62.

[12] El-Shamy OAA, Khidr TT, Doheim MM. Effect of ethoxlate chain length on the pour point depressant of middle distillate fuel oil. Journal of Dispersion Science and Technology, 2011; 32: 654–658.
[13] Khidr TT, Doheim MM, El-Shamy OAA. Pour point depressant of fuel oil using non-ionic surfactants. Petroleum Science and Technology, 2015; 33: 1619–1626.
[14] Souaya ER. El-Kholy SA, El-Rahman AMA, Elshafie M, Abo-Shanab ZL. Evaluation and application of surfactants synthesized from asphalt components. Egyptian Journal of Petroleum, 2012; 21: 45–54.
[15] Badr EE, El-Shamy OAA, Ahmad EM, Hilal NM. Synthesis of hydrazide derivatives and study their application as corrosion, Der Chemica Sinica, 2014, 5(1):161-168.
[16] Hafiz AA, Negm NA, Elawady MY. Influence of structure on the cationic polytriethanolammonium bromide derivatives. III. Biological activity. Egyptian Journal of Chemistry, 2005; 48: 245–250.
[17] El Feky AA, Shalaby MN, El-Shamy OAA, Selim SA. Adsorption of some surfactants onto polyvinyl alcohol as hydrophobic polymer surface. Journal of Dispersion Science and Technology, 2010; 31: 1091–1099.
[18] Ghosh P, Das M. Study of the influence of some polymeric additives as viscosity index improvers and pour point depressants–Synthesis and characterization. Journal of Petroleum Science and Engineering, 2014; 119: 79–84.
[19] Ghannam MT, Hasan SW, Abu-Jdayil B, Esmail N. Rheological properties of heavy & light crude oil mixtures for improving flowability. Journal of Petroleum Science and Engineering, 2012; 81: 122–128.
[20] Ghannam MT, Esmail N. Flow enhancement of medium-viscosity crude oil. Petroleum science and technology, 2006; 24: 985–999.
[21] Hafiz AA, Khidr TT. Hexa-triethanolamine oleate esters as pour point depressant for waxy crude oils. Journal of Petroleum Science and Engineering, 2007; 56: 296–302.
[22] Yi S, Zhang J. Relationship between waxy crude oil composition and change in the morphology and structure of wax crystals induced by pour-point-depressant beneficiation. Energy & Fuels, 2011; 25: 1686–1696.
[23] Alzueta MU, Glarborg P, Dam-Johansen K. Low temperature interactions between hydrocarbons and nitric oxide: an experimental study. Combustion and flame, 1997; 109: 25–36.
[24] Keskin A, Gürü M, Altıparmak D. Influence of tall oil biodiesel with Mg and Mo based fuel additives on diesel engine performance and emission. Bioresource technology, 2008; 99: 6434–6438.

To whom correspondence should be addressed: Dr. Omnia A. A. El-Shamy, Egyptian Petroleum Research Institute (EPRI), Department of Analysis and Evaluation, Nasr City, 11727, Cairo, Egypt, e-mail: omniaelshamy@yahoo.com

Petroleum and Coal

Article **Open Access**

CALCULATION MIXING RULE AND MODIFICATION SEMI-EMPIRICAL MODELS FOR SOLUBILITY MODELING IN SUPERCRITICAL CARBON DIOXIDE

Zoha Vatani[1], Mahboobeh Mohammad-Taheri[2], Reza Orouj[3]

[1] *Refining Technology Development Division, Research Institute of Petroleum Industry (RIPI), Tehran, Iran*
[2] *Chemical, Polymer and Petrochemical Technology Division, Research Institute of Petroleum Industry (RIPI), Tehran, Iran*
[3] *National Iranian oil Company (NIOC), Tehran, Iran*

Received July 27, 2018; Accepted October 2 April 24, 2019

Abstract

In this work, Soave-Redlish-Kowang (SRK) and Peng-Robinson (PR) equations of state with Huran-Vidal mixing rules was used to estimate the solubility of Tributyl phosphate (TBP) in supercritical CO_2. Since there were no available data for critical properties of TBP, A new method for evaluating of C_2 (Huran-Vidal mixing rule parameter) is recommended as a function of temperature and pressure. Also for solubility modeling by semi-empirical correlation, the new forms of Chrastil equation with variable coefficients were used which resulted in 6% of AARD%. The amounts of AARD% were obtained 8.97% for SRK-EOS and 17.01% for PR-EOS. Finally, the modeling of solubility for 21 compounds (The solubility data were obtained from literatures) by these methods has been investigated. Results show that the AARD% for the models with Charstil and modified Charstil are 12.07 and 11.17 respectively. Also the AARD% for SRK and PR-EOS are 14 and 19.85 respectively.

Keywords: *Solubility Modeling; Group Contribution Method; Equation of State; Semi-Empirical Model; Extraction.*

1. Introduction

One of several important advantages of supercritical fluid extraction (SFE) is the enhancement of extraction efficiency and the selectivity enhancement by tuning the pressure and/or temperature. Another advantage of SFE is a higher diffusivity and lower viscosity of a liquid, and much stronger solvent power than a gas [1]. Solubility is the concentration or mole fraction of a substance in the supercritical phase at a particular temperature and pressure when it is in equilibrium with the pure substance. For quantitative analysis, it is important that good solubility speeds up to initial stages of extraction and reduces the time of the process to some extent. The solubility of extracted compounds needs to be known if an efficient SFE process is to be designed [2].There is some different models to estimate solubility data and these models generally fall into the following categories: i) A density-based approach, ii) A solubility parame-ter approach where the SCF is treated as a liquid, iii) An equation of state (EOS) approach where the SCF is treated as a high-pressure gas [9]. The simplest available models for EOS are based on cubic equations of state, which require a minimum number of parameters. The general form of EOS is:

$$P = \frac{RT}{\upsilon - b} - \frac{a(T)}{\phi(b,T) + \varphi(b,T) \times \upsilon + \upsilon^2} \quad (1)$$

where $\phi(b,T)$ and $\varphi(b,T)$ are function of temperature and the co-volume b of the molecules of solute [3].

Critical properties (T_C, P_C) and the acentric factor (ω) of the solute and solvent are required for calculating of constant parameters, but these properties are not available for many of

compounds (Because large number of low-volatile natural substances decompose when heated before T_C is reached). Therefore, these parameters have been estimated by group contribution method (GCM) [4]. For example, application of group contribution method to approximate critical temperature leads in T_C=388.6 K for ethane, although the real value of T_C is 305.42 K. This error leads in consecutive errors in the calculations of solubility model [5]. Otherwise semi-empirical correlations are widely used and they are useful tools for experimental data correlation. These models are based on the simple error minimization and use only density of pure supercritical carbon dioxide and operational pressure and temperature. Thus, there is no need to calculate critical and thermo physical properties of the involved solutes. Several equations have been presented by different authors, covering from three to six parameters [6-7].

In this study, we investigated the modeling solubility of tributyl phosphate (TBP) in supercritical CO_2 (SC-CO_2). Also experimental data for solubility modeling are collected from Y. Meguro *et al.* literature [1]. Three models were used to estimate the solubility of TBP in SC-CO_2: Peng-Robinson equation of state (PR-EOS), Soave Redlish-Kowan equation of state (SRK-EOS) and modified Chrastil equation. According to obtained results, the proposed models present much more accurate estimation/prediction for in solubility. So, in order to accelerate the industrial processes, the proposed models can be employed and strongly recommended. TBP, belong to organ phosphorous compounds, is a liquid at ambient temperature, and this compound has widely employed in solvent extraction of metal ions because of their high extractability acid aqueous solution and high radiochemical stability.

2. Theory

2.1. Equation of state models

The solubility of a solid (2) in a SCF (1) system can be calculated using the following equation:

$$y_2 = \frac{f_2^{0l}}{\varphi_2^v P} = \frac{P_2^{sat}}{P} \frac{\exp(\frac{\upsilon_2^l (P - P_2^{sat})}{RT})}{\varphi_2^V} \quad (2)$$

where y_2 is the mole fraction of the solute in SCF phase; P_2^{Sat} is the saturation pressure of the pure liquid at the system temperature; φ_2^v is the fugacity coefficient of solute in SCF at the system temperature and pressure, and υ_2^l is the molar volume of the pure solute.

In this work, cubic EOSs (PR-EOS and SRK-EOS) will be used to estimate φ_2^v. The pressure-explicit form of SRK-EOS and PR-EOS respectively are:

$$P = \frac{RT}{\upsilon - b} - \frac{a}{\upsilon(\upsilon + b)} \quad (3) \qquad P = \frac{RT}{\upsilon - b} - \frac{a}{\upsilon(\upsilon + b) + b(\upsilon - b)} \quad (4)$$

Solvent properties (critical constants and acentric factor) are usually well known for solvent (CO_2), so its parameters can be calculated in the usual way:

$$A_1 = \frac{a_1 P}{R^2 T^2} = \eta_1 \alpha_1 \frac{P_{r_1}}{T_{r_1}^2} \quad (5) \qquad B_1 = \frac{b_1 P}{RT} = \eta_2 \frac{P_{r_1}}{T_{r_1}} \quad (6)$$

$$\alpha_1(T_{r_1}) = [1 + m_1(1 - \sqrt{T_{r_1}})]^2 \quad (7)$$

$$m_1 = \lambda_0 + \lambda_1 \omega_1 + \lambda_2 \omega_1^2 \quad (8)$$

The critical constants and acentric factor of the solute are not known, and then B_2 must be estimated. Constants of two EOSs for CO_2 are shown in Table 1.

Table 1. Constants of PR-EOS and SRK-EOS for CO_2

	η_1	η_2	λ_0	λ_1	λ_2
PR-EOS	0.45724	0.07796	0.379	1.485	-0.1644
SRK-EOS	0.42748	0.08664	0.48	1.57	-0.176

The co-volume B_2 of the solute can be assumed as equal to the known molar volume of the liquid:

$$B_2 = \upsilon_2^L \frac{P}{RT} \quad (9)$$

The mixing rules proposed by Huron and Vidal were applied:

$$B_m = \sum_i y_i B_i = y_1 B_1 + y_2 B_2 \quad (10)$$

$$\frac{A_m}{B_m} = \sum_i y_i \left(\frac{A_i}{B_i} - \frac{\ln \gamma_i^{\infty}}{\ln 2}\right) = \sum_i y_i C_i \quad (11)$$

γ_i^{∞} is the activity coefficient at infinite pressure. We can neglect γ_1^{∞} of the solvent, which is almost pure, therefore:

$$C_1 \cong \frac{A_1}{B_1} \quad (12)$$

and for C_2:

$$C_2 = \frac{A_2}{B_2} - \frac{\ln \gamma_2^{\infty}}{\ln 2} \quad (13)$$

Thus:

$$\frac{A_m}{B_m} = y_1 \frac{A_1}{B_1} + y_2 C_2 \quad (14)$$

As critical values and acentric factor for the TBP solute are not available, C_2 cannot be calculated from Eq. (13). In contrast with most of previous works which have used group contribution methods, this study tries to propose a new mathematical model to estimate C_2 values without using critical properties. Jafari Nejad *et al.* investigated EOSs for correlation solubility of TBP in supercritical CO_2 but they used thermodynamic properties of TBP (critical temperature, critical pressure and Pitzer's acentric factor) that obtained from fitting solubility experimental data [8]. Modeling results for C_2 values (by using Matlab 7 and Eviews 3.1 software) in terms of temperature and pressure are shown in Figures. 1(a) and 1(b) which refer to SRK-EOS and PR-EOS, respectively.

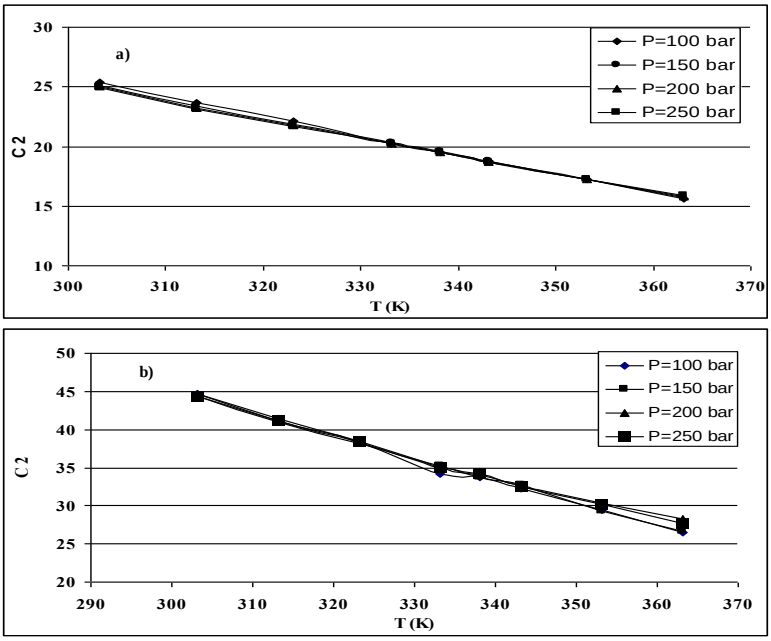

Figure 1. Variations of C_2 with temperature and pressure for (a) SRK-EOS and (b) PR-EOS

According to the above illustration C_2 is a function of temperature and pressure. We found that C_2 has:

1. A linear relationship with temperature at constant pressure,
2. and a logarithmic relationship with pressure at constant temperature.

Then the best model for C_2 is presented as:

$$C_2(T,P) = \alpha(T) - \beta(T)\ln(\frac{P}{P_{ref}}) \quad (15)$$

In which T is temperature (K); P is pressure (bar); $P_{ref} = 100bar$, $\alpha(T)$ and $\beta(T)$ are defined as:

$$\alpha(T) = a_1^{'}T + b_1^{'} \quad (16)$$
$$\beta(T) = a_2^{'}T + b_2^{'}$$

After modeling C_2 using software tools and experimental data, constants coefficients in Eq. (16) for SRK-EOS and PR-EOS are calculated and shown in Table 2.

Table 2. Constants of Eq. (16)

Equation of state	$a_1^{'}$	$b_1^{'}$	$a_2^{'}$	$b_2^{'}$
PR-EOS	0.8568	66.32	1.1432	-64.319
SRK-EOS	0.16196	74.3774	0.0314	10.9083

This function for C_2 has never been reported before in the literature. Using the Huron-Vidal mixing rules with the above approximation, the fugacity coefficient of the solute in gas phase will be calculated. An iterative procedure is required to calculate the solute concentration in the gas phase because the fugacity coefficient is a function of y_2. P_2^{sat} varies strongly with T and has a direct effect on y_2, so it must be determined separately at each temperature or expressed as a function of temperature:

$$\ln(P_2^{sat}) = 36.85 - \frac{11790}{T} \quad (17)$$

where P_2^{Sat} is vapor pressure (bar) and T is temperature (K).

2.2. Density-based model

The Charastil model [9] is based on the assumption of the formation of a solvate-complex between molecules of solvent and solute at equilibrium was used as a semi-empirical model. Eq. (18) leads to the linear relationship between the solubility of the solute, $S(g\ solute/L\ solvent)$, and the density of the solvent, $\rho(g/L)$, for a given temperature, T(k):

$$\ln S = k\ln\rho + \frac{a}{T} + b \quad (18)$$

where *a, b, and k* are the adjustable parameters of the model. The constant *k* is an association factor that represents the number of CO_2 molecules in the complex; *a* depends on the vaporization and salvation enthalpies of the solute; *b* depends on the molecular weights of the solute and solvent.

The parameters *a, b, and k* are obtained performing a multiple linear regression on the experimental solubility data. The advantages of the Chrastil model, it is simple to use and require a maximum of three fitting parameters to cover all temperature, pressure, and densities in supercritical region, thus it was successfully used to correlate system considered in this study. In contrast with the previous reports which have considered constant coefficient, we developed a new technique what the value of k is considered as function of temperature and simulation shows that the dependency is linear as follow:

$$k = n_1T + n_2 \quad (19)$$

Using Eq. (19) in Eq. (18), modified Chrastil equation would be as:

$$\ln S = (n_1T + n_2)\ln\rho + \frac{a}{T} + b \quad (20)$$

Constants in Eq. (20) after modeling with using software tools and experimental values are calculated and shown in Table 3:

Table 3. Constants of TBP for Eq. (20)

n_1	0.037721
n_2	-2.4929
a	17 630.75
b	-123.0075

The error for these models was estimated by average absolute relative deviation (AARD) between experimental (y_{exp}) and calculated (y_{calc}) solubility data according to the following equation:

$$AARD(\%) = \frac{1}{n}\left|\sum \frac{y_{2,\exp} - y_{2,calv}}{y_{2,\exp}}\right| \times 100 \quad (21)$$

where n is the number solubility of data used.

3. Results and discussion

After modeling C_2 for SRK and PR equations of state, estimate critical properties of TBP, and calculating the coefficient of density-based equations, y_2 is calculated in different operation conditions and shown in Figures 2, 3. Figure 2(a) shows that under about 333.15 K, vapor pressure is more effective which causes the solubility to be increased as the temperature increases. However, between temperature 333.15 K and 363.15 K, the fluid density is more on y_2 and it decreases the solubility.

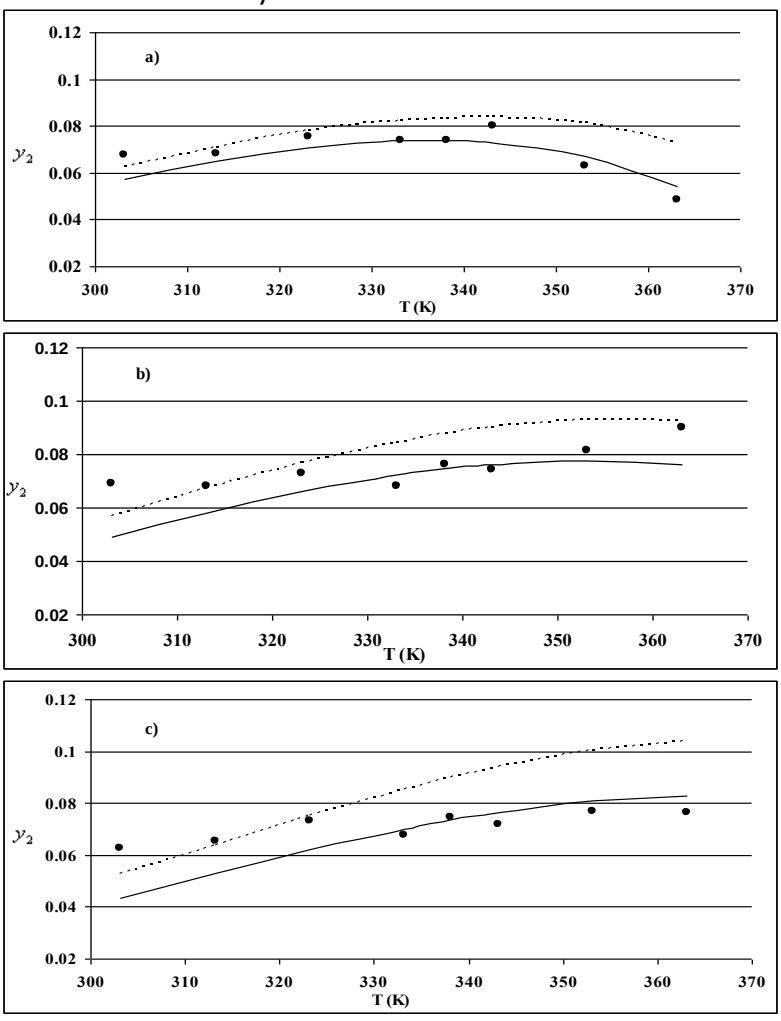

Figure 2. Solubility of TBP in SC-CO_2 at (a) P=150 bar, (b) P=200 bar and (c) P=250 bar (•) Experimental [4], (—) Calculated by SRK-EOS, (---) Calculated by PR-EOS

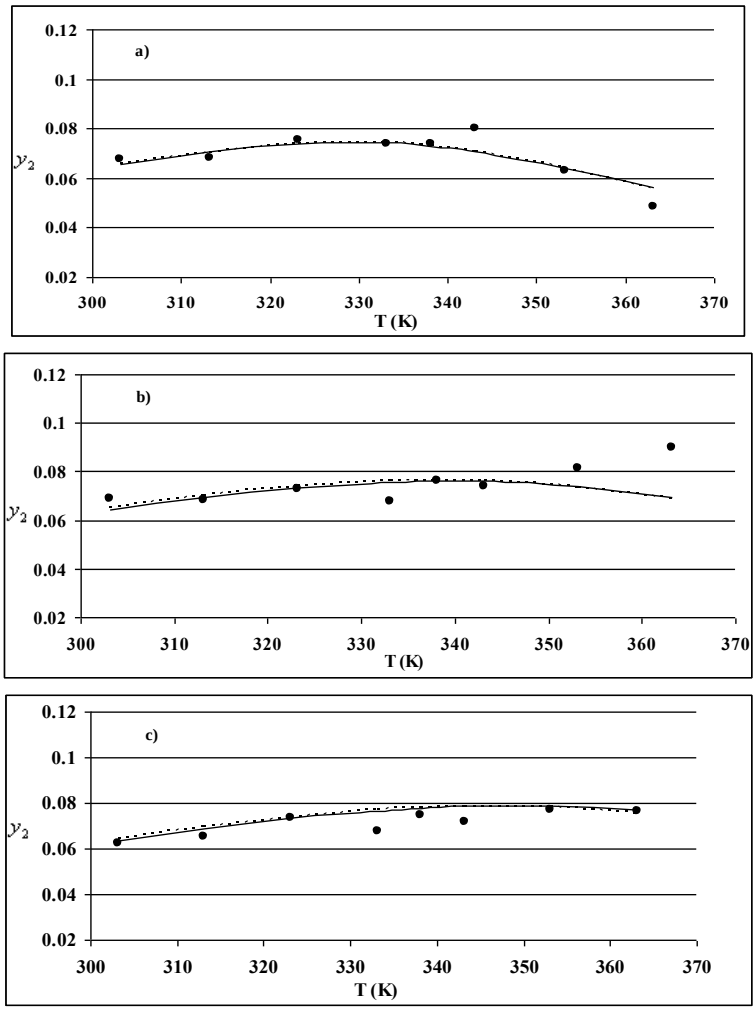

Figure 3. Solubility of TBP in SC-CO_2 at (a) P=150 bar, (b) P=200 bar and (c) P=250 bar (•) Experimental [4], (—) Calculated by Modified Chrastil Model, (---) Calculated by Modified Semi-Empirical Model

Other figures show the same results. As other researches such as Bordet *et al.* [3] has reported, equations of state have a considerable error in comparison with experimental results near the critical point (T=30^{0}C) in different pressures, as may be observed clearly in Figs. 2(a), 2(b), and 2(c). This shows that considering the high sensitivity of supercritical fluid density to temperature and pressure around the critical point, equations of state are not able to predict the solubility in this area accurately. As the error of SRK-EOS is lower than PR-EOS, the SRK-EOS predicts TBP solubility in supercritical CO_2 more accurately. The density based model derived from experimental data regression (It is just mathematical model) has an acceptable correlation near the critical point and is observed clearly in Figures 3(a), 3(b), and 3(c). According to these figures, when variable coefficients form of Chrastil is used, the result had very low errors (around 6%). This kind of model is simple because it resulted from the fit of just four parameters. The error of Chrastil (constant and variable coefficients) in addition to the errors for PR-EOS and SRK-EOS are listed in Table 4.

Table 4. The amount of AARD% for TBP solubility in SC-CO_2

	SRK-EOS	PR-EOS	Chrastil model	
			Modified form	Main form
AARD%	8.97	17.01	5.99	6.40

The usages of C_2 instead of GCM for substances for which the critical properties and acentric factor are not available, and temperature-dependent variable coefficients for semi-empirical equations in this study, are compared with Coimbra *et al.* [10] results. Coimbra et al. have estimated critical temperature and pressure for photochromic dye using GCM and have used the main form for semi-empirical equations. AARD% of the models is presented in Table 5.

Table 5. AARD% for modeling photochromic dye solubility

Chrastil model	SRK-EOS	PR-EOS
7.9	28.14	24.65
6.9	13.7	18.15

The results show a better solubility modeling for the usage of C_2 in comparison with the use of GCM for critical properties. The accuracy of the proposed model was evaluated using 21 published solubility data (about 350 data points) sets by calculating the average of absolute relative deviation. The error of Chrastil equation (constant and variable coefficients) in addition to the errors for PR-EOS and SRK-EOS are listed in Table 6.

Table 6. AARD% obtained for the prediction solubility in supercritical solvent

	Chrastil equation	Modified Chrastil	SRK-EOS	PR-EOS	Number of Data Points
Anthracene- CO_2	18.04	17.83	17.22	15.73	23
Anthracene-Ethane	9.94	9.30	7.78	8.18	27
Fluorene- CO_2	21.72	21.70	10.02	11.59	30
Fluorene-Ethylene	8.10	6.91	21.07	30.16	24
Naphthalene-Ethane	13.93	11.40	30.34	42.44	23
Pyrene- CO_2	23.43	20.28	16.41	26.07	21
Pyrene-ethylene	7.98	7.93	12.93	15.92	15
Phenanthrene- C_2H_4	11.15	10.63	15.74	20.25	15
Phenantrene- CO_2	5.86	4.28	9.87	9.30	21
Phenantrene-Ethlene	2.55	1.39	3.02	2.94	6
Triphenylmethane- CO_2	9.65	8.90	34.38	43.33	19
Ascorbyl Palmitate- CO_2	5.07	4.46	6.32	6.41	8
BHA- CO_2	8.30	3.78	16.50	29.52	6
Dodecyl Gallate- CO_2	5.58	1.50	7.12	10.59	8
Propyl Gallate- CO_2	3.60	2.29	3.98	6.00	8
2,3-Dimethylnaphthalene- CO_2	13.19	11.65	8.86	22.62	15
2,6-Dimethlnaphthalene- C_2H_4	10.03	10.39	18.01	26.66	18
2,6-Dimethylnaphthalene- CO_2	9.38	8.89	10.79	22.13	15
Benzoic acid- C_2H_4	8.88	8.86	3.35	4.29	15
Benzoic acid- CO_2	9.81	9.22	5.93	13.53	15
Hexachloroethane- CO_2	15.30	14.53	6.58	23.41	15
AARD%	**12.07**	**11.17**	**14.00**	**19.85**	**-**

4. Conclusions

The critical properties of a solute are required for modeling of the solubility by the equation of state. For many compounds, the critical properties are not available. So, group contribution method is utilized as a common method to estimate these properties. But, it leads to the consecutive errors in calculations of the solubility modeling. As critical values and acentric factor for the TBP solute are not available, in contrast with most of previous works which have used group contribution methods, this study tries to propose a new mathematical model to estimate C_2 values without using critical properties. As a result for TBP, photochromic dye and other solvents solubility modeling, it been concluded that using C_2 as a function of temperature and pressure results in good predictions of solubility in supercritical state and has the ability to be used in modeling accurately. A new four-constant empirical equation was developed for correlation of solute solubility in supercritical phase and validated by about 350 experimental data point collected from literature. The comparison between proposed model and published

models shows that the proposed model gives much more accurate results in solubility calculations than previously published models. Thus we strongly suggested using the same coefficients for the density-based models in future researches.

References

[1] Meguro Y, Iso S, Sasaki T, Yoshida Z. Solubility of Organophosphorus Metal Extraction in Supercritical Carbon Dioxide. Anal. Chem. 1998; 70(4): 774-779.

[2] Ozel MZ, Bartle KD, Clifford AA, Burford MD. Extraction, Solubility and Stability of Metal Complexes Using Stainless Steel Supercritical Fluid Extraction System. Anal. Chim. Acta. 2000; 417(2): 172-184.

[3] Bordet F, Passarello JP, Chartier T, Tufeu R, Baumard JF. Modeling Solutions of Hydrocarbons in Dense CO_2 gas. J. Eur. Ceram. Soc. 2001; 21(9): 1219-1227.

[4] Melo SABV, Melo RLFV, Costa GMN, Alves TLM. Solubility of L-Dopa in Supercritical Carbon Dioxide: Prediction Using a Cubic Equation of State. J. Supercrit. Fluids. 2005; 34(2): 231-236.

[5] Joback KG, Reid RC. Estimation of Pure-Component Properties from Group-Contributions. Chem. Eng. Commun. 1987; 57(1-6): 233-243.

[6] Murga R, Sanaz MT, Beltran S, Cabezas JL. Solubility of Three Hydroxycinnamic Acids in Supercritical Carbon Dioxide. J. Supercrit. Fluids. 2003; 27(3): 239-245.

[7] Asgarpour Khansary M, Amiri F, Hosseini A, Hallaji Sani A, Shahbeig H. Representing Solute Solubility in Supercriticalcarbon Dioxide: A Novel Empirical Model. Chem. Eng. Res. Des. 2015; 93: 355-365.

[8] Jafari Nejad Sh, Mohammadikhah R, Abolghasemi H, Moosavian MA, Maragheh MG. A Novel Equation of State (EOS) for Prediction of Solute Solubility in Supercritical Carbon Dioxide: Experimental Determination and Correlation. Can. J. Chem. Eng. 2009; 87(6): 930-938.

[9] Chrastil FJ. Solubility of Solids and Liquids in Supercritical Gases. Phys. Chem. 1982; 86(15): 3016-3021.

[10] Coimbra P, Gil MH, Duarte CMM, Heron BM, de Sousa HC. Solubility of a Spiroindolinonaphthoxazine Photo Chromic Dye in Supercritical Carbon Dioxide: Experimental Determination and Correlation. Fluid. Phase. Equilib. 2005; 38(1): 120-128.

To whom correspondence should be addressed: Dr. Z. Vatani, Refining Technology Development Division, Research Institute of Petroleum Industry (RIPI), P.O. Box 14665-1998, Tehran, Iran

Petroleum and Coal

Article **Open Access**

WELL TEST ANALYSIS IN EGYPTIAN NATURALLY FRACTURED OIL RESERVOIRS

Abd el Wahab Bayoumi[1], Sayed Gomaa[1,2], Saher Adel[1]

[1] *Al-Azhar University, Faculty of Engineering, Mining and Petroleum Engineering Department, Cairo, Egypt*
[2] *The British University in Egypt, Faculty of Engineering, Department of Petroleum Engineering and Gas Technology, El-Sherouk City, Cairo, Egypt*

Received March 6, 2019; Accepted May 3, 2019

Abstract

In this paper, well test data from three naturally fractured oil reservoirs were analyzed based on conventional semi – log plots, type curve matching, and Tiab's direct synthesis techniques. A computer program using C# was developed based on the direct synthesis method to be used in analyzing well test data in naturally fractured reservoirs.

The developed program gives accurate results compared with pan-system (one of the commercial softwares) which characterizes the naturally fractured reservoir using conventional semi-log and type curve matching techniques. The developed program characterizes the fractured reservoir in case of the infinite reservoir without wellbore storage effect whether all flow regimes are present, the early time infinite acting radial flow regime is absent, the late time infinite acting radial flow regime is absent or both infinite acting radial flow periods cannot be observed.

Keywords: *Well Test; Fracture Reservoir; Tiab's Method; Conventional Analysis, Dual Porosity.*

1. Introduction

More than 50% of oil and gas reservoirs all over the world are naturally fractured [1]. Some naturally fractured reservoirs are called dual porosity reservoirs as they consist of two porous media of different characteristics; which are the matrix and the fractures. The matrix has high porosity and low permeability. However, the fractures medium has high permeability and low porosity. The flow in the dual porosity system comes from the matrix towards the fractures, then from the fracture directly towards the wellbore.

A number of authors have developed different models for interpreting the pressure response in fractured reservoirs considering, among others, the characteristics of flow from the matrix to fractures, fracture orientation, and block-size distribution. In general, pressure-transient tests in NFR show a behavior consistent with the Amanat U. Chaudhry [2] model. The characteristic behavior of pressure response can be described with two dimensionless parameters; namely storativity ratio (ω) and interporosity flow coefficient (λ). Several models were developed to describe the pressure behavior of wells in dual porosity reservoirs. These models assume that the flow from the matrix to fractures is under transient or pseudosteady state flow conditions. The flow rate in pseudosteady state model is proportional to the pressure difference between the matrix and the adjacent fracture. In addition, the pseudosteady state conditions are assumed at initial flow conditions. On the other side, the flow rate in case of transient matrix flow model is proportional to the pressure gradient as the pressure drawdown starts at the interface between the matrix and fracture, and then propagates into the matrix. Finally, the pseudosteady state is achieved.

The presence of skin region of low permeability at the interface between matrix and fracture causes the pressure behavior to be predicted by pseudosteady state matrix flow model, although the flow in the matrix is under transient flow conditions. Therefore, most of the field

cases follow the pseudosteady state flow model. Fractures have been defined in different terms depending on the specific purpose or context of the definition. From reservoir point of view, Nelson [3] has defined fracture as a naturally macroscopic planar discontinuity in rock due to deformation or physical digenesis. Fractures can be produced by brittle or ductile failure. The characteristic of fractures will also be different depending on the generation process. Fractures can have a positive or negative effect on fluid flow. NFR are those reservoirs where fractures have or could have, any influence on reservoir performance. Nelson [3] has stressed the importance to collect information that allows identifying a reservoir as fractured in the early stage of development.

2. Naturally fractured reservoir

2.1. Fracture properties

The two major factors that govern permeability and porosity of fracture are fracture width and spacing. Fracture width (e) is the distance between two parallel surfaces that represent the fracture. Fracture spacing (D) is the average distance between parallel regularly spaced fractures. According to Nelson [3], the four most relevant properties of fractured reservoirs, in order of increasing difficulty to determine, are:

Fracture porosity.
Fracture permeability.
Fluid saturation within fractures.
Expected recovery factor.
Fracture porosity

2.1.1. Fracture porosity

Fracture porosity is the percentage of void space in fractures compared to the total volume of the system. Fracture porosity is estimated using the following expression:

$$\emptyset_f = \left(\frac{e}{D+e}\right) \quad (1)$$

As can be noticed from the expression, the fracture porosity is very scale-dependent. The value of $\emptyset_f$ can be 100 % in a particular location of the reservoir, but the value for the whole reservoir porosity is generally less than 1 %. According to Nelson [3], fracture porosity is always less than 2 %; in most reservoirs is less than 1 % with a general value of less than 0.5 %. An exception to this rules-of-thumb is vuggy fractures where porosity can vary from 0 to a very large value.

The importance of fracture porosity in reservoir performance depends on the type of fractured reservoir. If the fracture system provides an essential porosity and permeability to the reservoir, then fracture porosity is a critical parameter to be determined in the early stages of development. As the contribution of the matrix porosity to the whole system increases, the relevance of the fracture porosity decreases. Therefore, the estimation of the fracture porosity in the early stages is not so crucial in reservoirs where the matrix porosity is several orders of magnitude greater than the fracture porosity.

The Fracture porosity is one of the fracture properties that are difficult to be determined. The common sources of the fracture porosity estimation are:

Core analysis.
Porosity-Permeability relationship.
Field/Lab Determination.
Multiple–Well tests.

2.1.2. Fractured permeability

Permeability defines the ability of a porous medium to transmit fluids. The presence of open fractures has a great impact on reservoir flow capacity. Therefore, the fracture permeability is an important factor that determines reservoir quality and productivity.

Nelson [3] cited the work of Parsons [4], who combined the model for the fracture and matrix fluid flow and obtained the following equation for the fracture permeability:

$$k_f = \frac{e^2}{12} x \frac{\rho g}{\mu} \quad (2)$$

This equation assumes laminar flow between smooth, non-moving, parallel plates and homogenous fractures with respect to orientation, width, and spacing. Parson´s relationship is simple but is applicable to fluid flow through fractured reservoirs. Fractures do not always improve fluid flow in a reservoir. In some cases, partially or total filled fractures can act as flow barriers. The effect of the fractures on the permeability depends on several factors such as morphology, orientation, and others.

Fracture width and permeability are difficult to determine from direct sources such as core data or laboratory test. Well test analysis is the most common source of the fracture permeability information.

2.2. Classification of fractured reservoirs

Fractured reservoirs can be classified into:
Fractures provide the essential reservoir porosity and permeability.
Fractures provide the essential reservoir permeability.
Fractures assist permeability in an already producible reservoir.
Fractures provide no additional porosity or permeability but create significant reservoir anisotropy, such as barriers to flow.

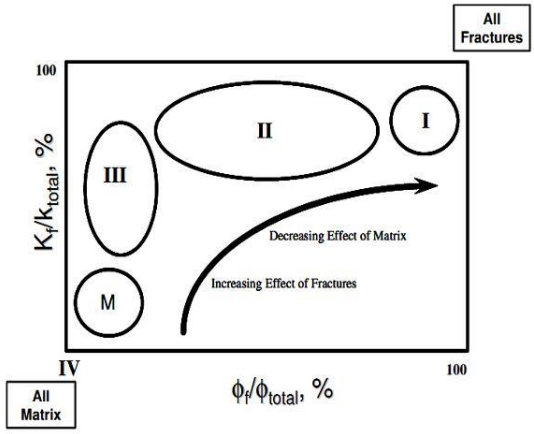

As shown in Figure 1, the effect of fractures is of paramount importance for type I reservoir, decreases for type II and so on. In the same way, the importance of the proper characterization of porosity and permeability changes with the reservoir type.

Figure 1. Schematic plot of fracture porosity and permeability percentage for four fractured reservoir types, *(after Nelson [3])*

3. Models of Well test analysis in a naturally fractured reservoir

In naturally fractured reservoirs, several sophisticated models were developed to describe the pressure response in dual porosity system. This section reviews the analytical and numerical models concerning well test analysis in this type of reservoirs.

The discovery of the first fractured reservoir was in 1880, according to Hubbert and Willis [5]. At this time, the well test methods were not used yet; they were first applied to homogenous reservoirs in 1950. One of the most useful methods to analyze well test data is presented by Horner [6]. His method is based on plotting bottom hole shut-in pressure versus $(t_0 + \Delta t)/\Delta t$ on a semi-log plot. Where t_p is the flowing is time prior to shut-in and Δt is the shut-in period. The slope calculated from the semi-log plot can be used to calculate the permeability thickness product of the formation.

3.1 Baker model

Baker [7] used the limestone formation in the Middle East. He assumed that the reservoir consists of parallel plates where the fluid can flow through them. This assumption was based on the model given by Lamb [8], Muskat [9], and Huitt [10]. The equation used was:

$$q = -\frac{g_c\, b\, W_f{}^2\, dp}{12\mu} \frac{dp}{dL} \ldots\ldots \quad (3)$$

The equation is valid only for steady state flow.

3.2. Warren and Root model

Warren and Root Model [11] presented a modified model for naturally fractured reservoirs. They considered that the reservoir has both primary and secondary porosity. In addition, they defined the fissured reservoir by two new parameters: (1) the relative storativity ω, which is defined as the ratio of pthe orosity-compressibility product of the fractures to the total system porosity-compressibility product, given as follows:

$$\omega = \frac{(QC_t)_f}{(QC_t)_m+(QC_t)_f} \ldots \quad (4)$$

and (2) the interporosity flow parameter, λ *which*, is defined by the dimensionless matrix/fracture permeability ratio:

$$\lambda = \alpha\, r_w{}^2 \frac{K_m}{K_f} \ldots \quad (5)$$

where the shape factor α, ft^{-2}, depends on the type of geometry of the matrix block (horizontal slap, rectangular cylinders, or spherical matrix block).

In the case of ω=1 and λ=∞, Warren and Root model can represent homogenous reservoir which is considered as a limiting case in their model.

Warren and Root model [11] is based on the following assumptions:

1. The rock matrix is homogeneous and isotropic and is contained within a systematic array of identical, rectangular parallelepipeds.
2. An orthogonal system of continuous, uniform fractures surrounding the matrix blocks contains the secondary porosity
3. Flow occurs between the matrix blocks (primary porosity) and the fractures (secondary porosity), then from the fracture network to the wellbore.

3.3. Sugar cube model

The Sugar cube model is based on the first two assumptions of Warren and Root model. This model considered the idealized representation of the fractured formation as shown in Figure (2).

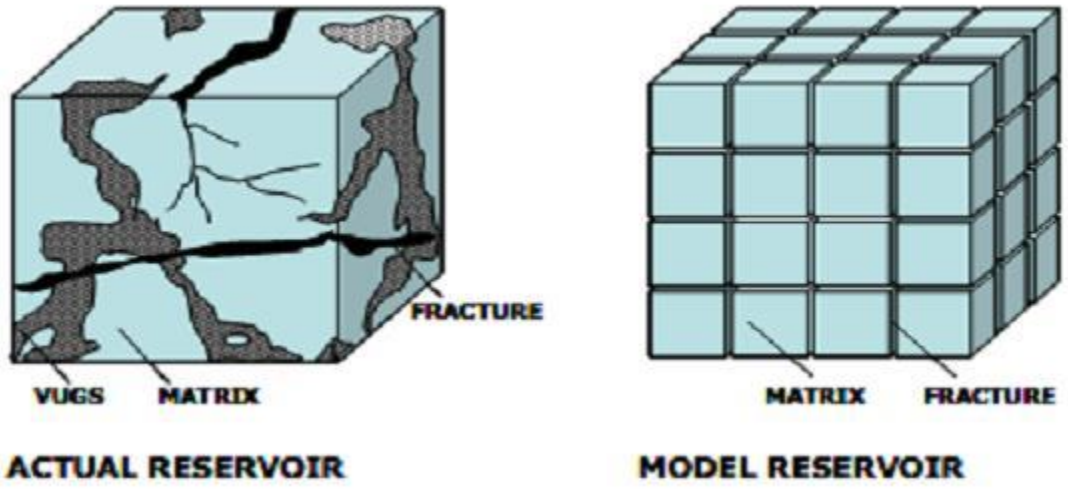

Figure 2. Ideal model for a naturally fractured reservoir *(after Warren and Root model [11])*

The slightly compressible radial flow equation that describes the flow in fractures can be expressed as:

$$\frac{1}{r}\frac{\partial}{\partial r}\left(r\frac{\partial P_f}{\partial r}\right) = \frac{\phi_2 C_f \mu}{K_2}\frac{\partial P_f}{\partial t} + \frac{\phi_1 C_m \mu}{K_2}\frac{\partial P_m}{\partial t} \ldots \quad (6)$$

The pseudosteady flow in matrix block can be written as:

$$\phi_1 C_m \frac{\partial P_m}{\partial t} = \frac{\alpha K_1}{\mu}\left(P_f - P_m\right)... \quad (7)$$

The porosity and permeability values are calculated with respect to bulk properties. The reservoir is infinite acting and producing at a constant rate.

Equations (6) and (7) can be expressed in dimensionless form as:

$$\frac{1}{r_D}\frac{\partial}{\partial r_D}\left(r_D \frac{\partial P_D f}{\partial r_D}\right) = \omega \frac{\partial P_D f}{\partial t_{Dw}} + (1-\omega)\frac{\partial P_{Dm}}{\partial t_{Dw}}... \quad (8)$$

$$(1\text{-}\omega)\frac{\partial P_{Dm}}{\partial t_{Dw}} = \lambda\left(P_{Df} - P_{Dm}\right)... \quad (9)$$

The solution is obtained by transforming the governing equations to Laplace space and approximating the modified Bessel function:

$$P_{Df} = \frac{1}{2}\left(lnt_{Dw} + 0.80908 + Ei\left(-\frac{\lambda t_{Dw}}{\omega(1-\omega)}\right) - Ei\left(-\frac{\lambda t_{Dw}}{(1-\omega)}\right)\right) + S... \quad (10)$$

Warren and Root model [11] found that the buildup pressure response exhibits two semi log straight lines, Figure 3.

The first straight line corresponds to the transient flow in the fracture media, and the second to the transient flow in the total system. The slopes of those lines are related to the flow capacity of the formation. The vertical separation of the two lines is related to the relative storage capacity of the fracture. They also defined two parameters describing the pressure behavior in a fractured system. The first parameter is the storativity ratio which is the ratio of fractured storage capacity to the total storage capacity of the system. The second parameter is the interporosity flow coefficient which governs the flow form the matrix to the fracture and is related to the heterogeneity of the system.

Figure 4 shows the effect of different values of ω. As ω decreases, the fracture depletes faster and that results in a shorter early straight line.

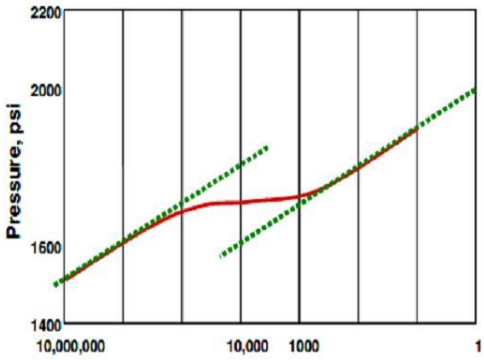

Figure 3. Semi log plot for pressure response in NFR

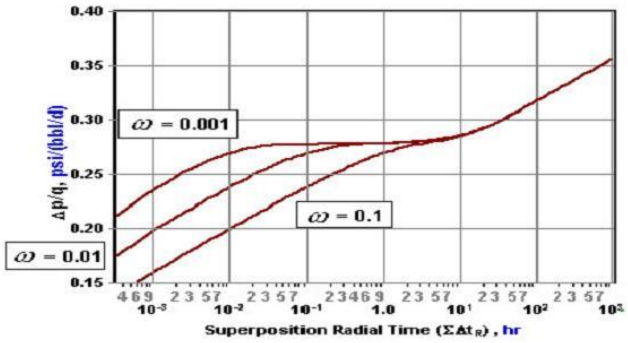

Figure 4. Effect of storativity ratio on the pressure response with pseudosteady state interporosity flow. $\lambda=10^{-7}$

The effect of various values of λ is shown in Figure 5. As λ decreases, the transfer of fluid from the matrix to the fracture becomes limited and consequently a delay in the pressure plateau. Small λ values are resulted from: (1) a large contrast between fracture and matrix permeability's with a constant α (shape factor), or (2) increasing matrix block sizes with a constant permeability ratio.

During early times, the pressure response is dominated totally by the fracture system behavior; Equation (10) is reduced to:

$$P_{Df} = \frac{1}{2}\left(lnt_{Dw} + 0.80908 + ln\left(\frac{1}{\omega}\right)\right) \quad (11)$$

When the reservoir behaves as homogeneous system($\omega = 1$), Equation (11) can be approximated as:

$$P_{Df} = \frac{1}{2}(lnt_{Dw} + 0.80908) \quad (12)$$

A plot of ΔP versus log of the flowing time can give the fracture permeability K_f by calculating the slope of either straight lines, m:

$$m = \frac{162.6 q \mu B_0}{K_f h} \quad (13)$$

Skin can be calculated from the first time straight line by:

$$S = 1.151\left(\frac{P_i - P_{wf(\Delta t=0)}}{m} - log\left(\frac{K_f}{(\phi_1 C_m + \phi_2 C_f)\mu r_w{}^2}\right) + 3.23 + log\left(\frac{1}{\omega}\right)\right) \quad (14)$$

Or from the second straight line by removing log $(1/\omega)$ term in Equation (14). In case of the two parallel straight lines are present, the relative storativity ratio can be calculated as follows:

$$\omega = e^{-2.3025\frac{\Delta P}{m}} \quad (15)$$

where ΔP is the vertical displacement separating the two parallel lines and m is the slope of them.

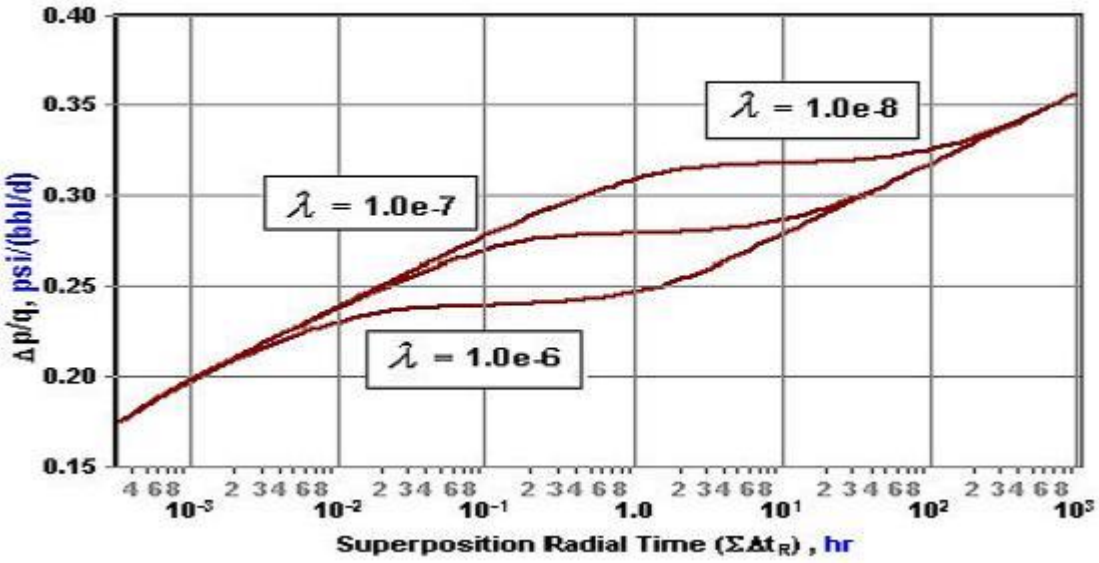

Figure 5. Effect of interporosity on the pressure response with pseudosteady state interporosity flow ω = 0.01

3.4. Odeh model

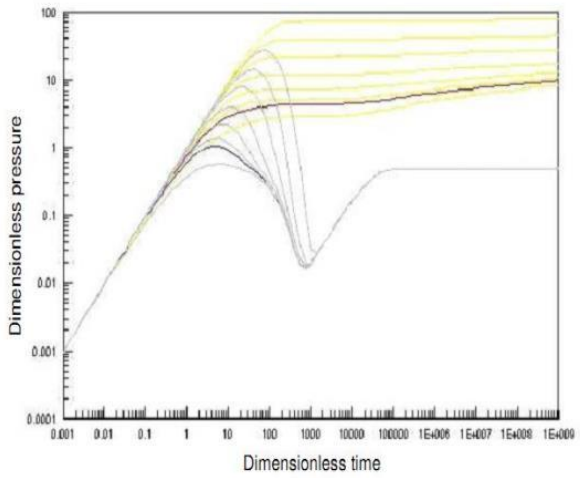

Figure 6. Derivative type curve for double-porosity reservoir, pseudo-steady state flow

Odeh [12] presented a model to analyze pressure transient tests in dual porosity reservoirs. By analyzing various pressure buildup and drawdown data, he concluded that there is no distinction between the behavior of fractured and homogeneous reservoir. Odeh [12] observed that no parallel straight lines ever appeared on the semi-log plot. This led him to conclude that there is no difference between the equations used to describe the fractured reservoir behavior and these used to describe the unsteady state behavior of homogeneous reservoir. Warren and Root [13] showed in a later publication that Odeh's presentation is a special case in Warren and Root model. The pseudosteady state matrix flow by Warren and

Root [13] has been used to analyze a large number of naturally fractured reservoirs. However, the duration of the transition period in some cases was longer and has less pressure drop. Therefore, transient matrix flow models were developed for this pressure behavior. Bourdet *et al.* [14] developed a set of type curves that is used to analyze well test data from fractured reservoirs. Bourdet *et al.* [15] developed another set of type curves that can be used in analyzing buildup and drawdown tests.

3.5. Direct synthesis technique

Direct synthesis method uses a log-log plot of pressure and pressure derivative data versus time to calculate various reservoirs and well parameters. It uses the pressure derivative technique to identify reservoir heterogeneities. In this method, the values of intersection points, the slopes, and the beginning and ending times of various flow regimes from the log-log plot can be used in analytical equations to calculate the different parameters. High accuracy pressure gauges are needed to make this method reliable. Engler and Tiab [16] developed direct synthesis method to analyze pressure transient tests in dual porosity formation without using type curve matching. They used analytical and empirical correlations to calculate the naturally fractured reservoir parameters.

Advantages of using the direct synthesis technique are:

- Accurate results of reservoir and well parameters.
- Independent verification is frequently possible from a third unique point.
- Very useful when not all flow regimes are observed.

The direct synthesis was applied to different models such as; homogeneous reservoir with skin and wellbore storage [17] and to fractured reservoir in closed systems [18].

4. Field description

This study is conducted on an X field which extends over 7500 acre. The reservoir is a naturally fractured reservoir (carbonate rock) and is characterized by a heterogeneous distribution of porosity and permeability.

The reservoir has low porosity and low permeability matrix blocks surrounded by a tortuous, highly permeable fracture network. As a result, the overall fluid flow in the reservoir strongly depends on the flow properties of the fracture network.

The reservoir has variable thicknesses generally between 60 to 250 ft and it consists of dolomite, and some silt. the reservoir boundary is a closed system, constant compressibility.

This reservoir has a crude oil of 34.8° API gravity and average GOR of 332 SCF/STB. The initial reservoir pressure was 4840 psi and the bubble point pressure is 1536.943 psi. The other reservoir and fluid properties are shown in Table 1. Table 1 presents the main reservoir characteristics.

Table 1. Main reservoir characteristics

Well	Vertical well	Well	Vertical well
Wellbore radius, ft	0.35	Formation temperature, °F	218
Gauge depth,ft	11 099	Reservoir pressure, psi	4 840
Net pay thickness, ft	60	GOR, SCF/STB	332
Porosity, %	10	API	34.8
Water saturation, %	10.3	Sp.gr	0.88
Compressibility, psi^{-1}	$5x10^{-6}$		

Pressure and temperature profiles and the rate schedule are shown in Figures 7 and 8.

Before the buildup test, the well is allowed to produce at a rate of 4052 BOPD for 11 hrs. After that, the well was shut in for a 24 hrs to allow the pressure to build-up.

Then the well was open to flow at a rate of 9010 BOPD for 3 hrs. Then, the flow rate was reduced to 8333 BOPD for 3 hrs.

Then, the flow rate was reduced to 990 BOPD for 5.5 hrs, for PVT sampling. The second draw-down was at a rate of 3809 BOPD on a choke size 32/64" for 19.5 hrs.

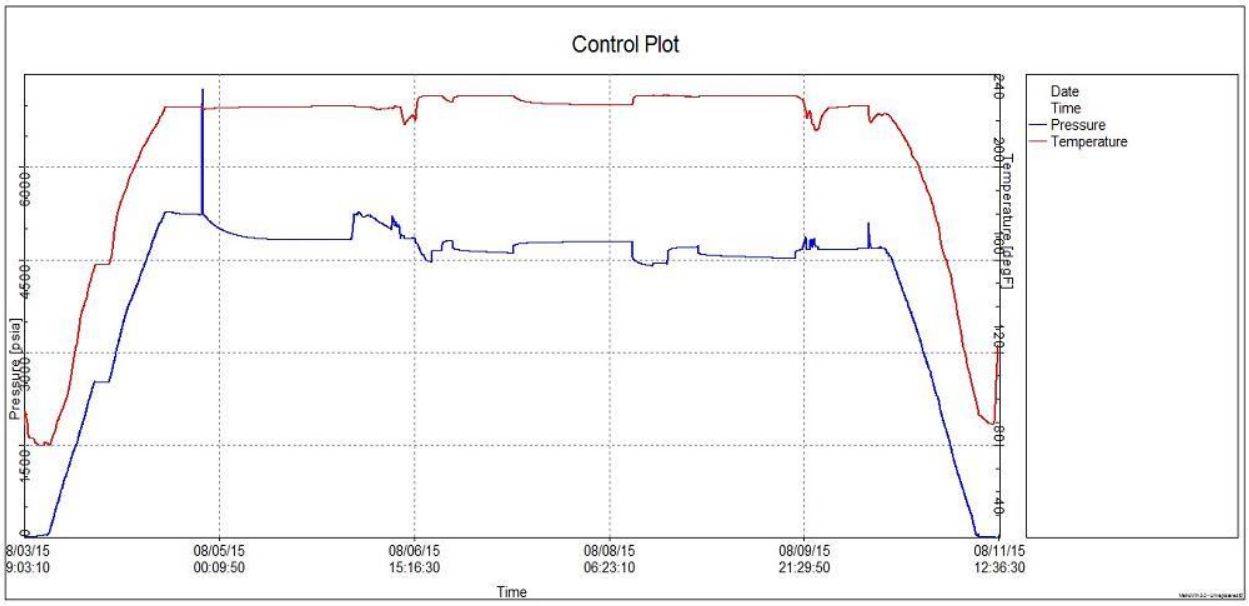

Figure 7. Pressure and temperature profiles

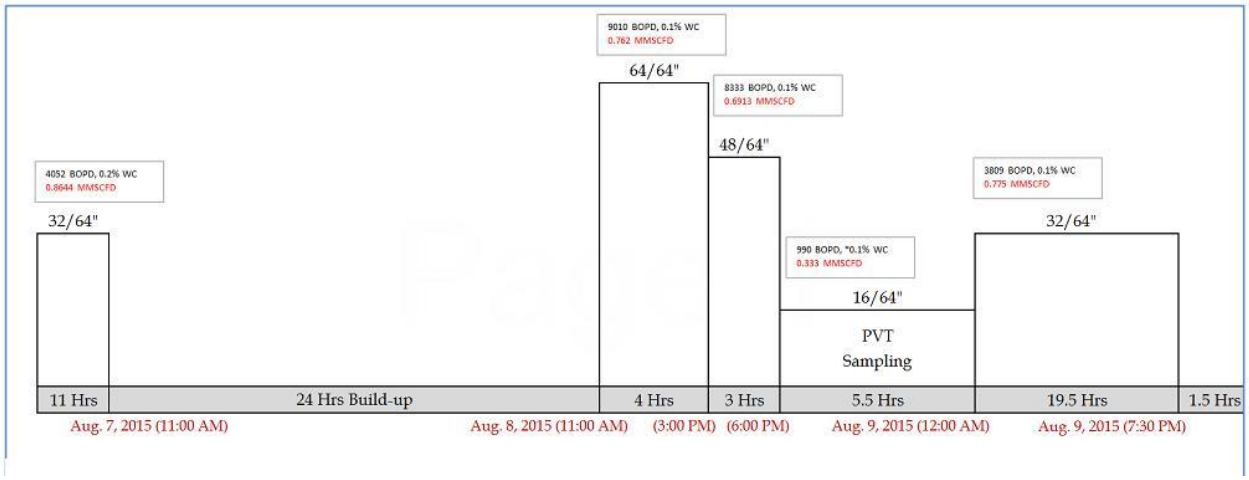

Figure 8. Rate schedule history used in test

5. Results and discussions

This section illustrates the results of applying the three techniques on different cases to analyze the naturally fractured reservoirs. First, the conventional semi-log analysis is applied, if it is possible. Then, the direct synthesis technique results are presented using the developed computer program. Finally, Type curve matching and automatic matching were used to analysis the performance of the subject reservoirs.

5.1. First draw-down period

After running the software, the first step is to import data by entering the pressure data and rate schedule of the test to plot pressure and rate versus time as shown in Figure 9. The second step is the data preparation by entering the well, reservoir and fluid properties mentioned above.

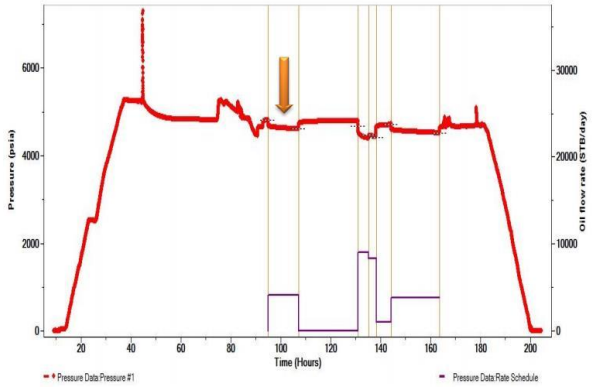

Figure 9. The first draw-down period

The third step is to analyze the data as shown in Figure 10. This figure shows the combined log-log plot of pressure difference and its derivative versus time for a dual – porosity system.

The derivative plot shows a "minimum" or a "dip" on the pressure-derivative curve caused by the interporosity flow during the transition period. The "minimum" is between two horizontal lines; the first represents the radial flow Controlled by the fissures, and the second describes the combined behavior of the double porosity system.

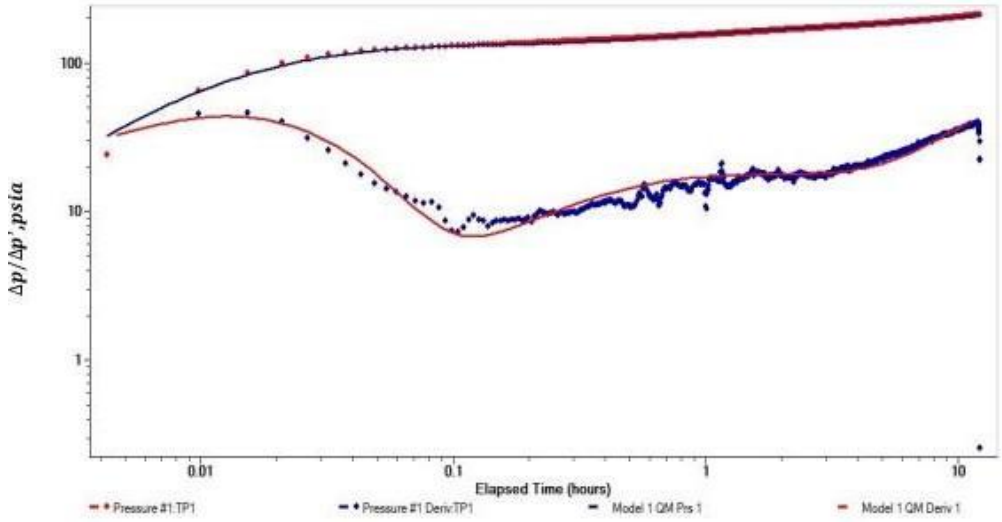

Figure 10. Log-log plot of pressure difference and its derivative versus time

At early time, the typical behavior of wellbore storage effects with the deviation from the 45° straight line to a maximum depects wellbore damage.

5.2. Conventional semi-log analysis

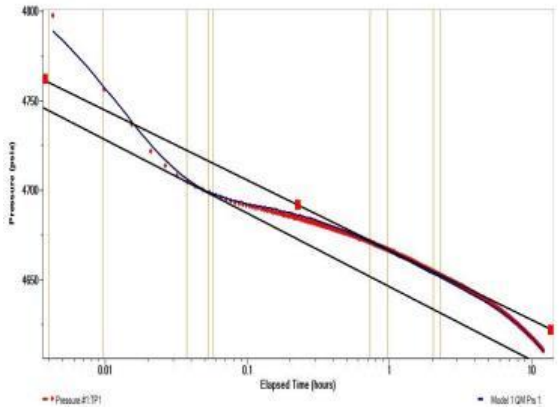

Figure 11. Conventional semi log plot

The semi log plot yields an S–shape curve with two parallel straight lines as shown in Figure 11. The two separate straight lines indicate that the double porosity nature of the reservoir. Secondary porosity (fissures), having greater transmissivity and being connected to the wellbore, respond first as described by the first semi log straight line which reflects the tran-sient radial flow through the fractures, and thus its slope is used to determine the system permeability-thickness product.

However, because the fracture storage is small, the fluid in the fracture is quickly depleted with a combined pressure decline in the fractures due to production. This pressure drop in the fracture allows more fluid to flow from the matrix into the fractures, which causes a slowdown in the pressure decline rate.

The matrix starts to discharge the fluid into the fracture throught the "minimum" or the transition zone, until the pressure is stabilized in the two systems and yield the second semi-log straight line.

As for the drawdown, wellbore storage effects may obscure the first semilog straight line. If both semi log straight lines are developed, the permeability –thickness product and the other reservoir parameters can be determined.

Storativity ratio and interporosity flow coefficient are estimated from the slope m of either straight line. Table 2 represents the results obtained from the conventional semi-log analysis.

Table 2. Semi-log analysis results

k_f,md	272.078
ω	0.07532
λ	3.59×10^{-6}
S	-2.4496

5.3. Direct synthesis technique

The pressure difference and its derivative curves are shown on Figure 12 with the characteristic points and line labelled.

From the plot:

$(\Delta p'w)_{r1} = 17.97psi$ $(t^*\Delta p'w)_{min} = 7.13psi$

$t_{min} = 0.13hrs$ $t_{e1} = 0.051hrs$

$t_{b2} = 0.97$ $t_{r1} = 0.037hrs$

$t_{r2} = 1.3hrs$ $(\Delta pw)_{r1=}116.13\ psi$

$(\Delta pw)_{r2} = 160.2psi$ $(t^*\Delta p'w)_{r2} = 17.97psi$

$(t^*\Delta p'w)_{r1} = 17.97\ psi$

where r_1 and r_2 stand for the early (fracture) and late (total system) radial flow; te_1 is the end time of the early radial flow line, and tb_2 is the beginning time of the late radial flow line.

The log-log plot shows a unique behavior of a naturally fractured reservoir. Different reservoir parameters can be calculated by direct synthesis technique.

The fracture permeability can be calculated from the early and late radial flow lines:

$$k_f = \frac{70.6q\mu\beta_o}{h(\Delta p'w)_{r1}} = \frac{70.6x4052x0.817x1.18}{60x17.97} = 256.2\,md$$

Two methods were applied to calculate the storativity coefficient (ω):

- From minimum to radial pressure derivative ratio:

$$\omega = 0.15866\left(\frac{(\Delta p'wfxt)_{min}}{(\Delta p'wfxt)_r}\right)0.54653\left(\frac{(\Delta p'wfxt)_{min}}{(\Delta p'wfxt)_r}\right)^2 = 0.15866\left(\frac{7.13}{17.97}\right) + 0.54653\left(\frac{7.13}{17.97}\right)^2 = 0.148$$

- From minimum, early radial, or radial time ratio:

$$\omega = 0.19211\left(\frac{5t_{min}}{tb_2}\right) + 0.80678\left(\frac{5t_{min}}{tb_2}\right)^2 = 0.19211\left(\frac{5*0.13}{0.97}\right) + 0.80678\left(\frac{5*0.13}{0.97}\right)^2 = \quad 0.4909$$

Four methods were employed to determine the interporosity flow coefficient parameter (λ):

- From the characteristic times:

$$\lambda = \frac{s_t\mu r_w^2}{0.0002637k_f}\frac{\omega ln\,{}^1/_\omega}{t_{min}} = \frac{0.1x4.8623x10^{-6}x0.817x0.35^2}{0.0002637x256.2}\ x\ \ \frac{0.148xln\left(\frac{1}{0.148}\right)}{0.13} = 2.2\times10^{-6}$$

$$\lambda = \frac{s_t\mu r_w^2}{0.0002637k_f}\frac{\omega(1-\omega)}{50t_{e1}} = \frac{0.1x4.8623x10^{-6}x0.817x0.35^2}{0.0002637x256.2}x\frac{0.148(1-0.148)}{50x0.051} = \quad 3.6x10^{-8}$$

$$\lambda = \frac{s_t \mu r_w^2}{0.0002637 k_f} \frac{5(1-\omega)}{t_{b2}} = \frac{0.1x4.8623x10^{-6}x0.817x0.35^2}{0.0002637x256.2} \; x \; \frac{5x(1-0.148)}{0.97} = 3.15x10^{-6}$$

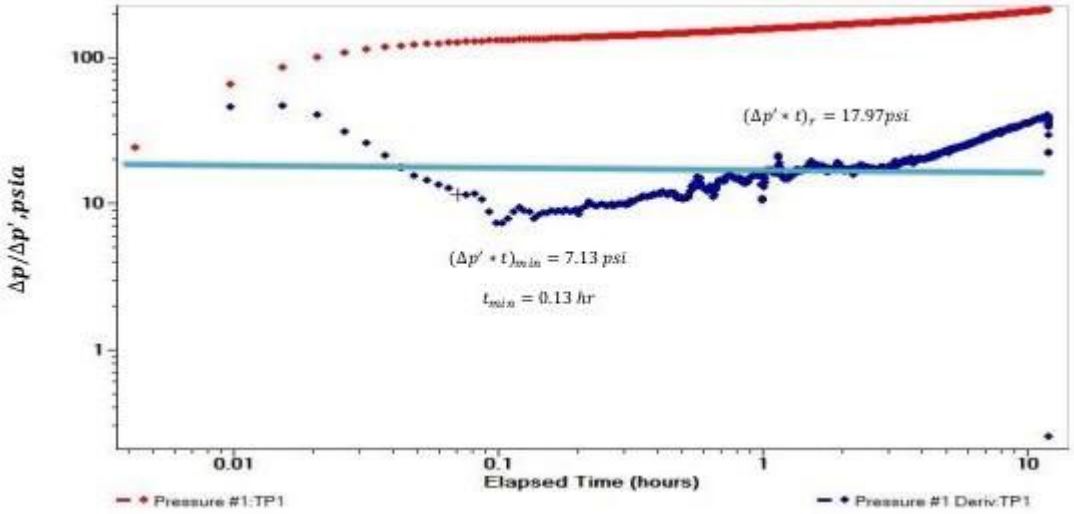

Figure 12. Pressure difference and its derivative plot

- From the minimum coordinates:

$$\lambda = \frac{42.5 h s_t r_w^2}{q \beta_o} \left(\frac{\Delta p_{wf'*t}}{t}\right)_{min} = \frac{42.5x60x0.1x4.8623x10^{-6}x0.35^2}{4052 * 1.18} x \left(\frac{7.13}{0.13}\right) = 2.33x10^{-6}$$

The skin factor is calculated from a convenient point during early or late radial flow period:

- From the early time pressure and pressure derivative data:

$$s_m = \frac{1}{2}\left[-ln\left(\frac{k_f t_{r1}}{s_t \mu r_w^2}\frac{1}{\omega}\right) 7.43\right] = \frac{1}{2}\left[\frac{116.13}{17.97} - ln\left(\frac{256.2x0.037}{0.1x4.8623x10^{-6}x0.817x0.35^2} x \frac{1}{0.15}\right) + 7.43\right] - 3.21$$

- From the late time pressure and pressure derivative data:

$$s_m = \frac{1}{2}\left[\left(\frac{\Delta p_{wf}}{\Delta p' wf * t}\right)_{r2} - ln\left(\frac{k_f t_{r2}}{s_t \mu r_w^2}\right) + 7.43\right] = \frac{1}{2}\left[\frac{160.2}{17.97} - ln\left(\frac{256.2x1.3}{0.1x4.8623x10^{-6}x0.817x0.35^2}\right) 7.43\right] = -2.8$$

Table 3 presents the results of analyzing well test data from naturally fracture reservoir by the developed program based on direct synthesis technique. Table 4. presents the results which are obtained from the type curve matching analysis.

Table 3. Direct synthesis technique results

$K_{f,md}$	256.2
ω	0.148
λ	$3.15.10^{-6}$
S	-2.8

Table 4. Type curve matching analysis result

$K_{f,md}$	279.9
ω	0.001
λ	$4.37.10^{-6}$
S	-2.665

5.4. Commercial software matching

A commercial software (Pan-System) was used for analyzing well test data from naturally fractured reservoir. Figure 14 depects that the response of pressure build-up and its derivative for the well is divided into six periods.

Period (1) is a unit-slope region which indicates the wellbore storage (WBS) impact. It should be noted that the WBS effect lasts for only 0.01 hour assuming negligible (or controlled) WBS period due to the low compressibility of the crude. This should be confirmed and assured by utilizing down-hole shut-in tool (DHST) to mitigate the WBS impact. In this case, a slight change in the pressure derivative trend would be expected.

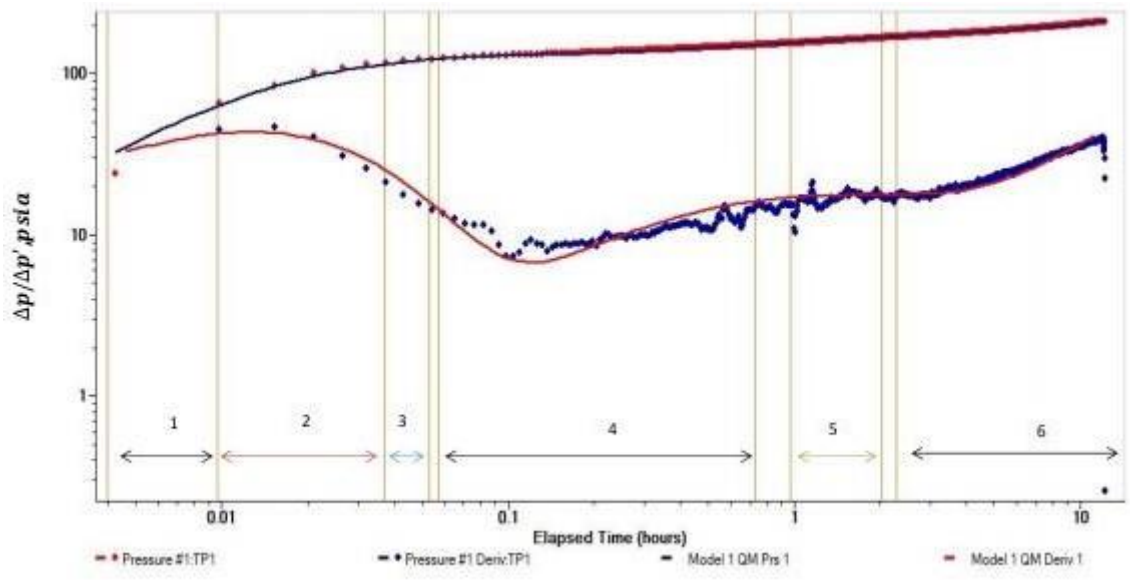

Figure 14. Typical pressure derivative and its periods

DHST is very important to avoid masking of later periods.

Period (2) is the skin hump period. It will be analyzed to estimate the skin factor (S) (which is related to damaged zone or stimulated zone).

Period (3) period refers to zero slope line which reflects the radial flow in the fracture. From this period, permeability and reservoir pressure can be estimate.

Period (4) period can be considered as an extension of IAFR period. The presence of the dual-porosity system (Φsec) can be detected from this period. This period may (or may not) exist based on the nature of rock petrography and pores-system of the formation.

This period is called the minimum and at which the interflow occurs between the fracture and the matrix. From this period, the main important two factors which describe the fluid flow and behavior of dual porosity system can be estimated.

The first parameter is the storativity ratio (ω) which describes the fracture porosity as a percentage of the matrix porosity. The duration and depth of the depression are linked by the value of ω; a small value produces a long and therefore deep transition. The second parameter is the interporosity flow coefficient (λ) which describes the fluid transfer between the matrix and fractures, and defines the position of the time axis of the transition regime.

Period (5) represents the homogenous behavior of both media when recharge from the least permeable medium (matrix) is fully established and pressure is equalized.

Period (6) represents the effect of boundary condition which is a closed system (unit slope on the pressure derivative). From this period, the distance to boundary and drainage area can be calculated.

Table 5 presents the model selected from the commercial software. Table 6 presents the main model parameters. Table 7 presents the reservoir and boundary parameters.

Table 5. The model selected from the software

Model option	Standard model
Well	Vertical
Flow regime	PSS
Reservoir	Dual porosity
Boundary	Closed system

Table 6. Main model parameter

$C_s, bll/psi$	0.018
V, bll	2596.79
$k/_{\mu, md/cp}$	322.813
$k_{f,md}$	263.869
$kh, md.ft$	15832.14
S	-2.5973

Table 7. Reservoir and boundary parameters

ω	0.083
λ	$4.89.10^{-6}$
$A, acre$	104.171
$OOIP, MMSTB$	3.689
p_i, psi	4 821.56
dp_s, psi	-90.573
R_{inv}, ft	1 715.814
$F.E$	1.4002
Ca	30.8815
L, ft	1 065.09

The standard model is selected as a dual porosity pseudo steady state to the reservoir due to a transformation between the least permeable media (matrix) and the high permeable media (fissures), and it is mathematically equivalent to the pseudo steady-state solution, i.e., the Warren and Root model, and selected as closed system for the reservoir boundary.

After setting the model, the main model parameters can be obtained. These are wellbore storage coefficient, skin factor, storativity ratio, interporosity flow coefficient and permeability thickness product.

Wellbore storage coefficient (C) which is very small value due to using down-hole shut-in tool ($DHST$) which is necessary to mitigate wellbore storage (WBS) effect and hence obtaining valuable pressure curve.

Skin factor has a value of -2.5973 which indicates that there is no damage around the wellbore (i.e., stimulation process is successful).

Permeability - thickness product (*K.h*) has a value of 15832.14 *md.ft*. This is very high value due to the higher permeability of the fracture.

One of the well test analysis results is the initial reservoir pressure (Pi), which has a value of 4821 psi, Pi is necessary for estimating the productivity index (*P.I*) and inflow performance relationship (IPR).

Pressure drop due to skin (*dps*), which equal to -90.573 *psi,* is a small value caused by lower value of skin effect (S). This means that there is no additional pressure drop due to damage of the formation around the wellbore which will give a higher production rate and higher productivity index.

Storativity ratio (ω) is related to the fracture porosity. A typical range of ω is from 0.1 to 0.001. In this work the value of ω is 0.0832 which means that the value of ω in this reservoir is a small value as compared to the typical one, i.e., large and deep transition period. This is because the fracture porosity is low as compared to the matrix porosity which takes small time to deplete the fracture due to lower porosity.

The pressure drop in the fracture which permits the matrix to discharge flow in to the fracture and the pressure stabilization occurs slowly (the duration and depth of the depression are linked by the value of ω).

By assuming that the fracture compressibility is equal to the matrix compressibility, the fracture porosity can easily be obtained from storativity ratio using the following equation:

$$\emptyset f = \left(\frac{\omega}{1-\omega}\right)\emptyset \qquad (15)$$

$$\emptyset f = \left(\frac{0.0832}{1-0.0832}\right)0.1 = 0.009$$

So, the storativity ratio is very important in understanding the performance of the dual porosity system and in finding the fracture porosity.

Interporosity flow coefficient (λ); is related to the fracture permeability. In this case the value of λ is 4.89×10^{-6}. This means that higher value of interporosity flow coefficient moves the dipression to the left side of the plot. This is clearly shown in Figure 14.

This occurs because the lower the value of λ, the lower the value of matrix permeability as compared to the fracture permeability which leads to delay the minimum from disappears and moves to the right of the plot.

The Interporosity flow coefficient λ value defining the position of the time axis of the transition regime. As shown on Figure 14, the shape of the "minimum" takes a "U – shape"

and this is due to a non-restricted interporosity flow coefficient (i.e., there is a low skin between the matrix face and the fracture). The fluid flows from the matrix system into the fractures under pseudo –steady-state conditions with the fracture acting like conduits to the wellbore (i.e., Warrenn and Root model).

Distance to boundary (L) which has a value of 1065.09 *ft.*, effects on the pressure derivative curve. For the case under steady, the OOIP has a value of 3.684MMSTB, and the drainage area has a value of 104.171 acre c. It should be noted that the test time should be long enough to reach the boundary of the reservoir.

Table 8 shows a comparison among the three techniques used in analyzing well test data in naturally fractured reservoirs.

The results show that, conventional semi-log technique gives an accurate permeability only, and type curve matching gives inaccurate matching during the transition period and leads to erroneous values of ω and λ. The direct synthesis gives accurate results of nearly all the reservoir parameters except permeability.

Table 8. Comparison of results

Parameter	Conventional semi-log	Direct synthesis technique	Type curve matching
k_f, md	272.078	256.2	279.9
ω	0.075	0.148	0.001
λ	$3.59.10^{-6}$	$3.15.10^{-6}$	$4.37.10^{-6}$
s	-2.449	-2.8	-2.66

The results of direct synthesis were used as inputs into a model to generate pressure vs. time data as shown on Figure 15. A comparison between the direct synthesis results and the software matching results with the actual field data are shown on Figure 16.

The direct synthesis technique gives a good match during the early time and the transition flow period.

However, the software match shows poor fit during the early and the transition flow period and a good match during the late time period.

The difference between the fracture permeability values obtained from the two techniques is directly related to the matching quality during the radial total system period.

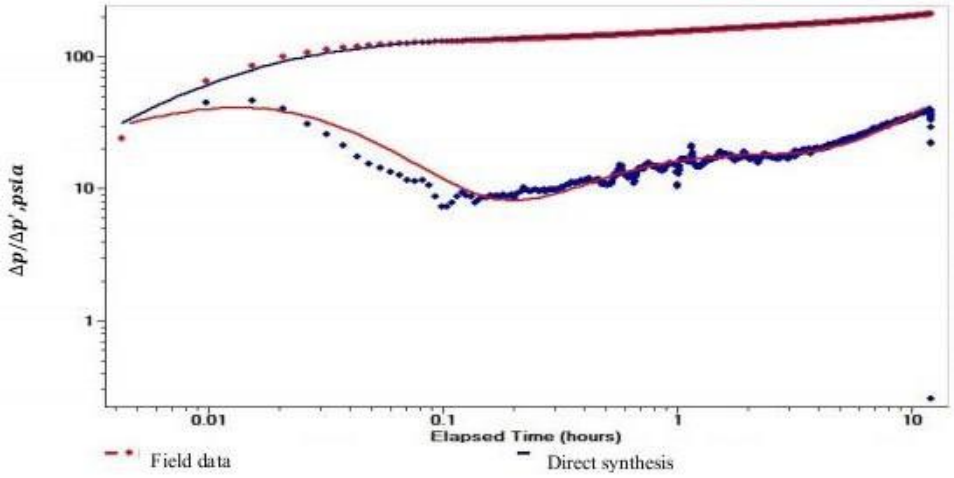

Figure 15. Direct synthesis model

The difference in the matching of the two techniques during the transition period gives different values of the dimensionless storage coefficient.

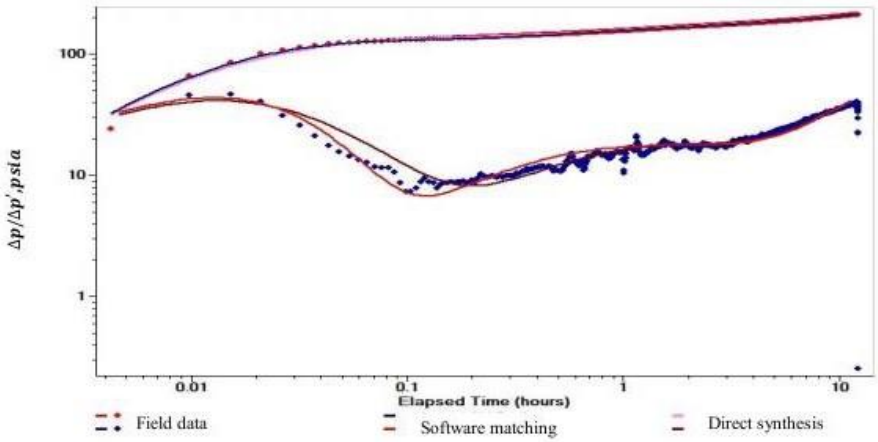

Figure 16. Comparison between direct synthesis results and software matching

6. Conclusions

From this work, can conclude that well test pressure response should exhibit a complete flow regimes (fracture radial flow, transition flow, and system radial flow) in order to obtain reliable estimates of storativity ratio and interporosity flow coefficient. The use of pressure derivatives plots improved the analysis of well test data. Different flow regimes can be identified on the derivative log-log plots. Type curve matching can give good results in case of all of the flow regimes are identified.

Tiab direct synthesis technique gives direct estimates of all reservoir parameters and fracture characteristics by using a log-log plot of pressure difference and its derivative data without type curve matching. In case of high wellbore storage, the conventional semi-log analysis gives inaccurate results and not all naturally fractured reservoir parameters can be estimated.

The developed computer program gives accurate results as compared to commercial software matching, conventional semi-log analysis, and the type curve matching.Interporosity flow coefficient obtained from well test analysis can also be used to estimate the fracture permeability provided that the shape factor and the matrix permeability values are known.

When all flow regimes are not identified, type curve matching gives incorrect reservoir and fracture parameters. However, the direct synthesis technique gives an accurate result of the naturally fractured reservoir parameters and fracture properties.

Nomenclature

A	*Area,* ft^2
$AOFP$	*Absolute open flowing potential,* STB
B	*Formation volume factor, res* bbl/STB
C	*Wellbore storage coefficient,* bbl/psi
C_A	*Shape factor*
C_t	*Total compressibility,* psi^{-1}
C_{dw}	*Dimensionless wellbore storage*
$DHST$	*Down-Hole Shutting Tool*
d_{p_s}	*Pressure drop due to skin,* Psi
$F.E$	*Flow efficiency*
GOR	*Gas Oil Ratio,* SCF/STB
h	*Total formation thickness,* ft
IPR	*Inflow performance relationship*
J	*Productivity index,* $STB/D/psi$
k_f	*Fracture permeability,* md
$k.h$	*Permeability-thickness product,* $md.ft$
k_m	*Matrix permeability,* md
L	*Distant to boundary,* ft
l_{ma}	*Fracture spacing,* ft

N_P	*Cumulative oil production,* STB
OOIP	*Original oil in place,* STB
p	*Pressure,* psi
P_D	*Dimensionless pressure*
P_{wD}	*Dimensionless bottom-hole pressure*
P_{int}	*Initial pressure,* psi
P_{wf}	*Bottom-hole flowing pressure,* psi
P_D'	*Dimensionless pressure derivative*
P_{wD}'	*Dimensionless bottom-hole pressure derivative*
Δp	*Pressure difference,* psi
$\Delta p'$	*Pressure difference derivative,* psi
q_t	*Total flow rate,* STB/D
r_e	*Reservoir outer radius,* ft
r_w	*Wellbore radius,* ft
S	*Skin factor*
t	*Test time,* hr
t^D	*Dimensionless time*
WOR	*Water oil ratio*
w_f	*Fracture width,* ft
ω	*Dimensionless storage coefficient*
λ	*Interporosity flow coefficient*
ρ_f	*Natural fracture density,* $frac/ft$
μ	*Viscosity,* Cp
$\emptyset$	*Porosity*

References

[1] Ahmed T. Reservoir Engineering Handbook (4th ed.), Amsterdam 2010: Gulf Professional Pub.

[2] Chaudhry AU. Oil Well Testing Handbook, Burlington 2004, Massachusetts: Gulf Professional Publishing/Elsevier. Houston, Texas.

[3] Nelson RA. Geologic analysis of naturally fractured reservoir, Gulf Professional Publishing 2001, Woburn, MA.

[4] Parsons RW. Permeability of Idealized Fracture Rock. SPEJ (December)1966: 451.

[5] Hubbert MK, and Wills DG. Important Fractured Reservoirs in the United States. Proc. 4th World Pet. Conger. 1995, Sect. I/AI1, pp. 58-81.

[6] Horner DR. Pressure Build-up in Wells. Proc. 5th World Pet. Conger. 1951, The Haugue, Sect. II.

[7] Baker WJ. Flow in Fissured Formation. Proc. 5th World Pet. Conger.1955, Sect. II/E, pp. 379-393.

[8] Lamb H. Hydrodynamics. Dover 1932, New York, N.Y., 6 th ed.

[9] Muskat M. The Flow of Homogeneous Fluids through Porous Media. McGraw-Hill 1937, New York

[10] Huitt JL. Fluid Flow in Simulated Fractures. Am. Inst. Chem. Eng. J., 1956; 2:259-264.

[11] Warren JE, and Root PJ. The Behavior of Naturally Fractured Reservoirs. Soc. Pet. Eng. J., 1963; 3: 245-255.

[12] Odeh AA. 1965. Unsteady-state Behavior of Naturally Fracture Reservoirs. Soc. Pet. Eng. J., 1965; March, pp. 60-66.

[13] Warren JE, and Root PJ. Discussion of Unsteady-state Behavior of Naturally Fractured Reservoirs. Soc. Pet. Eng. J., 1965; March, p. 64.

[14 Bourdet D, Ayoub JA, Whittle TM, Pirard YM, and Knlazeff V. Interpreting Well Tests in Fractured Reservoirs. World Oil,1983; 77-87.

[15] Bourdet D, Alagoa A, Ayoub JA. 1984, and Pirard YM. New Type Curves Aid Analysis of Fissured Zone Well Tests. World Oil, 1984; 111-125.

[16] Engler T, and Tiab D. Analysis of Pressure and Pressure Derivative without type curve Matching; 4. Naturally Fractured Reservoirs. Journal of Petroleum Science and Engineering, 1996; 15: 127-138.

[17] Taib D. Analysis of pressure and pressure derivative without type curve matching – Skin and wellbore storage. Journal of petroleum science and engineering, 1995; 12(3): 171-181.

[18] Tiab D. Analysis of pressure and pressure derivative without type curve matching; Fractured wells in Closed Systems. Journal of petroleum science and engineering, 1994; 11(4): 323-333.

To whom correspondence should be addressed: Dr. Saher Adel, Al-Azhar University, Faculty of Engineering, Mining and Petroleum Engineering Department, Cairo, Egypt

Petroleum and Coal

Article **Open Access**

INVESTIGATION OF POSSIBLE LOSSES OF COAL RAW MATERIALS DURING ITS TECHNOLOGICAL PREPARATION FOR COKING
MESSAGE 1.THE ACTUAL MASS VARIATION OF COAL IN THE PROCESS OF ITS DEFROSTING

I. D. Drozdnik[1], D. V. Miroshnichenko[2], E. O. Shmeltser[3], M. V. Kormer[3], S. V. Pyshyev[4]*

[1] *Ukrainian State Coal-Chemistry Institute, 61023, Kharkiv, Ukraine*
[2] *National Technical University «Kharkiv Polytechnic Institute», 61002, Kharkiv, Ukraine*
[3] *Kryvyi Rig Metallurgical Institute, Ukraine National Metallurgical Academy, Kryvyi Rig, Ukraine*
[4] *Lviv Polytechnic National University, 79013, Lviv, Ukraine*

Received February 19, 2019; Accepted May 9, 2019

Abstract

Particles begin to freeze when the moisture content in them exceeds the value of the maximum capacity. In turn, the magnitude of the maximum capacity depends on the degree of metamorphism and in the rank of coking coal has the maximum value or the low-metamorphosed coal.
Taking into account the fact that low-metamorphosed coals are characterized by the maximum values of water capacity, these coals may be less time in the defrosting garage compared to other coking coals. Using mathematical statistics, an equation was obtained describing the change in the mass of coal when it is thawed, depending on the moisture content, the average particle diameter of the coal, and time spent in the defrosting garage. This equation makes it possible to estimate the reduction in the mass of coal in the process of defrosting, depending on its quality indicators and the conditions in the defrosting garage.

***Keywords**:* coal; maximum water holding capacity; freezing; garage defrosting; weight loss.

1. Introduction

In the cold season, irregular coal supplies to coke plants are aggravated by the need to heat the coal cars. The individual coal particles freeze together and also bond with the floor and walls of the car. Such freezing occurs on account of heat transfer between the car and the surrounding cold air, between the car and its coal cargo, and at the open top of the car between the coal and the cold air. Freezing of the coal to the car hinders its discharge, while the freezing of the coal particles forms large conglomerates that cannot easily be manipulated.

Wet dispersed coals freeze during storage and transportation at low temperatures. The freezing and strength of the frozen coal-water-ice disperse system is due to the phase state of the water on the surface of the coal particles and the cementing effect of the ice formed.

The freezing of coal is a complex thermophysical process accompanied by the migration of moisture and temperature variation. It depends primarily on the thermal conductivity and specific heat of the coal, the duration of the low ambient temperatures, the moisture content of the coal, its metamorphic stage, the composition of mineral impurities, the granulometric composition, and the hydrophilic properties of the surface. However, the key factor is the moisture content of the charge [1].

The theory of the question of coal freezing is discussed in [2]; the main points of the theory are as follows.

A layer of strongly bound water is retained on the outer surface of the particles, which, under the influence of active surface centers, acquires special physicochemical properties. It freezes at temperatures below -70°C. When the external moisture is an adsorption layer of

tightly bound moisture, the freezing of particles at normal negative temperatures is absent. The bond strength of water with the surface decreases with an increase in the thickness of its film. Layers of water adjacent to the film of tightly bound, non-freezing water are less affected by the surface. This is the so-called loose water. It, unlike strongly bound water, is capable of crystallizing into ice, but at temperatures lower than the freezing point of water in volume. In contrast to the tightly bound, this water has greater mobility, which leads to its tightening to the points of contact between the particles of coal.

At negative temperatures, part of this water freezes, adhesions form between the particles, and the system loses flowability. The amount of bound non-freezing water and the amount of water crystallizing in ice depend (ceteris paribus) on the surface energy of the coal, which is a function of their petrographic features — the stage of metamorphism and petrographic composition.

The strength of freezing coal is determined by the strength of the ice, which depends on the surface energy of the particles. With decreasing temperature, the degree of coal freezing increases with increasing humidity and decreasing particle size [3].

In order to ensure the normal discharge of coal concentrates, they must be directed to special garages for their thawing before car dumpers [4–6]. In the process of finding cars with coal in these garages, there is an intensive removal of moisture, leading to a change in the actual mass of coal.

In the course of the research, the results of which are presented in this article, the influence of various factors (ambient temperature, initial humidity of coal concentrates and their particle size distribution, duration of coal in the defrosting garage) on the change in the actual mass of coal concentrates during their defrosting were studied.

2. Results and discussions

Currently, the raw material base of Avdeevskii coke plant contains coals from both the near (Taldinsky Zapadny open pit, Taybinskaya central processing plant, Shchedrukhinskaya central processing plant, Berezovskaya central processing plant) and long-distance (Wellmore, Rocklick, Teck Premium, Pocahontas) abroad. Coal concentrates of these suppliers enter the plant with moisture ~ 10%, which in winter, at a negative ambient temperature, leads to their freezing.

The quality indicators of the investigated coal concentrates are given in Table 1–4. It is nece-ssary to dwell on the maximum moisture capacity of the coals studied [7–11]. In [2], the freezing of Kuzbass coals at various stages of metamorphism and close petrographic composition was investigated. The degree of freezing of coal of different humidity was evaluated by the strength of frozen samples with uniaxial compression.

All tested coals do not freeze when the humidity changes to the maximum capacity. Particles begin to freeze when their moisture content exceeds the maximum moisture capacity. This condition was fulfilled for all tested size classes from 0.5–1 to 5–7 mm and temperature limits from –8 to –35°C. Therefore, the maximum moisture capacity can be taken as safe moisture in relation to the freezing of coal. With a further increase in the moisture content of dispersed coal, the moisture on the outer surface of the particles freezes and the system loses flowability.

The influence of the degree of metamorphism of coal on the value of their maximum capacity can be traced in Fig. 1, obtained on the basis given Table 1 data. Taking into account the fact that low-metamorphosed coal of the gas group is characterized by the maximum values of water capacity, these coals may remain less time in the defrosting garage compared to other coking coals.

The study of the dependence of the freezing temperature of coal on its granulometric composition and the level of working moisture is an urgent task, the solution of which will optimize the operation of the coal preparation plant as well as reduce the cost of heating the frozen coal.

Table 1. Technological properties of coal concentrates

Component; country	Coal rank	Proximate analysis, %				Thickness of plasto-metric layer, mm		Maximum moisture-holding capacity, %	Oxidation index, °C
		W^a	A^d	S^d_t	V^{daf}	x	y	W_{max}	Δt
Shchedrukhinskaya coal, Russia	G	3.3	7.5	0.53	38.2	32	10	4.12	1
Section Taldinsky West coal, Russia	G	4.0	8.5	0.44	37.0	33	10	3.79	4
Taybinskaya coal, Russia	G	2.9	9.0	0.50	34.1	30	10	3.14	3
Wellmore coal, USA	Zh	1.3	7.5	0.98	34.2	17	24	3.16	2
Rocklick coal, USA	Zh	1.3	7.5	0.98	34.2	17	24	3.17	2
Svyato-Varvarinskaya coal, Ukraine	K	1.1	9.1	0.73	26.8	14	14	2.33	2
Teck Premium coal, Canada	K+KO	1.1	8.6	0.56	26.2	18	14	2.22	5
Berezovskaya coal, Russia	KO	1.5	5.1	0.40	24.2	30	9	2.34	5
Pocahontas coal, USA	OS	0.8	8.03	0.85	18.3	11	12	2.91	2

Table 2. Petrographic characteristics of coal concentrates

Component; country	Coal rank	Petrographic composition (without mineral impurities), %					Mean vitrinite reflection coefficient, %	Distribution of vitrinite reflection coefficient, %					
		Vt	Sv	I	L	∑FC	R_o	0.50 – 0.79	0.80 – 0.89	0.90 – 1.19	1.20 – 1.49	1.50 – 1.69	1.70 – 2.59
Shchedrukhinskaya coal, Russia	G	74	0	24	2	24	0.69	96	4	0	0	0	0
Section Taldinsky West coal, Russia	G	69	0	29	2	29	0.64	100	0	0	0	0	0
Taybinskaya coal, Russia	G	66	0	31	3	31	0.72	94	6	0	0	0	0
Wellmore coal, USA	Zh	73	0	24	3	24	0.99	0	11	89	0	0	0
Rocklick coal, USA	Zh	69	0	26	5	26	0.97	2	18	79	1	0	0
Svyato-Varvarinskaya coal, Ukraine	K	83	1	14	2	15	1.20	0	0	48	52	0	0
Teck Premium coal, Canada	K+KO	70	0	29	1	29	1.09	0	6	80	14	0	0
Berezovskaya coal, Russia	KO	37	1	62	0	63	1.05	0	11	83	6	0	0
Pocahontas coal, USA	OS	77	0	23	0	23	1.60	0	0	0	12	76	12

Table 3. Ultimate composition of coal concentrates

Component; country	Coal rank	Ultimate composition, %				
		C^{daf}	H^{daf}	N^{daf}	S_t^d	O_d^{daf}
Shchedrukhinskaya coal, Russia	G	83.10	5.77	2.40	0.53	8.20
Section Taldinsky West coal, Russia	G	81.51	5.25	2.29	0.44	10.51
Taybinskaya coal, Russia	G	84.32	5.39	2.30	0.50	7.49
Wellmore coal, USA	Zh	86.94	6.15	1.66	1.10	4.15
Rocklick coal, USA	Zh	86.10	7.70	1.68	0.98	3.54
Svyato-Varvarinskaya coal, Ukraine	K	87.52	5.45	1.65	0.73	4.65
Teck Premium coal, Canada	K+KO	88.20	4.96	1.36	0.56	4.92
Berezovskaya coal, Russia	KO	84.14	4.85	2.30	0.40	8.31
Pocahontas coal, USA	OS	91.56	4.85	1.40	0.85	1.34

Table 4. Granulometric composition of coal concentrates

Component; country	Coal rank	Granulometric composition (%) by class (mm)									Mean particle diameter, mm
		>50	25–50	13–25	6–13	3–6	1–3	0,5–1	<0,5	0–3	
Shchedrukhinskaya coal, Russia	G	2.1	2.3	6.4	18.6	23.3	22.0	8.8	16.6	47.4	6.64
Section Taldinsky West coal, Russia	G	4.1	21.1	22.9	19.8	12.0	8.4	3.7	8.0	20.1	17.33
Taybinskaya coal, Russia	G	1.6	6.8	12.8	19.5	20.2	18.2	8.1	12.8	39.1	8.92
Wellmore coal, USA	Zh	0.0	2.8	7.6	22.8	20.6	18.4	8.6	19.2	46.2	5.61
Rocklick coal, USA	Zh	0.0	2.3	7.6	15.0	18.6	20.4	10.0	26.1	56.5	4.78
Svyato-Varvarinskaya coal, Ukraine	K	0.0	5.0	9.8	16.6	16.1	17.2	9.3	26.0	52.5	6.12
Teck Premium coal, Canada	K+KO	0.0	0.2	2.7	5.4	10.0	19.0	11.5	51.2	81.7	2.02
Berezovskaya coal, Russia	KO	10.3	21.5	16.4	13.1	8.4	7.6	4.4	18.3	30.3	20.31
Pocahontas coal, USA	OS	0.0	0.0	1.0	3.8	10.3	26.8	23.8	34.3	84.9	1.83

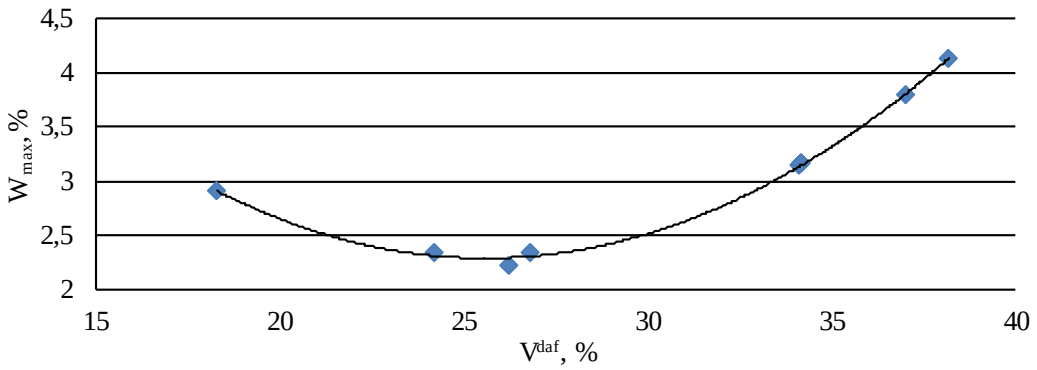

Fig. 1. Dependence of the maximum moisture-holding capacity of the index of the volatile matter of the investigated coal

A sample of coal from the company Wellmore (coal rank «Zh») was used as a model sample in laboratory studies. Data on the maximum capacity of its size classes – Table 5.

Table 5. Values of the maximum moisture-holding capacity of the coal sample Wellmore

Size class, mm	Maximum moisture-holding capacity Wmax, %
<0,5	5.2
<3	3.0
3–6	2.8
6-13	2.1
13–50	1.8

Analyzing the data given Table 5, it can be concluded that the value of the maximum water capacity decreases with an increasing particle size of the coal classes studied. Consequently, it can be expected that coal particles with a particle size of less than 3 and, especially, less than 0.5 mm will be characterized by the highest working moisture content and freezing conditions.

To determine the influence of the humidity level (6, 10 and 12%) on the freezing capacity of various classes of the coal sample examined, a special study was conducted.

Samples of coal of various sizes were loaded into metal forms with a diameter of 150 mm and a height of 150 mm, after which they were kept in a freezer with a gradual decrease in temperature to -15°C for 2 days. Then the sample was removed and the degree of coal freezing at temperatures of -5C, -10C and -15°C was determined as the ratio of spilled coal to the total mass of coal taken for the experiment. The results of determining the freezing capacity of various classes of coal size are summarized Table. 6

Table 6. Results of the determination of freezing

Size class, mm	W^r_t, %	Degree of freezing, %		
		-5°C	-10°C	-15°C
0–3	6	80	88	100
	10	88	96	100
	12	100	100	100
3–6	6	48	56	81
	10	64	76	96
	12	80	96	100
6–13	6	20	28	49
	10	36	48	64
	12	48	68	88
13–50	6	4	8	36
	10	6	16	45
	12	20	32	64

Analyzing the data given in Table 6, it can be concluded that with decreasing temperature, the degree of coal freezing increases with increasing its humidity and decreasing the particle size.

To determine the quantitative effect of the content of small classes on the value of coal freezing, mixtures containing a different amount of class 0–3 mm were prepared (Table 7). All samples were characterized by humidity equal to 12%.

Table 7. Composition of coal blends

Size class, mm	Samples composition of coal blend, %			
	1	2	3	4
0–3	25	50	75	75
3–6	25	25	0	25
6–13	50	25	25	0
Total	100	100	100	100
Mean particle diameter, mm	6.00	4.13	3.38	2.25

The results of determining the freezing capacity of mixtures containing different amounts of a class of 0–3 mm are shown in Table 8.

Table 8. Dependence of the degree of freezing of coal blends on its granulometric composition

Coal blend	Degree of freezing, %		
	-5°C	-10°C	-15°C
1	35.2	68.8	90.0
2	82.0	82.0	92.3
3	88.6	83,2	94.8
4	94.8	98.0	100.0

The data Table 8 shows that with an increase in the content of small classes in the coal, which is expressed by a decrease in its average diameter, there is an increase in the degree of freezing of coal over the entire range of temperatures studied.

Experimental data to determine the mass loss of coal during its defrosting are given in Table 9. In particular, it presents the name of the suppliers of the investigated coal, their brand identity, the date of the experiment, the average daily temperature on that day, as well as the number of the list for which the coal was received.

Analyzing the data presented, it can be concluded that 14 measurements of the mass loss of coal were made while it was in the defrosting garage, and the ambient temperature varied from -3.5 to +6.5°C.

Analysis of the results obtained suggests that during the stay of the coals in the garage of defrosting there is a loss of their mass (from 0.01 to 0.63%), which can be explained by evaporation or drainage of available moisture.

The maximum mass loss is observed in Wellmore coal concentrates (coal rank "Zh"), Rocklick (coal rank "Zh") and Pocahontas (coal rank "OS"), which amounted to 0.50–0.63%.

Due to the fact that coal freezing capacity largely depends on the working moisture content and its granulometric composition, and the only variable parameter when coal was in the defrosting garage was time, the change in the actual mass of coal was estimated from the change in these three factors.

Based on the Table 1 data, it can be stated that the working moisture content in the coals that took part in the industrial experiment varied from 8.5 to 11.6%, the average particle diameter varied from 2.02 to 20.31 mm, and their residence time in the defrosting garage changed from 170 to 475 minutes. At the same time, the mass loss of coal in the process of defrosting was 0.01–0.63% of the mass.

Table 9. Results of researches

Component; country	Coal rank	Moisture W_{rt}, %	Average daily temperature t, °C	Time spent in the garage defrosting, min	Mass variation of coal, Δm, %
Shchedrukhinskaya coal, Russia	G	11.6	4.5	220	0.03
Section Taldinsky West coal, Russia	G	10.2	4.5	195	0.08
Taybinskaya coal, Russia	G	9.5	-2.0	190	0.03
		10.5	-1.0	375	0.29
Wellmore coal, USA	Zh	8.9	0.5	310	0.50
		8.9	0.5	475	0.27
Rocklick coal, USA	Zh	8.5	-3.5	245	0.10
		8.9	1.0	195	0.63
Svyato-Varvarinskaya coal, Ukraine	K	9,7	2.5	230	0.34
		10.3	0.5	310	0.04
Teck Premium coal, Canada	K+KO	9,7	0.5	265	0.16
Berezovskaya coal, Russia	KO	8.9	6.5	250	0.03
Pocahontas coal, USA	OS	10.5	0.5	170	0.50
		10.1	1.0	300	0.01

Using the methods of mathematical statistics, equation (1) was obtained that describes the change in the mass of coal when it is thawed, depending on the moisture content in it, the average diameter of its particles, and the time it spent in the defrosting garage.

$$\Delta m = 1{,}161723 - 0{,}00033\tau - 0{,}007677W_t^r - 0{,}01529d_{me} \quad (1)$$

Figure 2 shows the graphical dependence of the calculated (by equation 1) and the actual values of the mass loss of coal in the process it's defrosting.

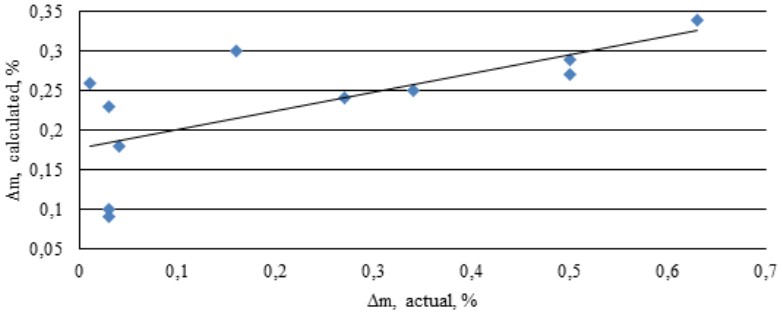

Fig. 2. Graphic dependence of the calculated and actual values of change in the mass of coal in the process of defrosting

Equation (1) makes it possible to estimate the decrease in the mass of coal in the process of defrosting, depending on the indicators of its quality and the conditions in the defrosting garage. In general, it can be noted that an increase in the initial moisture content, the average diameter of the coal particles and the residence time in the defrosting garage leads to an increase in the loss of the actual mass of the coal concentrates when they are thawed.

3. Conclusions

Based on the laboratory and pilot studies, the following main conclusions can be formulated:

1. The freezing of particles begins when the content of moisture in them exceeds the value of the maximum capacity. In turn, the magnitude of the maximum capacity depends on the

degree of metamorphism and in the rank of coking coal has the maximum values for the low-metamorphosed coal of the gas group.

Taking into account the fact that low-metamorphosed coals of the gas group are characterized by the maximum values of water capacity, these coals may be less time in the defrosting garage compared to other coking coals.

2. With decreasing temperature, the degree of coal freezing increases with increasing humidity and decreasing particle size.

3. Using mathematical statistics, an equation was obtained describing the change in the mass of coal when it is thawed, depending on the moisture content in it, the average diameter of its particles and the time it takes to defrost the garage. This equation makes it possible to estimate the reduction in the mass of coal in the process of defrosting, depending on its quality indicators and the conditions in the defrosting garage.

Symbols

W^r_t	*water content in coal, as received state, %;*
A^d	*ash content of coal in the dry state, %;*
V^{daf}	*volatile matter in the dry ash-free state, %;*
$S_t{}^d$	*sulphur of coal in the dry state, %;*
R_0	*mean vitrinite reflection coefficient, %;*
Vt	*vitrinite, %;*
Sv	*semivitrinite, %;*
I	*inertinite, %;*
L	*liptinite, %;*
$\sum FC$	*sum of fusinized components, %;*
y	*thickness of the plastic layer, mm;*
C^{daf}, H^{daf}, N^{daf}, Od^{daf}	*carbon, hydrogen, nitrogen, oxygen in the dry, ash-free state, %;*
W_{max}	*maximum moisture-holding moisture capacity, %;*
d_{me}	*mean particle diameter, mm;*
Δt	*oxidation index, °C;*
τ	*the residence time of coal in the defrosting garage, min.*

References

[1] Matasov SF, Kurtunov LM, and Khorunzhii AS. Bor'ba so smerzaemost'yu pri perevozke po zheleznym dorogam (Prevention of freezing in railroad transportation), Moscow: Metallurgiya, 1974.

[2] Eremin IV, Lebedev VV, and Tsikarov DA. Petrografiya i fizicheskie svoistva uglei (Petrography and physical properties of coal), Moscow: Nedra, 1980. 263 p.

[3] Kormer MV, Lyalyuk VP, Uchitel AD, Shmeltser EO, Lyakhova IA. Dependens of coals freezing point on its granulometric composition. Coke and Chemistry, 2015; 58(1): 9–14.

[4] Starovoit A, Chemerinskii M, Malyi E. Mechanisms of gas-coal thermal preparation in electromagnetic field. Chemistry and Chemical Technology, 2014; 8(4): 475–478.

[5] Brodsky EV, Babitsin SM, Fedorov AP. Improving the efficiency of convective defrost garages. Koks I Khimiya, 1990; 3: 4–6.

[6] Zashkvara VG, Vvozny GF, Baydalinov PA. Coal and Chemistry, Foulness and Unloading of Coals, 1966; 1: 1–3.

[7] Balaeva YS, Kaftan YS, Miroshnichenko DV, Kotlyarov EI. Influence of coal properties on the gross calorific value and maximum moisture content. Coke and Chemistry, 2018; 61(1): 4–11.

[8] Balaeva YS, Miroshnichenko DV, Kaftan YS. Moisture-holding capacity of coals. Solid Fuel Chemistry, 2017; 51(6): 337–348.

[9] Balaeva YS, Miroshnichenko DV, Kaftan YS. Moisture-holding capacity of coal. Pet coal. 2017; 59(3): 302–310.

[10] Balaeva YS, Miroshichenko DV, Kaftan YS, Shmalko VM. Relation between the maximum moisture content of coal and its porous structure. Coke and Chemistry, 2016; 59(11): 407–410.
[11] Balaeva YS, Miroshnichenko DV, Kaftan YS. Predicting the classification charac-teristics of coal. Part 2. Maximum moisture content. Coke and Chemistry, 2015; 58(12): 459–464.

To whom correspondence should be addressed: Dr. E. O. Shmeltser, Kryvyi Rig Metallurgical Institute, Ukraine National Metallurgical Academy, 50006, Kryvyi Rig, Ukraine

Petroleum and Coal

Article **Open Access**

MULTI-SCALE METHOD FOR MODELING AND SIMULATION OF TWO PHASE FLOW IN RESERVOIR USING MRST

M. Aslam Abdullah[1], Abhishek Panda[1], Shivam Gupta[1], Saurabh Joshi[1], Aruna Singh[1], Nagamalleswara Rao[1]*

[1] Department of Chemical Engineering, VIT University, Vellore, India
[2] Centre for Disaster Management and Mitigation, VIT University, Vellore, India

Received February 12, 2019; Accepted May 13, 2019

Abstract

The multi-scale method which is being used is generally used for solving coupled equations, and this method is widely used for reservoir simulation. The coupling factors which needs to be solved are the pressure equation and the transport equation .Both the equations are going to be solved as a decoupled system, while the pressure equation will be solved in a coarser grid and the transport equation will be solved in a finer grid. There are several multi-scale methods which can be used for reservoir simulation, but the multi-scale mixed finite element (MsMFE) method is the one which grabs all the sub grid topographical diverseness into the coarse scale using mathematical basis functions. A global formulation can be used to couple the important multi-scale information which will be grabbed by the basis functions thereby providing good resemblance to the solution for the subsurface flow.According to the literature the most commonly used formulation which is being used for the multi-scale mixed finite element method (MsMFE) for incompressible two phase flow mainly deals with common flow physics. In this paper, the formulation which is being used takes into considerations the gravity, compressibility, spatially dependent capillary and relative permeability effects. Our main aim is to find out the efficiency of this formulation and the Multi-scale mixed finite element method (MsMFE) by comparing our results with the results obtained from two different reservoirs in India. We have used MRST (MATLAB Reservoir Simulation Toolbox) for the simulation of the reservoir. Our results will include pressure distribution, Flux distribution and the saturation fields throughout the reservoir.

Keywords: *MRST; MSMFE; Modeling; Simulation; Reservior.*

1. Introduction

During reservoir rock formation, there are many physical processes which occur on multiple time and length scales. These processes affect the movement of hydrocarbons in the subsurface rock formation. There is a lot of information that can be extracted from these different scales, i.e. time and length scales varying from micrometer scale to kilometer scale to be integrated to build multi-million cells incorporated high-resolution models. These models describing the non-homogeneous reservoir properties in proper structure can be built using contemporary reservoir characterization and geostatistical modeling techniques. It is preferred to use a coarser model with the reduced data to derive discrete flow equations rather than using highly detailed geo-cellular models to solve multi-phase flow equations as the later involves a very high computational cost. This upscaling process affects the simulation because prominent fine scale properties are lost as well as it takes a lot of time to get finished.

To simulate reservoirs having multiple scales, using the upscaling method is very cumbersome, so the need for upscaling had to be reduced. Efendiv and Hou proposed multiscale method [12] in 2009 which were designed to get definite and adequate results. This method offers an effective scheme such that the global flow equations are assimilated with effects from irresolute scale and underlying differential operators are also consistent. With this

method, there was no need of computing effective coarse-scale properties, and it also promised the advantage of capturing fine scale petrophysical and geological details directly into the coarse scale simulation model.

There are several multi-scale methods applicable to reservoir simulation, and the literature contains some of it namely Dual-grid methods [6-8,14], (adaptive) local- global methods [10-11], finite-element methods [17], mixed finite-element methods [1-5,9] and finite volume multi-scale methods [15-18,30].All these methods include the basic idea of integrating fine scale into coarse scale equations. Local flow problems are solved to estimate local flow effects of petro-physical properties in fine scale and served as a fine scale sub-resolution multiscale basis function. Local or global information or a combination of both could be used as boundary conditions to localize each basis function. A reduced set of degrees-of-freedom which is affiliated with a coarser grid is computed using the global flow problems represented in terms of multi scale basis function. Flow equations can be upscaled very accurately using this technique. Alternately, pressure and mass conservative flux field can be constructed using the basis functions which is then solved using a transport solver formulated on some intermediate grid.

Upscaling method and multiscale method are very different from each other despite their few similarities. Coarse scale solutions are generated using the upscaling method whereas the main intent of the multiscale method is to obtain efficient and proper approximations on the fine or intermediate scale [13]. Many upscaling techniques use the non-physical coarse scale properties which are avoided by the multiscale method during the natural coupling between local and global scales.

Our main aim is to find out the efficiency of the formulation used in the method and the Multi-scale mixed finite element method (MsMFE) by comparing our results with the results obtained from two different reservoirs in India. We are going to use MRST (MATLAB Reservoir Simulation Toolbox) for the simulation of the reservoir. Our results will include pressure distribution, Flux distribution and the saturation fields throughout the reservoir.

2. Mathematical modeling

The coupled system of the equation that is the elliptical pressure equation and the parabolic transport equation is used for the modeling of two-phase flow in the reservoir. The transport equation which is to be used for modeling is derived from two basic equations which describe fluid flow in the reservoir [1-2,30-31]. The two basic equations are the continuity equation and Darcy's law. The continuity equation is a mathematical representation of the law of conservation of mass whereas the Darcy's law is being used to derive a relation between the pressure and the velocity for flow in a reservoir which is a porous material.

$$\nabla . v = q \qquad \vec{v} = -K\lambda[\nabla p_o - \tilde{g}(S_w)\nabla z + h(S_w)\nabla p_c] \tag{1}$$

$$\phi \partial S_w/\partial t + \nabla . f_w(S_w)[v + K\lambda_o(S_w)\left((\rho_w - \rho_o)g\nabla z + \nabla pc((S_w))\right] = \frac{q_w}{\rho_w} \tag{2}$$

The parameters which are being used in the above-mentioned equations are as follows: S_w represents the saturation of water in the porous reservoir; S_o represents the saturation of oil in the porous reservoir, $S_w+S_o=1$. Hence, we can say that $S_w, S_o \leq 1$. f_w represents fractional flow function of water and f_o represents fractional flow function of oil where $f_{wfff}=\lambda_w/\lambda$. λ_w represents phase mobility of water and λ_o represents phase mobility of oil and λ represents the total mobility. $\lambda = \lambda_w + \lambda_o$. u_w represents the velocity of water whereas u_o represents the velocity of oil and $u = u_w + u_o$ where u is the total velocity. ϕ represents the porosityand K is the permeability tensor. ρ_w represents the density of water and ρ_o represents the density of oil. g is the acceleration due to gravity. P_w is the pressure of water and p_o is the pressure exerted by oil. p_c is the capillary pressure, $p_c=p_o-p_w$ .q is the source/sink term in the above equation $\tilde{g}(S_w) = (f_w(S_w)\rho_w + f_o(S_w)\rho_o)g$ and $h(S_w) = f_w(S_w)$.

3. Discretization (finite scale)

Discretization of the computational domain Ω leads to a set of $\{C_i\}$ of N non overlapping and matching polyhedral cells. There will be a sequential solving of flow and transport equation. First flow equation will be solved to get explicit fluxes at the cell interfaces which is used

to evolve the saturations in time step Δt using the transport equation. Following unknowns will be used in the paper: vector of outward fluxes from the cell C_i is denoted by u_i, the pressure at the cell center is denoted by p_i, and the pressure at the cell faces is denoted by π_i. To relate the three quantities, we will use the Darcy's law through a matrix T_i of one-sided transmissibilities.

$$ui = T_i[e_i p_i - \pi_i - \tilde{g}(S_i)\Delta z_i + h(S_i)(e_i p_c(\vec{x_i}, S_i) - p_{ci})],\ e_i = (1, \ldots\ldots 1)^T \quad (3)$$

The vector of differences in the z coordinate of the cell center $\vec{xi}$ and and the face centroids is denoted by Δz_i and the capillary pressure p_{ci} at the cell faces is defined as the linear interpolation of the capillary pressure in the neighboring cells. On the other hand, one can utilize multipoint techniques to characterize transmissibilities on organized and unstructured lattices utilizing multi-point fluxes, see e.g., [26-27,29,31].

The following discrete linear system for global flow problem can be derived by augmenting eq. 3 with pressure and flux continuity across cell faces.

$$\begin{bmatrix} \boldsymbol{B} & C & D \\ C^T & 0 & 0 \\ D^T & 0 & 0 \end{bmatrix} \begin{bmatrix} u \\ -p \\ \pi \end{bmatrix} = \begin{bmatrix} -G(S)\Delta z + H(S)\Delta p_c \\ q \\ 0 \end{bmatrix} \quad (4)$$

Here, Cell wise ordered outward face fluxes is denoted by u, the pressure at the cell center and pressure at the cell faces is denoted by p and π respectively.

The first row within the block matrix equation corresponds to eq. 3 for all grid cells and the right-hand terms $G(S)\Delta z$ and $H(S)\Delta p_c$ are the one-sided face contributions similar to gravity and capillary effects. The matrix B represents block diagonal with single block T_i^{-1} defined per cell. The matrix C is additionally block diagonal and has one block entry e_i per cell that duplicates the cell pressures to one value for every cell face. Hence, within the second row of eq. 4, the converse matrix C^T sums the face fluxes to outline one mass-conservation equation per cell. Finally, every column of D corresponds to a singular face and has one (for boundary faces) or two (for interior faces) unit entries resembling the index of the face within the cell wise ordering. In the following, the transport equation, eq. 2 is solved on the fine-scale employing a normal transport problem solver with upstream- weighted mobilities and two-point discretization of the second-order capillary term. The temporal discretization could also be explicit or implicit. If needed, improved numerical accuracy can be obtained by exploiting higher-order upwind schemes, just like the wave-oriented multi-dimensional schemes Lamine and Edwards [20-21].

4. Multi-scale mixed finite elements

The main concept behind using multiscale mixed finite-element method is to build a special approximation space consisting of a set of coarse-scale basic functions that meet the local flow equation. Therefore, the MsMFE method is formulated on the basis of two hierarchically nested grids. Rock and rock fluid properties are displayed on the geo-cellular fine-scale grid, while the basic functions and corresponding degrees of freedom are associated with a coarse simulation grid used to solve the problem of global flow. The coarse grid blocks are defined as a connected set of fine grid cells and can have arbitrary shapes in principle. However, if the blocks are somewhat regular, the best numerical resolution is obtained, following the layered structures of stratigraphic grids [2] or adapting to high-contrast characteristics [24].

4.1. Approximations for multiscale method

We begin by writing the solution to Eq 4 to formally define the MsMFE method as the sum of the basic functions and a residual on a fine scale.

$$u = \psi u_c + \tilde{u} \quad , \quad p = \phi p_c + \tilde{p}, \quad \pi = \Pi \pi_c + \tilde{\pi} \quad (5)$$

Here, the vector of outward fluxes over the coarse-block interfaces is denoted by u_c; p_c denotes the coarse-block pressure vector, and π denotes the coarse-block face pressure vector. Similarly $\tilde{u}$, $\tilde{p}$ and $\tilde{\pi}$ represent the reminder which have variations on the fine grid. The fine scale reconstruction operators for $\vec{v}$, p and π is denoted by the matrices Ψ, Φ, and π. Each

column in Ψ corresponds to a multi-scale base function for the flux associated with a unique coarse-grid face and is represented as a fine-scale flux vector of n_f x 1.

For incompressible flow, the pressure is rarely explicitly used, with the exception of determining well rates by using appropriate good models. Therefore, we define the pressure within each coarse block to be constant and replace Φ with a simple extension operator I, which maps the block cells with a constant value from each coarse block. Similarly, an extension operator J replaces ∏, which maps a constant value from each coarse face to the individual cell faces of the coarse face. A reconstruction operator R= diag(ψ , I, J) is thus defined which makes it possible to map the degrees of freedom x_c=[u_c,-p_c, π_c] on the coarse scale to the corresponding fine scale quantities x= [u,-p, π].

In case of coarse system In order to create a global system on the coarse grid, we need a compression operator to bring the Eq 4 which is a fine scale system to the space covered by our multi-scale functions. R^T is a natural choice here since the transposed operators I and J correspond to the sum of all fine cells of a coarse block and all fine cell faces, which are part of the faces of the coarse blocks. Multiply eq. 4 from the left with R^T, substitute x=Rx_c and rearrange the terms to get

$$\begin{bmatrix} \psi^T B\psi & \psi^T CI & \psi^T DJ \\ I^T C^T \psi & 0 & 0 \\ J^T D^T \psi & 0 & 0 \end{bmatrix} \begin{bmatrix} u_c \\ -p_c \\ \pi_c \end{bmatrix} = \begin{bmatrix} \psi^T (H(S)\Delta p_c - G(S)\Delta z) - \psi^T (B\tilde{u} - C\tilde{p} + D\tilde{\pi}) \\ I^T q - I^T C^T \tilde{u} \\ -J^T D^T \tilde{\pi} \end{bmatrix} \quad (6)$$

The terms of the fine- scale reminder can be eliminated as follows: If we interpret the coarse- scale pressure as the w- weighted average of the real pressure, $p_c^i = \int_{Bi} wpd\vec{x}$ (where w is the source term used to define basis function) then $\tilde{p}$ disappears. The following coarse-scale system is obtained after neglecting the terms $\tilde{u}$ and $\tilde{\pi}$.

4.2. Methods to find Multiscale basis function

$$\begin{bmatrix} \psi^T B\psi & \psi^T CI & \psi^T DJ \\ I^T C^T \psi & 0 & 0 \\ J^T D^T \psi & 0 & 0 \end{bmatrix} \begin{bmatrix} u_c \\ -p_c \\ \pi_c \end{bmatrix} = \begin{bmatrix} \psi^T (H(S)\Delta p_c - G(S)\Delta z) \\ I^T q \\ 0 \end{bmatrix} \quad (7)$$

There are two different ways of calculating basic functions: In the single-block method, fine-scale fluxes must be specified over the coarse interface associated with the basis function. The method is not very accurate unless some kind of global flow information is included in the interface flux. Therefore, we will use a two-block method which does not impose any condition on the interface between two coarse blocks. The resulting method is not convergent, but usually gives reasonable precision on finite grids. In order to define the method, we consider two blocks of B_i and B_j, which share the common coarse face $\Gamma_{ij}=\partial B_i \cap \partial B_j$ and let B_{ij} be a sub-set of Ω containing B_i and B_j. The two- block multiscale base function is defined after neglecting the influence of gravity and capillary forces as:

$$\psi_{ij} = -K\nabla\phi_{ij}, \qquad \nabla.\psi_{ij} = w_{ij}(\overrightarrow{x}) = \begin{cases} w_i(\overrightarrow{x}), & if\ \vec{x} \in B_i, \\ -w_j(\overrightarrow{x}), & if\ \vec{x} \in B_j, \\ 0, & otherwise, \end{cases} \quad (8)$$

If we consider capillary forces, then the following basis function must be added to the already formed set,

$$\psi^c{}_{ij} = -K\left(\nabla\phi^c{}_{ij} - h(S)\nabla p_c(S)\right), \qquad \nabla.\psi^c{}_{ij} = 0 \quad (9)$$

5. Codes and results

Creating a grid. Here we have created a 200-200-50 rectangular reservoir in 10-10-10 Cartesian grid (Figure 1).

```
[nx, ny, nz] = deal( 10,  10, 10);
[Dx, Dy, Dz] = deal(200, 200, 50);
G = cartGrid([nx, ny, nz], [Dx, Dy, Dz]);
```

```
G = computeGeometry(G);

plotGrid(G), view(3), axis tight
```

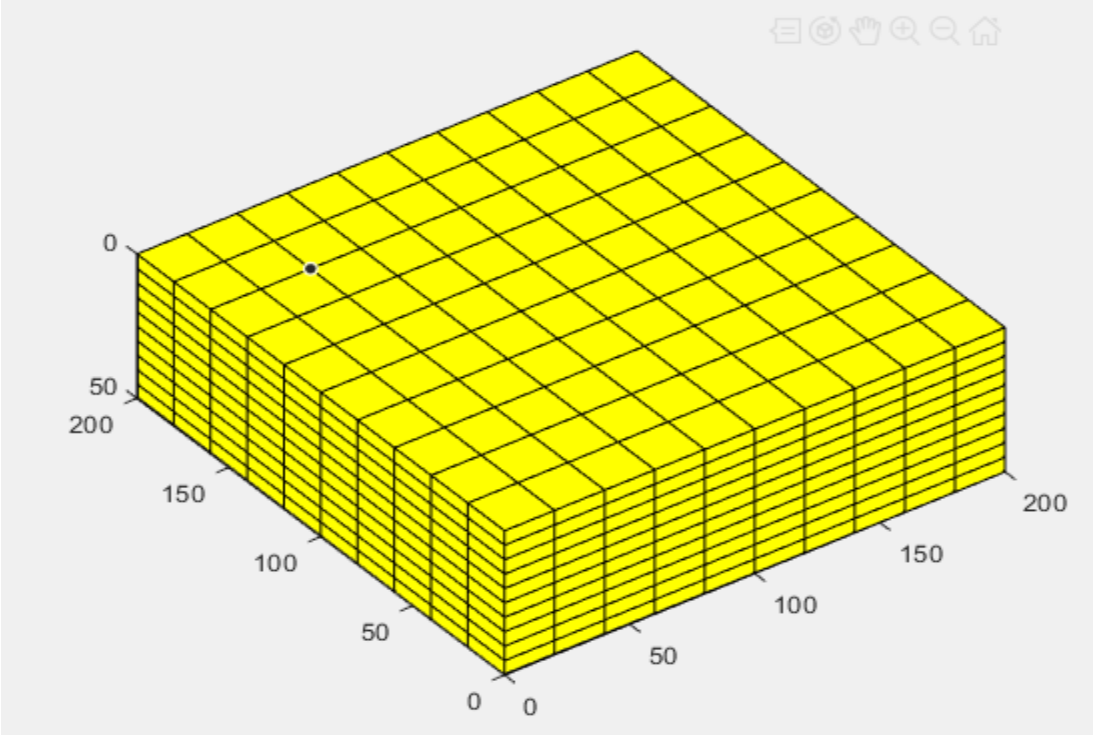

Figure 1. 200-200-50 rectangular reservoir in 10-10-10 Cartesian grid

We assume a 'Horizontal' well which is drilled into 6 grids of reservoir. The theoretical representation of the reservoir is mentioned. (Figure 2)

```
nperf = 6;
I = repmat(2, [nperf, 1]);
J = (1 : nperf).' + 1;
K = repmat(5, [nperf, 1]);

cellInx = sub2ind(G.cartDims, I, J, K);
W = addWell([], G, rock, cellInx, 'Name', 'P1', 'Dir', 'y' );
gravity reset on, g = norm(gravity);
[z_0, z_max] = deal(0, max(G.cells.centroids(:,3)));
equil  = ode23(@(z,p) g .* rho(p), [z_0, z_max], p_r);
p_init = reshape(deval(equil, G.cells.centroids(:,3)), [], 1);  clear equil
clf
show = true([G.cells.num, 1]);
cellInx = sub2ind(G.cartDims, ...
   [I-1; I-1; I; I;   I(1:2) - 1], ...
   [J  ; J;   J; J;   nperf  + [2 ; 2]], ...
   [K-1; K;   K; K-1; K(1:2) - [0 ; 1]]);

show(cellInx) = false;

plotCellData(G, convertTo(p_init, barsa), show, 'EdgeColor', 'k')
plotWell(G, W, 'height', 10)
view(-125, 20), camproj perspective
```

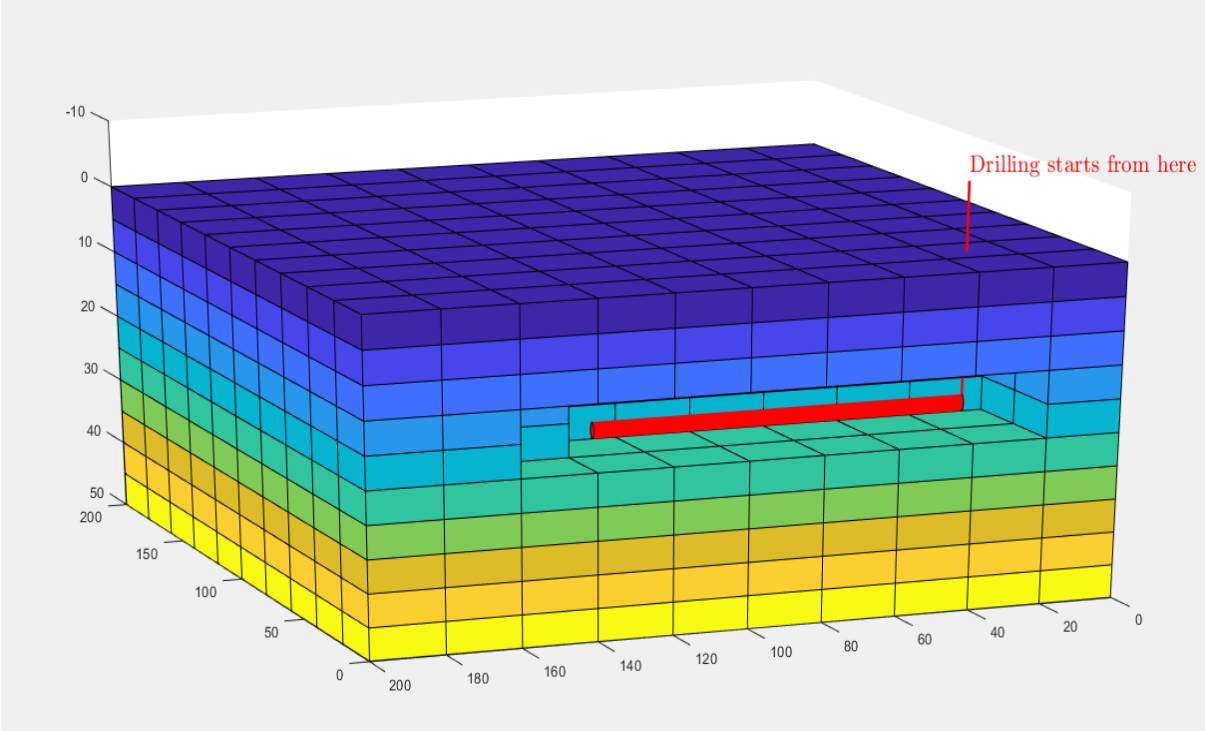

Figure 2. Theoretical representation of model of Reservoir having 'Horizontal Well'

Constructing in a Cartesian grid with assuming 200 mD permeability and 1 viscosity and 1000 density (Figure 3).

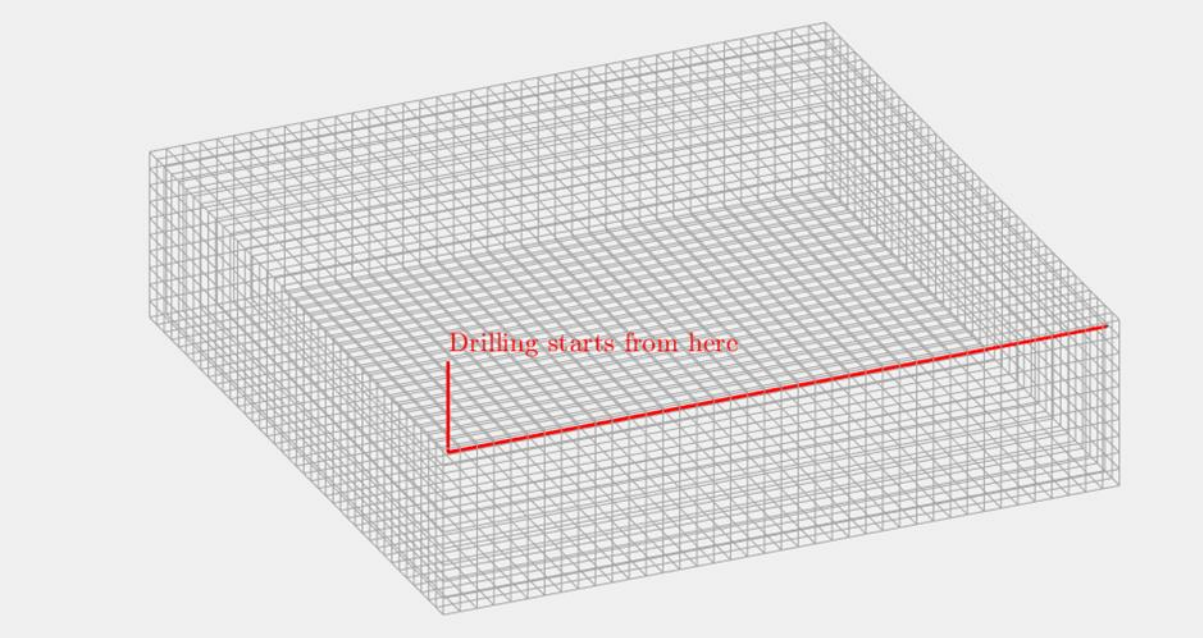

Figure 3. Cartesian grid with assuming 200 mD permeability and 1 viscosity and 1000 density

Plotting the pressure distribution at our reservoir (Figure 4). Assuming 200 bar or 2900 psi at top of reservoir.

```
[nx, ny, nz] = deal( 10,  10, 10);
[Dx, Dy, Dz] = deal(200, 200, 50);
```

```
gravity reset on
G = cartGrid([nx, ny, nz], [Dx, Dy, Dz]);
G          = computeGeometry(G);
rock.perm  = repmat(0.2*darcy(), [G.cells.num, 1]);
fluid = initSimpleFluid('mu' , [   1,  10]*centi*poise     , ...
                            'rho', [1014, 859]*kilogram/meter^3, ...
                            'n'  , [   2,   2]);bc          = pside([], G,
'TOP', 100.*barsa);
S   = computeMimeticIP(G, rock);
sol = incompMimetic(initResSol(G , 0.0), G, S, fluid, 'bc', bc);
newplot;
subplot(8, 1, [1 3])
   plotCellData(G, convertTo(sol.pressure(1:G.cells.num), barsa), ...
                'EdgeColor', 'k');
   set(gca, 'ZDir', 'reverse'), title('Pressure Distribution')
   view(45,5), cx = caxis; colorbar
```

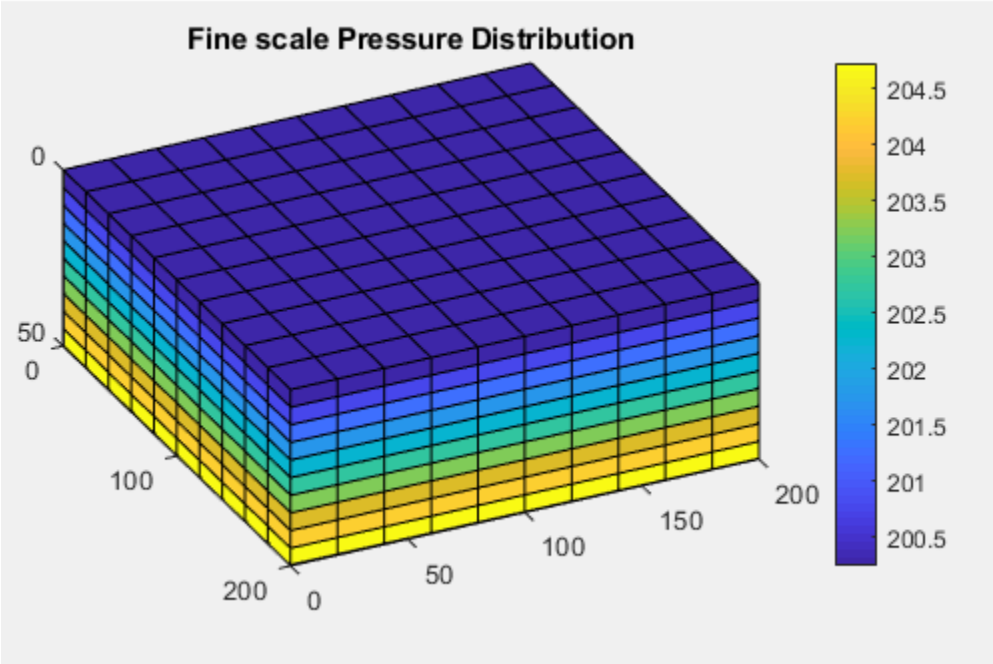

Figure 4. Fine scale pressure distribution

For the multiscale system, plotting the coarse scale solution (Figure 5).

Multiscale only captures coarse-scale gravity effects. To get fine scale result, we are adding finescale equation which we did earlier to solution of multiscale effect, which gives us following result –

```
p  = partitionUI(G, [Nx, Ny, Nz]);
p  = processPartition  (G, p);
CG = generateCoarseGrid(G, p);

CS = generateCoarseSystem(G, rock, S, CG, ones([G.cells.num, 1]),'bc', bc);
xrMs = solveIncompFlowMS (initResSol(G, 0.0), G, CG, p, ...
                          S, CS, fluid, 'bc', bc);
subplot(8, 1, [1 3])
   plotCellData(G, convertTo(xrMs.pressure(1:G.cells.num), barsa), ...
                'EdgeColor', 'k');
   set(gca, 'ZDir', 'reverse'); title('Coarse scale Pressure Distribution')
```

```
    view(45,5); caxis(cx); colorbar

subplot(3, 2, [5 6]);
   plot(1:nz, convertTo(sol .pressure(1:nx*ny:nx*ny*nz), barsa()), '-o',...
        1:nz, convertTo(xrMs.pressure(1:nx*ny:nx*ny*nz), barsa()), '-*');
   legend('fine','coarse','Location','NorthWest');
```

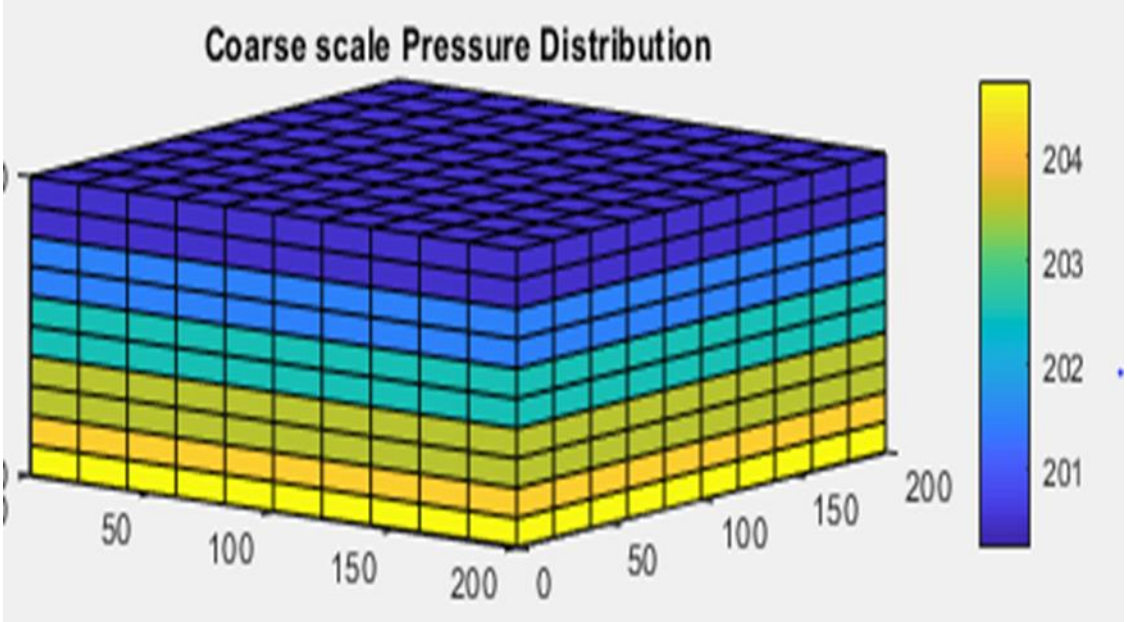

Figure 5. Coarse scale pressure distribution

Now if we compare both, we get the following result. We get the following pressure distribution per grid (Figure 6)

```
subplot(8, 1, [1 3]);
   plot(1:nz, convertTo(sol .pressure(1:nx*ny:nx*ny*nz), barsa()), '-o',...
        1:nz, convertTo(xrMs.pressure(1:nx*ny:nx*ny*nz), barsa()), '-*');
   legend('fine','coarse','Location','NorthWest');
```

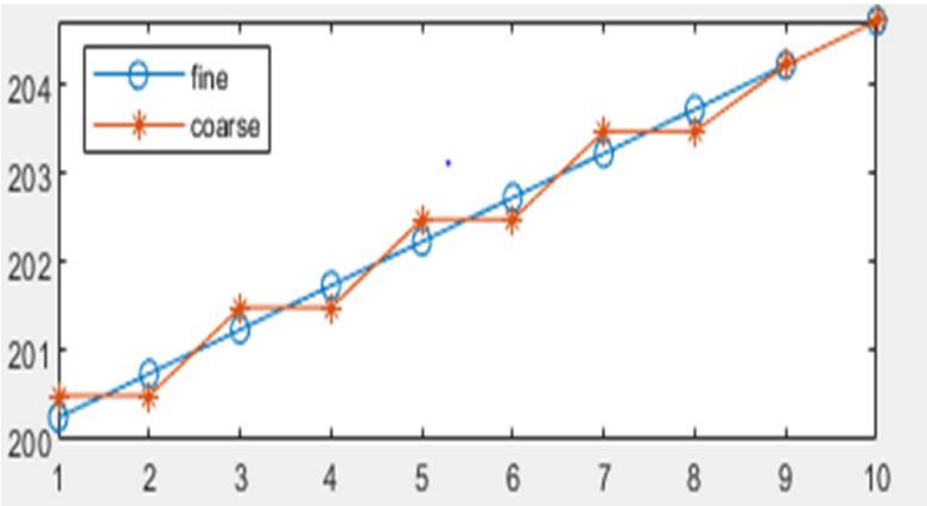

Figure 6. Pressure distribution grid

Now we are checking Permeability distribution over reservoir (Figure 7). We use boundary condition of flux of 1 on the LHS and Dirichlet boundary conditions p = 0 on RHS of grid.

```
verbose = true;
[nx, ny, nz] = deal( 10,  10, 10);
[Dx, Dy, Dz] = deal(200, 200, 50);
G = cartGrid([nx, ny, nz], [Dx, Dy, Dz]);
G = computeGeometry(G);
K         = logNormLayers([nx, ny, nz], 1); K = 10 * K / mean(K(:));
rock.perm = bsxfun(@times, [10, 1, 0.1], convertFrom(K, milli*darcy()));
fluid = initSimpleFluid('mu' , [   1,  10]*centi*poise     , ...
                        'rho', [1014, 859]*kilogram/meter^3, ...
                        'n'  , [   2,   2]);
gravity off
bc = fluxside([], G, 'LEFT',  100*meter()^3/day());
bc = pside   (bc, G, 'RIGHT', 0);
newplot
plotCellData(G,log10(convertTo(rock.perm(:,1),milli*darcy))); shading faceted;
title('Permeability Distribution');
view(3), camproj perspective, axis tight off
cs = [50 100:100:1000];
h=colorbar;
```

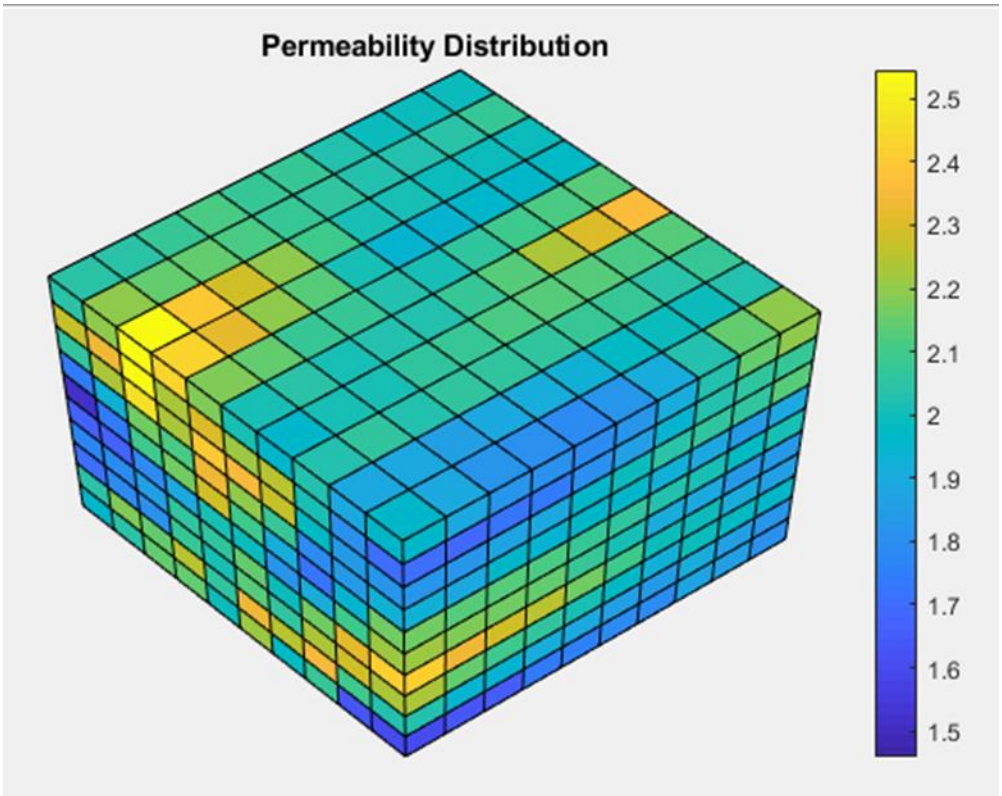

Figure 7. Permeability distribution

Then we find flux intensity distribution (Figure 8)

```
p  = partitionUI(G, [Nx, Ny, Nz]);
p  = processPartition(G, p);
```

```
CG    =    generateCoarseGrid(G,    p,    'Verbose',    verbose);display(CG);
disp(CG.cells); disp(CG.faces);
S  = computeMimeticIP(G, rock, 'Verbose', verbose);
display(S);
CS = generateCoarseSystem(G, rock, S, CG, ones([G.cells.num, 1]), ...
                          'Verbose', verbose, 'bc', bc);


newplot;
subplot(1,2,1),
cellNo  = rldecode(1:G.cells.num, diff(G.cells.facePos), 2) .';
C       = sparse(1:numel(cellNo), cellNo, 1);
D       = sparse(1:numel(cellNo), double(G.cells.faces(:,1)), 1, ...
                 numel(cellNo), G.faces.num);


   spy([S.BI                  , C        , D        ; ...
        C', zeros(size(C,2), size(C,2) + size(D,2)); ...
        D', zeros(size(D,2), size(C,2) + size(D,2))]);

   xRef = incompMimetic    (initResSol(G, 0.0),  G, S, fluid, ...
                          'bc', bc, 'MatrixOutput',true);
xMs  = solveIncompFlowMS(initResSol(G, 0.0), G, CG, p, S, CS, fluid, ...
                          'bc', bc, 'MatrixOutput', true, 'Solver', 'hybrid');
 clf
plot_var  = @(x) plotCellData(G, x);
plot_pres = @(x) plot_var(convertTo(x.pressure(1:G.cells.num), barsa()));
plot_flux = @(x) plot_var(accumarray(cellNo, ...
   abs(convertTo(faceFlux2cellFlux(G, x.flux), meter^3/day))));
subplot('Position',[0.02 0.02 0.46 0.42]),
   plot_flux(xRef); title('Flux intensity Distribution')
   view(3), camproj perspective, axis tight equal, camlight headlight
   cax2 = caxis; colorbar
```

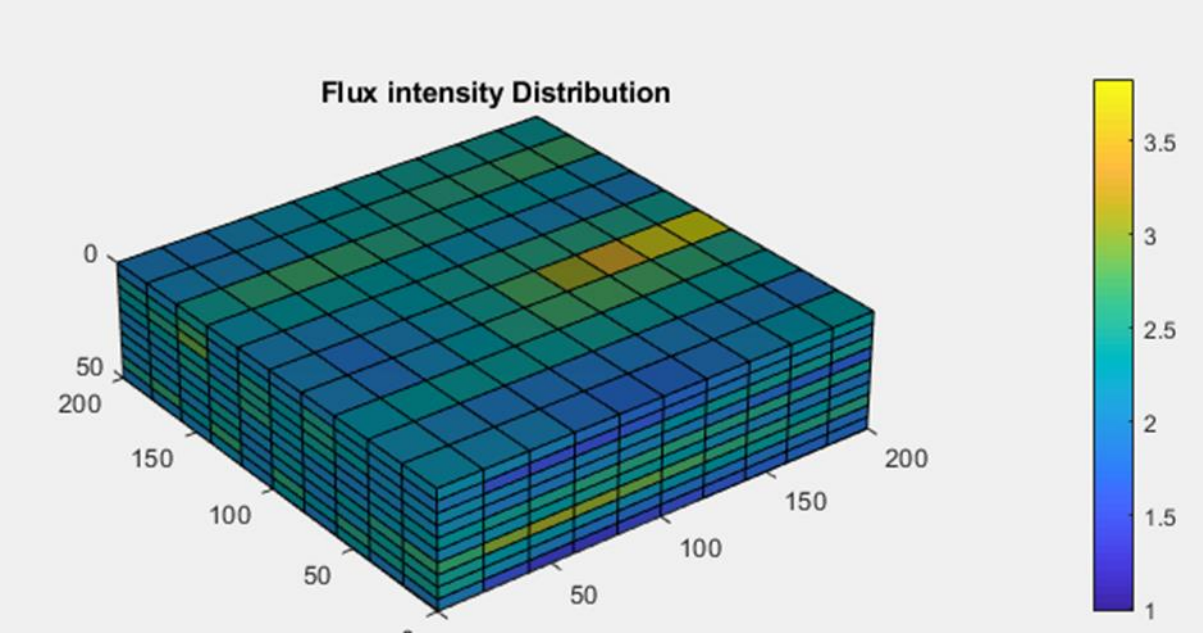

Figure 8. Flux intensity distribution

Now after trying our Simulation on 'Cartesian grid', we simulated our reservoir on 'Corner-point grid' aswell, for experimental purposes (Figure 9).

We have used same values for all properties like we did on Cartesian grid. For boundary condition: we used Dirchlet condition for 1 bar pressure on LHS and 0 bar at RHS.

```
nx = 10; ny = 10; nz = 10;
Nx = 200; Ny = 200; Nz = 50;
verbose = true;
grdecl  = simpleGrdecl([nx, ny, nz], 0.15);
G       = processGRDECL(grdecl); clear grdecl;
G       = computeGeometry(G);
[rock.perm, L] = logNormLayers([nx, ny, nz], [100, 400, 50, 500]);
fluid = initSimpleFluid('mu' , [   1,  10]*centi*poise     , ...
                        'rho', [1014, 859]*kilogram/meter^3, ...
                        'n'  , [   2,   2]);
rock.perm      = convertFrom(rock.perm, milli*darcy);
westFaces = find(G.faces.centroids(:,1) == 0);
bc        = addBC([], westFaces, 'pressure',        ...
                  repmat(1*barsa(), [numel(westFaces), 1]));

xMax      = max(G.faces.centroids(:,1));
eastFaces = find(G.faces.centroids(:,1) == xMax);
bc        = addBC(bc, eastFaces, 'pressure',        ...
                  repmat(0, [numel(eastFaces), 1]));
clf
   plotCellData(G, log10(rock.perm(:))); shading faceted
   title('Reservoir using Corner-point grid')
   view(3), camproj perspective, axis tight off, camlight headlight

   set(h, 'YTick', c, 'YTickLabel', num2str(10.^c'));
```

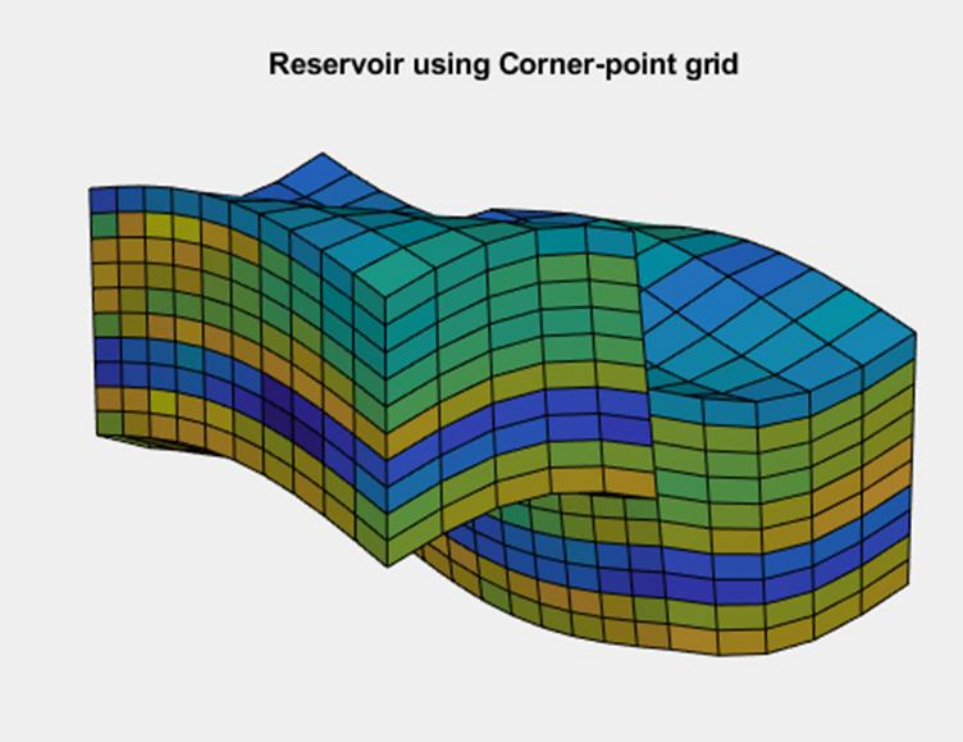

Figure 9. Reservoir using Corner-point grid

After this, we have also plotted our reservoir using Multiscale Finite Volume method with experimental data (Figure 10).

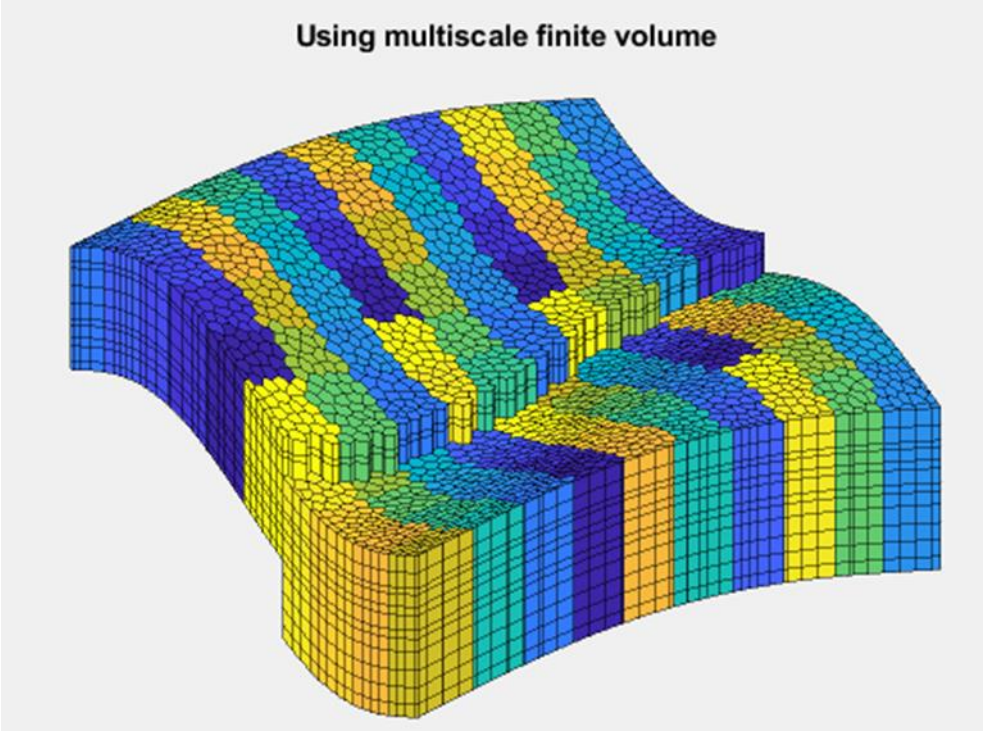

Figure 10. Reservoir using Multiscale Finite Volume

6. Conclusion

In this paper, we have modified multi scale mixed finite element method (MsFEM) for incompressible flow including two phases. We have also implemented the same for simulation of two-phase flow in a porous reservoir and we have compared our results with the results obtained from highly reputed companies from India.

References

[1] Aarnes JE. On the use of a mixed multiscale finite element method for greater flexibility and increased speed or improved accuracy in reservoir simulation. Multiscale Modeling & Simulation, 2004; 2(3):421-39.

[2] Aarnes JE, Efendiev Y. A multiscale method for modeling transport in porous media on unstructured corner-point grids. Journal of Algorithms & Computational Technology, 2008 Jun; 2(2):299-318.

[3] Aarnes JE, Krogstad S, Lie KA. Multiscale mixed/mimetic methods on corner-point grids. Computational Geosciences, 2008 Sep 1; 12(3):297-315.

[4] AGMG 2012. Iterative solution with AGgregation-based algebraic MultiGrid. http://homepages.ulb.ac.be/~ynotay/AGMG/.

[5] Alpak FO, Pal M, Lie KA. A multiscale adaptive local-global method for modeling flow in stratigraphically complex reservoirs. SPE Journal, 2012; 17(04):1-056.

[6] Arbogast T. Implementation of a locally conservative numerical subgrid upscaling scheme for two-phase Darcy flow. Computational Geosciences, 2002;6(3-4):453-81

[7] Arbogast T, Bryant SL. A Two-Scale Numerical Subgrid Technique for Waterflood Simulations. SPEJ, 7(4): 446-457. SPE-81909-PA; 2002.

[8] Audigane P, Blunt MJ. Dual mesh method for upscaling in waterflood simulation. Transport in Porous Media, 2004; 55(1):71-89.

[9] Chen Z, Hou T. A mixed multiscale finite element method for elliptic problems with oscillating coefficients. Mathematics of Computation, 2003; 72(242):541-76.

[10] Chen Y, Durlofsky LJ. Adaptive local–global upscaling for general flow scenarios in heterogeneous formations. Transport in porous Media, 2006; 62(2):157-85.
[11] Chen Y, Durlofsky LJ, Gerritsen M, Wen XH. A coupled local–global upscaling approach for simulating flow in highly heterogeneous formations. Advances in Water Resources, 2003; 26(10):1041-60.
[12] Efendiev Y, Hou TY. Multiscale finite element methods: theory and applications. Springer Science & Business Media; 2009 Jan 10.
[13] Farmer CL. Upscaling: a review. International journal for numerical methods in fluids, 2002; 40(1-2):63-78.
[14] Guérillot DR, Verdiere S. Different pressure grids for reservoir simulation in heterogeneous reservoirs. InSPE Reservoir Simulation Symposium 1995 Jan 1. Society of Petroleum Engineers.
[15] Hajibeygi H, Jenny P. Multiscale finite-volume method for parabolic problems arising from compressible multiphase flow in porous media. Journal of Computational Physics, 2009; 228(14):5129-47.
[16] Hajibeygi H, Jenny P. Adaptive iterative multiscale finite volume method. Journal of Computational Physics, 2011; 230(3):628-43.
[17] Hou TY, Wu XH. A multiscale finite element method for elliptic problems in composite materials and porous media. Journal of computational physics, 1997; 134(1):169-89.
[18] Jenny P, Lee SH, Tchelepi HA. Multi-scale finite-volume method for elliptic problems in subsurface flow simulation. Journal of Computational Physics, 2003; 187(1):47-67.
[19] Kippe V, Aarnes JE, Lie KA. A comparison of multiscale methods for elliptic problems in porous media flow. Computational Geosciences, 2008; 12(3):377-98.
[20] Lamine MS, Edwards MG. Higher order multidimensional wave oriented upwind schemes for flow in porous media on unstructured grids. InSPE Reservoir Simulation Symposium 2009 Jan 1. Society of Petroleum Engineers.
[21] Lamine S, Edwards MG. Higher order multidimensional upwind convection schemes for flow in porous media on structured and unstructured quadrilateral grids. SIAM Journal on Scientific Computing. 2010 Apr 14;32(3):1119-39.
[22] Lee SH, Wolfsteiner C, Tchelepi HA. Multiscale finite-volume formulation for multiphase flow in porous media: black oil formulation of compressible, three-phase flow with gravity. Computational Geosciences, 2008; 12(3):351-66.
[23] Lie KA, Krogstad S, Ligaarden IS, Natvig JR, Nilsen HM, Skaflestad B. Open-source MATLAB implementation of consistent discretisations on complex grids. Computational Geosciences, 2012; 16(2):297-322.
[24] Natvig JR, Lie KA, Krogstad S, Yang Y, Wu XH. Grid adaption for upscaling and multiscale methods. In Proceedings of ECMOR XIII–13th European Conference on the Mathematics of Oil Recovery 2012 Sep 13.
[25] Notay Y. An aggregation-based algebraic multigrid method. Electronic transactions on numerical analysis, 2010; 37(6):123-46.
[26] Pal M, Edwards MG. Quasimonotonic continuous Darcy-flux approximation for general 3d grids of any element type. InSPE Reservoir Simulation Symposium 2007 Jan 1. Society of Petroleum Engineers.
[27] Pal M, Edwards MG, Lamb AR. Convergence study of a family of flux-continuous, finite-volume schemes for the general tensor pressure equation. International journal for numerical methods in fluids, 2006; 51(9-10):1177-203.
[28] Pal M, Lamine S, Lie KA, Krogstad S. Multiscale method for two and three-phase flow simulation in subsurface petroleum reservoirs. In ECMOR XIII-13th European Conference on the Mathematics of Oil Recovery 2012 Sep 10.
[29] Parramore ET, Edwards MG, Pal M, Lamine S. CVD-MPFA based multiscale formulation on structured and unstructured grids. In ECMOR XIII-13th European Conference on the Mathematics of Oil Recovery 2012 Sep 10.
[30] SINTEF 2011. Matlab Reservoir Simulation Toolbox (MRST), version 2011a. http://www.sintef.no/MRST.
[31] Wheeler MF, Xue G, Yotov I. A multiscale mortar multipoint flux mixed finite element method. ESAIM: Mathematical Modeling and Numerical Analysis, 2012; 46(4):759-796.

To whom correspondence should be addressed: Dr. M. Aslam Abdullah, Department of Chemical Engineering, VIT University, Vellore, India

Petroleum and Coal

Article **Open Access**

EFFECT OF POLYMETHACRYLATE AND BIOSURFACTANT MIXTURE AS POUR POINT DEPRESSANTS FOR WAXY CRUDE OIL

*T.T. Khidr, and H.S. El-Sheshtawy**

Egyptian Petroleum Research Institute (EPRI), Cairo, Egypt

Received February 22, 2019; Accepted May 13, 2019

Abstract

This paper describes the synthesis copolymers by having as an initial step the synthesis of the alkyl methacrylate monomers by transesterification of methyl methacrylate (MMA) with NAFOL20+A and NAFOL 1822B blend alcohols. The copolymerization of these monomers with MMA was then performed, with molar ratios of 50:50 for alkyl methacrylate: methyl methacrylate. All products were characterized by FTIR and gel permeation chromatography (GPC). Also, the rhamnolipids biosurfactant was synthesized by *Pseudomonas aeruginosa* ATCC-10145. The prepared copolymers were evaluated individually and mixed with the biosurfactant as pour point depressants improvers for waxy crude oil. It was found that; 1000 ppm PC22MMA copolymer with 250 ppm biosurfactant was exhibited the maximum pour point (Δpp= 30°C). From the results indicated that, the performance of the polymeric flow improver dissolved in chloroform was better than the effect of pure copolymer. Also, the results indicate that the higher molecular weight copolymer PC22MMA has better efficiency on pour point of waxy crude oil. In general, the biosurfactant enhanced the depression of the polymer additive and prevent them to grow up, consequently the pour point depress.

***Keywords**:* Copolymer; Biosurfactant; Pour point; Solvent; Waxy crude oil.

1. Introduction

Crude oil consists of n-paraffin waxes that tend to be separated from oil when the temperature of crude oil falls below the wax appearance temperature. With decreasing temperature, the waxes generally crystallize as an interlocking network of fine sheets; thereby entrapping the remaining liquid fuel in cage-like structures [1]. Several methods Khidr and Omar [2] have been available to improve the low-temperature properties of crude oil. Pretreatment with pour point depressants (PPD) is an attractive solution for transportation of waxy crude oils via pipelines. The bio-chemical treatments such as, polymeric compounds with biosurfactants referred to as ''wax-crystal modifier'', is being widely used to improve flow properties and/or combat wax deposition for waxy crude oils. Biosurfactants are surface active compounds produced by different living microorganisms. These compounds are mostly on microbial cell surfaces or excreted extracellular hydrophobic and hydrophilic moieties that confer the ability to accumulate between fluid phases, thus reducing surface and interfacial tension at the surface and interface respectively [3]. They possess the characteristic property of reducing the surface and interfacial tension using the same mechanisms as chemicals surfactants [4]. Biosurfactants are fundamentally classified according to their chemical structure and microbial origin. The major classes of biosurfactants are glycolipids, phospholipids, polymeric biosurfactants and lipopeptides (surfactin). The best known glycolipids are rhamnolipids, sophorolipids and trehalolipids [5].

The wax crystal modifiers are materials that have similar chemical structure to the wax that is precipitating. The model wax crystal modifiers are polymeric compounds constituted by one or more hydrocarbon chain(s) (wax-like) and polar portion. This kind of compounds can co-precipitate or co-crystallize with wax by taking the position of wax molecules on the crystal lattice through the hydrocarbon chains. Meanwhile, it also places a steric hindrance on the crystal

which can be interfere the growth and aggregation of wax crystals, and frequently reduce the pour point of crude oils [6]. Recently avoiding and/or solving the wax deposition problems is therefore an economically beneficial target which can be highly achieved by introducing a polymeric chemical additive in the ppm level to the crude oil in order to reduce its pour point temperature [7]. Although, crude oil treatment with chemical additives is not the only known solution for inhibition of wax deposition, it can be also preferred solution over other options like pigging, heating, and biological treatments. Pour point depressants (PPD) and flow improvers are polymeric additives that used to decrease the pour point and enhance the flow characteristics of crude oil, respectively. In doing that PPD's and flow improvers should posse oil-loving long chains in addition to polar groups such as ester, amine, and hydroxyl groups [8].

In this work synthesis, characterization and evaluation of the performance of various methyl methacrylate–blended alkyl methacrylate copolymers individually or in mixtures with biosurfactant as flow improvers as pour point depressant additives for crude oil and the present study is to produce of biosurfactant by *Pseudomonas aeruginosa* ATCC-10145.

2. Experimental

2.1. Materials

The following chemicals were used, methacrylic acid, methyl methacrylate**,** p-toluene sulphonic acid, toluene were attained as analytical reagents from Aldrich chemical. Two linear long chain alcohol blend (NAFOL 20+A) and (NAFOL 1822 B) were supplied from CONDE chemical company with the typical analysis listed in Table 1.

Table 1 Typical analysis of linear long-chain alcohol blends (NAFOL)

Properties	NAFOL 20+A	NAFOL 1822 B
Composition , wt %		
C16-OH	0.9	0.2
C18-OH	24.3	15.0
C20-OH	24.4	14.8
C22-OH	38.2	69.8
C24-OH	9.9	0.2
C26-OH	2.3	-
Average carbon number Cav, (calculated)	20	22
Density g/cm^3 at 70 ºC	0.803	0.802
Solidification point, ºC	56-60	63-65
Ester No. mg KOH/g	9.9	0.16
Acid No. mg KOH/g	0.05	0.01
Water, wt%	0.06	0.04
Flash point, ºC	208	204
Iodine No. mgL/100 mg	8.2	0.23

Egyptian waxy crude oil sample was collected from Qarun Petroleum Company. Their physicochemical properties are listed in Table 2.

Table 2. Physicochemical properties of the investigated crude oil

Test	Method	Result
Density@15°C Kg/L	ASTM D1298	0.8652
Pour point °C	ASTM D97	21
Flash point °C (PMC)	ASTM D93	200
Kinematic viscosity, cSt at 40°C	ASTM D445	243.59
at 100°C		18.94
Wax content, wt%	UOP 46/64	11.01
n-paraffins, wt%	ASTM D2887	62.27
Iso- paraffin, wt%	ASTM D2887	4.12
Total paraffins content, wt%	Urea adduct	66.39
Average carbon number (n)	calculated	28.56

2.2. Synthesis of the alkyl methacrylate

2.2.1. Esterification of methacrylate monomers

NAFOL 1822B methacrylate ester monomer was prepared by the reaction of 62.4 g (0.2 mol) of NAFOL 1822B alcohol blend and 25.8 g (0.3 mol) of methacrylic acid in a round bottom flask equipped with a Dean and Stark trap to remove the water of reaction azeotropically as it is formed. The reaction was carried out by 100 ml of toluene as a solvent, at reflux temperature, P-toluenesulphonic acid (0.5 g) was used as a catalyst and hydroquinone (0.6 g) as a polymerization inhibitor. Esterification reactions were repeated at the same preceding conditions for preparing NAFOL 20+A methacrylate. The two prepared monomers were then purified by distilling off the solvent at the end of esterification at reduced pressure, then the reaction mixture was extracted with n-hexane, washed with distilled water to remove the catalyst and any unreacted acid until the washings become neutral, then separation of organic layer. Eventually, the crude esters were recrystallized twice from acetone (3.0 mL/g) at 0°C. The prepared monomers showed white waxy like appearance.

2.2.2. Synthesis of alkyl methacrylate copolymer

In a two-necked round-bottomed flask, methyl methacrylate and NAFOL1822B/20+A methacrylate were added in the molar ratio of 50:50. Polymerization was performed in a toluene solution, using benzoyl peroxide (1 mol %) as the initiator. The reaction was per- formed at 80°C for 10 h, under nitrogen atmosphere and magnetic stirring. Afterwards, the toluene was evaporated under low pressure. The poly (NAFOL1822B methacrylate-co-methyl methacrylate) (P22MMA) / poly (20+A) methacrylate-co-methyl methacrylate) (P20MMA) were then purified in chloroform/methanol, and vacuum dried at 75°C, until constant weigh.

2.3. Characterization of additives

Spectra of the synthesized esters and different copolymer were measured by using FTIR. Spectrometer Model Type Mattson–Infinity Series Bench top 961. The mean molecular weight (Mn) of the polymers was determined by (GPC) Waters model 510 using polystyrene standard, ultra-styragel column, and tetrahydrofuran as an eluent.

2.4. Bacterial strains

Pseudomonas aeruginosa ATCC-10145 was purchased from the microbial resources center (MIRCEN), Faculty of Agriculture, Ain Shams University, Cairo, Egypt.

2.5. Media preparation and production of biosurfactant

The bacterial strains were streaked on a nutrient agar slant and incubated for 24 h at 30°C. Two loops of culture were inoculated in 25 mL of nutrient broth in a 50 ml Erlenmeyer flask and incubated in a rotary shaker 150 rpm at 30°C for 8–12 h until cell numbers reach 108 CFU/mL, an aliquot of 2 mL of inoculum was transferred to 100 ml of Bushnell Huss Mineral Salt medium (BHMS) in a 250 ml Erlenmeyer flask and the cultures were incubated on a temperature controlled shaker incubator at 150 rpm and 30°C for 96 h, the medium contained (g/L): dipotassium phosphate 1.0, magnesium sulfate 0.2, calcium chloride 0.02, potassium dihydrogen phosphate 1.0, ammonium nitrate 1.0, ferric chloride 0.05. The carbon source as glucose was added to make the final concentration 1% (w/v).

2.6. Recovery of biosurfactant

The crude rhamnolipids biosurfactant produced by *Pseudomonas aeruginosa* was recovered from the culture supernatant after the removal of cells by centrifugation at 10.000·g for 20 min. Rhamnolipids were then precipitated by acidification of the supernatant to pH 2.0 and allowing the precipitate to form at 4°C overnight. The precipitate thus obtained was pelleted at 10.000·g for 15 min, the precipitate was dissolved in 0.05 M sodium biocarbonate (pH 8.6), reacidified, and recentrifugation at 12.000·g for 20 min, following centrifugation, the precipitate

was extracted with chloroform/methanol (2/1) three times. The organic solvent was evaporated using a rotary evaporator and a yellowish oily residue was obtained [9].

2.7. Testing for surface activity

2.7.1. Measuring surface tension

An efficient biosurfactant with high efficiency must be able to reduce surface tension to less than 40 mN/m. To measure the surface tension, 50 mL of culture liquid containing biosurfactants was isolated and transferred to a sterile falcon. In this study, a tensiometer device ((Krüss-tensiometer K6, GmbH Hamburg, German) was used. It should be noted that, since surface tension is a function of ambient temperature, to obtain a more accurate result, influx surface tension of all the samples was measured at the same temperature of 24°C by the tensiometer device. For each sample, surface tension was measured for three times [10].

2.7.2. Emulsification activity (E_{24})

A volume of 3 mL of kerosene was vortexed with 3 mL of supernatant for 2 min and allowed to settle for 24 h, and then the emulsification index (E_{24}) was estimated as follows:

$(E_{24}) = h_{mulsion}/h_{total} \times 100\%$,

where $h_{emulsion}$ is the height of emulsion layer and h_{total} is the height of total liquid column.

2.7.3. Critical micelle concentration (CMC)

The determination of CMC was performed by several dilutions of free-cell fermented medium containing rhamnolipid. Superficial tension was measured using SIGMA 70 digital tensiometer (KSV Instruments LTD, Helsinki, Finland) at room temperature (ASTM D71).

2.7.4. Antimicrobial tests

The rhamnolipid compound was tested for antibacterial activity against Gram positive bacteria such as (*Bacillus pumilus* and *Micrococcus luteus*) and Gram negative such as (*Sarcina lutea*) and the antifungal activity was screened against *Penicillium chrysogenum*, yeast against *Candida albicans* by agar diffusion technique. This technique was tested in [11].

2.7.5. Evaluation pour point depressant for additive with crude oil

The prepared compounds were evaluated as pour point depressants using crude oil through the pour point tests according to the ASTM-97-93 respectively. The effect of additive concentration was investigated by using different concentration ranging from (500-2500) ppm.

3. Results and discussion

3.1. Synthesis of the additives

A representative IR pattern of NAFOL 1822B methacrylate monomer is shown the C-H stretching vibration of -CH3- and -CH2- groups absorbed strongly at 2917-2850 cm^{-1}'.The ester C=O appeared as a strong absorption at 1720cm^{-1} and the presence of the ester functionality was further supported by the appearance of a C-O stretching vibration at 1180cm^{-1}. Appeared at 1637cm^{-1} the characteristic C=C stretching whereas the C-H in plane deformation. Vibrations of methacrylate ester monomers appeared as doublets at 1322 and 1297cm^{-1}. A strong absorption of the bending vibration of C-(CH_2) N-C of the long alkyl chain of the ester appeared at 719cm^{-1}. The poly (NAFOL1822B methacrylate-co-methyl methacrylate) (P22MMA)/poly (20+A) methacrylate-co-methyl methacrylate) (P20MMA), all of them present bands in the region corresponding to stretching vibration band of C–H (2850 and 2920 cm^{-1}) that are much more intense than for the methyl methacrylate, accompanied by stretching vibration band for C=O (1720 cm^{-1}), C=C (1640 cm^{-1}) and multiple bands of C–C(C=O)–O, characteristic of a ,b-unsaturated esters (1320, 1295 and 1160 cm^{-1}). These bands, related with the absence of the stretching vibration band for the O–H bond of fatty alcohol in the

3200–3300 cm^{-1}, not only indicated the formation of methacrylic monomers but also confirmed the purity of the products.

3.2. Effect of molecular weight of additive on pour point of waxy crude oil

From the results demonstrated influence of the copolymer additive on the pour points. It can be observed that high average molecular weight wax inhibitor of P22MMA additive (15.896) shows better efficiency for reduction of pour point of waxy crude oil. The crystal growth rate of the lower molecular weight of P20MMA additive (10.891) wax inhibitor is much slower than that of the higher molecular weight wax inhibitor. As the crystal growth rate of higher molecular weight flow improver is faster, it cannot co-crystallize with reduced size of wax crystals. This is the reason why higher molecular weight wax inhibitor shows better efficiency for waxy oil.

3.3. Effect of concentration of additive on pour point of waxy crude oil

The results are shown in Figure 1 the polymeric additives PC20MMA and PC22MMA were investigated as PPDs on crude oil. From the Figure 1 it can be noticed that with increasing the concentration of the additives an increase in the pour point depression was achieved. This means that at this concentration ranges the additives may co-crystallize with the paraffin wax and modify their crystal structure. At higher concentrations of additives, the side way growth becomes more difficult for the wax crystals [12].

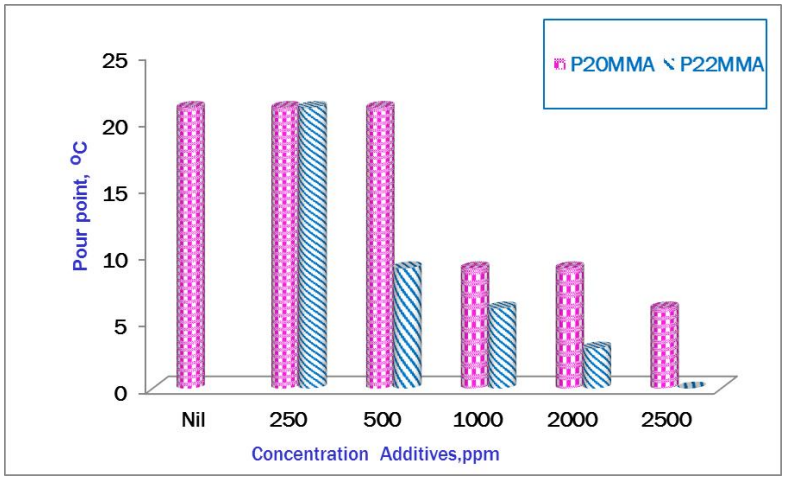

Fig. 1. Relation between additive concentration and pour point for crude oil

3.4. Results of studying surface activity

Biosurfactant production was studied using *Pseudomonas aeruginosa* with Bushnell Huss Mineral Salt medium (BHMS). In the present the yield of the biosurfactant was (1 g/L), Moussa *et al.* [13] was represented that the most favorable carbon sources for rhamnolipid (RL) biosurfactant production were glucose and glycerol (both at 40g/L), giving a RL yield of 0.3 and 0.25g/L, respectively. Also, Ndlovu *et al*. [14] was investigated that maximum rhamnolipid production was observed in the MSM supplemented with glucose (307mg L^{-1}).

Surface activity of the obtained biosurfactant, Table 3 proved that the rhamnolipids biosurfactant could reduce the surface tension to 31 mN/m, which was acceptable in terms of its purity.

Table 3 Evaluation of some surface properties of the biosurfactant produced by *Pseudomonas aeruginosa*

Surface tension (mN/m)	CMC (mg/L)	Emulsification activity (%)
31	50	70

It was stated by Mulligan [15] that a good surfactant can lower the surface tension of water from 72 to 35 mN/m. Moreover, the production of biosurfactants by *Pseudomonas aeruginosa* AK6U lowered the surface tension to 30 mN/m [16]. Figure 2 displays the results of surface tension related to different concentrations of rhamnolipids present in free-cell medium. A lower CMC of the surfactant means that the concentration required for this surfactant to form micelles is also lower. Therefore, the surfactant can change the surface properties and exhibit functions such as emulsification, solubilization and foaming even at a relatively low concentration.

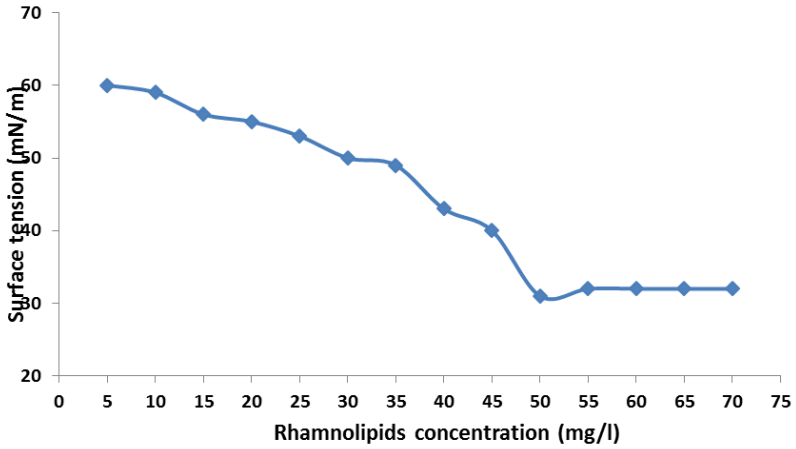

Fig. 2. Determination of critical micelle concentration of rhamnolipids biosurfactant

In the present study the surface tension decreased from 60 to 31 mN/m with small increases in the rhamnolipids concentrations up to 50 mg/L. Further the addition of rhamnolipids concentration had no effect until 70 mg/L. Nitschke and Pastore [17] reported that the CMC of biosurfactant obtained from *Bacillus subtilis* was 33 mg/L. The CMC of rhamnolipid fermentation liquor was 386 mg/L was investigated by Daoshan *et al.* [18]. Determination of emulsification power of rhamnolipids depends on the carbon source used to produce rhamnolipids [19]. In the present study the glucose was examined for their effectiveness of biosurfactant production. The *P. aeruginosa* was able to obtained 60 % emulsification activity using kerosene as hydrocarbon source. Rahman *et al.* [20] was illustrated that emulsification activity of the rhamnolipid biosurfactant produced by *P. aeruginosa* DS10-129 was higher than 70% using all the hydrocarbons tested, including xylene, benzene, hexane, crude oil, kerosene, gasoline and diesel.

3.5. Effect of solvent on pour point of waxy oil

Chloroform is good solvent for methacrylates. Effect of crude oil dilution with different solvent concentration was shown in Table 4. As shown influence of wax inhibitor/pour point depressant and solvent concentration was compared.

Upon addition of 10% solvent, pour point of waxy oil reduced from 21 to less than -3°C. The reduction of pour point by addition of solvent is due to the dissolution of asphaltenes. Of course, the effect of dilution may also play a major role in reducing the pour point. Probably the pour point reduction is achieved due to the effect of dilution. This study showed that treatment of crude oil with P20MMA, P22MMA with biosurfactant and P22MMA with biosurfactant additives alone are lower sufficient. In fact the crude oil will give lower viscosity after dissolution of crude oil by solvent and subsequent treatment with additives.

Table 4. Effect of solvent with additives on the pour point of crude oil

Symbol	Concentration of solvent (chloroform)	Concentration of different additive (wt%)	Pour point reduction,°c							
			Nafol 20+A		Nafol 1822B		Nafol 20+A+bio-surfactant		Nafol 1822B+bio-surfactant	
			PP	Δ PP	PP	Δ PP	PP	Δ PP	PP	Δ PP
A1	0	0	21	0	21	0	21	0	21	0
A2	0	1	21	0	18	3	18	3	15	6
A3	2	1	18	3	15	6	18	3	12	9
A4	5	1	12	9	9	12	15	6	6	18
A5	8	1	6	15	3	18	12	9	0	21
A6	10	1	6	15	0	21	9	12	-3	24

PP = pour point, ℃, Δ PP = change of pour point depression, ℃

3.6. Effect of blended biosurfactant with polymeric additive on pour point of crude oil

The polymeric additive PC20MMA/ PC22MMA were blended with biosurfactant at different ratios and the results were listed in Table 5 and Figure 3.

Table 5 Effect of the blends ratios of PC20MMA and PC22MMA with biosurfactant on the pour point of crude oil

Blend number	PPD (ppm)	Biosurfactant (ppm)	PP (°C)	Δ PP (°C)
B1	2000 PC20MMA	-	6	15
B2	1000 PC20MMA	1000	3	18
B3	1000 PC20MMA	500	3	18
B4	1000 PC20MMA	250	-3	24
B5	500 PC20MMA	1000	12	9
B6	2000 PC22MMA	-	0	21
B7	1000 PC22MMA	1000	-3	24
B8	1000 PC22MMA	500	-6	27
B9	1000 PC22MMA	250	-9	30
B10	500 PC20MMA	1000	9	12

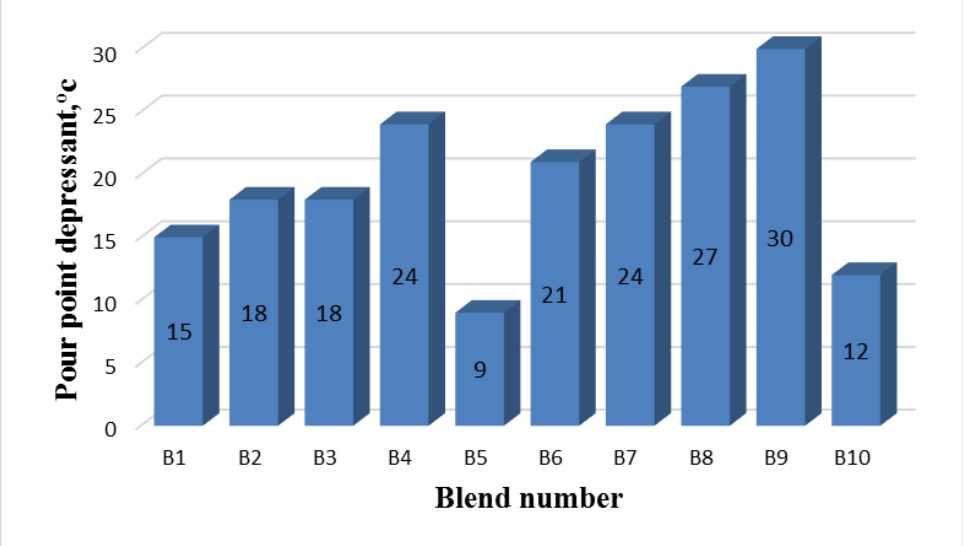

Fig.3. Effect of the blend ratios of PC20MMA and PC22MMA with biosurfactant on pour point depressant of crude oil

By inspecting the presented data in Table 5 it was found that B2 and B3 achieved Δpp=18°C and C4 exhibit Δpp=24°C while B7and B8 exhibited Δpp=24°C and 27 °C respectively. The maximum depression in pour point was obtained by B9 Δpp=30°C, as shown in Figure 3. This

observation means that the positive synergistic effect of the blend depends on the number of alkyl groups in the surfactant molecule and its concentration in the blend. So that the best results as pour point depressant for crude oil achieved with1000 ppm PC22MMA + 250 ppm biosurfactant. In general, the biosurfactant enhanced the depression of the polymer additive and prevent them to grow up, consequently the pour point depress.

4. Conclusion

Synthesis of the poly (NAFOL1822B methacrylate-co-methyl methacrylate) (P22MMA)/poly (20+A) methacrylate-co-methyl methacrylate) (P20MMA) by polymerization between NAFOL 1822B methacrylate/NAFOL20+A methacrylate with methyl methacrylate, all the products were characterized by Fourier transform infrared spectrometer FTIR and gel permeation chromatography analysis GPC.

The efficiency of the prepared compounds as pour point depressants increases by increasing the concentration and by increasing the molecular weight of the prepared additives. When the additive dissolved in chloroform was better effect as pour point depressant for crude oil than the effect of pure one. Higher molecular weight additive PC22MMA showed better efficiency as a flow improver than additive PC20MMA. When the polymeric additive blended with biosurfactant has better effect than that of polymeric additive alone as pour point depressant for crude oil.

References

[1] Al-Sabagh AH, El-Hamouly SH, Khidr TT, El-Ghazawy A, Higazy SA. Synthesis of phthalimide and succinimide copolymers and their evaluation as flow improvers for an Egyptian waxy crude oil. Egy J Pet., 2013; 22: 381–393.

[2] Khidr TT, Omar MA. Anionic/nonionic mixture of surfactants for pour point depression of gas oil. Egy J Petr., 2003; 12: 21-26.

[3] Mnif I, Elleuch M, Chaabouni SE, Ghribi D. *Bacillus subtilis* SPB1 biosurfactant: production optimization and insecticidal activity against the carob moth *Ectomyelois ceratoniae.* Crop Pro., 2013; 50: 66- 72.

[4] Singh A, Van Hanne JD, Ward OP. Surfactants in microbiology and biotechnology: *Part 2.* Appl. Asp Biotechnol Adv., 2007; 25: 99-121.

[5] Yin H, Qiang Y, Jia Y, Ye J, Peng H. Characteristics of biosurfactant produced by *Pseudomonas aeruginosa* S6 isolated from oil–containing wastewater. Process Biochem., 2009; 44: 302-308.

[6] Al-Sabagh AM, Khid TT, Moustafa HY, Mishrif MR, Al-Damasy MH. Synergistic effect between surfactants and polyacrylates-maleicanhydride copolymers to improve the flow properties of waxy crude oil. J Disp Sci Technol., 2017; 38 (7): 1055-1062.

[7] Khidr TT, Ahmed SM. The effect of cationic surfactant additives on flow properties of crude oil. Petro Sci Technol., 2016; 34: 1219-1225.

[8] Al-Sabagh AM, El-Hamouly SH, Khidr TT, El-Ghazawy RA, Higazy ShA. Preparation the esters of oleic acid-maleic anhydride copolymer and their evaluation as flow improvers for waxy crude oil. J Disp Sci Technol., 2013; 34: 1585-1596.

[9] Zhang Y, Miller RM. Enhanced octadecane dispersion and biodegradation by a *Pseudomonas* rhamnolipid surfactant (biosurfactant). Appl Environ Microbiol., 1992; 58 (10): 3276–3282.

[10] Deziel E, Paquette G, Villemur R, Lepine F, Bisaillon J. Biosurfactant production by a soil *Pseudomonas* strain growing on polycyclic aromatic hydrocarbons. Appl Environ Microbiol., 1996; 62: 1908–1912.

[11] El-Sheshtawy HS, Doheim MM. Selection of *Pseudomonas aeruginosa* for biosurfactant production and studies of its antimicrobial activity. Egy J Petro., 2014; 1–6.

[12] Khidr TT. Preparation of terpolymer additives and used their as pour point depressant for crude oil. Pet Coal, 2017; 59(4): 420-428.

[13] Moussa TA, Mohamed MS, Samak N. Production and characterization of di-Rhamnolipid produced by *Pseudomonas aeruginosa* TMN. Braz J Chem Eng., 2014; 31(4): 86 -880.

[14] Ndlovu T, Rautenbach M, Khan S, Khan W. Variants of lipopeptides and glycolipids produced by *Bacillus amyloliquefaciens* and *Pseudomonas aeruginosa* cultured in different carbon substrates. AMB Express. 2017; 7: 109-121.

[15] Mulligan CN. Environmental applications for biosurfactants. Environ Pollut., 2005; 133 (2): 183–198.

[16] Ismail W, Shammary SA, El-Sayed WS, Obuekwe C, El Nayal AM, Abdul Raheem AS, Al Humam A. Stimulation of rhamnolipid biosurfactants production in *Pseudomonas* AK6U by organo sulfur compounds provided as sulfur sources. Biotechnol Reports., 2015; 7: 55–63.
[17] Nitschke M, Pastore GM. Production and properties of a surfactant obtained from *Bacillus subtilis* grown on cassava wastewater, Bioresou. Technol., 2006; 97: 336–341.
[18] Daoshan L, Shouliang L, Yi L, Demin W. The effect of biosurfactant on the interfacial tension and adsorption loss of surfactant in ASP flooding. Colloids Surf A., 2004; 244: 53–60.
[19] Pornsunthorntawee O, Arttaweepor, N, Paisanjit S, Somboonthanate P, Abe M, Rujiravanit R, Chavadej S. Isolation and comparison of biosurfactants produced by *Bacillus subtilis* PT2 and *Pseudomonas aeruginosa* SP4 for microbial surfactant-enhanced oil recovery. Biochem Eng J., 2008; 42(2): 172-179.
[20] Rahman KS, Rahman TJ, McClean S, Marchant R, Banat IM. Rhamnolipid biosurfactant production by strains of *Pseudomonas aeruginosa* using low-cost raw materials. Biotechnol Prog., 2002; 18: 1277-1281.

To whom correspondence should be addressed: Dr. H. S. El-Sheshtawy, Egyptian Petroleum Research Institute (EPRI), 1 Ahmed El-Zomor Street, El- Zohour Region, Nasr city, 11727 Cairo, Egypt,
e-mail ***hudaelsheshtawy@yahoo.com***

Petroleum and Coal

Article **Open Access**

DETERMINATION OF COMBUSTION HEAT OF DIESEL FUEL COMPOSITIONS USING THE METHODS OF QUANTUM CHEMISTRY

E. V. Frantsina, M. V. Maylin, A. A. Sycheva

Department of Fuel Engineering and Chemical Cybernetics, National Research Tomsk Polytechnic University, Russia

Received March 15, 2019; Accepted April 3, 2019

Abstract

In this paper, we calculated the average values of the formation enthalpies and calorific values of hydrocarbon groups using quantum chemical methods of calculation. The dependence of the calorific value of diesel fuel compositions on the group composition at the operating parameters of the diesel engine was studied. The calorific values of five diesel fuel compositions having a different hydrocarbon composition were calculated, and the dependence of the calorific value of diesel fuel on the group and fractional composition was established.

Keywords*: diesel fuel compositions; hydrocarbons; enthalpies; the calorific value; quantum chemical methods.*

1. Introduction

In the conditions of a new strategy of economic development in Russia increasing attention is given to the processes of deep petroleum refining for the production of high quality motor fuels. The problem is becoming now becoming even more relevant because of the increase in the demand for diesel fuels of winter and arctic grades, which is due to reclaiming north and arctic regions [1-2]. For this reason, production of low-freezing diesel fuels is a topical issue for Russia, having large north territories [3]. Meanwhile, fuel compositions must meet specifications to operation in the conditions of low temperature, ignition quality as well as they must have the maximum calorific capacity. These properties include cold filter plugging point, cetane number and combustion heat of volume unit (energy output) [4].

As far as the production of diesel fuel is performed by the mixing petroleum fractions, which consist of paraffinic, olefinic, naphthenic and aromatic hydrocarbons, the obtained mixtures are complex multi-component systems, which properties are determined both by the ratios between them and molecular interactions [5]. These explain the main complexity of their determination. As far as the determination of low-temperature properties and cetane number is performed mainly by experimental methods, the calculation of heat effects of fuel combustion in laboratory conditions is a challenging task.

The fuels combustion heat is determined by calorific values of the components, which contents depend on hydrocarbon compositions of mixing fractions. The last depends on feedstock composition, technological conditions and catalyst activity in the processes of production of these fractions [6] and the ratio between mixing fractions at the stage of production of diesel fuels.

Thus, this work aimed to determine combustion heat of diesel fuel compositions using the calculation methods of quantum chemistry and to evaluate the influence of different hydrocarbon groups on the value of combustion heat for prediction of their heat capacity.

2. Research object and methods

The objects of research are diesel fuel compositions, obtained by the mixing of diesel fractions of the following boiling ranges: 150-310°C, 180-240°C, 200-360°C; and denormalization

process product (the fraction, purified from paraffinic hydrocarbons). Table 1 shows hydrocarbon compositions and physical properties of fractions, involved in the process of diesel fuel production.

Table 1. Hydrocarbon composition and properties of fractions, involved in the process of diesel fuel production

Hydrocarbon composition and properties of fractions	Petroleum fractions					
	Fr.1	Fr.2	Fr.3	Fr. 4	Fr.5	DN
N-Paraffins, wt.%	30.7	29.5	19.0	19.3	19.9	23.0
I-Paraffins, wt.%	23.0	24.1	33.1	32.9	32.4	29.6
Naphthenes, wt.%	13.6	14.2	19.0	18.9	18.6	17.1
Aromatic hydrocarbons, wt.%	32.6	32.2	28.9	29.0	29.2	30.2
Boiling temperature of 50 %, °C	184	191	283	281	267	253
Density at 20°C, kg/m^3	794	799	838	837	835	823
Molecular weight, g/mol	92.5	98.1	171.7	170.1	158.9	147.7

Fr.1 (boiling between 180-240°C, composition 1); Fr. 2(boiling between 180-240°C; composition 2); Fr. 3(boiling between 200-360°C, composition 1); Fr. 4(boiling between 200-360°C; composition 2); Fr. 5 (boiling between 150-310°C); DN (Denormalization process product)

In order to calculate molecular weights of fractions the following formulae were used [7-8]:

$M = 0.4448.T_{Rankine} - 273.56$

$T_{Rankine} = (T_{50°C} + 273.15).9/5$, where $T_{50\%}$ – the boiling temperature of 50% fraction.

3. Results and discussion

Because combustion heat of diesel fuel compositions depends on the calorific value of the components, constituting the composition, as was mentioned above, at the first stage of the research the enthalpies of formation of hydrocarbon groups, oxygen, and products of combustion (carbon dioxide and water steam) were calculated at operating parameters of diesel engine: the temperature in the combustion zone is 2273 K, the pressure is 110 atm. Using the calculation methods of quantum chemistry. Further, according to the Hess law the reaction heat effects of the combustion of individual hydrocarbons, constituting diesel fuel compositions, were calculated and their average values were determined for the following homological groups: n-paraffins, i-paraffins, naphthenes, aromatic hydrocarbons (Table 2).

Table 2. The combustion reaction of the different hydrocarbon group

Hydrocarbon group	General reaction of combustion
N-Paraffins	$C_nH_{(2\cdot n+2)}+(1,5\cdot n+0,5)\cdot O_2 \rightarrow n\cdot CO_2+(n+1)\cdot H_2O$
I-Paraffins	$C_nH_{(2\cdot n+2)}+(1,5\cdot n+0,5)\cdot O_2 \rightarrow n\cdot CO_2+(n+1)\cdot H_2O$
Naphthenes	$C_nH_{2\cdot n}+1,5\cdot n\cdot O_2 \rightarrow n\cdot CO_2+n\cdot H_2O$
Aromatic hydrocarbons	$C_nH_{(2\cdot n-6)}+(1,5\cdot n-1,5)\cdot O_2 \rightarrow n\cdot CO_2+\frac{(2\cdot n-6)}{2}\cdot H_2O$

In order to calculate enthalpies of hydrocarbons Gaussian software, which implements the methods of quantum chemistry, was applied. The models of substances, taking part in reactions, were created in GaussView software. The Density Functional Theory (DFT) was applied for calculations. The advantage of this method lies in that DFT takes into account the effect of electron correlation, i.e. the fact that electrons in molecule bounce off as a result of interaction between them. The method DFT is accurate enough for the calculation of hydro-carbons of diesel boiling range [9-11]. The theoretical approximation was the model B3LYP [12-14].
Table 3 shows the average values of enthalpies of formation and heat effects (combustion heat) of combustion reactions for each group of hydrocarbons of diesel fuel compositions.

Table 3. The average enthalpies of formation and combustion heats of hydrocarbon groups

	Enthalpy of formation $\Delta_r H_f$, MJ/mol	Combustion heat $Q=-\Delta_r H$, MJ/mol
Hydrocarbon group		
N-Paraffins	−1438.66	10.29
I-Paraffins	−1592.48	11.37
Naphthenes	−692.18	4.87
Aromatic hydrocarbons	−708.54	4.53
Components of the combustion reaction		
O_2	−392.4	–
CO_2	−492.4	–
H_2O	−199.4	–

**Q – combustion heat, MJ/mol; $\Delta_r H$ – heat effect of combustion reaction of a hydrocarbon group, MJ/mol.*

Thus, in series "n-paraffins" – "i-paraffins" – "naphthenes" – "aromatic hydrocarbons" the enthalpies of formation and combustion heats decrease, which is due to increase in the ratio (C:H) in the molecule. Because the combustion heat of hydrogen is much higher than combustion heat of carbon (143 MJ/kg and 32 MJ/kg [15]), the increase in the ratio (C:H) in diesel fuel corresponds to decrease in the heat effects of combustion reactions.

According to the calculated values of combustion heats of different hydrocarbon groups, the heats of combustion reactions of diesel fuel compositions, obtained by mixing the fractions presented in Table 1 in different ratios, were determined (Table 4).

Table 4. The content of different fractions at the stage of diesel fuel compositions production (vol.%)

Fractions, vol.%	Compositions				
	1	2	3	4	5
Fraction boiling between180-240ºC, Composition 1	10	–	26	75	85
Fraction boiling between180-240ºC, Composition 2	–	85	–	–	–
Fraction boiling between 200-360ºC, Composition 1	85	–	55	25	15
Fraction boiling between 200-360ºC, Composition 2	–	10	–	–	–
Fraction boiling between 150-31 ºC	5	5	–	–	–
Denormalization process product	–	–	19	–	–
Density at 20°C, kg/m^3	834	805	824	805	801

Table 5 shows the compositions of diesel fuels in wt.% and calculates the molecular weight.

Table 5. The content of different fractions at the stage of diesel fuel compositions production (wt.%)

Fractions, wt.%	Compositions				
	1	2	3	4	5
Fractions, vol.%	9.5 –	– 84.4	25.0 –	74.0 –	84.3 –
Fraction boiling between180-240 ºC, Composition 1	85.5	–	56.0	26.0	15.7
Fraction boiling between180-240 ºC, Composition 2	–	10.4	–	–	–
Fraction boiling between200-360 ºC, Composition 1	5.0	5.2	–	–	–
Fraction boiling between200-360 ºC, Composition 2	–	–	19.0	–	–
Molecular weight, kg/mol	0.164	0.109	0.147	0.113	0.105

For the obtained diesel fuel compositions (1-5), according to the rule of additivity, the thermal performance (combustion heat), and hydrocarbon composition were determined. The combustion heat effects were determined at the conditions of the internal combustion engine (temperature in the combustion zone is 2273 K, the pressure is 110 atm.). Calculation results are presented in Table 6.

Table 6. Hydrocarbon composition and thermal performance of diesel fuel compositions

	Compositions				
	1	2	3	4	5
N-Paraffins, wt.%	20.1	27.9	22.7	27.7	28.9
I-Paraffins, wt.%	32.1	25.4	29.9	25.7	24.6
Naphthenes, wt.%	18.4	14.9	17.3	15.0	14.5
Aromatic hydrocarbons, wt.%	29.3	31.7	30.1	31.7	32.0
(N-Paraffins+I-Paraffins), wt.%	52.2	53.3	52.6	53.4	53.5
(Naphthenes+Aromatichydrocarbons), wt.%	47.7	46.6	47.4	46.7	46.5
Density at 20 °C, kg/m^3	834	805	824	805	801
Molecular weight, kg/mol	0.164	0.109	0.147	0.113	0.105
Combustion heat, MJ/mol	7.94	7.92	7.94	7.94	7.93
Combustion heat, MJ/kg	48.42	72.67	54.02	70.26	75.49
Combustion heat, MJ/m^3	40372	58463	44514	56577	60461

As can be seen from Table 6, the lighter the composition (lower molecular weight and density), the higher the heat of fuel combustion. For example, for fuel composition 2, 4 and 5, which have the lowest molecular weights (0.109, 0.113 and 0.105 kg/mol) and densities (805, 804 and 801 kg/m^3), the calculated values of combustion heat are maximum (58463, 56577 and 600461 MJ/m^3). This is due to the speciality of hydrocarbon composition. Namely, the contents of n-paraffins and i-paraffins in diesel fuel compositions 2, 4 and 5 is the highest (53.3, 53.4 and 53.5 wt.%). These hydrocarbons have the highest combustion heats in comparison to naphthenes and aromatic compounds. Contrariwise, compositions 2 and 3 have the lowest combustion heats (40347 and 44514 MJ/m^3). These compositions are heavier (the molecular weights are 0.164, and 0.147 kg/mol and densities are 834 and 824 kg/m^3). They also have the highest contents of naphthenes and aromatic hydrocarbons (47.7 and 47.4 wt.%).

The obtained regularities of dependency of diesel fuels composition combustion heats on the hydrocarbon composition are explained by different contents of carbon and hydrogen, which are characterized by different calorific values (hydrogen has much higher calorific value), as well as by the structure of the molecules. That is why the more the content of saturated hydrocarbons and lower the content of unsaturated hydrocarbons in fuel composition, the higher its calorific value. Herewith, while developing optimal diesel fuel compositions, the contribution of different hydrocarbons in low-temperature properties and cetane number should be taken into account.

4. Conclusions

1. Using the methods of quantum chemistry the average values of enthalpies of combustion and combustion heats of hydrocarbon groups, constituting diesel fuel composition, were calculated at the conditions of their combustion in an internal combustion engine (temperature in the combustion zone is 2273 K, the pressure is 110 atm.). Combustion heats constitute for n-paraffins and i-paraffins 10.29 and 11.37 MJ/mol, for naphthenes 4.87 MJ/mol, for aromatic hydrocarbons 4.53 MJ/mol.

2. It was established, that increase in the ratio C:H in diesel fuel in series "n-paraffins" – "i-paraffins" – "naphthenes" – "aromatic hydrocarbons" the enthalpies of formation and combustion heats decrease, which is due to higher combustion heat of hydrogen than combustion heat of carbon.

3. The combustion heats of five diesel fuel compositions, which have different hydrocarbon composition, were calculated. It was shown, that their value comprises from 32000 to 49500 MJ/mol, which influences much on the power efficiency of the internal combustion engine.

4. The influence of hydrocarbon composition of diesel fuel on the combustion heat at the conditions of combustion inside the internal combustion engine was shown: the higher the ratio between saturated and unsaturated hydrocarbons, the higher the calorific value of the fuel. It was also established, that the lighter the fuel compositions (lower molecular weight and density), the higher the combustion heat. Thus, compositions 2, 4 and 5, which are characterized by the lowest molecular weights (0.109, 0.113 and 0.105 kg/mol) and densities (805, 804 and 801 kg/m^3), have maximum combustion heats (58463, 56577 and 60461 MJ/m^3). Contrariwise, compositions 1 and 3, which are heavier (molecular weights are 0.164 and 0.147 kg/mol, densities are 834 and 824 kg/m^3) and are characterized by higher content of naphthenic and aromatic hydrocarbons (47.8 and 47.4 wt.%), have the lowest combustion heats (40347 and 44514 MJ/m^3).

Acknowledgements

The research was performed at the National Research Tomsk Polytechnic University with the financial support of the Russian Science Foundation under grant № 18-79-00095.

References

[1] Gulyaeva LA, Shmel'kova OI, Khavkin VA, Krasil'nikova LA, Boldushevskii RE. Production of motor fuels for cold climates with simultaneous refining of vegetable and crude oil stocks. Chemistry and technology of fuels and oils, 2016; 52(5): 480-487.

[2] Kameshkov AV, Burmistrov SYu, Abramova LV, Tishov NV, Simanova TA. Optimization of production of various kinds of winter dieselby a combination of dewaxing process and processing with depressor-dispersive additives based on JSC «KINEF». Petroleum Refining and Petroleum chemistry, 2016; 3: 22-26.

[3] Mitusova TN, Lobashova MM, Nedayborsch AS, Titarenko MA. Production of Arctic diesel fuel in Russia. World of Oil Products. The Oil Companies' Bulletin, 2015; 12: 4-7.

[4] Bakulin VN, Dubovkin NF, Kotova VN, Sorokin VA. Energy-capacity fuels for aviation and rocket engines. Edited by Yanovskii NS. M.: Fysmatlit.2009: 400 p.

[5] Kapustin VM, Chernysheva EA, Glagoleva OF, Piskunov IV, SadyrovA Yu, Kuvykin VI, Gainetdinova AN. Not additive changes of properties of hydrocarbon systems while mixing. Petroleum Refining and Petroleum chemistry, 2017; 3-9.

[6] Belinskaya NS, Frantsina EV, Ivanchina ED, Popova NV, Belozertseva NE. Determination of optimal temperature of catalytic dewaxing process for diesel fuel production. Pet Coal, 2016; 58(7): 695-699.

[7] El-Hadi D, Bezzina M. Improved empirical correlations for petroleum fraction composition quantitive prediction. Fuel, 2005; 84: 611-617.

[8] Riazi MR, Daubert TE. Prediction of the composition of petroleum fraction. Industrial & Engineering Chemistry Process Design and Development, 1980; 19. 289-294.

[9] Belinskaya NS, Frantsina EV, Ivanchina ED. Mathematical modelling of "Reactor - Stabilization column" system in catalytic dewaxing of diesel oil cuts and atmospheric gasoil. Chemical Engineering Journal, 2017; 329:283-294.

[10] Burshtein KYa, Burygin PP. Quantum chemical calculations in organic chemistry and molecular spectroscopy. M.: Nauka, 1989, 104 p.

[11] Gerzeliev IM, Gyul'maliev AM, Popov AY, Khadzhiev SN. Thermodynamic and quantum-chemical study of the oxidative dehydrogenation of ethane to ethylene. Petroleum Chemistry, 2015; 55(2): 146-153.

[12] Clark T. Computer chemistry. M.: Mir, 1990, 383 p.

[13] Yusupov AI, Kirillova LB, Pashchenko KP. Application of Quantum Chemistry Computational Methods for Creation of Interaction Models in Oil Dispersed Systems. Oil and Gas Technologies, 2017; 1: 15-19.

[14] Borshch VN, Lyubimenko VA, Kilyanov MYu, Kolesnikov IM, Vinokurov VA. Quantum-chemical study of the complexation of maleimide with benzene and water molecules. Russian Journal of Physical Chemistry B, 2011; 5(4): 571-581.
[15] Stull DR, Westrum EF, Sinke GC. The chemical thermodynamics of organic compounds. – John Wiley & Sons, Inc., 1969, 806 p.

To whom correspondence should be addressed: Dr. E. V. Frantsina, Department of Fuel Engineering and Chemical Cybernetics, Tomsk Polytechnic University, 30, Lenin Avenue, Tomsk, 634050, Russia, e-mail: evf@tpu.ru

Petroleum and Coal

Article **Open Access**

EFFECTIVE CANDIDATE SELECTION FOR STIMULATION: CASE STUDY OF THE NIGER DELTA OIL FIELD

K. K. Ihekoronye, I. V. Nwankwo*

Petroleum Engineering, Federal University of Technology Owerri, Nigeria

Received March 1, 2019; Accepted May 9, 2019

Abstract

Well tests are typically used to evaluate formation damage before and after workovers. Buildup test are the most commonly used transient analysis because less flow rate measurement uncertainties leading in more reliable results. In this research study, buildup tests were carried out in three wells A, B and C in the Niger Delta Oil Fields to determine their damage, permeability and skin. The result from the study shows that well A is damage having R-factor of 0.62. R-factor of >0.6 means the formation is damaged. However, well B and C have R-factor of 0.22 meaning the reservoir is undamaged. In addition, the skin factor in well A is 10.6 which indicate formation damage. On the other hand, well B and C have skin of (-1.45) which is a negative skin indicating that the reservoir is not damage. Furthermore, damage ratio due to skin is 2.68 in Well A as a result of skin while Well B and Well C is 0.82 which is very low to enhance well productivity. In conclusion, well A needs to be stimulated. While well B and C is stimulated.

***Keywords**: Well test; Horner plot; Build up; Skin; Formation damage.*

1. Introduction

Stimulation is often used to describe different operation that is carried out in an oil well to get optimum hydrocarbon productivity. This technique is very vital to encourage production of flow from the reservoir rocks to the wellbore since the hydrocarbons are located between the pores spaces of the reservoir rocks. As part of the reservoir characterization process and monitoring of reservoir conditions, the use of buildup test is well know, not only to determine the reservoir pressure but to evaluate well performance based on wellbore damage and effective permeability under varying flow conditions. Many of these tests are performed by shutting-in the well at the surface. This procedure results in the after flow effects, which is a sandstone flow for a short period of time, and it may be affected by fluid properties, petro physical properties and the pipe volume fluid, multiple phase segregation among others. Nitters *et al.* [1] presented a structured approach to stimulation candidate selection and treatment design. In their research, they isolated the real skin caused by formation damage from the portion of the total skin that can be removed by matrix treatment to the total skin. Afolabi *et al.* [2] also considered a candidate selection criterion that is based on minimum economic reserve. Jennings [3] in their research noted a candidate selection based on well capacity and concluded that well stimulation treatments in high-productivity wells allow better reservoir management through sustained productivity and more uniform reservoir depletion throughout the life of the well.

Thomas and Milne [4] noted that the candidate selection consists of identifying wells with low productivity relative to what they are capable of producing and also, the possible mechanical problems in these wells.

Buildup tests using downhole shut-in tools reduce substantially the wellbore storage effects [1]. Buildup test is conducted by producing a well at constant rate for some time, shutting the well in (usually at the surface (that is, q = 0), allowing the pressure to build up in the wellbore, and recording the down-hole pressure in the wellbore as a function of time. Martin [5] noted

that candidate selection requires an accurate assessment of what a well can produce without impairment and the current productivity of the well. Onyekonwu [6] reported that skin and permeability of the formation could be determined through bottom hole pressure tests and other parameter that can help in well candidate stimulation. Gatlin *et al.* [7] wrote pressure build up method analysis is one of the quantitative ways of analyzing formation damage. Guoynes *et al.* [8] noted that one of the current typical issues related to hydraulic fracture is selection of candidate-wells. Moore and Ramakrishnan [9] wrote that it is possible to formulate a framework for the candidate-well selection for a certain field. It is possible to estimate the formation permeability and current drainage area pressure, and to characterize damage or stimulation and reservoir heterogeneity or boundaries frequently. Onyekonwu [6] noted that skin may not be the only yardstick for determining stimulation candidates. He also noted that R – factor is also a good yardstick for selecting stimulation candidate.

2. Objective of this study

The main objective of this study is aimed at implementing the principle of the R-factor, quantify and characterize the extent of damage using a pressure buildup analysis of these wells and hence achieve a good and effective candidate selection based on these parameters.

2.1. The possible sources of formation damage

1. Filter cake plugging; Drilling fluids serve to balance formation pressures while drilling to ensure wellbore stability. They also carry drilled cuttings to the surface and cool the bit. Filter cake plugging can result to problems like stuck pipe, differential sticking and large filtrate loss.
2. Fines in sandstone: Particle invasion and fines migration are among the major factors causing formation damage. Field studies and laboratory experiments have indicated that the fines cause permeability reduction [10].
3. Scale formation: The formation of mineral scale associated with the production of hydrocarbon is a concern in oilfield operation [11]. Depending on the nature of the scale and the fluid composition, the deposition can take place within the reservoir which causes formation damage
4. Polymer precipitation; polymers tend to reside in formation due to precipitation, and adsorption [11].

3. Methodology

3.1. Factor to consider when selecting stimulation candidate

3.1.1. Productivity index

Productivity index (PI or J) is a measure of the capability of a reservoir to deliver fluids to the bottom of a wellbore for production. It defines the relationship between the surface production rate and the pressure drop (drawdown) across the reservoir. Expressed mathematically, it is given as:

$$PI = J = \frac{q_s}{p_{e-P_{wf}}} \quad \ldots \qquad (1)$$

For steady state flow of incompressible fluid

$$PI = J = \frac{q_s}{p_{e-P_{wf}}} = \frac{7.08kh}{UBIn\frac{r_e}{r_w}} \qquad (2)$$

For semi steady state

$$PI = \frac{q_s}{P_{-P_{wf}}} = \frac{7.08kh}{UB\left[In\frac{r_e}{r_w}-\frac{3}{4}\right]} \text{ for average pressure} \qquad (3)$$

$$PI = \frac{q_s}{P_{e-P_{wf}}} = \frac{7.08kh}{UB\left[In\frac{r_e}{r_w}-\frac{1}{2}\right]} \text{ for normal pressure} \qquad (4)$$

3.1.2. Productivity ratio

$$PR = \frac{Avearage\ actual\ permeability}{Average\ undamged\ permeability}$$

S> 0=damaged formation (PR<1) S=0=No damage (PR=1) S<0=Enhanced production (PR>1)

3.1.3. Skin factor

The skin factor does affect the shape of the pressure buildup data. In fact, an early-time deviation from the straight line can be caused by skin factor as well as by wellbore storage. Positive skin factor indicates a flow restriction,

For s>0 there is formation damage. On the other hand, if s<0 (-ve) there is enhancement or stimulation that is., wellbore damage. A negative skin factor indicates stimulation. To calculate skin factor, s from the data available in the idealized pressure buildup test. At the instant a well is shut-in, the flowing BHP, P_{wf} is

At shut-in time Δt is the buildup test

$$P_{wf} = P_i + m\left[log\left(\frac{tp+\Delta t}{\Delta t}\right)\right] \quad (5)$$

$$S = 1.151\left(\frac{P_{ws}-P_{wf}}{m}\right) + 1.151\ log\left(\frac{1688\Theta U_0 C_t\ r^2{}_w}{K\Delta t}\right) + 1.151\log\left(\frac{tp+\Delta t}{\Delta t}\right) \ldots \quad (6)$$

Before shut-in at Δt = 0. With these simplifications, the skin factor is

$$S = 1.151\left[\frac{p_{1hr} - p_{wf}(\Delta t=0)}{m} - log\left(\frac{K}{\Theta U_0 C_t\ r^2{}_w}\right) + 3.23\right] \ldots \quad (7)$$

3.1.4. Flow efficiency and damage ratio

The flow efficiency is defined as the ratio of the actual productivity index of a well to its productivity index if there were no skin (s — 0):

$$\text{flow efficiency} = F.E = \frac{J_{actual}}{j_{ideal}} \quad \text{since} \quad \mathrm{J_{actual}} = \frac{\mathrm{q_0}}{\mathrm{P-P_{wf}}} \quad (8) \quad \text{and} \quad J_{ideal} = \frac{q_0}{P-P_{wf-(\Delta p)_{skin}}} \quad (9)$$

Therefore

$$F.E = \frac{P - p_{wf} - (\Delta p)_{skin}}{P - p_{wf}} \ldots \quad (10)$$

3.1.5. R-factor

R-factor > 0.6 damaged, while R- factor < 0.6 undamaged

3.2. Equations used for the well test analysis in this study

$$S = 1.151\left[\frac{p_{1hr} - p_{wf}(\Delta t=0)}{m} - log\left(\frac{K}{\Theta U_0 C_t\ r^2{}_w}\right) + 3.23\right] \quad (11)$$

$$\frac{k_0\ h}{u_0} = \frac{162.6\ q_0\ B_0}{m} \ldots \quad (12)$$

$$k_0\ h = \frac{k_0}{u_0} \times u_0 \ \ldots \quad (13)$$

$$PI = \frac{q_s}{P - P_{wf}} \ldots \quad (14)$$

$$E = \frac{PI_{actual}}{PI_{ideal}} = \frac{P_R - P_{wf} - \Delta P_S}{P_e - P_{wf}} \quad (15)$$

$$P_{ws} = P_i - \frac{162.6\ qB\ U}{K_h}\ log\ \frac{t_p+\Delta t}{\Delta t}. \quad (16)$$

$$r_i = \left(\frac{K_0\ t}{948\ \Theta\ u_0\ c_t}\right)^{1/2} \ldots \quad (17)$$

$$\Delta P_s = 141.2 = \frac{q_0\ u_0\ B_0}{K_0\ h} \times S \quad (18)$$

$$R - factor = \frac{141.2\ \frac{Q_0\ B_0\ U_0}{K_0\ h} \times S}{P - P_{ws}} \quad (19)$$

3.3. Effective candidate selection procedure

1. Monitor the trend in performance of the well over time and establish a persistent decline that is different from the expected natural decline of the well.
2. Shut in the well and perform a detailed build up test.
3. Analyze the build up test using Horner's procedure.
4. Evaluate the reservoir parameters required for quantifying damage (example, skin, pressure drop due to skin, K-factor and check whether value is up to 0.6.
5. If the condition is satisfied, the well is qualified as a stimulation candidate

Quantifying formation damage –well test analysis approach for Well A

Table 1 Reservoir rock and fluid properties for Well A

Parameter	Values	Parameter	values
Flow rate (B/d)	725	Oil formation volume factor	1.174
Porosity (%)	0.26	Area (acres)	40
Total compressibility (psi)	0.0000189	Pws ($\Delta t = 0$) psi	3409.37
Height (ft)	88.0	Dimensional time (hrs)	24
Viscosity (cP)	3.0	Wellbore radius (ft)	0.51

Table 2. Data used for the Horner plot analysis for WELL A

∆t (hrs)	Pws (psi)	(td+ t)/∆t	∆t (hrs)	Pws (psi)	(td+ t)/∆t
0	3409.37	0	0.1104	3535.22	218.39
0.0024	3419.23	10001.00	0.1272	3538.85	189.68
0.0048	3429.09	5001.00	0.1416	3541.71	170.49
0.0096	3437.14	2501.00	0.1632	3544.04	148.06
0.0144	3446.74	1667.67	0.2208	3546.12	109.69
0.0192	3454.78	1251.00	0.3432	3548.71	70.93
0.0240	3464.90	1001.00	0.6552	3548.97	37.63
0.0288	3473.72	834.33	0.0032	3549.23	24.92
0.0336	3481.25	715.28	1.3632	3549.49	18.61
0.0384	3486.70	626.00	1.7232	3549.75	14.92
0.0456	3496.56	527.32	2.0832	3550.01	12.52
0.0508	3503.82	473.44	2.4480	3550.27	10.80
0.0624	3510.57	385.62	2.8032	3551.05	9.56
0.0720	3518.87	334.33	3.1632	3551.53	8.58
0.0816	3525.10	295.11	3.5328	3551.57	7.79
0.0888	3527.95	271.27	3.8880	3551.82	7.17
0.0984	3530.55	244.90			

Quantifying formation damage –well test analysis approach for Well B

Table 3. Reservoir rock and fluid properties for WELL B

Parameter	Values	Parameter	Values
Flow rate (B/d)	984	Oil formation volume factor	1.362
Porosity (%)	0.25	Area (acres)	40
Total compressibility (psi)	0.0000173	Pws ($\Delta t = 0$) psi	3679.18
Height (ft)	30.0	Dimensional time (hrs)	24
Viscosity (cP)	0.53	Wellbore radius (ft)	0.4

Table 4 Data used for the Horner plot analysis for WELL B

∆t (hrs)	Pws (psi)	(td+ t)/∆t	∆t (hrs)	Pws (psi)	(td+ t)/∆t
0	3679.18	0	1.8083	3761.87	14.27
0.006	3694.38	4001.00	2.1683	3763.09	12.06
0.0083	3714.14	2892.56	2.5308	3764.60	10.48
0.0108	3732.69	2223.22	2.8908	3764.91	9.30
0.0132	3744.24	1819.18	3.2508	3766.13	8.38
0.0157	3747.58	1529.66	3.6108	3767.04	7.65

∆t (hrs)	Pws (psi)	(td+ t)/∆t	∆t (hrs)	Pws (psi)	(td+ t)/∆t
0.018	3748.80	1334.33	3.9708	3767.04	7.04
0.0203	3750.02	1183.26	4.326	3767.95	6.55
0.0252	3751.54	953.38	4.86	3768.87	5.94
0.126	3755.79	191.47	5.053	3769.08	5.74
0.3708	3757.72	65.72	5.410	3771.3	5.44
0.738	3758.53	33.52	5.768	3772.21	5.16
1.0932	3759.14	22.95	6.044	3772.82	4.97
1.4508	3760.05	17.54			

Quantifying formation damage –well test Analysis approach for WELL C

Table 5. Reservoir rock and fluid properties for WELL C

Parameter	Values	Parameter	Values
Flow rate (B/d)	984	Oil formation volume factor	1.362
Porosity (%)	0.24	Area (acres)	40
Total compressibility (psi)	0.0000173	Pws $(\Delta t = 0)\ psi$	3679.18
Height (ft)	30.0	Dimensional time (hrs)	24
Viscosity (cP)	0.55	Wellbore radius (ft)	0.4

Table 6. Data used for the Horner plot analysis for WELL C

∆t (hrs)	Pws (psi)	(td+ t)/∆t	∆t (hrs)	Pws (psi)	(td+ t)/∆t
0	3679.18	0	1.8083	3761.87	14.272
0.006	3694.38	4001.00	2.1683	3763.09	12.069
0.0083	3714.14	2892.566	2.5308	3764.60	10.48
0.0108	3732.69	2223.222	2.8908	3764.91	9.302
0.0132	3744.24	1819.182	3.2508	3766.13	8.385
0.0157	3747.58	1529.70	3.6108	3767.04	7.65
0.018	3748.80	1334.333	3.9708	3767.04	7.044
0.0203	3750.02	1183.266	4.326	3767.95	6.60
0.0252	3751.54	953.381	4.86	3768.87	5.94
0.126	3755.79	191.476	5.053	3769.08	5.80
0.3708	3757.72	65.725	5.410	3771.3	5.44
0.73	3758.53	33.52	5.768	3772.21	5.20
1.0932	3759.14	22.954	6.044	3772.82	4.97
1.4508	3760.05	17.543			

4. Result presentation well test analysis for WELL A, B and C

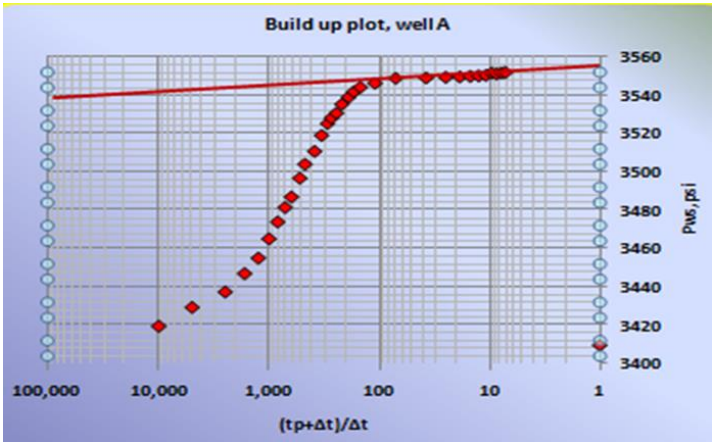

Fig. 1. Graph of Well A test using Horner's plot

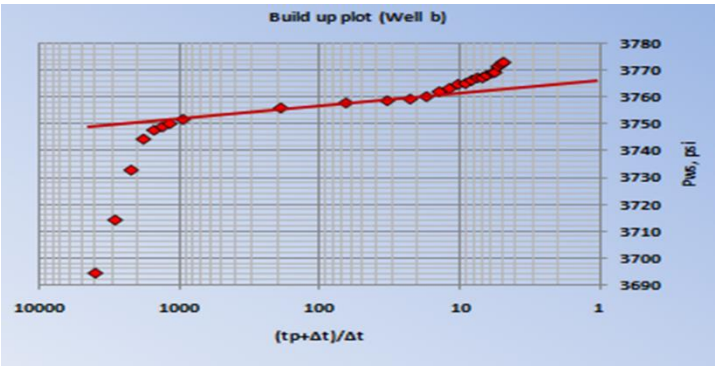

Fig. 2. Graph of Well B test using Horner's plot

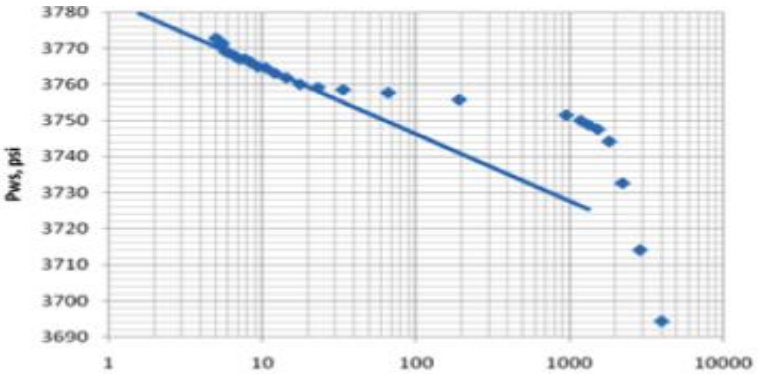

Fig 3. Graph of Well C test using Horner's plot

Tab. 7. Summary result for Well A, B, and C

Parameter	Well A	Well B	Well C
Initial reservoir pressure psi	3 556	3 784	3 784
Transmissibility (mD-ft/cP)	13 839.7	12 106.55	12 106.53
Flow capacity (mD-ft)	41 519.1	64 16.469	64 16.469
Flow efficiency	0.372233	1.217795	1.217795
Pressure drop due to skin Psi	92.04947	-22.8293	-22.8293
Effective permeability (MD)		213.8823	213.8823
Skin factor	10.59257	-1.45949	-1.45949
Damage ratio	2.686489	0.821156	0.821156
Potential production rate without skin (B/D)	-	808.0178	808.0178
Productivity index (B/D/psi)	4.944418	9.387521	9.387521
Radius of investigation ft	900.1313	1 536.943	1 536.943
slope psi/cycle	10	18	18
Effective permeability (m D)	471.8079	-	-
R-Factor	0.627767	0.217795	-0.2000

4.1. Discussion of results

Three wells were analyzed as shows in Figs. 1, 2 and 3. The result from the study shows that the well A has damage having R-factor of 0.62. R-factor of >0.6 means the formation is damage. However, well B and C have R-factor of 0.22 meaning the reservoir is undamaged. The skin factor in well A is 10.6 which is high indicating that the reservoir needs to be stimulated. On the other hand, well B and C have skin of (-1.45) which is a negative skin indicating that the reservoir is not damage. In addition to, damage ratio due to skin is 2.68 in Well A while Well B and Well C is 0.82. Table 7 shows the summary of the different well test analysis carried out in this research work. In conclusion, well A needs to be stimulated. While B and C is enhanced or stimulated.

5. Conclusion

From the well under the study (well A, B, C), the following conclusions can be drawn:

i. The evident from the calculated permeability, skin factor, flow efficiency shows that damage occurred in well A.
ii. Any damage to the near wellbore formation created by drilling & completion can act as a barrier to the movement of fines through the formation.
iii. Mobile fine in producing formation can lead to pore blockage, which will affect the well productivity

5.1. Recommendation

This study recommends that for good profitability in the oil business and minimization of damage from work over fluids, drilling fluids and completion fluids in the Niger Delta wells, the following should be done:

i. Use fluids which are compatible with formation and its content if possible.
ii. Good stimulation jobs should be properly carried out on a well before putting it into production to avoid damage to the well.
iii. Build up test and analysis should be performed on newly completed wells, especially the exploratory wells to determine the onset of formation damage by indicators lie the R-factors, skin factor.
iv. Minimize exposure time of drilling and completion fluids as much as possible.

References

[1] Nitters G, Roodhart L, Jongma H, Yeager V, Buijse M, Fulton D, Dahl J, and Jantz E.: Structured Approach to Advanced Candidate Selection and Treatment Design of Stimulation Treatments. Paper SPE 63179, presented at the SPE Annual Technical Conference and Exhibition held in Dallas, Texas (Oct. 1-4) 2000.

[2] Afolabi A, Opusunju A, Henri J, Onyekwere C, Onyekwere C, and Davalos J. Increasing Production in Brown Field with Heavy Crude and Fines Problem by Application of a New HF-Acid System: Case Histories. Paper SPE 112558 presented at the SPE International Symposium on Formation Control, Lafayette, Louisiana (Feb 13-15) 2008.

[3] Jennings AR. Good Wells Make the Best Candidates for Well Stimulation. SPE Production Engineering 1991; pp 371-376.

[4] Amaefule JO, Ajufo A, Peterson E, Durst K. Understanding Formation Damage Processes: An Essential Ingredient For Improved Measurement And Interpretation Of Relative Permeability Data. Paper SPE 16232-MS, presented at the SPE Production Operations Symposium 1995, Oklahoma City, Oklahoma.

[5] Martin AN, and Rylance M. Hydraulic Fracturing Makes the Difference: New Life for Old Fields. Paper SPE 127743 presented at the North Africa Technical Conference and Exhibition. 14-17 February 2010. Cairo, Egypt.

[6] Onyekonwu MO. General Principles of Bottom Hole Pressure Test. Department of Petroleum Engineering 1997, University of Port Harcourt.

[7] Gatlin C, Nemir CE. Some Effects of Size Distribution on Particle Bridging in Lost Circulation and Filtration Tests. Society of Petroleum Engineers. 1960; doi:10.2118/1652-G-PA

[8] Guoyness J, Squire K, Blauch M, Yeager V, Yater J, Wallace R, Frame R, and Clark R. Optimizing Deliverability in Five Gas-Storage Reservoirs- Case Studies. Paper SPE 65636 presented at the SPE Eastern Regional Meeting. 17-19 October 2000. Morganton, West Virginia, USA.

[9] Moore LP, and Ramakrishnan H. Re-stimulation: Candidate Selection Methodologies and Treatment Optimization. Paper SPE 102681 presented at the SPE Annual Technical Conference and Exhibition. 24-27 September 2006. San Antonio, Texas, USA.

[10] Gray DH, and Rex RW. Formation Damage in Sandstones Caused by Clay Dispersion and Migration. Clays, Clay Minerals, 1996; 14 (1): 355.

[11] Moghadasi J, Jamialahmadi M, Müller-Steinhagen H, Sharif A. Formation Damage Due to Scale Formation in Porous Media Resulting From Water Injection. SPE-86524-MS International Symposium and Exhibition on Formation Damage Control, 18-20 February 2004, Lafayette, Louisiana DOI https://doi.org/10.2118/86524-MS

To whom correspondence should be addressed: Dr. K. K. Ihekoronye, Petroleum Engineering, Federal University of Technology Owerri, Nigeria

Petroleum and Coal

Review **Open Access**

A REVIEW ON SOLIDS SEPARATION, DISPOSAL AND HANDLING SYSTEM FOR THE PETROLEUM REFINING INDUSTRY

Angela Onose Mamudu[1] and Howard Chandler[2]*

[1] *Department of Chemical Engineering, Covenant University Ota, Nigeria*
[2] *Department of Petroleum Engineering, University of Aberdeen, United Kingdom*

Received March 5, 2019; Accepted May 9, 2019

Abstract

A typical reservoir fluid comprises of a mixture of hydrocarbons, salt, water and solids (sand, clay, corrosion products and gravel packs). The presence of solids triggers bacteria and hydrogen sulphide growth, which leads to intense corrosion of both pipe works and valves. The decline in the overall retention time, damages in the formation and a regular shutdown of the plant are parts of its negative impacts. This paper, therefore, reviewed all available solid cleanout systems currently being used in the industry highlighting their strength, weakness and suitability's. On a global view, case studies on four different drilling platforms (Exxon Grand Isle Block 16L /West Delta 73 A-D, South Pass Field, Albacora Deep Water and Dagang Oilfield) encountering intricate solid disposal issues were analysed. Production limits encourage drilling of wells in areas where zero amount of sand is recorded, which is rarely obtainable. Convectional exclusion approach combines various techniques (mechanical retention, gravel packs, downhole equipment and chemical consolidation) with the main aim of preventing the solids from entering the wellbore. The inclusion methodology in collaboration with a de-sander works by injecting a working fluid into the wellbore, which helps to circulate, lift and carry the solid particle to the surface for proper separation and disposal. The four different models of an integrated solid handling system used on the platforms experienced complex operational problems ranging from erosion, leakages, wears, equipment failure, sulphate reducing bacteria growth, emulsion stabilization, pluggingand an increase in pressure drop. The root cause of each issue and solutions were analysed.

Keywords: *Convectional Exclusion; De-sanders; Production Limits; Reservoir Fluid; Review; Solid Cleanout.*

1. Background study

The production of solids alongside the reservoir fluid is a phenomenon that occurs during the drilling stage of every well [1-2]. These solids are inorganic insoluble or semi- soluble de-formable particles that come from a natural or artificial source [3]. Currently, research has it that roughly 90% of the world's oil and gas wells are being discovered in sandstone reservoirs, among which 25-30% of the wells experience sand production at a stage in their well life, with concentrations varying within the range of 5-250 parts per million [4]. These result in the decline of the overall rate of production; leading to the discovery and implementation of a solid separation, disposal and handling system.

Naturally, solids emerge from the reservoir material either in the form of detrital grains of sand (S_i0_2 oxide) or clay (hydrous aluminium silicates) [3]. Artificially, solids are being intro-duced into the well stream via the addition of foreign bodies [3]. Table 1 highlights the physical properties of both natural and artificial solids.

Asides the troubling figures listed in the table, the effects of produced sand triggers the presence of bacteria and hydrogen sulphide, which eventually leads to intense corrosion of both pipe works and valves. Other negative effects include a decline in the overall retention time, damages in formation during the process of re- injection and finally, a regular shutdown of the plant during separation processes [4-5]. The aim of this research, therefore, is to review

solid cleanout systems currently being used in the industry highlighting their strengths, weaknesses and suitability's. On a global view, case studies on four different drilling platforms encountering intricate solid disposal issues were analysed. []

Table 1. Physical properties of natural and artificial solids [3]

Property	Natural		Artificial		
	Sand	Clay	Fracture sand	Corrosion products	Gravel pack
Specific gravity	2.5-2.9	2.6-2.8	2.6-3.6	5.5-6.0	2.6-3.0
Shape Factor	0.2-0.5	0.1-0.3	0.5-0.9	0.1-0.5	0.5-0.9
Size Range(μm)	50-1000	5-30	150-2000	10-10000	250-3500
Conc. (ppmv)	5-100	<1	0-10000	<2	0(unless failure)

ppmv-part per million by volume; μm-micrometre; >-Greater than and <-Less than

2. Solids separation methodologies

Generally, the three methods currently being adopted in the industry for the disposal of sands and solids generally are production limits, convectional exclusion and the inclusion approach [3]. The production limits use the conservative approach of Zero Sand Production. For this, wells are drilled in areas where there is zero amount of sand production. This is effectively done with the aid of a reservoir versus bottom hole pressure map. Although it reduces the overall capital expenditure, it has its limitations of reducing the rate of production when continuous redefining of the boundaries due to alteration in the well profile is detected [3].

The convectional exclusion approach combines various techniques with the main aim of preventing the solids from entering the wellbore. They include the use of mechanical retention systems (screen or slotted liner), gravel packs and chemical consolidation. Generally, this approach protects the production tubular's, wellhead chokes, flow lines and facilities equipment from damage. However, there will be an accumulation of solids near the well bore [3]. Downhole equipment ensures that gravel packing is positioned around the external surface of the separator screen.

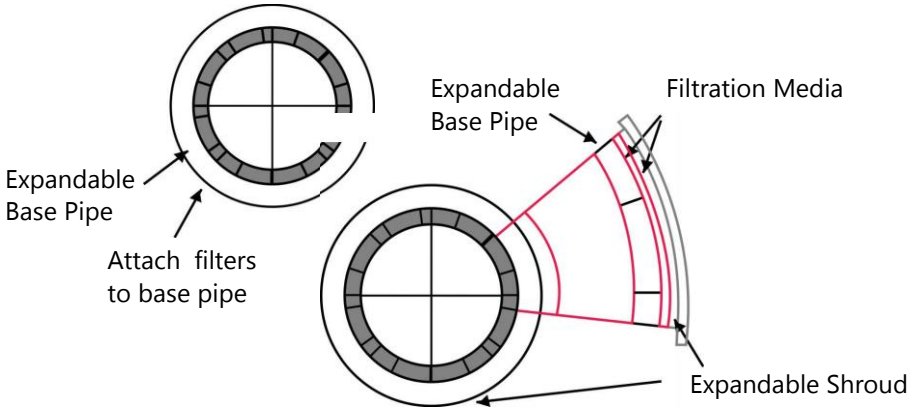

Figure 1. Expandable sand screen construction [7]

Wire wrap screen are keystone shaped designed majorly for the separation of coarse well-sorted sands. They ensure that gravel placed between the screen and the formations are maintained while trying to minimise other production constraints. It provides extra strength, eliminates the tendency of screen erosion and ensures better filtration assurance. Expandable sand screen as shown in Figure 1 is considered the strongest in the industry with a collapse strength of 2500pounds per square inch (psi), it provides better reliability via slotted base pipe structures, filter media and an outer protecting/ encapsulating layer [6-7]. The metal mesh screen, which was first adopted in 1980, comprises of a base pipe, layered filtration jacket,

an outer shroud, a perforated base plate and several spacer rings. When compared to the rest, it has a high corrosion resistance and a slimmer chance of being damaged during the installation stage [8-9].

The gravel packs consist of a perforated liner placed in the well, enclosed by a mass of gravel that acts as a depth filter to prevent the sand from entering the wellbore [10]. Chemical consolidation involves the sealing of sand grains several feet down by the use of environmentally accepted chemicals. The major aim is to raise the residual strength of the formation, thereby intensifying the sand maximum free rate [3,11]. An example of such a chemical is organosilane.

The inclusion methodology works by injecting a working fluid into the wellbore, which helps to circulate, lift and carry the solid particle to the surface for proper separation and disposal. The separation of the solid is then carried out via a multiphase de-sander prior to the crude oil separating vessel [3-4].Although it reduces skin damages due to the free flow of sand alongside the well fluid, there is always a large tendency for the working fluid to leak into the formation. It can also lead to erosion of the tubular's, choke, and flow lines that ultimately results in flooding of the production separator. The working fluid might also be in the form of energised fluid or foam that can lead to separation complications if not properly handled [3-4].

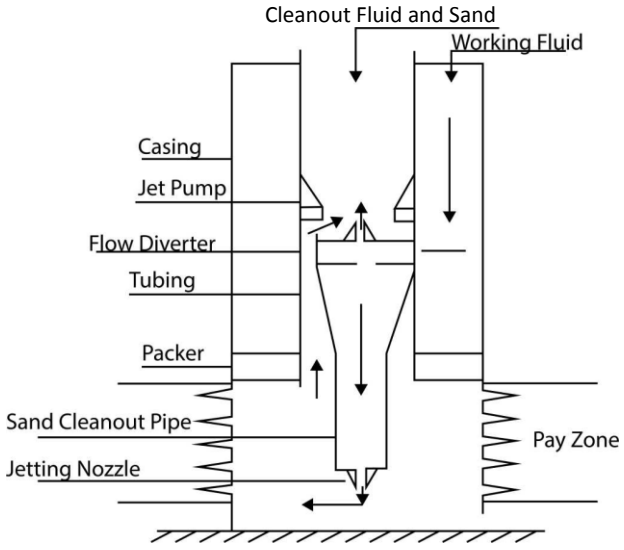

Fig. 2. Sand cleanout system [4]

As shown in Figure 2, a multistage centrifugal pump helps boost up water (working fluid) pressure, which is introduced into the well hole through the annulus. The flow diverter separates this fluid into two parts: sand carrier and power fluid for the jet pump. The sand carrier fluid flows downward through the jetting nozzle located at the sand cleanout pipe. The jetting nozzle converts the high-pressure into a high velocity head, which helps to lift the sand particle from the bottom of the wellbore to the throat of the jet pump [4]. The power fluid produces a high velocity, which helps in lowering the pressure at the bottom hole. This aids the absorbing of the carrier fluid alongside the sand particles into the fluid [4].

De- sanders are solid liquid hydro-cyclones, which are known to incur the following benefits: the ability to remove sand without necessarily shutting down the system, lesser weight, capital effective, requires little or no labour and most importantly little cost for maintenance and operations [5]. It comes in two forms: vessel and liner. The vessel type which nominal diameter is within a range of 3-30 inches, uses its vessel itself as the de-sander. Although cost effective when compared to the liner type, they are more effective in large flow rate areas with a combination of coarse separation size. The liner style is always designed to have multiple liners, each having a nominal diameter within a range of 0.5-4 inch. It can be applied to any flow rate in combination with fine separation size, making it more flexible [5].

All de-sanders have four major components: inlet, overview, cone and tailpipe. The inlet, which serves as the cylindrical feed chamber regulates the degree of turbulence that comes with the incoming flow via tangential velocity at the hydro cyclone inlet [12]. The overview houses the vortex finder also called the Core Stabilizing Shield. It protects the fluid core from any potential turbulence and decreases the available cross sectional area, thereby boosting tangential velocity.

Although the cane varies in different angles and geometrics, it increases the amount of centrifugal force needed as the fluid flows through the narrowed cross sectional area. The

tailpipe increases the retention time required for the separation process. Generally, the smaller the diameter of the tail pipe, the greater the tangential velocities [12]. New generation de-sander introduce an internal header with an educator, which helps to handle issues of slugging of ≤ 50,000ppm. It is associated with smaller footprints, a significant reduction in weight, and lower pressure drop with zero liquid loss [13].

3. Case studies

3.1. Grand Isle Block 16L and West Delta 73 A-D Production Platform

Initially, Exxon Company faced major problems with respect to solid handling both on their offshore platforms and generally in pipelines. In addition, existing anti-pollution laws were in place that restricted improper handling and disposal of solids. A sand handling model was designed with Centrifugal force as the underlying principle. This model was first introduced and tested on the Grand Isle Block 16L and West Delta 73 A-D Production Platform, paying critical attention to the reliability of the sand discharge system [14].

3.1.1. Sand handling system

As shown in Figure 3 below, the model is divided into three sections, namely: sand removal, sand transporting and the sand cleaning/disposal system [14]. The convectional cyclone (1) separates the sand from the produced fluid; this fluid moves into a surge tank where they are transported to a shore facility via pipeline. The separated sand settles in the silt pot below each cyclone, where they are forced out by differential pressure. The centrifugal pump (2) then supplies water to the sand, which moves it to the collection trough. The two phase mixture of sand, water, and oil moves to the classifier vessel (3) where the sand and free water moves to the bottom and top of the cone respectively due to the difference in their density. The adjustable regulator (4) helps to control the vessel pressure by venting gas to the surge tank [14].

The dump valve (6) is actuated by both the water level control (5) and the oil level control (7) which maintains the level of the water in the vessel and discharges the oil to the surge tank. Both the mixture of water and sand moves to number one cyclone (9) of the sand washer at the opening of the dump valve (6).The cyclone separates the sand to the sand washer while the water and free oil go to the separation vessel (10) through the cyclone overflow line (11) [14].

Figure 4 refers to the separator where the water and the oil are allowed to separate to the bottom and top, respectively due to their difference in density. The water acts as a source for the recirculation pump (2), while the cyclone banks (1) act as both an entry and exit point for the water. It was also observed that as the sand exits the cyclone banks (1), both water and oil comes out with it. The classifier (3) removes the excess oil while water and sand go to the sand washer number one cyclone (9). The equality of both the amount of water that is being separated and discharged by the cyclone banks (1) will keep the volume of re-circulation constant; otherwise, the volume will continually fall. The high-level controller automatically opens the dump valve (15) when it senses an increase in the water level at the separator where the water is discharged into the sump tank [14].

3.1.2. Sand washer

As illustrated in Figure 5 below, the mixture of water, sand and oil moves into the number one cyclone (9) from the classifier vessel (3). The sand is separated from the mixture and moves to number one compartment (3) of the sand washer while the mixture of the oil and water flows to the separation vessel (10). The gas line prevents air from entering the cyclone as it internally spins the fluid. In the centre vortex, gas is mixed with the separated fluid where they are deposited in the separation vessel (10) [14].

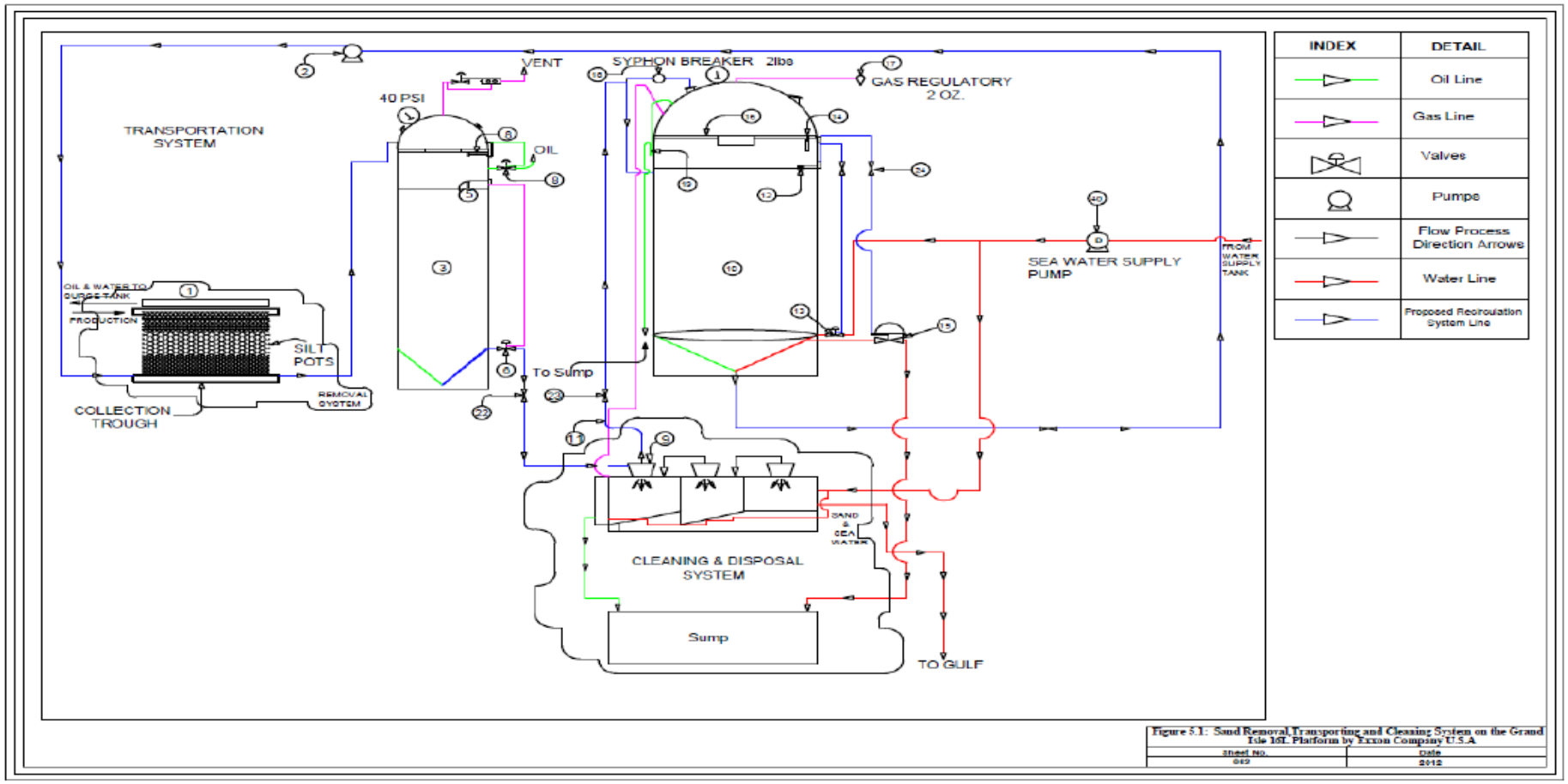

Figure 3. Sand removal, transporting and cleaning system on the Grand Isle 16L Platform by Exxon Company U.S.A [14]

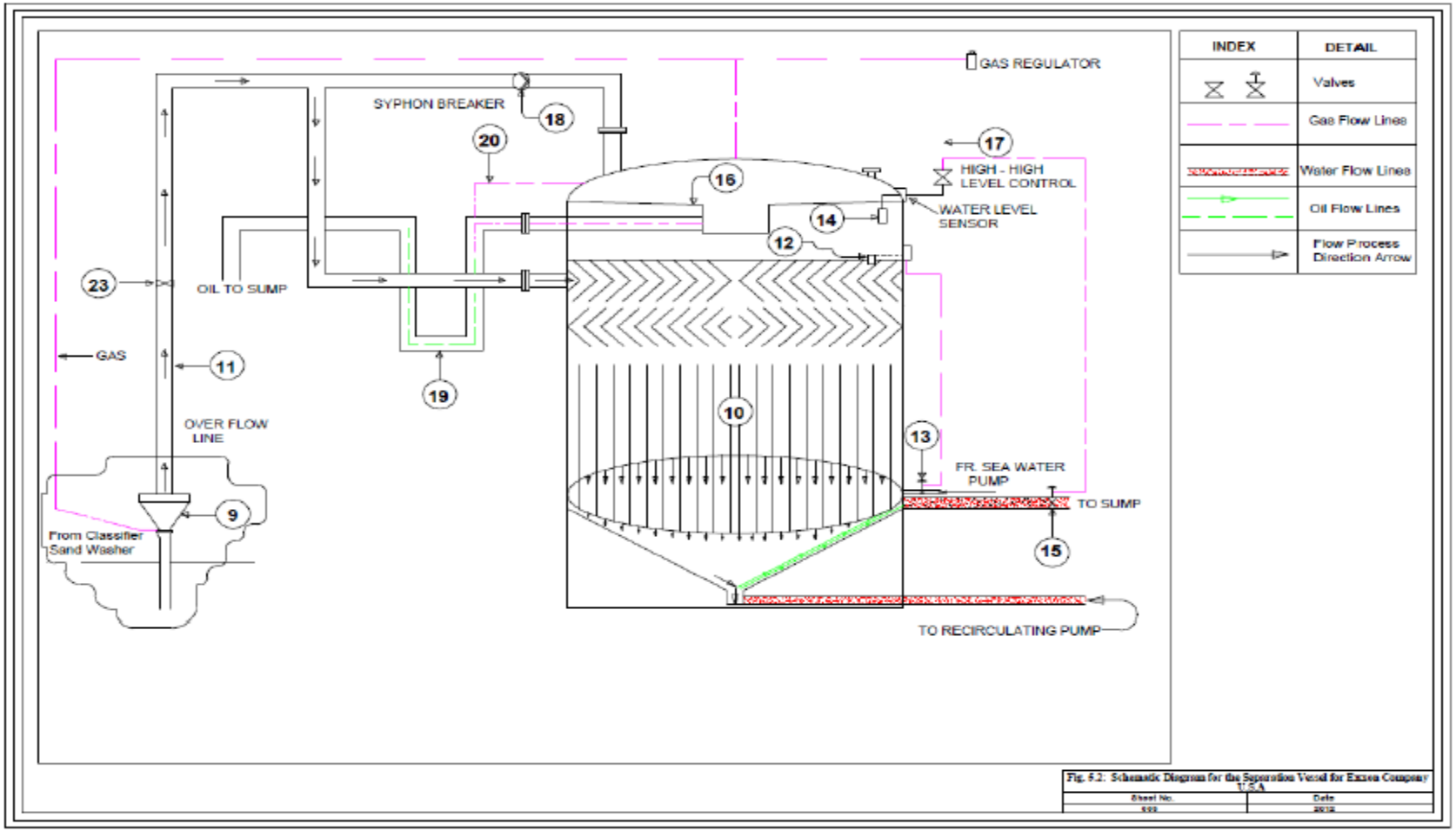

Figure 4. Schematic diagram for the Separation Vessel for Exxon Company USA [14]

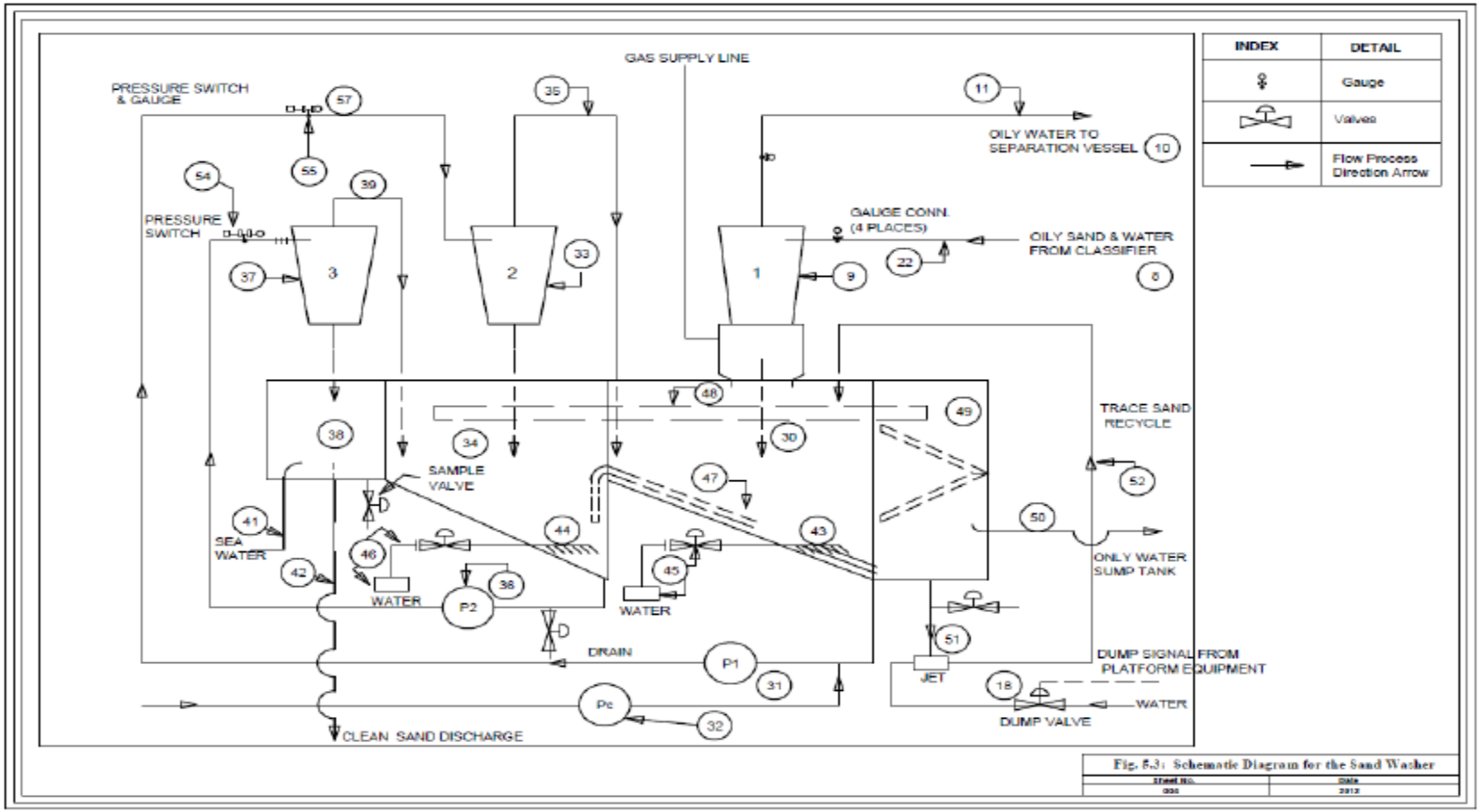

Figure 5. Schematic Diagram for the Sand Washer [14]

From the compartment, the sand moves to the suction end of the number one pump where sand cleaning chemicals are added. Sand, water and the chemicals then move to the number two cyclone (33) where the actual washing and separation takes place. Through the overflow line (35) the oil, water with the dispersed air moves to the compartment (30) while the sand is discharged into the compartment (34) that is introduced into number three cyclone (37). While the sand moves into the flush troughs (38), the water returns back to the compartment (34). Seawater then enters into the flush trough and the compartment where the sand is carried to the gulf. The valve rotameters (45 and 46) regulates the volume in each container, while the sand is collected at the bottom of the separation compartment

After several days of operation, Table 2 highlights several problems encountered and the ways they were solved [14].

Table 2. Problems and solution for Grand Isle Block and West Delta 73 A-D Platform

S/N	Problems encountered	Solution(s)
1	Erosion occurred due to leakages in the pump and wearing of the cone, which resulted in the failure of the unit within two months of operation.	Cone erosion was reduced by substituting the rubber liners with highly reliable polyurethane liners.
2	Leaking/ wearing of the shaft occurred due to the migration of sand from the pump	Regular replacement of the liners and packing's
3	A major pump failure occurred after ten months of operation which was caused by the combination of erosion and corrosion	Ceramic-coated plastic sealed housing was used to handle the issue of both corrosion and erosion. Ceramic has a high resistance to erosion but susceptible to corrosion while the plastic material, on the other hand, is not resistant to erosion but prevents the fluid from having surface contact with the coated metals thereby preventing corrosion
4	Sulphate reducing bacteria growth began to surface around the stagnant corners of the sand washer. This was due to the usage of the sea water that contained a lot of bacteria	Continuous injection of water between the gland and the seal section of the pump was done.

3.2. South Pass 98 Field

South pass 98 fields is sited in the Gulf of Mexico oil production facility and has 41 production wells. They encountered operational problems such as emulsion stabilization, erosion and equipment plugging. These occurred because of the continuous passing of produced solid through a corrugated plate interceptor, which led to a decline in the efficiency of the separator [5]. A sand handling system, as shown in Figure 6 below, was designed following the five basic steps (separation, collection, cleaning, De- watering and Haul aging) [5]. It is simple to operate, requires minimal human intervention and minimal footprint.

The de-sander starts operation once process fluid is passed through it, and the required pressure drop (40psi) has been obtained. Although the disk valve is configured to open every 10seconds to discharge its content, care has to be taken to ensure drainage of excess liquid to the collection bin does not occur. The dumped slurry is taken to the DOT (department of transport) bins, which drains the liquid via porous standpipe drains while the solid is retained. The bin continuously receives this slurry at regular interval until it reaches a gross limit of 7,700lbm and a tare weight of 1,100lbm. Table 3 highlights the problems that were encountered during operation and the ways they were tackled [5].

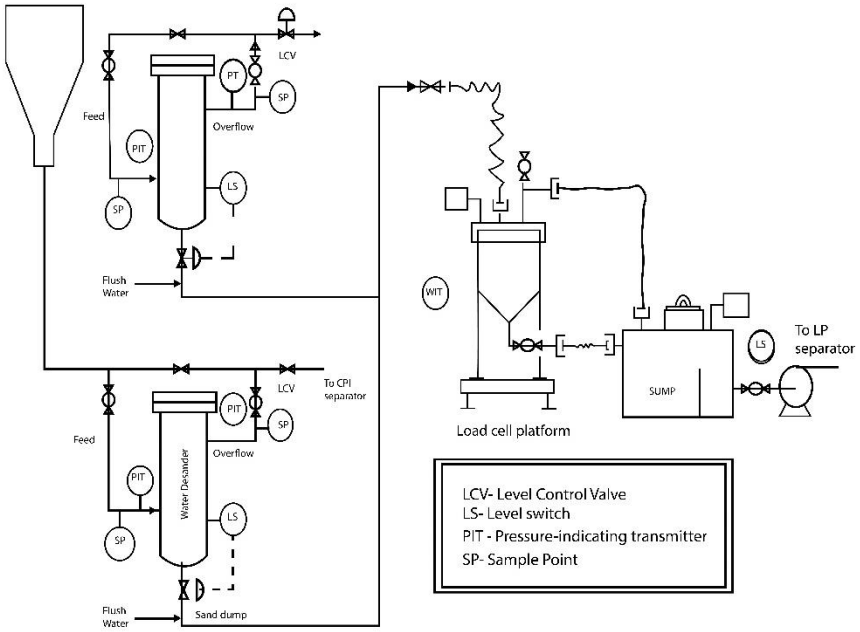

Fig. 6. South Pass 98 Field oil de-sander with integral solid dewatering and haulage system [5]

Table 3. Problems and solutions on the South Pass 78 Field

S/N	Problems encountered	Likely cause(s)	Solutions
1	An increment in the pressure drop at the initial stage of the operation when different levels of surges were experienced.	The high flow rate was suspected to be the cause, as the start- up was 13,300bpd while the measured flow rate was 16,000 bpd	Four blanks were replaced with active liners which reduced the pressure drop to 35psi
2	The dump valve refused to operate automatically, even though the sand level was found to be 3 inches above the sand probe	The probe calibration of the valve was done with tap water, and beach sand as produced solid was not available during the time of calibration	Proper calibration of the valve was done with the de-sander sample before it was put back into operation
3	After several weeks, the high pressure drop was again experienced at the water de-sander	This was solely due to the addition of more wells	An ultrasonic flowmeter was used to measure the flowrate of both the inlet and the outlet where a net flowrate was established as 20,000bpd. All blanks in the system were also replaced with active liner
4	Drainage problem surfaced at the DOT (Department of Transport) bin	Flexible drain hole was too long and badly located at the bin intervals and connections. This resulted in a 10-12ft drop below the sump level which brought back pressure to the bin	The hose was replaced and later inspected for blockage
5	Plugging of the drain screen was observed	Presence of big particles of sand	The tapping of the hard drain pipe proved as a temporary solution while the instalment of two different sized pneumatic vibrators directly below the bin proved a permanent solution
6	Dump valves open without indication of liquid flow	The drained pipe was filled with sand, caused by the insufficient slope in the drain pipe allowing the sand to accumulate in the drain line	The slight slope was added to the drain line that assisted in the flow of slurry

3.3. Installation of New Generation De-sander System at Albacora Deep Water Field

The Albacora field composed of sixty- five wells with two production units (5000bbld). The production unit includes a semi- submersible platform and a Floating Production Storage and Offloading (FPSO) platform. During the production of oil and gas, they experienced a decline in both the residence time and the rate of production [13]. Series of investigations were carried out where it was observed that the recession was caused due to the accumulation of sand in the production separator. In addition, erosions of pumps, valves, and other accessories were experienced, which led to the shutting down of the plant at regular intervals. More bills were incurred for clean out, labour, and disposal cost. The new generation de-sander system was installed on both platforms where a field test was carried out to verify the reliability of the system and to ensure that no form of an emulsion or solid entrainment will occur [13].

The separation process was recorded to be 90% efficient while the amount of solid separated by the de-sander was as much as 145 litres per shift. The amount of solid retained at the bottom of the separator after the testing period was very insignificant as compared to other conventional methods. The outcome of the test showed that both objectives were met, which confirmed it to be both a reliable and effective method [13].

3.4. Integrated Sand Cleanout System at the Dagang Oilfield in China, 2006

Excessive leakage of the working fluid into the formation, which leads to frequent stoppage of both the separation and production process were earlier recorded which led to the installation of an integrated sand cleanout system with the following attributes as highlighted in Table 4. During the cleaning operation, the amount of work fluid circulated from the wellbore equals the amount of working fluid injected, which simply means no significance leakage of the working fluid into the formation. The volume of the sand brought to the surface was 0.86 m^3 [4].

Table 4. Designed operation parameters of Dagang Oil Well [4]

Parameters	Value	Parameters	Value
Working fluid flowrate	$416.4 m^3/d$	Carrier fluid bottom hole pressure	19.80MPa
Carrier fluid flow rate	$138.6 m^3/d$	Wellhead back pressure	0.49 MPa
Power fluid flow rate	$277.8 m^3/d$	Wellhead Pressure of Working Fluid	11.42 MPa
Jet pump throat diameter	5.47mm	Power Fluid Pressure at the Jet Pump Intake (Nozzle)	34.82 MPa
Cleanout pipe jetting nozzle diameter	1.95mm	Suction Pressure at the Pump Intake (Throat)	19.01 MPa
Jet pump efficiency	29.89%	Pump discharge pressure	24.92 MPa

4. Conclusion

Technically, the different technologies currently adopted for the proper separation, disposal and handling of solids all fall under the umbrella of production limits, convectional exclusion and inclusion methodology (de-sanders). Production limits encourage drilling of wells where there is zero or insignificant amount of sand. Wire wrap screen is effective for coarse well-sorted sands. Expandable sand screen is considered the strongest due to its collapse strength of 2500psi. Metal mesh screen records a high corrosion resistance rate and has a slimmer chance of being damaged during installation. Chemical consolidation involves sealing of the sand grains several feet down by using environmental accepted chemicals. De-sanders generally have an upper edge in terms of lesser weight, capital effective, the little cost for maintenance and operation. Dagang Oilfield, Albacora Deep water, South Pass 98 Field, Grand Isle Block 16L and West Delta 73 A-D Production Platforms were cases studied that reflected their strength, weakness and general suitability.

Acknowledgement

I want to express my deep and profound appreciation to my supervisor Professor Howard Chandler from the University of Aberdeen, Scotland, for his invaluable contribution to the success of this review.

My special thanks to the management of Covenant University, Nigeria for providing an enabling environment for this research.

References

[1] Abdel-Aal HK, Mohamed A, and Fahim MA. Petroleum and Gas Field Processing. Marcel Dekker: New York 2003, ISBN: 0824709624.
[2] Havard D. Oil and Gas Production Handbook. ABB 2006, ISBN: 978-82-997886-3-2.
[3] Rawlins CH, and Hewett TJ. A Comparison of Methodologies for Handling Produced Sand and Solids to Achieve Sustainable Hydrocarbon Production. In: European Formation Damage Conference. Scheveningen 2007, Netherlands, 30 May- 1 June. SPE 107690.
[4] Chen S, Yang D, Zhang Q, and Wang J. 2007. An Integrated Sand Cleanout System by Employing Jet Pumps. Journal of Canadian Petroleum Technology, 2017; 48(5). PETSOC-09-05-17-TN, DOI: https://doi.org/10.2118/09-05-17-TN.
[5] Rawlins CH, Staten SE, and Wang II. Design and Installation of a Sand Separation and Handling System for Gulf of Mexico Oil Production Facility. In: SPE Annual Technical Conference and Exhibition. Dallas, Texas, 1-4th October 2000. Society of Petroleum Engineers. SPE 63041MS. DOI: https://doi.org/10.2118/63041-MS.
[6] Al-Baggal ZA, Al-Refai I, and Abbott JW. Unique Expandable Sand Screen and Expandable Liner Hanger Completion for Saudi Aramco 2006.
[7] Matanovic D, Cikes M, and Moslavac B. Sand Control in Well Construction and Operation. Springer Environmental Science and Engineering, 2012 ISBN 978-3-642-25613-4. DOI 10.1007/978-3-642-25614-1.
[8] Williams K. Selection and Design Criteria for Sand Control Screens. In: SPE Distinguished Lecturer Series. Houston, Texas, 13th March 2008. Society of Petroleum Engineers.
[9] Gillespie G, Beare SP, and Jones C. Sand Control Screen Erosion- When are you at Risk? In Eight European Formation Damage Conference 2009. Society of Petroleum Engineers.
[10] McReynolds PS. Gravel Packing Controls Unconsolidated Sand in Venezuela Field, 1958.
[11] Kotlar HK, Moen A, Haavind F, and Strom S. Field Experience with Chemical Sand Consolidation as a Remedial Sand Control Option. In: Offshore Technology Conference, Houston, Texas. 5-8 May 2008. Offshore Technology Conference. OTC- 19417-MS. https://doi.org/10.4043/19417-MS.
[12] Ditria JC, and Hoyack ME. The Separation of Solids and Liquids with Hydrocyclone Based Technology for Water Treatment and Crude Processing. In: SPE Asia Pacific Oil and Gas Conference, Melbourne, Australia. 7-10 November 1994, SPE 28815.
[13] Coffee SD. 2008. New Approach to Sand Removal. In: Offshore Technology Conference, Houston, Texas. 5-8 May 2008, OTC 199465.
[14] Juan AG. 1974. A System for Removing and Disposing Of Produced Sand. Journal of Petroleum Technology; 1974; 26: 450-454. Society of Petroleum Engineers. SPE- 4014PA. https://doi.org/10.2118/4015-PA.

To whom correspondence should be addressed: Dr. Angela Onose Mamudu, Department of Chemical Engineering, Covenant University Ota, Nigeria

Petroleum and Coal

Article **Open Access**

EVALUATING THE PERFORMANCE OF *CALOPHYLLUM INOPHYLLUM AND HURA CREPITANS* PLANT OIL ON THE RHEOLOGICAL AND FILTRATION PROPERTIES OF WATER-BASED MUD

C. Y. Onuh[1], A. Dosunmu[2], P. A. L. Anawe[1], S Agbator[1]*

[1] *Department of Petroleum Engineering, Covenant University, Ota, Nigeria*
[2] *Department of Petroleum and Gas Engineering, University of Portharcourt, Nigeria*

Received March 11, 2019; Accepted May 21, 2019

Abstract

The performance of drilling mud is a function of the rheological and filtration properties, if these properties are not properly managed, could lead to drilling challenges. This research work is aimed at evaluating the potential of plant oils in the rheological and filtration properties of the water-based mud. In this experiment, the *Calophyllum inophyllum and Hura crepitans* were extracted from their seeds using a Soxhlet extractor and a distillation apparatus. Water-based mud was formulated using bentonite, carboxyl-methyl-cellulose (CMC), potassium hydroxide (KOH), deionized water, and the diesel oil, *Calophyllum inophyllum and Hura crepitans* oil was added in 5, 10, to 25 ml concentrations. The flash point, fire point, specific gravity, emulsion stability, pH, the kinematic viscosity of oil were measured. The rheological, physicochemical, and filtration properties of the mud were also measured. The result revealed appreciable properties of *Calophyllum inophyllum and Hura crepitans* plant oil are within and close to the ASTM standard. The plant oils are better fluid loss controllers than the diesel oil as they reduced the volume of fluid loss when added to ordinary water-based mud. *Hura crepitans* oil-in-water emulsion mud had relatively acceptable rheological properties than the *Calophyllum inophyllum* and diesel oil-in-water emulsion mud. Increasing rheological properties was observed as the concentration of the *Calophyllum inophyllum*, *Hura crepitans*, and diesel oil was increasing.

***Keywords**: plastic viscosity; yield point; gel strength; fluid loss; water-based mud.*

1. Introduction

Drilling mud is used in drilling operations whether offshore or onshore, to control or prevent so many unwanted challenges during drilling such as kicks and blow out, control formation pressure, maintain well integrity and prevent well collapse. The use of drilling mud in carrying out drilling operations is mainly for transportation, suspension and dropping off cuttings, supporting walls of the wellbore, lubricating the drill string thereby reducing friction, controlling pressure, and wellbore stabilization [1]. Oil based mud systems such as the diesel oil based mud or that of the synthetic are made to withstand certain undesired characteristics of water-based mud (WBM). This is basically because of the properties of water to break up salts, meddle with a stream of oil and gas through porous rocks, advance the crumbling and spreading of clays, and to react with shale resulting to swelling [4]. The use of oil based mud (OBM) has demonstrated compelling effects throughout the years. Nevertheless, they are costlier with potential contamination or pollution issues; this makes OBM a challenging decision for environmentally delicate regions.

Oil based drilling mud are in varying degree of toxicity; it is quite costly to handle in an environmentally friendly manner. The disposal of water-based mud is preferrably due to its low cost of formulation, less aromatic contents and toxicity, and low cost of disposal [5]. Hence, improving the technical performance of water-based mud will enhance their application since they have acceptable cost and environmental characteristics. The rheological and filtration properties of drilling mud are one of the mud properties that determine their performance in

drilling operations [6]. Agricultural waste materials used in water-based mud have proved to be of technical benefit; they have been used to improve the rheological behaviour of mud and the filtration properties [9]. Plant oil has also been introduced in drilling mud formulation; they are known to be prospective environmentally friendly potential lubricant oil in WBM wit. They have lesser toxic content, low cost of production, with synonymous potential lubricity as the OBM [2-3]. The linear swelling test was carried out on shale samples in the presence of de-ionised water-based mud by [7], the interaction between the shale samples and mud caused swelling of the shale after been immersed for 24 hours. The introduction of plant oils in WBM is sometimes to reduce the mud fluid loss and minimize the interaction between the shale and mud, thereby inhibiting potential swelling. Plant oils have been introduced in water-based mud to measure the lubricity performance and ability to reduce the physicochemical interaction between the shale and mud filtrate [8], the plant oil reduced the interaction and further minimized the swelling rate of the shale when immersed in the mud filtrate. This work is focused on evaluating the effect of *Hura crepitans* and *Calophyllum inophyllum* plant oil on the rheological properties of water-based mud.

2. The rheological properties of drilling mud

The rheological and filtration loss properties are vital parameters of mud which determines the performance of the drilling mud. One important function of drilling mud is to clean the wellbore hole, suspend and carry cuttings to the surface. It is the rheological property that determines the cutting carrying capacity of cuttings to the surface, and are also used in analysing the equivalent circulating density, hole cleaning, barite sag, and surge pressure. It also determines the rate of penetration of drill bit and filtrate loss into the formation. The higher the fluid loss into the formation, the potential it is for the mud to form cakes on the wall of the formation, causing stuck pipe [6]. The rheology affects the differential pressure in the drill-pipe and the annulus, and by so doing affects the pumping rates and pressure required to initiate mud flow. The rheological properties are the plastic viscosity, gel strength, and yield point.

2.1. Plastic viscosity of drilling mud

The plastic viscosity relates to the resistance of fluid flow due to mechanical friction. The higher the plastic viscosity of the mud, the more viscous it is and difficult it is to initiate flow; hence, hole cleaning and cuttings transportation to the surface will be challenging. High viscous mud directly impacts on the frictional pressure drop, and this proportionally increases the pump rate required to flow the mud into the hole and up the annulus. The increase in pump rate of the mud will cause a corresponding increase in the cost of pumping the fluid, which may un-intentionally fracture the formation leading to wellbore instabilities. The higher the plastic viscosity, the higher the equivalent circulating density, the higher the surge and swab pressures, the higher tendency for differential pipe sticking due to possible, solid content, and the lower the rate of drill bit penetration.

2.2. Yield point of drilling mud

One important function of drilling fluid is in the lifting of cuttings to the surface; the Yield stress determines the capacity of the mud to carry cuttings generated during drilling to the surface under a dynamic condition. It is the yield stress extrapolated to a shear rate of zero. Hence, tt is the initial stress required to move the fluid into motion.

2.3. The gel strength of drilling mud

The gel strength is the shear stress of drilling mud that is measured at the low shear rate when static for a certain period. It is used to evaluate the forces binding the mud particles together, and by so doing, determines the setting rate of cuttings in the drilled hole. The gel strength is the mud property that determines mud capacity to suspend cuttings when circulation is static.

2.4. Fluid loss properties of drilling mud

The filtration or fluid loss property is also an important property in determining the performance of mud; there are two types called the API and HPHT fluid loss test. The previous measures the volume of fluid loss at ambient temperature and pressure of 100 psi while the latter determines the fluid loss at high temperature and pressures. Good drilling mud has a lower fluid loss, which leaves a thin and impermeable cake, but a poor drilling mud usually has a higher fluid loss, leaving thick and permeable cake from the mud. This thick cake has the possibility of causing pipe sticking as a result of the large contact area of the cake between the formation and the pipe [8].

3. Materials and methods

The seeds of *Hura crepitans* and *Calophyllum inophyllum* were harvested from the vicinity of Covenant University, Ota, Ogun State, Nigeria. It was then dried, cleaned, pilled, and pulverized for oil extraction. The extraction method is as stated below.

3.1. Extraction of oil from their seed

The oil extraction from the pulverized seed samples was done using the chemical extraction method, where 60 g of the pulverized seed was measured and packed into a thimble, and then into the Soxhlet extractor apparatus containing 250 mL of N-Hexane in the round bottom flask. The Soxhlet apparatus was then mounted on a heating mantle, controlled at 69°C and allowed to reflux for about two hours. The liquid containing the seed extract and solvent was filtered to remove impurities and evaporated using a distillation evaporator set up to remove the solvent. The percentage of oil yield was calculated by measuring the weight of the oil recovered and dividing by the weight of the seed samples used. The seed in its fresh form, dried/oven dried form, pulverized form, and extracted *Hura crepitans* oil (HCO) and *Calophyllum inophyllum* oil (CIO) are as shown in Figure 1 and Figure 2 respectively.

Figure 1. The seed and oil of *Hura crepitans*

Figure 2: The seed and oil of *Calophyllum inophyllum*

3.2. Properties of the oil samples

American Society for Testing and Materials was employed in measuring the following properties: viscosity index was measured using the kinematic viscosity tester, flash and fire point using the open cup flash point tester, oil density/specific gravity using the density bottle, and pH using the pH meter.

3.3. Preparation of mud samples

20 grams bentonite, followed by 2 grams CMC, and 0.2 grams KOH additives was poured in intervals of 20 minutes into a mixer containing 350 ml of deionized water. The rheological and filtration properties were measured, and oil samples of diesel, *Hura crepitans*, and *Calophyllum inophyllum* were added to the ordinary water-based mud at different concentrations of 5mL, 10mL, 15ml, 20mL, and 25mL. This is to measure the effect of the oil on the rheological and filtration properties. Other mud properties such as the mud density, electrical stability, and cake thickness were also measured.

4. Results and discussions

4.1. Analysing the properties of the oil samples

Table 1 shows the properties of the extracted *Calophyllum inophyllum* (CIO) and *Hura crepitans* (HCO) oil.

Table 1. Physicochemical properties of the oil samples

Properties	*Calophyllum inophyllum* oil	*Hura crepitans* oil	ASTM D6751
Flash point (°C)	164	204	≥120
Fire point (°C)	172	260	≥93
Density (kg/m^3)	923	908	860-900
Kin. viscosity at 40 (°C)	32.52	28.60	1.9-6
Viscosity index	163	167	-
Colour	Greenish black	Orange	

The flash and fire point conforms to the API standard. Hence, the plant oil samples are less volatile or flammable if used in a volatile environment. The density of *Calophyllum inophyllum* and *Hura crepitans* plant oils are higher than that of the ASTM standard. However, the density of the *Hura crepitans* oil is closer than that of the *Calophyllum inophyllum* oil. The kinematic viscosity of *Calophyllum inophyllum* oil was higher than of *Hura crepitans*, resulting in a higher viscosity index than the *Hura crepitans*. This property infers *Hura crepitans* oil is more thermally stable than the *Calophyllum inophyllum* oil.

4.2. Analysing the properties of the mud samples

Table 2 below shows the properties of the ordinary water-based mud without the application of the oil samples. The mud properties apart from the volume of the fluid loss are within the API standard range, the filtrate recovered from the ordinary WBM has a higher volume of fluid loss than the standard. The higher the mud fluid loss, the tendencies for more of the deposited thick filter cakes on the formation, the negative tendencies of this is pipe sticking and formation damage. The cake thickness is considered acceptable since it is not greater than 2/32". The rheological properties are also within the API standard with lower plastic viscosity value

Table 2. Properties of ordinary water-based mud without any oil

Properties	Value	API
pH	9.58	8.5-10
Mud density (ppg)	8.6	7.5-22
Specific gravity	1.02	-
Filtrate loss after 30 mins (mL)	26	10-25
Electrical stability (ES)	55	< 400
Gel strength @ 10 secs ($Ibf/100ft^2$)	16	3-20
Gel strength @ 10 min ($Ib/100ft^2$)	17	8-30
Plastic viscosity ($Ib/100ft^2$)	2	< 65
Yield point ($Ib/100ft^2$)	38	15-45
Cake thickness (1/32'')	≈ 2/32"	2/32"

Table 3 shows the properties of water-based mud formulated with diesel oil ranging from 5 to 25 mL. The pH, mud density, specific gravity, electrical stability, and gel strength were increasing with the concentration of the diesel oil. The increases of the mud properties are still within the API standard. Increase in the pH values makes the mud more alkaline, thereby reducing the rate of corrosion. Increase in the electrical stability denotes the emulsion stability between the mud components. Increase in the gel strength implies increases tendency in the suspension of cuttings when circulation is stopped. A decrease in the fluid loss was observed with increase oil quantity. However, the fluid loss remains constant between 10 and 20 mL, and cake thickness increased from 15 to 25 mL of the diesel oil in the water-based mud.

Table 3. Properties of WBM formulated with diesel oil

Properties	5 mL	10mL	15 mL	20 mL	25 mL	API
pH	9.35	9.42	9.56	9.68	9.87	8.5-10
Mud density (ppg)	8.20	8.50	8.50	8.55	8.60	7.5-22
Specific gravity	0.98	1.20	1.20	1.25	1.30	-
Filtrate loss after 30 mins (mL)	20	19	19	19	18	10-25
Electrical stability (ES)	94	99	105	107	112	< 400
Gel strength @ 10 secs ($Ibf/100ft^2$)	8	6	15	21	21	3-20
Gel strength @ 10 min ($Ib/100ft^2$)	9	9	15	21	22	8-30
Plastic viscosity ($Ib/100ft^2$)	7	15	8	10	11	< 65
Yield point ($Ib/100ft^2$)	16	5	24	34	34	15-45
Cake thickness (1/32'')	≈ 2/32"	≈ 2/32"	> 2/32"	> 2/32"	> 2/32"	2/32"

Table 4 shows the properties of water-based mud formulated with extracted oil from the seed of *Calophyllum inophyllum* ranging from 5 to 25 mL. The trend of the pH, mud density, emulsion stability, and specific gravity was not as stable as that of the diesel oil-in-water

emulsion mud. An increase in the mud properties is seen in oil concentration of 5 to 10 mL, while a decrease is seen in the 15 and 20 mL the fluid loss decreases with increase in the oil concentration of the oil. The mud properties, however, are still within the API range.

Table 4. Properties of WBM formulated with oil from *Calophyllum inophyllum*

Properties	5 mL	10mL	15 mL	20 mL	25 mL	API
pH	9.25	9.54	8.50	8.48	8.77	8.5-10
Mud density (ppg)	8.20	8.50	8.10	8.10	8.40	7.5-22
Specific gravity	0.99	1.02	0.98	0.98	1.01	-
Filtrate loss after 30 mins (mL)	22	21	21	18	17	10-25
Electrical stability (ES)	87	106	108	177	223	< 400
Gel strength @ 10 secs ($Ibf/100ft^2$)	12	23	24	23	25	3-20
Gel strength @ 10 min ($Ib/100ft^2$)	13	24	23	23	25	8-30
Plastic viscosity ($Ib/100ft^2$)	8	11	11	8	12	< 65
Yield point ($Ib/100ft^2$)	25	30	35	42	36	15-45
Cake thickness (1/32″)	≈ 2/32″	> 2/32″	> 2/32″	> 2/32″	> 2/32″	2/32″

Table 5 shows the properties of water-based mud formulated with extracted oil from *Hura crepitans* ranging from 5 to 25 mL. The mud properties reveal an unstable trend similarly with the *Calophyllum inophyllum* oil. However, they are still within the API range. The fluid loss decreases with the concentration of the plant oil. The cake thickness increased beyond the API standard.

Table 5. Properties of WBM formulated with oil from *Hura crepitans*

Properties	5 mL	10mL	15 mL	20 mL	25 mL	API
pH	9.14	8.92	8.83	8.87	8.86	8.5-10
Mud density (ppg)	7.80	8.35	8.40	8.60	8.60	7.5-22
Specific gravity	0.94	0.99	1.01	1.03	1.03	-
Filtrate loss after 30 mins (mL)	21	20	18	16	15	10-25
Electrical stability (ES)	58	95	95	109	112	< 400
Gel strength @ 10 secs ($Ibf/100ft^2$)	13	11	19	18	14	3-20
Gel strength @ 10 min ($Ib/100ft^2$)	15	12	20	18	12	8-30
Plastic viscosity ($Ib/100ft^2$)	15	11	8	21	21	< 65
Yield point ($Ib/100ft^2$)	26	18	30	14	14	15-45
Cake thickness (1/32″)	15	12	20	18	12	8-30

From the mud properties in Tables 2, 3, 4, and 5, it was discovered that the ordinary water-based mud had a higher fluid loss than the various oil-in-water emulsion mud (Tables 3, 4, and 5). The fluid loss at 25 mL of *Calophyllum inophyllum* and *Hura crepitans* oil was better than that of diesel oil, revealing the high fluid loss is preventing the property of plant oil over the diesel oil.

4.3. Analysing the effect of the emulsion oil on the rheological properties

The effect of the oil samples was tested on the rheological properties of the formulated drilling mud. The plastic viscosity, yield point, and 10 s/10 min gel strengths were tested and calculated at room temperature. The diesel oil, *Calophyllum inophyllum* oil, and *Hura crepitans* oil samples were added to the water-based mud from 5 to 25 ml concentration, and rheological analysis was measured and calculated. Figure 3 is a plot of plastic viscosity for the ordinary water-based mud, diesel oil-in-water emulsion mud, *Calophyllum inophyllum* oil-in-water emulsion mud, and *Hura crepitans* oil-in-water emulsion mud. It can be observed that the ordinary water-based mud had the lowest plastic viscosity value. It was also observed that all the oil-in-water emulsion mud had increasing plastic viscosities with increasing oil concentration. The *Hura crepitans* having the highest, followed by the *Calophyllum inophyllum*, and diesel oil. Increase in plastic viscosities as lubricating oil is added to drilling fluid is undesirable. Hence, the plastic viscosities value with diesel and *Calophyllum inophyllum* have acceptable

values. It was also noted that the plastic viscosity values are still within the API standard (<65).

The effect of the oil samples on the yield point values are as shown in Figure 4**,** the yield point values for ordinary WBM, WBM with diesel oil, WBM with *Calophyllum inophyllum* oil, and WBM with *Hura crepitans* oil are within the API standard of 15-45 $(Ib/100ft^2)$. The oil-in-water emulsion mud with *Calophyllum inophyllum* oil and diesel oil have increasing yield point values with incran ease in the oil concentration. Increase in yield values due to lubricant application is not desirable in drilling mud, the mud with *Hura crepitans* oil have a lower yield compared to other oil samples. Hence, they are acceptable. However, the yield point values for all the oil-in-water emulsion muds are within the API standard.

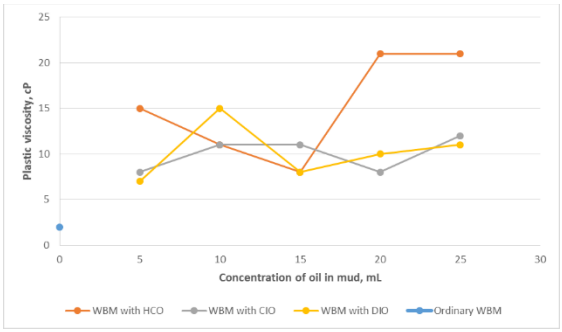

Figure 3. Plastic viscosity of the various oil-in-water emulsion mud

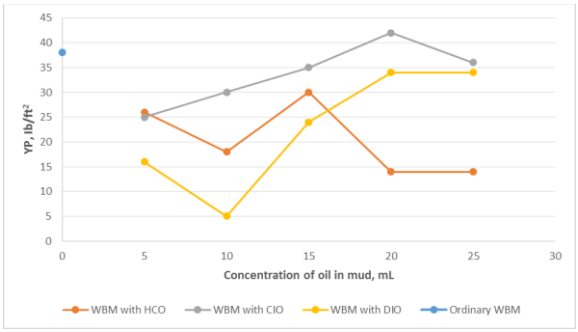

Figure 4. Yield point values of the various oil-in-water emulsion mud

The 10 s/10 min gel strength values of ordinary water-based mud, mud with diesel oil, mud with *Hura crepitans* oil, mud with *Calophyllum inophyllum* oil are shown in Tables 2, 3, 4, and 5. The gel strength values decreased when 5 mL of oil was added to the ordinary WBM, and start to increase as the oil concentration increases. The increase in the gel strength values is higher for the plant oils than the diesel oil, with *Calophyllum inophyllum* oil-in-water emulsion mud having the highest. However, the values are in the acceptable ranges of the API standard, except the 10 s gel strength of 20 and 25 ml oil concentration of the diesel oil and 10 to 25 ml of the *Calophyllum inophyllum oil*.

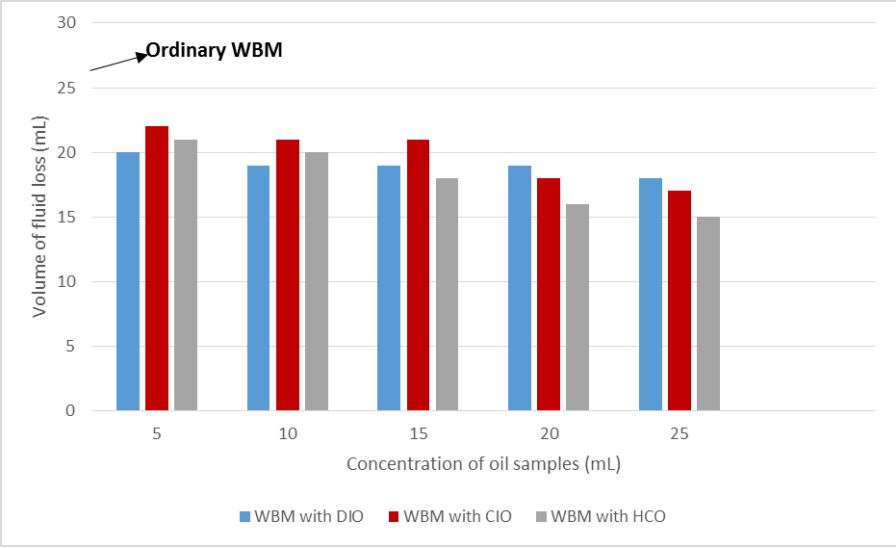

Figure 6. Volume of fluid loss of the various oil-in-water emulsion mud

4.4. Analysing the effect of the emulsion oil on the fluid loss properties

The API low temperature fluid loss of the drilling mud was tested using OFITE API filter press. The fluid loss of the ordinary water-based mud was measured, and the diesel oil, *Calophyllum inophyllum* oil, and *Hura crepitans* oil were added to the water-based mud in 5 to 25 mL. As observed from Figure 6**,** the fluid loss generally reduces with an increase in the volume of the oil for all samples. The ordinary WBM formulated without any oil has the highest volume of fluid loss (26 mL). The fluid loss decreased in addition to the oil samples. The diesel oil-in-water emulsion mud had the lowest fluid loss when 5 and 10 mL of oil was applied. The *Hura crepitans* oil-in-water emulsion mud reveals a lower fluid loss from 15 to 25 mL of the oil samples. The WBM formulated with *Hura crepitans* oil has a lower fluid loss than others, implying its ability to reduce tendencies of leaving the thick cake on the formation. The fluid loss reduces from an oil concentration of 15 to 25 mL.

5. Conclusion

In this study, the effect of diesel oil and two non-edible plant oil extracted from *Calophyllum inophyllum, Hura crepitans* seed was investigated on the rheological and filtration properties of water-based mud. The effect of the oil samples was also measured on the mud properties.

The application of the diesel oil in the water-based mud caused an increase in the pH, mud weight, specific gravity, and emulsion stability. The plant oils in the water-based mud were sensitive to the concentration of the oil as they increased and decreased at some concentrations.

The emulsion stability of all mud samples increased with the oil concentration. Mud formulated with *Hura crepitans* oil performed well in reducing the volume of fluid loss than that of *Calophyllum inophyllum*.and diesel oil. However, the plant oils are better fluid loss controllers than diesel oil. *Hura crepitans* oil-in-water emulsion mud reveals more stable and acceptable rheological properties than other oil samples

References

[1] Darley HCH, and Caenn R. Composition and properties of drilling and completion fluids. Waltham, USA: Gulf Publishing Company 2011, Book Division.

[2] Dosunmu A, and Joshua O. Development of environmentally friendly oil based mud using Palm-oil and groundnut-oil. In 34th Annual SPE International Conference and Exhibition (pp. 1–9). Calabar 2010, Nigeria: Society of Petroleum Engineers.

[3] Fadairo A, Falode O, Ako C, Adeyemi A, and Ameloko A. (2012). Novel formulation of environmentally friendly oil based drilling mud. Covenant Journal of Engineering and Technology, 2012; 1(1) INTECH.

[4] Friedheim J, and Candler J. The Base fluid dilemma : What can we use and where can we use It?. In AADE Fluids Conference and Exhibition (pp 1-6). Houston 2008, Texas: American Association of Drilling Engineers.

[5] Ismail AR, Hadi A, Rosli W, Sulaiman W, and Zaidi M. Drilling fluid waste management in drilling for oil and gas wells. Chemical Engineering Transactions, 2017; 56: 1351–1356.

[6] Tehrani A. Behaviour of suspensions and emulsions in drilling fluids, Annual Transactions of the Nordic Rheology Society, 2007; 15, 1-9.

[7] Okoro EE, and Dosunmu A. (2014). Experimental analysis of shale for evaluating shale drilling fluid interaction in Agbada formation. British Journal of Applied Science and Technology, 2014; 4(35): 4878–4908.

[8] Onuh CY, Dosunmu A, Anawe PAL, Ogunkunle TF, Rotimi OJ, and Ogbogu N. (2017). Experimental study of the swelling capacity of Ewekoro shale, south western Nigeria: Case study-using oil-in-water emulsion mud, Pet Coal, 2017; 59 (5): 653-661.

[9] Onuh CY, Igwilo KC, Anawe PAL, Olakunle D, and Omotoke O. (2017). Environmentally friendly fluid loss control agent in water-based mud for oil and gas drilling operations, Int. J. Appl. Eng. Res., 2017; 12(8): 1520–1523.

To whom correspondence should be addressed: Dr. C. Y. Onuh, Department of Petroleum Engineering, Covenant University, Ota, Nigeria, e-mail: charles.onuh@covenantuniversity.edu.ng

Petroleum and Coal

Article **Open Access**

PETROGRAPHIC AND PALYNOLOGICAL ANALYSES OF THE EZE-AKU GROUP IN AKPOHA AND ENVIRONS, SOUTHERN BENUE TROUGH, NIGERIA

O. N. Ikegwuonu[1], O. I. Chiaghanam[2], K. K. Nwozor[2], C. U. Ibe[3], K. C. Chiadikobi[2], and E. U. Aniwetalu[1]*

[1] *Department of Physical & Geosciences, Godfrey Okoye University, Enugu, Nigeria*
[2] *Department of Geology, Chukwuemeka Odumegwu Ojukwu University, Uli, Anambra State, Nigeria*
[3] *Departmentof Geology, University of Nigeria, Nsukka, Nigeria*

Received February 13, 2019; Accepted April 30, 2019

Abstract

Cretaceous sediments outcropped extensively in the Abakaliki sedimentary basin.Petrographic and palynological analyses of selected outcrop samples from Akpoha and environs were carried out, using the conventional method of acid macerationin order to re-establish the depositional history of the sediments in the area and their provenance, establish the age of sediments and reconstruct their paleoenvironments of deposition, and evaluate the hydrocarbon source rock potential. Lithological units encountered include sandstones, shales, mudstones, and limestone. Result from sandstone petrography shows that most of the sandstones in the area were mostly derived from the metamorphic /igneous basement sources, and were deposited in a very low energy environments where sediments are rapidly deposited with little reworking. Palynological investigation revealed a Late Cenomanian - Middle Turonian age for the sediments, with the following index sporomorph assemblage: *Cretacaeiporitesscabratus, Ephedripitesmulticostatus, Cretacaeiporitesmulleri, Monosulcites* sp., *Tricolporopollenites* sp. and *Tricolpites* sp. Palynomorphs of environmental value indicated that the sediments in the area were mostly deposited under openmarine condition, with minor terrigenous input. Kerogen examination features mostly the amorphous organic matter (AOM), followed by opaque debris, giving rise to type 11 / type 111 kerogen, which are generally over mature but have potential to generate oil or gas.

Keywords: *Cretaceous; Palynomorph; Kerogen; Petrography; Paleoenvironment.*

1. Introduction

In an attempt to explore petroleum in the Anambra basin and Afikpo synclinorium by the shell D' Archy Petroleum Development Company of Nigeria (now known as Shell BP), which started in the year 1938, a lot of geological and geophysical surveys of southern Nigeria have been carried out. This led to the drilling of many test holes/wells which provided important information about the stratigraphy of southern Nigeria. Many previous research works have been undertaken on the regional scale within the Afikpo sub-basin. Simpson [1] was the first to describe the Eze-Aku Formation as comprised of hard grey to black shale, deposited in a shallow marine environment. Barber [2], Reyment [3], Murat [4], Nwachukwu [5] and Kogbe [6], established some paleontological evidence on the Turonian Eze-Aku Formation, indicated to be well developed and enriched by ammonites and other fauna such as ammonites and *Inoceramus* spp.

Reyment [3] described the Amasiri Sandstone facies exposed around Nkalagu market as the lateral equivalent of the Eze-Aku Formation and held that they might not require a separate status. He further remarked that the formation is mildly folded and the fossils are mainly Vascoceratids, pelecypods, gastropods, echinoids, fish-teeth decapod fragments, and plant fragments. Ofodile [7] established the existence of an unconformity between the Turonian Eze-

Aku Formation and the overlying Campano-Maastrichtian Nkporo Group in southern Nigeria. Petters [8] believed that the Eze-Aku and Awgu Formations are equivalent because they are indistinguishable in the field both in lithology and fauna. In the eastern flank of Abakaliki Anticlinorium, Banerjee [9-10] and Amajor [11] identified and described similar lithofacies, which were established on the western flank of the same Anticlinorium by Umeji, [12], who subdivided the Eze-Aku unit into several lithofacies, which include shales, sandstones, siltstones, and limestones. Umeji [12-13] described the ammonite paleoecology, sub-tidal shelf sedimentation and trace fossils from the Eze-Aku Formation, and assigned a shallow marine environment of deposition. She posited that at Nkalagu the Eze-Aku Group consists of a sequence of cross-bedded, medium-grained sandstone, grey bioturbated calcite-cemented siltstone, laminated dark shale, and bioclastic limestone. On the basis of palynomorphs, Ojoh [14] identified and established Cenomanian facies in Ezillo and Ohana areas as Ezillo Formation. Umeji [15] recorded the palynological evidence for the Turonian/ Campanian boundary between the Abakaliki and Anambra basin, as exposed at Leru. She remarked that the Turonian/Campanian boundary, within which reworked Turonian palynomorphs are mixed with the indigenous Campanian flora, marking the sequence boundary, and in the absence of the Coniacian-Santonian Awgu Shale, the Campanian Nkporo Shale oversteps onto the Turonian Eze-Aku Shale. *Igwe et al.*, [16] assigned a Late Cenomanian to Turonian age to the Eze-Aku Shale facies based on the planktonic foraminiferal assemblages of *Hedbergellids* and *Heterohellicids, Whitenella* and *Archeoglobelina blowi.* Igwe and Okoro [17] noted that there is underlying controversy over the status of Amasiri Sandstone (Eze-Aku Group) and the problem of misnaming of its type locality. They identified two component formations for the Eze-Aku Group in the basin: the late Cenomanian-early Turonian Eze-Aku Shale (transgressive phase) and the middle-late Turonian Amasiri Sandstone (regressive phase). The present study attempts to re-establish the depositional history of the sediments in the area and their provenance, establish the age of sediments and reconstruct their paleoenvironments of deposition, and evaluate the hydrocarbon source rock potential and the degree of thermal maturation, using the organic-walled microfossils.

2. Location and physiography

The study area is located along the Abakaliki-Afikpo Road, about 46 kilometer and 13 kilometers respectively, in Afikpo North local Government Area of Ebonyi State, in the southeastern Nigeria (Fig. 1). It lies between latitudes $5^0\,56^1$ N and $6^0\,00^1$ N and longitudes $7^0\,56^1$ E and $8^0\,00^1$ E, with an area extent of about 86 sqkm (Fig. 2 and Fig. 3). The study area is bounded on the north by Afikpo, on the south by Ndibe and on the west by Amasiri town. It covers areas such as Amata and Ekerekunta. The area has a road network and footpaths. The main road divides the area into roughly two equal parts. The major access route into the area is Abakaliki road and the Afikpo-Okigwe road (Fig. 3). The area is easily accessible through footpaths that start from the main road into the hinterland. Due to sparse vegetation, cultivated farmlands traversing the area are not difficult except in the swampy shaly terrains. The study area falls within the zone of 27°-30° of annual temperature [18]. The climate of this area is classified as a tropical wet and dry savannah climate.

3. Regional geologic setting and stratigraphy

The study area lies within the Afikpo Syncline, a depression formed in the eastern flank of the southeastern edge of the Benue Trough, as a result of Santonian tectonism and uplift of the Abakaliki Anticlinorium [19]) (Fig. 4). The area study is part of the Benue trough which is an elongated fault-bounded depression lying in the eastern and north-eastern direction containing deformed Cretaceous as well as the early Cenozoic sedimentary and volcanic rocks. Tectonism in southern Nigeria started in the early Cretaceous period, with the separation of Africa from South America and consequently the opening up of the Atlantic [5,20] (Fig. 4). Murat [4] noted the three major phases that gave rise to the formation of Abakaliki-Benue Trough, Anambra Basin and Niger Delta Basin (Fig. 4). The first phase occurred during Albian

times and was characterized by trending faults resulting in the formation of the rift like Abakaliki-Benue Trough. The second phase commenced from upper Santonian to middle Eocene time. At the end of the Eocene, the third phase occurred given rise to the formation of Niger Delta Basin.

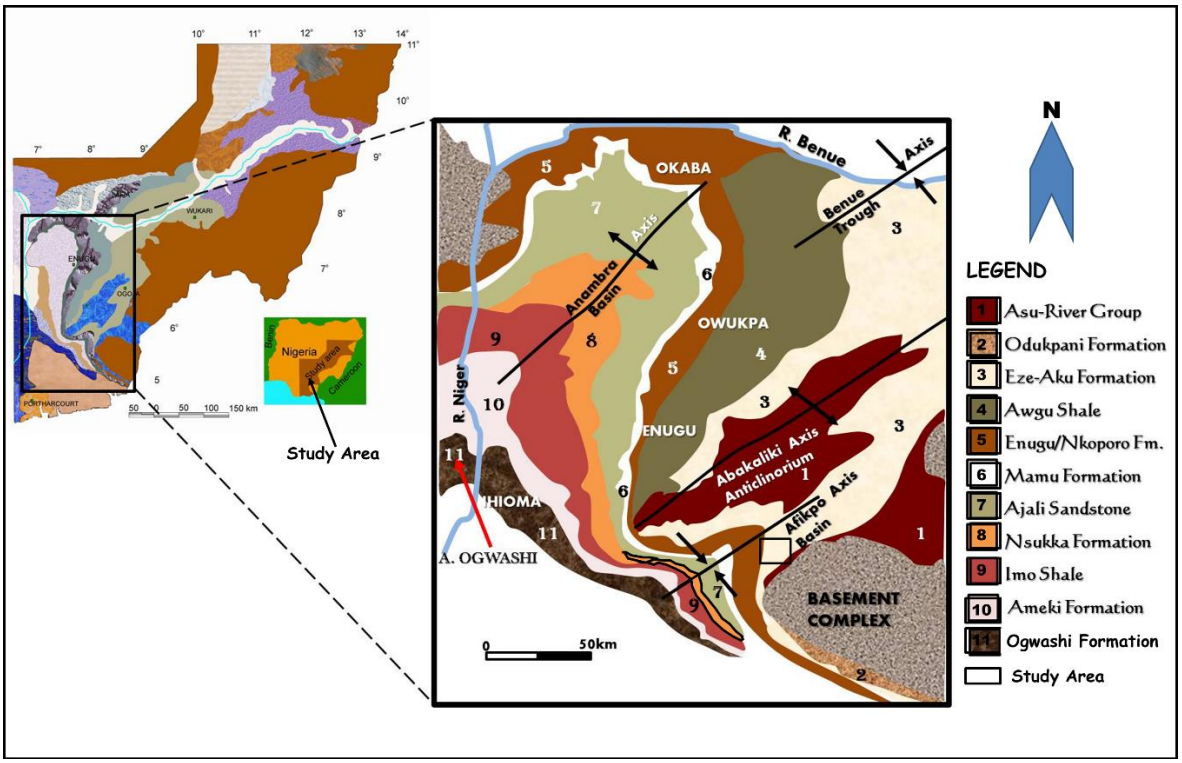

Fig. 1. Geological map southern Benue Trough showing location of study area (*modified from Ojo et al.* [38])

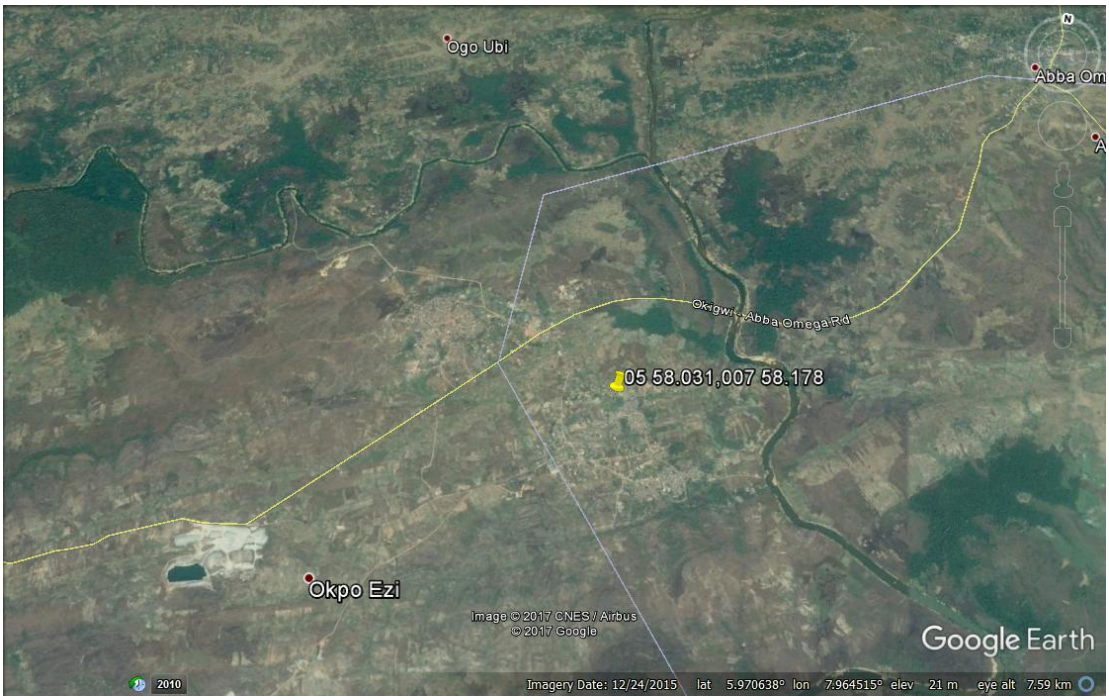

Fig. 2. Satellite imagery map showing the locations and access routes in the study area

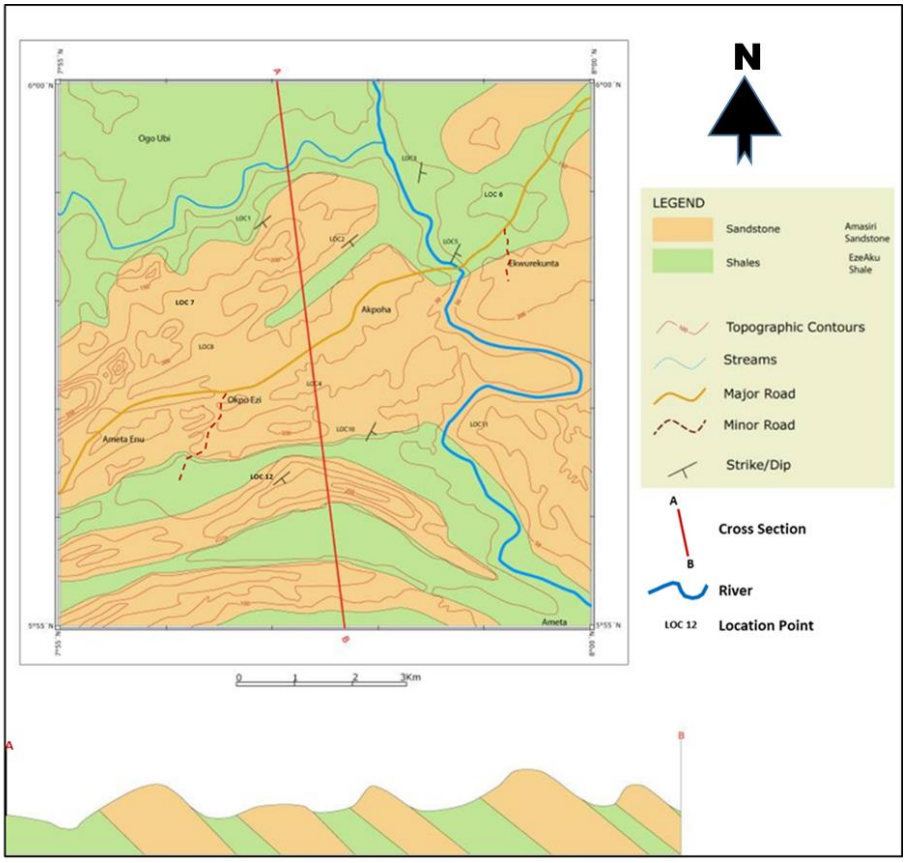

Fig. 3. Geologic map showing the cross-section of the study area

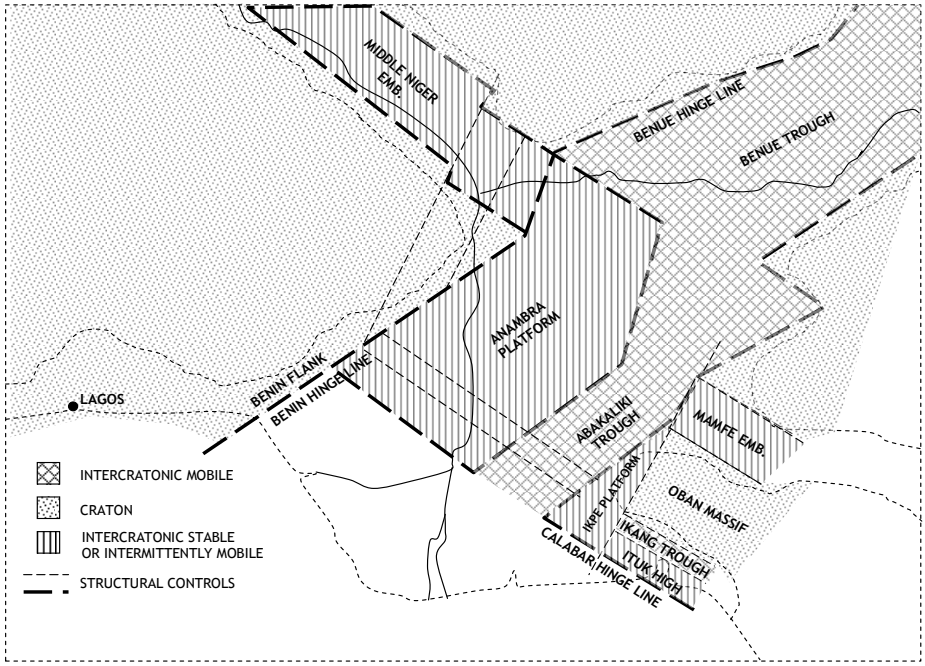

Fig. 4. Albian-Santonian Tectonic Framework for the Benue Trough (*after Murat* [19])

The sedimentation and stratigraphy of the southern Nigerian sedimentary were controlled by four transgressive-regressive cycles, which resulted from the eustatic and isostatic rise and

fall of sea levels and global tectonics (Table 1). The oldest sediments belong to the Upper Cretaceous during Albian period represented by the deposits of the Asu River Group. The Asu River Group unconformably overlies the basement rock. The Asu River Group consists of shale, sandstone and limestone beds, with a maximum thickness of about 6,000 m containing ammonites. During the Cenomanian, the regressing Sea resulted in the deposition of Odukpani Group in the Calabar Flank and Agala Formation in the Abakaiki Basin. This was followed by an extensive Turonian marine transgression, which deposited the Eze-Aku Shale, Amasiri Sandstone and Nkalagu limestone. The Turonian transgression extended into the Coniacian, with the deposition of Awgu Group in the western part of the Abakaliki Anticlinorium, whereas in part, the resultant Santonian tectonic event truncated the deposition Awgu Group, given rise to an Angular unconformity. The Uplift of the Abakaliki Anticlinorium gave rise to the contemporaneous subsidence of Anambra Basin and Afikpo sub-basin to the West and East of the Anticlinorium respectively (Table 1).

Table 1. Regional stratigraphy of southern Nigerian sedimentary basins. (*after Murat* [39])

Age	Group/Formation	Sedimentary cycle
Pliocene	Benin Formation	Niger-Delta Basin (Third sedimentary cycle)
Oligo-Miocene	Ogwasi Formation	
Eocene	Ameki Formation	
Paleocene	Imo Shale	
Maastrichtian	Nsukka Formation Ajali Sandstone	Anambra-Afikpo Basin (Second sedimentary cycle)
Campanian	Mamu Formation Nkporo/Enugu Shale, Afikpo Sandstone, Owelli Sandstones	
	HIATUS	
Coniacian-Santonian	Awgu Group	Abakaliki-Benue Basin (First sedimentary cycle)
Cenomanian-Turonian	Eze-Aku Group Odukpani Group	
Albian	Asu-River Group (Abakaliki Shale)	

4. Materials and methods

The materials for this study were collected through systematic logging of various outcrop sections in the area from base to top. A total of 11 selected field samples, distributed as follow, were studied: Eze-Aku Formation (7 samples) and Amasiri sandstone (4 samples) Fig. 3.

The method of the study included lithologic logging, laboratory processing, and transmitted light microscopy. Four (4) sandstone samples were subjected to petrographic study in order to examine the textural and mineralogical compositions. Each sample was first to cut into the slab and then sawed to obtain a slice of approximately 1/8 inch thick. It was then cemented on a glass slide with Canada balsam, pressing the slice at an oblique angle against the glass slide to eliminate air bubbles. The slice is then ground on a rotating lap with IF silicon carbide until the standard thickness of 0.03 mm diameter was obtained when the cover glass was cemented firmly to the section. The thin slide was then subjected to detailed microscopic study.

Seven (7) outcrop samples of shale, mudstone and limestone were selected from the locations 1, 2, 8 and 12 (Fig. 3) and subjected to palynological sample processing for their palynomorph contents. The sample preparation was carried out using the conventional method of maceration technique for recovering acid-insoluble organic-walled microfossils from sediments. Each sample was thoroughly cleaned to remove the field contaminants. 10 g of each sample was weighed out in a standard weighing balance and gently crushed with agate mortal and piston. The crushed sample was digested for 30 minutes in 40 % hydrochloric acid to remove traces of carbonate and 72 hours in 48 % hydrofluoric acid for removal of silicates. The digested sample was diluted with distilled water and sieve-washed through 10 microns nylon mesh. The sieve-washed 10 g residues equivalent was partitioned into two parts, 5 g

each, for oxidation and for kerogen assessment. The 5 g residues extract were oxidized for 30 minutes in 70 % HNO_3 and 5 minutes in Schulze solution to render the fossils translucent for transmitted light microscopy. The acid-free oxidized residues were rinsed in 2 % KOH solution to neutralize the remaining traces of acid; swirled to remove the resistant coarse mineral particles and undigested organic matter. The swirled residues were collected on the sieve and stained with Safranin – O to increase the depth of contrast for microscopic study and photography.

Aliquots were dispersed with polyvinyl alcohol, dried on cover-slips and mounted in petropoxy resin. One slide was made from each sample and microfossils were searched, counted and recorded. Light photomicrographs were taken with a Leica lll binocular microscope.

4.1. Kerogen

The simple classification mentioned in Tyson [21], Ibrahim *et al.* [22]) and Chiaghanam *et al.* [23] for rapid assessment of hydrocarbon potentialities may be used as follows:

1- Kerogen type I (highly oil-prone material): It includes alginitic material derived from chlorococcale algae, prasinophyte algae, cyanobacteria and some of the bacteria. Resins are the only significant terrestrially derived components belonging to this group.

2- Kerogen type II (oil-prone material): It includes amorphous organic matter, but sporopollenin palynomorphs, cuticle, and non-cellular membraneous debris are also included.

3- Kerogen type III (gas-prone material): Orange or brown, translucent, phytoclasts or structureless materials. Woody fragments are typical.

4- Kerogen type IV (inert material): Opaque to semi-opaque, black, or very dark brown particles, representing oxidized or carbonized phytoclasts.

Five (5) outcrop samples of shale and mudstones from the Locations 1, 2, 8 and 12, were selected and subjected to palynological sample processing for their particulate organic matter (POM) contents. Sample preparation was carried out using the conventional method of acid maceration for recovering acid insoluble organic-walled microfossils from sediments. Each calcite-free sample was digested for 72 hours in 40% hydrofluoric acid for removal of silicate. The extracts were sieve-washed through 10 microns nylon mesh. The sieve-washed residues were mounted on the cover-slip and then on the glass slide using petro-poxy resin mountant.

Five (5) kerogen slides were made, one for each, of the examined samples. Each slide was examined using the transmitted light microscopy at X10 and X40 magnifications in order to make a qualitative as well as a quantitative analysis of particulate organic matter (POM), determine the palynofacies associations and kerogen types, examine spores /pollen colouration, estimate the Thermal Alteration Index (TAI), Vitrinite Reflectance (Ro %), as well as the degree of organic thermal maturation. Each slide was counted for its (POM) contents, in which the first 200 particles were counted in terms of *abundant* (>35 %), *frequent* (16-35 %), *common* (5-15 %) and *rare* (>5 %).

5. Results

5.1. Petrography: Classification of sandstones

Numerous classifications of sandstones have been proposed by different workers, but sandstones can best be classified within the Ternary scheme proposed by Folk [24]. The major components, i.e., the framework elements, namely: quartz (Q), feldspars (F) and rock fragments (RF) are placed at the poles of a composition triangle (Fig. 5). In this classification, the Q pole consists of both monocrystalline and polycrystalline quartz grains, the F pole includes all types of feldspars, and the RF pole incorporates both rock fragments and micas. Since mica is fairly represented in the samples and may have some genetic significance, it is considered expedient to place it in the RF pole (Tabs. 2, 3, and Fig. 6).

Table 2. Summary of framework elements of the sandstone

Unit	Quartz (%)		Feldpar (%)	Rock fragment (%)	Matrix (%)	Total (%)
	Polycrystalline	Monocrystalline				
AM/L1/04	14.3	20.3	9	4.3	55	100
AKP/L7/01	15	19	5.5	15.5	45	100
AM/L2/04	22	20	13	25	20	100
AM/L3/02	15	20	15	5	45	100

Table 3. Frequencies of Quartz, Feldspar, Mica and Rock fragment in the sandstones with matrix more or less than 15%

Sample	Quartz		Feldspar		Mica+Rock Fragment	
	Value	Recalculated*	Value	Recalculated*	Value	Recalculated*
AM/L1/04	34.6	72	09	18.75	4.3	09
AKP/L7/01	34	62	5.5	10	15.5	28
AM/L2/03	42	52	13	23	25	31
AM/L3/02	35	63	15	27	05	09

**(recalculated to 100% from table above F Frequencies of Quartz, Feldspar, Mica and Rock fragment in the sandstones with matrix more or less than 15% recalculated to 100% from table*

Table 4. The absolute occurrence and distribution of the palynomorph counts in the examined samples

PALYNOMORPHS SPECIES Sample→	AM/L1/01	AM/L1/02	AM/L2/01	AM/L2/02	AKP/L8/01	OKP/L12/01	LST
TERRESTRIAL SPECIES							
Spores							
Laevigatosporites ovatus	7	4	3	5	4	3	2
Leiotriletes adriennis	2	0	1	0	0	0	0
Cyathidites minor	0	2	0	0	2	1	0
Pollen							
Ephedripites multicostatus	2	0	1	1	3	1	0
Cretacaeiporites scabratus	3	1	4	2	I	2	0
Cretacaeiporites mulleri	1	3	1	0	1	3	0
Tricolpites sp. S427	4	0	2	2	0	0	0
Cretacaeiporites krutzschi	0	2	1	0	0	3	0
Tricolporopopollenites sp	2	0	3	0	1	0	0
MARINE SPECIES:							
Dinogymnium euclaensis	2	1	2	0	1	4	2
Oligosphaeridiums pp.	4	2	2	3	0	3	1
Leiosphaeridea sp.	0	0	1	0	2	0	0
Spiniferites ramosus	5	7	2	0	2	5	3
Cyclonephelium spp	0	1	0	2	1	4	0
Trichodinium c.f. casaneum	2	0	2	4	2	0	1
Baliacashaera compta	0	1	1	0	1	3	0
Scuticabolus lapidaris	4	2	3	0	2	0	0
Pediastrum sp.	2	1	1	0	0	2	0
Substilisphaera spp.	4	2	1	2	1	0	0
Foraminifers test lining	0	2	2	0	2	1	3

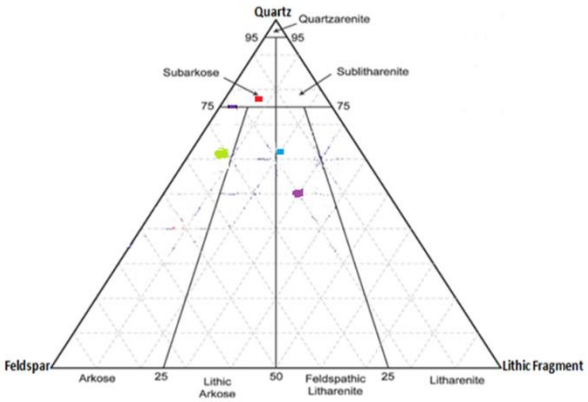

Fig. 5. Plots of AM/L1/04 (red), AKP/L7/01 (blue), AM/L2/03 (purple) and AM/L3/02 (green) sandstones from this study on a compositional triangle for sandstone classification *(after Folk* [24]*)*

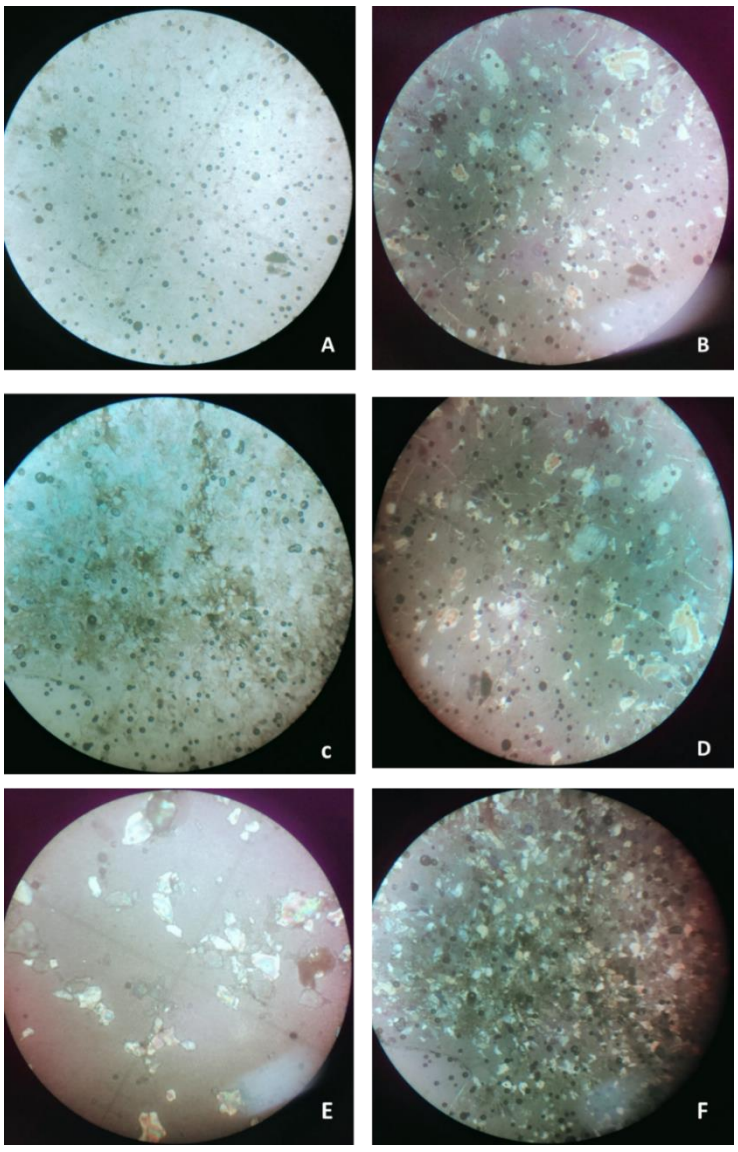

Fig. 6. Micrographs of sandstone petrography: (A) AM/L1/04 plane polarized light, (B) AM/L1/04 cross polarized light, (c) AKP/L7/01 plane polarized light, (D) AKP/L7/01 cross polarized light, (E) AM/L2/03 plane polarized light, and (F) AM/L2/03 cross polarized light

5.2. Palynological result

Table 4 shows the absolute occurrence and distributions of palynomorph counts present in the given examined samples from the locations 1, 2, 8 and 12. The shale and mudstone samples yielded moderately rich palynomorph assemblages while the limestone sample recorded very few palynomorph counts. The sandstones were barren of palynomorphs. The species of marine origin such as Dinoflagellate cysts were the most abundant and diverse. The terrigenous species recorded more pollen and spores while freshwater algal spores yielded low counts (Table 4).

Table 5. Summary of % frequency distributions of the total particulate organic matter (POM) present in the examined samples

Sample NO.	Phytoclasts	AOM	Opaques	Palynomorphs
AM/L1/01	15 %	50 %	30 %	5 %
AM/L1/02	8 %	62 %	24 %	6 %
AM/L2/01	20 %	55 %	25 %	0 %
AKP/L8/01	5 %	65 %	28 %	2 %
OKP/L12/01	10 %	52 %	33 %	5 %

Table 6. Summary of the kerogen assessment and interpretation

Sample No	Palynofacies association	S/P colour	TAI	Vitrinite reflectance (R%)	Thermal maturation	Kerogen type	Source rock potential
AM/L1/01	Mostly dark AOM followed by opaque debris	Very dark brown-dark	+3 to -4	1.3= - 2.0%	Over mature	Type II/III	Oil –gas prone
AM/L1/02	Mostly dark AOM followed by opaque debris				Over mature	Type II	Oil prone
AM/L2/01	Mostly dark AOM followed by opaque debris				Over mature	Type II/III	Oil –gas prone
AM/L2/02	Mostly dark AOM followed by opaque debris				Over mature	Type II	Oil –prone
AKP/L8/01	Mostly dark AOM followed by opaque debris				Over mature	Type II/III	Oil –gas prone

Table 7. Summary of palynomorphs % frequency distribution and their paleoenvironmental inferences

Sample no.	Palynomorphs % frequency			Paleo-salinity	Paleoenvironments of deposition
	Spores	Pollen	Marine Species		
AM/L1/01	**21 %**	**27 %**	**52 %**	Brackish – Normal marine	Marginal - Open marine (probably shallow shelf)
AM/L1/02	**19 %**	**19 %**	**62 %**	Normal marine	Open marine (probably open shelf)
AM/L2/01	**11 %**	**33 %**	**56 %**	Brackish – Normal marine	Marginal – Open marine (probably shallow shelf)
AM/L2/02	**24 %**	**24 %**	**52 %**	Brackish – Normal marine	Marginal – Open marine (probably shallow shelf)
AKP/L8/01	**22 %**	**22 %**	**56 %**	Brackish – Normal marine	Marginal – Open marine (probably shallow shelf)
OKP/L2/01	**11 %**	**26 %**	**63 %**	Normal marine	Open marine (probably Open shelf)

5.2.1. Amachi River Section (AM/LI/01 and AM/L1/02)

The samples from this location documented more marine (52-62 %) of the total palynomorph counts over terrestrial (36-48 %) species (Tabs. 4 and 7). Freshwater species were poorly recovered.

Terrestrial species: Among the sporomorph group were spores, pollen, and algal spores. The spores include *Leiotriletes adriennis, Laevigatosporites ovatus,* and *Cyathidites minor*. The pollen is *Ephedripites multicostatus*, *Cretacaeiporites scabratus*, *Cretacaeiporites mulleri*, *Tricolpites sp.* S 427, *Cretacaeiporites krutzschi* and *Tricolporopopollenites sp*.

Marine species: The group of marine species includes dinoflagellate cysts, acritarchs, prasinophytes and foraminifer inner test lining. The dinoflagellate cysts encountered included both gonyaulacacean and peridinecean species. They include *Dinogymniumeuclaensis, Spiniferites* spp*., Oligosphaeridium* sp, *Operculodinium centrocarpum,* and *Substilisphaera* sp.

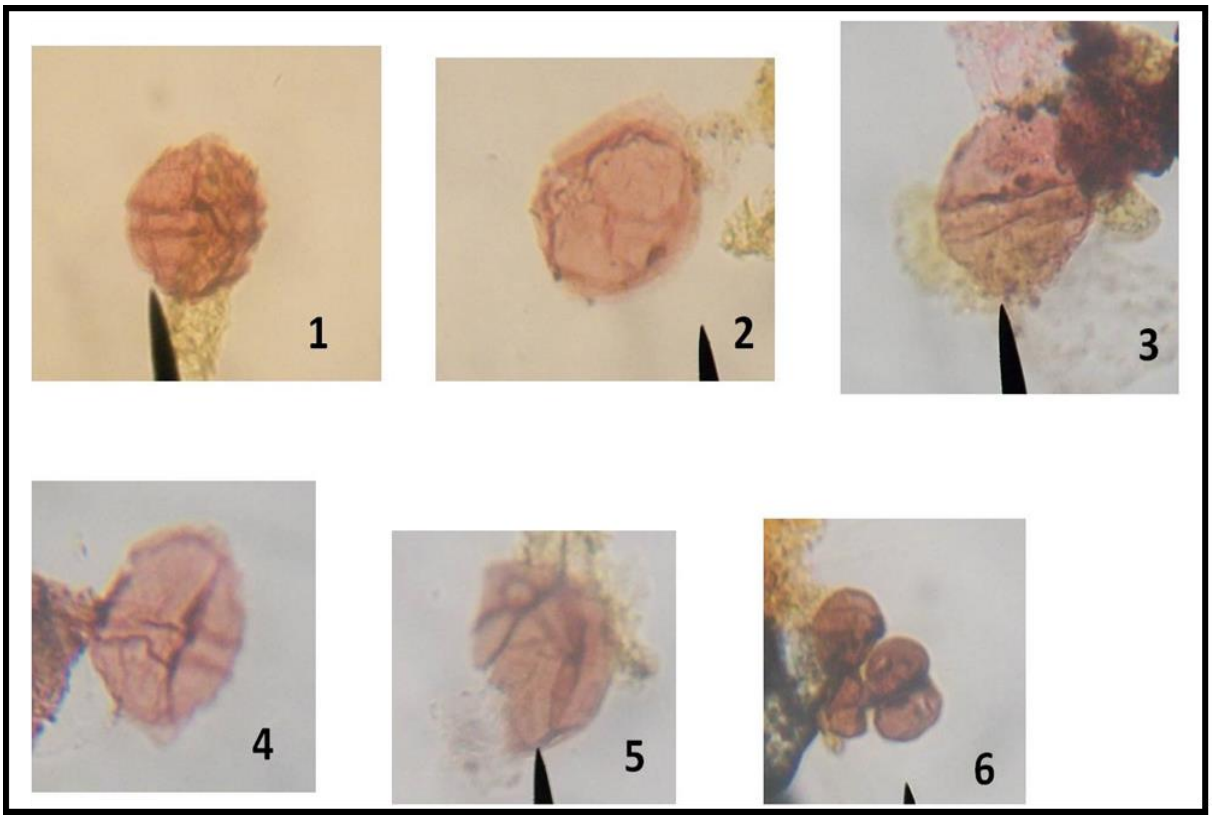

Fig. 7. Micrographs of some Late Cenomanian to Turonian dinoflagellate cysts and forams test lining from the study area, magnification (X 40)

1. *Substilisphaera senegalensis*
2. *Substilisphaera hyaline*
3. *Pterodinium cingulatum*
4. *Substilisphaera* sp.
5. *Baltiacasphaera compta*
6. *Forams inner test lining*

5.2.2. Amachi Quarry Section (AM/L2/01 and AM/L2/02):

The shales and mudstone samples from this location produced more marine (51-52 %) than the terrigenous (44-48 %) species (Table 4&7). The pollen predominate over spores. The fresh water *Pediastrum* sp. and foraminifer inner lining were occasionally encountered.

Terrestrial species: The recovered spores included only two species of fresh water ferns, *Laevigatosporites ovatus* and *Leiotriletes adriennis*. Among the pollen are*Cretacaeiporitesmulleri,Tricolporopollenites* ssp*.*, *Ephedripites multicostatus*, *Cretacaeiporites scabratus*, *Cretacaeiporites mulleri* and *Tricolpites sp.* S 427.

Marine species: The dinoflagellate cysts and the acritarchs *Scuticabolus lapidaris,* forams inner lining and *Leiosphaeridia* spp. were recorded. Thedinoflagellate cysts predominate over other marine species. The gonyaulacacean (open marine species) predominate over peridinecean(near-shore brackish water) species. They include *Spiniferites ramosus, Oligosphaeridium*spp, *Operculodinium centrocarpum, Substilisphaera* spp*., Dinogymnium euclaensis, Cyclonephelium*spp*., Trichodinium c.f. casaneum,* and *Baltiacaphaera compta* (Table 4and Fig. 7)

5.2.3. Locations 8 and 12 (AKP/L08/01 and OKP/L12/01):

Thissamples recorded both marine and terrigenous palynomorphs. The marine species (56-63 %) predominate over terrigeneous (37-44 %) of the total palynomorph counts. The pollen were recorded more than the spores (Table 4&7). Fresh water species were also encountered.

Terrestrial species: The fern spores are *Laevigatosporitesovatus*and*Cyathidites minor*. Among the pollen included *Tricolporopollenites* sp., *Cretacaeiporites scabratus*, *Cretacaeiporites mulleri*, *Ephedripites multicostatus* and *Cretacaeiporites krutzschi*.

Marine species: Dinoflagellate cysts species encountered include *Trichodinium*c.f.*casaneum, Dinogymnium euclaensis, Spiniferites* spp., *Oligosphaeridium* spp, *Operculodinium centrocarpum, Cyclonephelium* spp., and *Baltiacaphaera compta*.

The limestone (LST) yielded very low palynomorph counts. The terrigenous species encountered included one single grain of fern spore *Laevigatosporites ovatus* while pollen were absent. Few species of marine origin such as *Dinogymnium euclaensis, Trichodinium c.f. casaneum* and *Oligosphaeridium* spp., and foraminifers test lining were recorded while fresh water algae was not observed (Table 4).

5.3. Kerogen results

Table 5, shows the summaryofthe percentage frequency distributions of the total particulate organic matter (POM) present in the given examined samples. Almost all the samples in the area (from location 1 - 12) have similar palynofacies associations, constituted mostly of dark AOM followed by opaque debris (Table 6). The estimated spores/pollen colouration generally ranged from very dark brown to dark, which are overmature, and correspond to +3 to -4 TAI, 1.3 - 2.0 Vitrinite Reflectance (Ro %) in the standard colour chart. The kerogen types are generally type II/III (Table 6).

6. Interpretation and discussion

6.1. Provenance and depositional environment

The major objective of sandstone petrography of a unit is to decipher the paleogeographic setting which controlled the derivation, transportation, and deposition of the detritus. This involves the identification of the provenance, the mode of transportation and the kind of depositional environment.

A brief discussion of the results of the study is aimed at relating these results to depositional processes and possible identification of environments of deposition. The roundness of sand grains is slightly modified in a single cycle. The studied samples are characterized by subrounded and subangular grains which indicate a first cycle deposit since rounded quartz sands generally indicate recycling. However, as long distances of transport or reworking may not effectively round clastic quartz grains. It may nevertheless be noted that organic acids cause the dissolution of corners of clastic grains in soils and weathering profiles and so effects some rounding. Form, like size, is also often inherited [26]. Abrasion is thought to play little or no part in determining form. The preponderance of prismatic, elongate feldspars and highly strained polycrystalline quartz grains in the samples is indicative of derivation from mostly gneissic sources. Bokman [27] has shown that granitic quartz has a greater tendency towards equality as compared to metamorphic quartz. Equant and very equant quartz grains, indicative of granitic sources are rare in the studied sandstone units.

Contacts between sand grains are normally the point type at a deposition; the other types are modifications of this initial fabric. The ubiquity of line and concavo-convex types in the studied samples show that a considerable amount of condensation has occurred in the sandstone [28]. According to Pettijohn [28], condensation is the process of bringing the grains closer together, resulting in more extended contacts. Taylor [29] attributed the modification of point contact to solid flow and pressure solution of quartz grains. The overgrowths on the quartz

grains are normally produced as diagenetic features. Young [30] attributed segmented undulosity to the mode of response of quartz to stress and in general the undulose extinction to the differences in orientation of the c- axis in various parts of a crystal formed either as a response to bending gliding or progressive misorientation of various parts of a quartz crystal developed by parallel walls of dislocation.

6.1.1. Provenance

The term provenance includes all the factors relating to the production of sediment [28]. Most often it refers to geology, relief, climate, and location of the source region.

6.1.1.1. Composition of source rocks

The clastic grains that provide most information in this regard are quartz, feldspars and rock fragments.

Quartz: Quartz grains usually bear clues as to their source. According to Blatt et al, (1980), quartz grains derived from gneissic rocks are polycrystalline and are commonly composed of more than five crystals. The polycrystalline grains dominate in the AKP/L7/01 and AM/L3/02 sandstone units (Table 2) and consist of five to seven crystals, having sutured boundaries indicating a metamorphic source rock (Fig. 6).The samples representing all the lithologic units showed a higher proportion of undulose quartz grains. The significance of this with respect to the provenance is not very clear since no real difference exists in the degree of undulosity in quartz from igneous and metamorphic rocks [30-31]. Folk [32] however thinks strong undulosity is a characteristic feature of quartz grains from gneisses and schist.

Feldspar: Potash and sodic feldspars which were observed in the studied samples may equally be derived from gneissic and granitic sources. K-feldspars are associated with gneissic sources and plagioclase with granitic sources. The feldspar grains may have been derived from polygenetic sources since the two types of feldspars were represented in the samples (Table 2&3). The major fact that emerges from the analysis is that the source area is a basement complex containing perhaps all these rock types in various proportions with the metamorphic rock type appearing to dominate the region.

6.1.1.2. Climate and relief of the source area

The key indicator of paleoclimate is thought to be detrital feldspar [28]. The presence of large quantities of feldspars in sandstone implies a very arid or cold climate in the source region. Conversely, a very humid or wet climate is postulated for the absence of detrital feldspars. Such a rigorous climatic theory was questioned by Krynine [35] who argued that the presence or absence of detrital feldspar in sandstone depends not only on a suitable climate but also on the time through which the processes of decomposition operate.

The proportion of feldspar in the AM/L1/04, AKP/L7/01, AM/L2/03 and AM/L3/02 sandstone units (9%, 5.5%, 13%, and 15% respectively) (Table 3), does not appear considerable, though diagenesis might have reduced the original content of the feldspar grains of all the studied samples representing the three lithologic units and are on the average finer and rounder than the quartz grains. All the feldspars are also generally weathered. These factors would place the source region of the sandstone under study in a tectonically active zone, characterized by a rugged to moderate relief and a humid and warm climate.

From the foregoing, the provenance is most likely the metamorphic Precambrian Basement Complex of southeastern Nigeria in the Oban and Bamenda massifs/cratons located at the eastern border of the rift, towards the eastern border of the study area (Fig. 4).

6.1.2. Depositional environment

A depositional environment is a geographically restricted complex that can be described in geomorphic terms (e.g. marine environment, shelf environment) etc. The depositional environment of the sandstone units are discussed as deciphered from primary sedimentary structures and lithologic characteristics. However, the observed parallel lamination of the sandstone

unit in the field is strong indication of low energy environment of deposition. The presence of mica in the sandstones (Table 2&3) indicates deposition in low energy environment where sediments are rapidly deposited with little reworking.

6.2. Age determination/Correlations

The designation of age to the examined samples was based on selected key age marker palynomorphassemblageencountered.The samples in the study area were dated **Late Cenomanian** to **Middle Turonian** based on the following index sporomorph assemblage: *Cretacaeiporites scabratus, Ephedripites multicostatus, Cretacaeiporites mulleri, Monosulcites sp.,Tricolporopollenites* sp.,and *Tricolpites sp.* S427.This assemblage is typical of the **Turonian** of Herngreen [34], Lawal and Moullade [35], and Abubakar *et al*. [36], in the Upper Benue Basins, Nigeria. *Cretacaeiporites scabratus* Herngreen, 1975, made its earliest appearance in the Upper Cenomanian [36-37]. Other important dinocysts assemblage present are *Cycloneph-elium cf. membraniphorum, Spiniferites ramosus, Batiacasphaera compta.* The presence of *Substilisphaera hyaline* and *Substilisphaera senegalensis* species (Table 4, Fig. 7), which are typical of Late Cenomanian, as well as *Dinogymnium euclaensis,*which first appeared in the **Turonian** [35-37], strongly confirmed the above designated age for the samples. Meanwhile, the absence of *Droseridites senonicus* (an index pollen of Coniacian-Santonian) in the examined samples overruled Coniacian age [35-37].

6.3. Paleoenvironments of deposition

Table 7, shows the summary of palynomorphs percentage frequency distribution and their paleoenvironmental inferences. The obtained values of 38-40 % marine influence, as was reported by Umeji [37] in the formation, indicate nearshore marine condition, with terrigenous input (usually spores and pollen) as much as 60 %. Here, on the contrary, the obtained values of 52-62 % marine influence (Table 7), with terrestrial input as low as 40 %, is indicative of open marine environment of deposition. This, therefore, has showed that almost all the examined samples from the Eze-Aku Formation in the area were probably laid down during the period of transgressive Turonian Sea, which later gave way for the deposition of the overlying Amasiri Sandstone by the regressive Turonian Sea. Moreover, the occurrence of marine association of *Scuticabolus* spp. and *Subtilisphaera* spp.**,** with structureless organic matter also gave credence to open marine depositional setting.

7. Summary and conclusion

The geology of Akpoha and environs has been undertaken. The result from the petrographic analysis shows that most of the sandstone where deposited in a very low energy environment where sediments are rapidly deposited with little reworking. The palynological result indicates Late Cenomanian to Early Turonian age for the sediments in the study area. Environmentally significant palynomorphs indicate that most of the sediments were deposited in an open marine environment, with minor terrestrial input. The results from kerogen analysis indicated that most of the samples were generally overmature characterized mostly by dark amorphous organic matter followed by opaque black debris, and have the potential to generate mainly oil and or gas.

Acknowledgments

Our sincere thanks go to the final year students of Godfrey Okoye University, for their concerted efforts and assistance during the fieldwork exercise. We thank in a special way the technologists of the Geology Department, University of Nigeria, Nsukka, especially Mrs. Ifenyinwa and Mr. Nebo, for their help in the thin-section cuttings and preparation. Mr. Lucky helped in preparing the palynological slides for microscopic examination.

References

[1] Simpson A. The Nigerian coalfield, The Geology of parts of Onitsha, Owerri and Benue Provinces. Geological Survey Nigeria Bulletin, 1954; 24, 85 pp.

[2] Barber WM. Lower Turonian ammonites from northeastern Nigeria. Bull. Geol. Surv. Nigeria, 1957; 6: 91, pp. 8 pls.

[3] Reyment RA. Aspect of Geology of Nigeria. University Press 1965: Ibandan, Nigeria

[4] Murat RC. Stratigraphy and Paleogeography of the Cretaceous and Lower Tertiary in Southern Nigeria. In: Dessauvagie, T.F.J and Whiteman, A.J (Eds) Proceeding of the Conference on African Geology 1972, Ibadan, pp. 251-266.

[5] Nwachukwu SO. 1972. Tectonic Evolution of the Southern Portion of the Benue Trough, Nigeria. Geol. Mag., 1972; 411-419.

[7] Offodile ME. A Review of the Geology of the Cretaceous of the Benue Valley. In: Kogbe, C. A., (Ed); the Geology of Nigeria: Elizabethan Publishing Co. 1976, Lagos, pp. 365-368

[8] Petters SW. Stratigraphic evolution of the Benue Trough and its implicationsfor the upper cretaceous paleogeography of West Africa. J. Geol., 1978; 86: 311–322.

[9] Banerjee I. A subtidal model bar model for the Eze-Aku Sandstones, Nigeria. Sedimentary Geology, 1980; 15: 291-309.

[10] Banerjee, I. Storm-lag and related facies of the bioclastic limestones of the Eze-Aku Formation, (Turonian), Nigeria. Sedimentary Geology, 1981; 30: 133-147.

[11] Amajor LC. The Eze-Aku Sandstone ridge (Turonian) of Southeastern Nigeria: A re-interpretation of their depositional origin. Journal of Mining Geology, 1987; 23: 17-26.

[12] Umeji OP. Ammonite paleoecology of the Eze-Aku Formation, Southeastern Nigeria. J. Min. Geol., 1984; 21: 55–59.

[13] Umeji OP. Subtidal shelf sedimentation: an example from the Turonian Eze-Aku Formation in Nkalagu, southeastern Nigeria. J. Min. Geol., 1985; 22: 119–124.

[14] Ojoh KA. Cretaceous geodynamic evolution of the southern part of the BenueTrough, Nigeria in the equitorial domain of the south Atlantic. Stratigraphy, basin analysis and paleo-oceanography. Bull. Explor. Prod. Elf-Aquitaine, 1990; 14: 419–442.

[15] Umeji OP. Palynological evidence of the Turonian/Campanian boundary between the Abakaliki and Anambra Basins, as exposed at Leru along the Enugu-Port-Harcourt expressway, South-Eastern Nigeria. J. Min. Geol., 2006; 42(2): 21-30.

[16] Igwe EO, Okoro AU, Obasi AI. Foraminiferal Biostratigraphic Analysis of the Late Cenomanian – Turonian Eze-Aku Shale in the Afikpo Synclinorium, Lower Benue Trough, Nigeria. American Journal of Science and Technology, 2015; 2(6): 274-282.

[17] Igwe EO, and Okoro AU. Field and lithostratigraphic studies of the Eze-Aku Group in the Afikpo Synclinorium, Southern Benue Trough, Nigeria. Journal of African Earth Sciences, 2016; 117: 137-150.

[18] Ofomata CEK. Nigeria in Maps: Eastern States. Midwest mass communication corporation, Benin City, Nigeria. 2016, 144 pp.

[19] Murat RC. The tectonic evolution of the southern portion of the Benue Trough, Nigeria. In Dessauvagie, T. F. W. and Whiteman, A. J. (eds): African Geology, University of Ibadan Press 1970, pp. 252-266.

[20] Wright JB. 1970. South Atlantic Continental Drift and the Benue Trough: Tectonophysics, 1970; 4: 300-310.

[21] Tyson RV. Palynofacies analysis. Applied Micropalaeontology, Kluwer Academic Publishers 1993, pp. 153-191

[22] Ibrahim MIA, Abul Ela NM, and Kholeif SE. 1997. Paleoecology, palynofacies, thermal maturation and hydrocarbon source-rock potential of the Jurassic-Lower Cretaceous sequence in the subsurface of the north Eastern Desert, Egypt. Qatar University Science Journal, 1997; 17(1): 153-172.

[23] Chiaghanam OI, Chiadikobi KC, Ikegwuonu ON, Omoboriowo AO, Onyemesil OC, and Acra EJ. Palynofacies and Kerogen Analysis of Upper cretaceous (Early Campanian to Maastrichtian) Enugu Shale and Mamu Formation in Anambra Basin, South Eastern, Nigeria. International Journal of Scientific and Technology Research, 2013; 2(7): 225-229.

[24] Folk RL, Andrews PB, and Lewis DW. 1970. Detrital sedimentary rock classification and nomenclature for use in New Zealand. New Zealand Journal of Geology and Geophysics, 1970; 13: 937-968.

[25] Pearson DL. Pollen/Spore Color "Standard", Version 2. Phillips Petroleum Company 1984, privately distributed.
[26] Moss AJ. Bed-load sediments. Journal of the International association of sedimentologists, 1972; 18(3-4): 159-219.
[27] Bokman J. 1952. Clastic quartz particles as indices of provenance: Journal of sedimentary Petrology, 1952; 22: 17-24.
[28] Pettijohn FJ, Potter PE, and Siever R. Sand and sandstone, New York 1975: Springer-Verlag, 618 pp.
[29] Taylor SR. The origin of the Earth. In understanding the Earth (eds. G.C Brown, C.J. Hawkesworth and M.S Mathews). Cambridge University Press 1992, Cambridge, UK.
[30] Young KP. Environmental Geology of the Austin area: an aid to urban planning; University of Texas at Austin, Bureau of Economic Geology 1975; Report of Investigation R1-86
[31] Blatt H, and Ehlers EG. Petrology: Igneous, Sedimentary and Metamorphic, Nazia Printers, Lal Kuan, Delhi 1982, India. 707 pp.
[32] Folk RL. Stages of textural maturity in sedimentary rocks. Journal of Sedimentary Petrology, 1951; 21: 127-130.
[34] Herngreen GFW. Palynology of Middle and Upper Cretaceous strata in Brazil. Mededelingen Rijks Geologische Dienst Nieuwe serie, 1975; 26(3): 39-91.
[35] Krynine PD. Arkose deposits in the humid tropics. A study of sedimentation in Southern Mexico. American Journal of Science 1935, Published book.
[35] Lawal O, and Moullade M. Palynological Biostratigraphy of Cretaceous Sediments in the Upper Benue Basin, N.E. Nigeria. Rev. Micropal., 1986; 29(1): 6 –83.
[36] Abubakar MB, Luterbacher HP, Ashraf AR, Ziedner R, Maigar, AS. Late Cretaceous palynostratigraphy in the Gongola Basin (Upper Benue Trough, Nigeria). Journal of African Earth Sciences, 2011; 60: 19–27
[37] Umeji OP. Late Albian to Campanian Palynostratigraphy of Southeastern NigerianSedimentary Basins: Unpublished Ph.D. thesis, University of Nigeria 2007, Nsukka, Department of Geology, 280 pp.
[38] Ojo OJ, Ajibola UK, Akande SO. 2009. Depositional environments, organic richness petroleum generating potential of the campanian to Maastrichtian Enugu Formation, Anambra Basin, Nigeria. Pac. J. Sci. Technol., 2009; 10: 614–628.
[39] Murat RC. Stratigraphy and Paleogeography of the Cretaceous and Lower Tertiary in Southern Nigeria In: Dessauvagie, T.F.J and Whiteman, A.J (Eds) Proceeding of the Conference on African Geology 1972, Ibadan, pp. 251-266.

To whom correspondence should be addressed: Dr. O. N. Ikeguwonu, Department of Physical & Geosciences, Godfrey Okoye University, Enugu, Nigeria

Petroleum and Coal

Article **Open Access**

A SIMULATION STUDY OF WATER INVASION IN THE FRACTURED GAS RESERVOIR BY USING A FULLY IMPLICIT COMPOSITIONAL SIMULATOR

*Majid Nikpey, Seyed Roohollah Taghizadeh**

Department of Chemical Engineering, Technical Engineering Faculty, Gachsaran Branch, Islamic Azad University, Gachsaran, Iran

Received May 25, 2018; Accepted August 27, 2018

Abstract

Water coning is a complicated process which relies on a set number of parameters which are production rate, perforation interval, mobility ratio, capillary pressure, etc. Its production can mainly influence the efficiency of a well and the reservoir. In fractured reservoirs, the process is more complicated because of high fracture permeability. With this compliance in mind, water coning phenomenon in the fractured gas reservoir was investigated by simulating a reservoir using ECLIPSE-300 Compositional Simulator. A sensitivity analysis of different parameters including permeability and porosity of fracture and matrix was conducted to better describe and understand the mechanism of water coning in the studied gas reservoir. Results of the present work showed that vertical and horizontal permeability of the fracture, horizontal permeability of the matrix, the porosity of the fracture and the matrix have a significant effect on the time between water breakthrough and its production, which leads to better understanding of the coning phenomenon.

Keywords: *Water conning; Gas reservoir; Simulation; Eclipse-300; Sensitivity analysis.*

1. Introduction

Water production from oil wells is a natural process in oil reservoirs [1-3]. This is referred to one some indexes including; an increase of oil-water contact (WOC), water coning in addition to water fingering. Production of oil from a well completed in oil layer surrounded by water may result in the oil/water interface to change into a bell shape [4-5]. This change is namely water coning [6-8]. On the other hand, coincide production of oil and water from the well due to the difference between viscous and gravitational forces is usually called water coning. Water coning process is a complicated problem in the oil industry [9-13]. This phenomenon is more complicated in fractured reservoirs [9]. In another word, this process in fractured reservoirs usually leads to the massive production of water which can damage a well or drastically its production efficiency [14]. Three parameters are important in the investigation of water conning phenomenon namely: critical rate, the breakthrough time and water cut performance after breakthrough [3-6, 15-18]. The critical rate is usually defined as the maximum possible oil flow rate which can be produced from the well to prevent a cone breakthrough [19]. In fractured reservoirs, the critical rate is effected by additional parameters including fracture storativity (ω) and fracture transmissivity (λ) [1]. According to the rates, a cone with high velocity can be presented in the fracture while cone with low velocity is developed in the matrix. The position of these cones relative to each other is dependent on the rate and reservoir properties [21]. It is important to note that the main factor in evaluating water coning is the ration of permeability in the vertical and horizontal directions, kv/kh [14]. High value of vertical permeability in fractures are connected to increase the rate of the coning phenomenon leading to a decrease in the critical rates and more fast breakthrough times. Moreover, the channels of fluid flow within the fractures usually occured in fractured reservoirs is expected to influence wells [21]. In this study, the water coning behavior of a gas reservoir is investigated and the main parameters

are influencing on this phenomenon were determined by applying a sensitivity analysis to obtained results.

2. Mathematical model

There are different mathematical models utilized in various circumstances in the Eclipse-300. The mathematical model of simulation is as below:

For the water and gas phases [22]:

$$\nabla\left[\frac{KK_{rw}}{B_w\mu_w}\nabla(p_w-\rho_w gD)\right]_f+q_w+\tau_{mfw}=\frac{\partial}{\partial t}\left(\frac{\varphi S_w}{B_w}\right)_f \quad (1)$$

$$\nabla\left[\frac{KK_{rg}}{B_g\mu_g}\nabla(p_g-\rho_g gD)\right]_f+q_g+\tau_{mfg}=\frac{\partial}{\partial t}\left(\frac{\varphi S_g}{B_g}\right)_f \quad (2)$$

In which K depicts absolute permeability; K_{rw} and K_{rg} stand relative permeability; B_w and B_g denote the formation volume factor; μ_w and μ_g indicate viscosity values; p_w and p_g depict pressure; ρ_w and ρ_g show the density of water and gas; g denotes the acceleration constant; D is depth; ∇ is gradient vector; q_w and q_g denote flow rates of water and gas, respectively; τ_{mfw} and τ_{mfg} are transfer equations from matrix and fracture, given by [22]:

$$-\tau_{mfw}=\frac{\partial}{\partial t}\left(\frac{\varphi S_w}{B_w}\right)_m \quad (3)$$

$$-\tau_{mfg}=\frac{\partial}{\partial t}\left(\frac{\varphi S_g}{B_g}\right)_m \quad (4)$$

In which *φ show the effective porosity of the reservoir; S_w and S_g denote the saturation of water and gas; subscripts "f" and "m" are stand for fracture and matrix.*

3. Reservoir model description

ECLIPSE-300 Simulator is utilized in the present study to investigate water coning in fractured gas reservoir. The model is dual porosity dual permeability. A Cartesian model is used in present work. The model has 50 layers in the vertical-direction, and 12, 24 grids in the x-direction and y-direction, the XY view of the model is depicted in Figure 1.

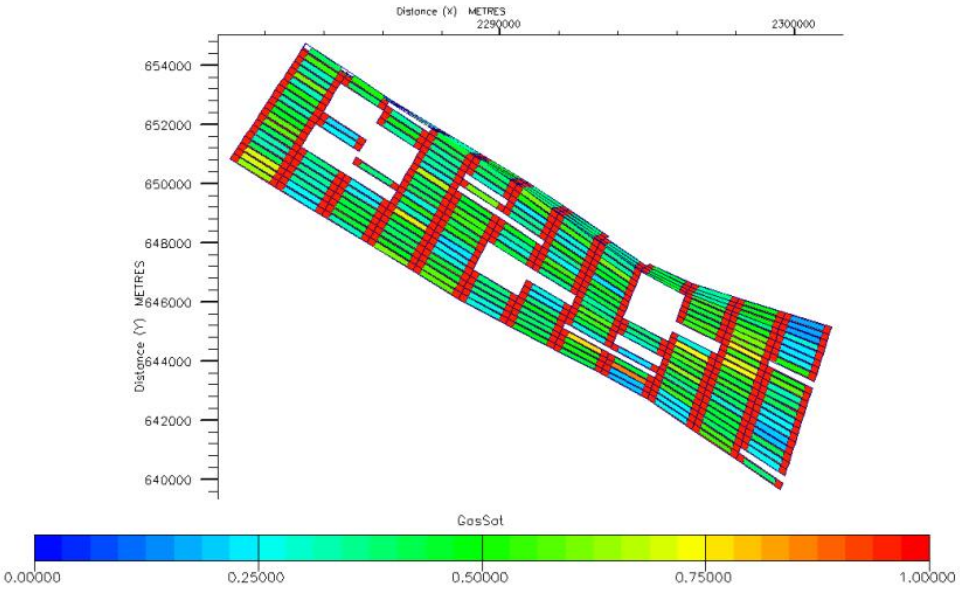

Figure 1. The XY view of the model

Since the conning phenomenon is occurred in the perforated interval of a well and below it, it is not required to have all grids of the model, and only the grids which are around the production well are required. In order to have a better simulation of conning phenomenon near the production well, an LGR is applied to the grids near the production well which is shown in Figure 2.

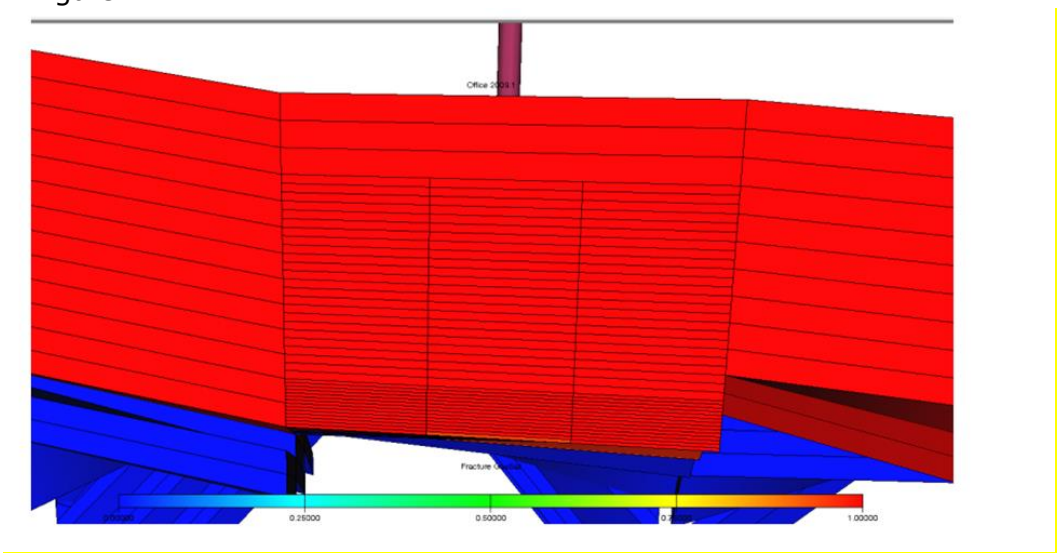

Figure 2. The LGR view applied to the perforated layers of the production well

Table 1 through 5 shows the properties of the rock and fluid utilized in the model. The formation volume factor, compressibility and viscosity of formation water at a pressure of 161.3 bar are 1.009317 rm^3/sm^3, 4.2878e-05 $bar^{-1,}$ and 0.4562 cP, respectively. The formation rock compressibility factor was 4.45e-05 $bar^{-1,}$ and reservoir temperature was 61.33°C. The PVTi software is utilized to describe the phase behavior of the reservoir fluid. The 3 parameter Peng-Robinson equation of state and Lohrenz-Bray-Clark viscosity model is used to simulate the phase behavior of reservoir fluid. The reservoir fluid composition data is depicted in Table 5.

Table 1. The water relative permeability and water-gas capillary pressure of matrix

S_w	K_{rw}	P_{cgw}	S_w	K_{rw}	P_{cgw}
0	0	13.79	0.6	0.415	1.38
0.1	0.006	5.16	0.7	0.56	1.11
0.2	0.033	3.69	0.8	0.72	0.83
0.3	0.117	2.8	0.9	0.86	0.34
0.4	0.193	2.07	1	1	0
0.5	0.3	1.72			

Table 2. The water relative permeability and water-gas capillary pressure of fracture

S_w	K_{rw}	P_{cgw}
0	0	0
0.5	0.5	0
1	1	0

Table 3. The gas relative permeability and water-gas capillary pressure of matrix

S_g	K_{rg}	P_{cgw}	S_g	K_{rg}	P_{cgw}
0	0	0	0.6	0.092	0
0.1	0.004	0	0.7	0.24	0
0.2	0.007	0	0.8	0.5	0
0.3	0.008	0	0.9	0.76	0
0.4	0.016	0	1	1	0
0.5	0.03	0			

Table 4. The gas relative permeability and water-gas capillary pressure of fracture

S_w	K_{rw}	P_{cgw}
0	0	0
0.5	0.5	0
1	1	0

Table 5. The composition of reservoir fluid

Component	Mole fraction	Component	Mole fraction
N_2	0.35	C_{4+}	0.0079
C_1	0.8883	C_6	0.0016
C_{3+}	0.529	C_{7+}	0.00310205
C_3	0.106	C_{12+}	0.0005795

4. Results and discussion

As mentioned before, several factors were utilized for the sensitivity analysis namely; anisotropy ratio (kv/kh), permeability and porosity of the fracture and porosity, permeability and porosity of matrix. The outcomes of this simulation are described as below:z

4.1. Anisotropy ratio

Figure 3 through 4 and Table 6 depicts the impact of anisotropy ratio in comparison to the base model. Figure 3 shows the impact of this ratio of various conditions on the water cut. The outcomes reveal that the increase in this ratio will increase the water cut. In another word, the coning process will be more severe with high vertical permeability (Kv) values. This due to the fact that coning is a cause of the movement of water in the vertical direction due to pressure drawdown in the wellbore.

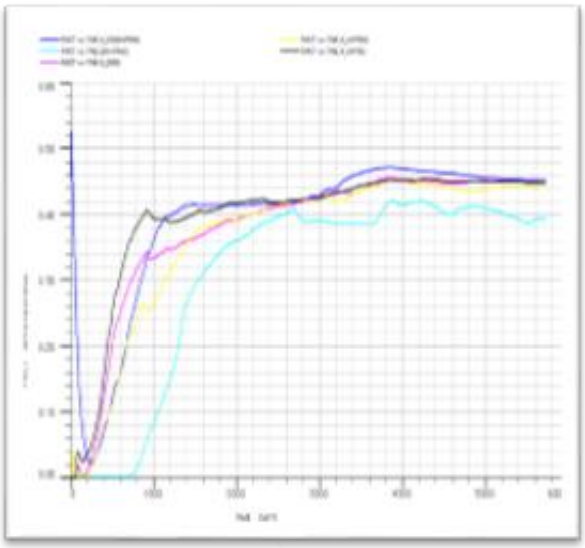

Figure 3. Effect of reservoir anisotropy on water conning

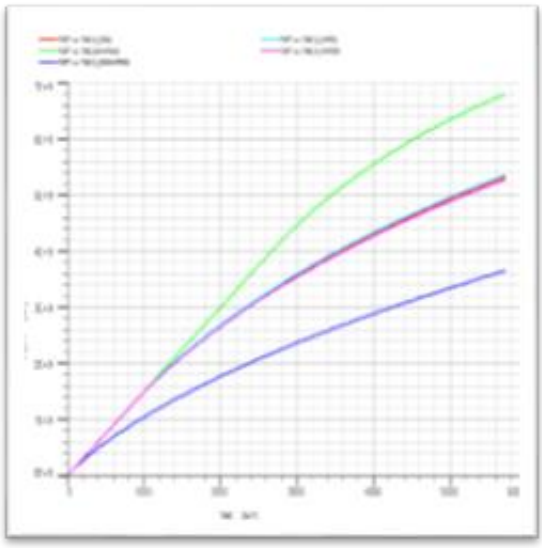

Figure 4. Effect of reservoir anisotropy on cumulative gas production

Table 6. Comparison between results of different horizontal and vertical fracture permeability

No	Work over type	Breakthrough time (day)	Fwct (15 years)	FGPT (SM^3)
1	0.5 Kh	5	0.46	3.65×10^6
2	2 Kh	808	0.40	6.79×10^9
3	0.5 Kv	254	0.44	5.27×10^9
4	2 Kv	76	0.44	5.35×10^9

According to Table 6, change in this ratio due to the change in the vertical permeability (Kv) enhances the movement of water in the vertical direction and leads to a decrease in the breakthrough time.

4.2. Fracture permeability

One of the most prominent factors in conning is fracture permeability. This is because the movement of the cone in the fracture is faster than that of the matrix. Figure 5 depicts the sensitivity analysis of various values of fracture permeability and the base model. Figure 5 shows the water cut from the various conditions in comparison with the base model. The outcomes show that the fracture permeability has an important influence on the break through time from the coning investigation. Results reveal that an increase in the fracture permeability increases the breakthrough time. In addition, the water cut and cumulative gas production of the reservoir with an increase in fracture permeability will remain constant.

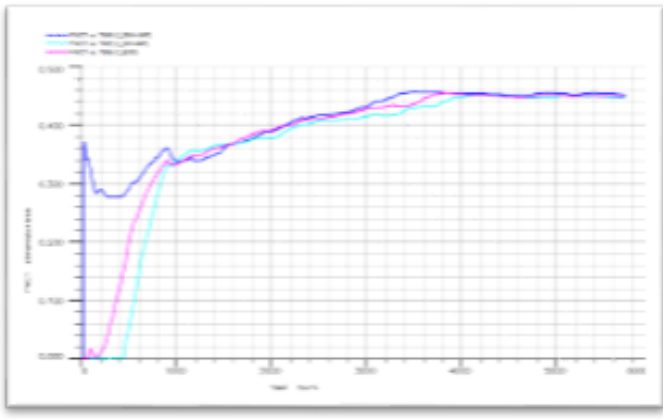

Figure 5. effect of horizontal fracture permeability variation on water cut

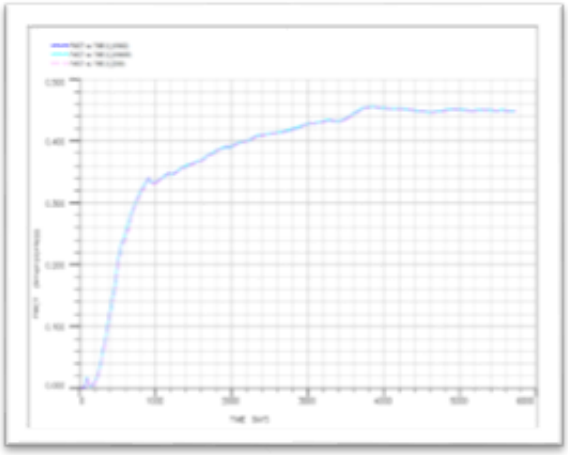

Figure 6. effect of vertical fracture permeability variation on water cut

Table 7. Comparison between results of different horizontal fracture permeability

No	Work over type	Breakthrough time (day)	Fwct (15 years)	FGPT (SM^3)
1	1.5 Kh	230	0.45	5.31×10^9
2	0.5 Kh	14	0.45	5.30×10^9
3	2 Kh	4449	0.44	5.32×10^9

The influence of variation of vertical permeability of fracture on breakthrough time, water cut, and cumulative gas production is depicted in Figure 6 and Table 8. Results show that the variation of vertical fracture permeability has no significant effect on water cut and cumulative gas production of the reservoir and these parameters remain nearly constant for all cases.

Table 8. Comparison between results of different vertical fracture permeability

No	Work Over Type	Breakthrough Time (day)	Fwct (15 years)	FGPT (SM^3)
1	1.5 Kv	230	0.45	5.31×10^9
2	0.5 Kv	230	0.45	5.31×10^9
3	2 Kv	230	0.45	5.31×10^9

4.3. Fracture porosity

Figure 7 shows the outcomes of the sensitivity analysis of fracture porosity in the model. The various conditions of fracture porosity are put into comparison with the base model. Figure 7 shows the water cut from various conditions of fracture porosity in comparison with the base

model. According to these results, in can be concluded that the water cut is almost constant in various cases. But there was an increase in breakthrough time with an increase in fracture porosity. Hence, the increased fracture porosity leads to fast movement of gas from the matrix into the fracture. Hence, cone in the fracture and movement of water by gas will lead to high breakthrough time. Table 9 also shows that the increase in the fracture porosity will increase the cumulative gas production from the reservoir.

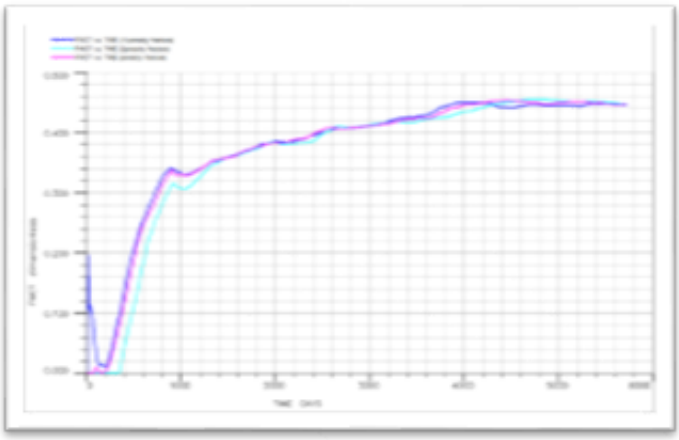

Figure 7. Effect of fracture porosity variation on water cut

Table 9. Comparison between results of different fracture porosity values

No	Work over type	Breakthroug time (day)	Fwct (15 years)	FGPT (SM^3)
1	φ_f	230	.45	$5.3181x10^9$
2	$.5\varphi_f$	7	.44	$5.2983x10^9$
3	$2\varphi_f$	352	.45	$5.3438x10^9$

4.4. Matrix porosity

According to the results of this case which are presented in Figure 8 through 9 and Table 10, it was observed that with an increase in matrix porosity, the amount of breakthrough time and cumulative gas production would increase. In addition, the value of water cut decreases with the increase in matrix porosity.

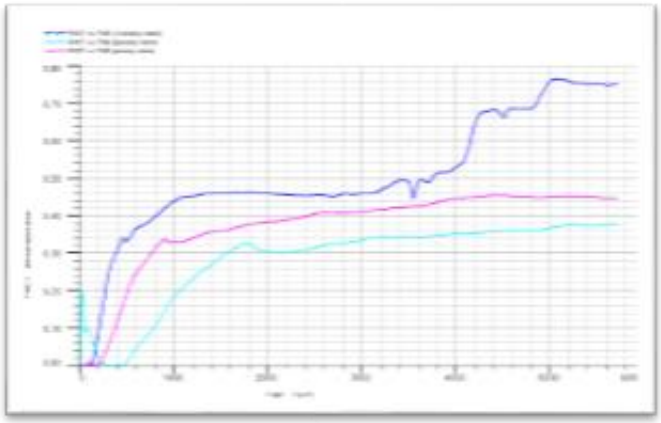

Figure 8. Effect of matrix porosity variation on water cut

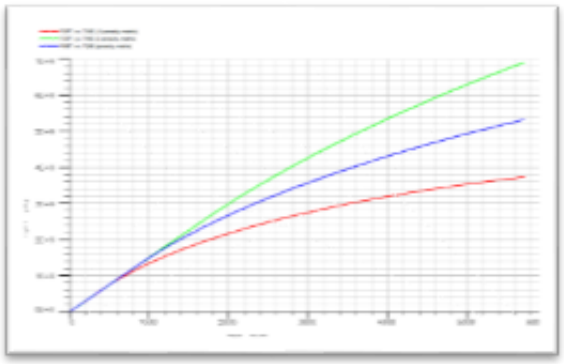

Figure 9. Effect of matrix porosity variation on cumulative gas production

Table 10. Comparison between results of different matrix porosity values

No	Work over type	Breakthroug time (day)	Fwct (15 years)	FGPT (SM^3)
1	φ_f	230	.45	$5.3181x10^9$
2	$.5\varphi_f$	147	.76	$6.2886x10^9$
3	$2\varphi_f$	518	.37	$3.7257x10^9$

5. Conclusion

Water coning phenomenon is very important in the oil industry. This process is more complicated in the fractured reservoirs. In present work, a sensitivity analysis was done to evaluate the dependency of several factors to the coning phenomenon in a fractured reservoir. The production rate of the reservoir has the most impact on the conning behavior. The breakthrough time decreases with an increase in production rate. The most effective way of reducing the conning of the studied fractured gas reservoir in reducing the production rate. The sensitivity of breakthrough time to fracture porosity is higher than the matrix porosity. Conversely, the sensitivity of water cut after breakthrough time to fracture porosity is lower than the matrix porosity. Among different types of reservoir permeability, the breakthrough time is most sensitive to vertical fracture permeability compared to matrix horizontal permeability. In addition, the water cut is most sensitive to fracture horizontal permeability, while vertical matrix permeability has no effect on water cut. Increase in fracture porosity increases the water breakthrough time. This is due to the fact that with an increase in the fracture porosity, the width of fractures will increase which will result in better distribution of fluids within the reservoir and decrease in flow velocity of fluids. This will reduce the arrival time of reservoir fluids to the production interval.

References

[1] Namani M, Asadollahi M, Haghigh, M. Investigation of water coning phenomenon in Iranian carbonate fractured reservoirs. in: International Oil Conference and Exhibition in Mexico, Society of Petroleum Engineers, 2007.

[2] Foroozech J, Barzegari D, Ayatollahi S, Abdolhosain J. Investigation of water coning in naturally fractured oil reservoirs. Research Proposal Submitted to Center of Excellence for Enhance Oil Recovery, Shiraz University School of Chemical and Petroleum Engineering, Shiraz 2008, Iran.

[3] Boyun G, Lee R-H. A simple approach to optimization of completion interval in oil/water coning systems. SPE Reservoir Engineering, 1993; 8 (04), 249-255.

[4] Meyer H, Searcy D. Analog study of water coning. Journal of Petroleum Technology, 1956; 8 (04): 61-64.

[5] Perez-Martinéz E, Rodríguez de La Garza R, Samaniego-Verduzco F. Water coning in naturally fractured carbonate heavy oil reservoir-a simulation study, SPE 152 545 in: SPE Latin America and Caribbean Petroleum Engineering Conference, Society of Petroleum Engineers, 2012.

[6] Høyland LA, Papatzacos P, Skjaeveland SM. Critical rate for water coning: correlation and analytical solution. SPE Reservoir engineering, 1989; 4(04): 495-502.

[7] Recham R, Osisanya S, Touami M. Effects of water coning on the performance of vertical and horizontal wells-a reservoir simulation study of Hassi R'mel Field, Algeria, in: SPE/CIM International Conference on Horizontal Well Technology, Society of Petroleum Engineers, 2000.

[8] Sobocinski D, Cornelius AJ. 1965. A correlation for predicting water coning time. Journal of Petroleum Technology, 1965; 17(05): 594-600.

[9] Saad SEDM, Darwich TD, Asaad Y. Water coning in fractured basement reservoirs, in: Middle East Oil Show, Society of Petroleum Engineers, OSTI Identifier:113374, 1995.

[10] van Golf-Racht TD. Water-coning in a fractured reservoir. in: SPE Annual Technical Conference and Exhibition, Society of Petroleum Engineers, 1994.

[11] van Golf-Racht TD. Fundamentals of fractured reservoir engineering, Elsevier 1982, eBook ISBN**:** 9780080868660.

[12] Bahrami H, Shadizadeh SR, Goodarzniya I. Numerical simulation of coning phenomena in naturally fractured reservoirs. Technology, 2014; 23, 25.

[13] Bournazel C, Jeanson B. Fast water-coning evaluation method, in: Fall Meeting of the Society of Petroleum Engineers of AIME, Society of Petroleum Engineers, 1971.
[14] Beattie D, Roberts B. Water coning in naturally fractured gas reservoirs, in: SPE Gas Technology Symposium, Society of Petroleum Engineers, 1996.
[15] Chaney P, Noble M, Henson W, Rice T. How to perforate your well to prevent water and gas coning. Oil Gas J, 1956; 55 (53): 108-114.
[16] Chaperon I. Theoretical study of coning toward horizontal and vertical wells in anisotropic formations: subcritical and critical rates, in: SPE annual technical conference and exhibition, Society of Petroleum Engineers, 1986.
[17] Chierici GL, Ciucci GM, Pizzi G. A systematic study of gas and water coning by potentiometric models. Journal of Petroleum Technology, 1964; 16 (08): 923-929.
[18] Salavatov TS, Ghareeb A. Predicting the behaviour of water and gas coning in horizontal wells. Oil and Gas Business, 2009; 2: 1-6.
[19] Al-Afaleg N, Ershaghi I. Coning phenomena in naturally fractured reservoirs, in: SPE Western Regional Meeting, Society of Petroleum Engineers, 1993.
[20] Shen W-J, Liu X-H, Li, X-Z, Lu J-l. 2015. Water coning mechanism in Tarim fractured sandstone gas reservoirs. Journal of Central South University, 2015; 22(1): 344-349.

To whom correspondence should be addressed: Dr. Seyed Roohollah Taghizadeh, Department of Chemical Engineering, Technical Engineering Faculty, Gachsaran Branch, Islamic Azad University, Gachsaran, Iran, roohollahtaghizadeh1355@gmail.com

Petroleum and Coal

Article **Open Access**

INVESTIGATION OF POSSIBLE LOSSES OF COAL RAW MATERIALS DURING ITS TECHNOLOGICAL PREPARATION FOR COKING
MESSAGE 2.THE ACTUAL MASS VARIATION OF COAL IN THE PROCESS OF ITS STORAGE AND CRUSHING

I. D. Drozdnik[1], D. V. Miroshnichenko[2], E. O. Shmeltser[3], M. V. Kormer[3], S. V. Pyshyev[4]*

[1] *Ukrainian State Coal-Chemistry Institute, 61023, Kharkiv, Ukraine*
[2] *National Technical University «Kharkiv Polytechnic Institute 61002, Kharkiv, Ukraine*
[3] *Kryvyi Rig Metallurgical Institute, Ukraine National Metallurgical Academy, 50006, Kryvyi Rig, Ukraine*
[4] *Lviv Polytechnic National University, 79013, Lviv, Ukraine*

Received March 12, 2019; Accepted May 21, 2019

Abstract

The authors of the article conducted a comprehensive study aimed at determining the actual mass loss of coal concentrates during their preparation and the coal charge during its transportation to the coal tower. As a result of carrying out the actual definitions of moisture changes of incoming coal on the path of a car dumper – a silo of a closed warehouse, coal, and coal charge on the crusher path - coal tower of coke oven batteries in the summer, it was established that the loss of moisture in coal concentrates during transportation significantly depends on the ambient temperature: the higher the temperature, the more moisture is lost, and vice versa.

It was determined that the unloading and transportation of coal to a silo of a closed coal warehouse is accompanied by a loss of ~ 0.9% moisture at an ambient temperature of 23.5° C and ~ 0.2% at a temperature of +4°C. When crushing and transporting the coal batch to the coal tower of the coke oven battery, the variation its actual weight is ~ 0.1% at an ambient temperature of +4° C and ~ 0.7% at an ambient temperature of 23.5–25.5° C

Keywords*: coal concentrates; temperature condition; coal transportation scheme; mass variation; moisture.*

1. Introduction

The coal raw material base of the coke production of PrJSC Avdeevskii coke plant, like the majority of the coke enterprises of Ukraine, has a multi-basin character, and the share of domestic raw materials is about 20%. The increase in the share of imported coal (coal concentrates in Russia, and the United States) is associated both with a shortage of Ukrainian coal of suitable quality (low sulfur content, $I_0 \leq 2.5$ basicity index), and with an increase in the quality requirements for coke to reduce its consumption in blast smelting, as well as in connection with the introduction of pulverized coal injection technology in blast furnace production [1].

Under the conditions of the formed multi-basin raw material base of coking, it is necessary to improve the basic technological methods of preparation for their use in coal mixtures. Achieving optimal characteristics of coke for blast furnace smelting conditions is possible with a comprehensive, scientifically based approach to improving the technology of preparing coal for coking, which consists in developing methods and technological measures aimed at optimizing the composition, properties and degree of grinding of the batch, taking into account its petrographic characteristics [2-3].

The supply of foreign coal due to the considerable distance of suppliers takes quite a long time, including long-term transportation by water transport, during which they undergo an oxidation process, which leads to changes in their technological properties [4-5] and requires

compliance with the developed recommendations on the use of oxidized coal for the production of blast-furnace coke [6].

It should be noted that during transportation and technological operations for the preparation of coal raw materials for coking (storage, crushing) its humidity changes. Thus, Ukrainian suppliers supply coal concentrates with the moisture of more than 10%. When the ambient temperature rises, the moisture evaporates intensively, which leads to the loss of the total mass of coal concentrates.

In general, the above circumstances lead to a discrepancy in the balance of the coal preparation workshop in part of the mass of incoming coal concentrates and the mass of the finished coal batch to the tower. Based on the above, it became necessary to determine the actual mass loss of coal concentrates during their preparation and the coal batch during its transportation to the coal tower.

2. Results and discussions

Currently, in the raw materials base of the coal preparation department PJSC Avdeevskii coke plant ("AKHZ"), there are coals of both the neighbor (Uskovskaya mine, Shchedrukhinskaya Central Processing Plant, Section Bochatsky, Berezovskaya) and long-distance (Carter Roag, Goonyella, Toms Creek) abroad. Coal concentrates of the above suppliers in the process of transportation over long distances can lose moisture, which entails the actual loss of their mass.

The analysis showed that coal moisture loss can occur when coal is unloaded from coal cars on wagon tipplers, when coal is pumped into a silo of a closed coal storage, during storage in silos of a closed coal storage, during their dosing and transportation to the coal batch crushing department, as well as further transportation of the coal batch to the coal towers.

Studies have been performed to determine changes in the moisture content of coal concentrates during their transportation from the car dumper to the top of the coal preparation warehouse silos as well as during the crushing of coal in the coal preparation shop.

For the study, 8 coal concentrates of various degrees of metamorphism were selected, which were part of the raw materials base of the coal preparation department PJSC Avdeevskii coke plant, namely:

- Shchedrukhinskaya coal, Russia, coal rank "G";
- Uskovskaya coal, Russia, coal rank "GZh";
- Carter Roag coal, USA, coal rank "Zh";
- Toms Creek coal, USA, coal rank "Zh";
- Svjato-Varvarinskaya coal, Ukraine, coal rank "K";
- Goonyella coal, USA, coal rank "K";
- Berezovskaya coal, Russia, coal rank "KO";
- Section Bochatsky, Russia, coal rank "KO."

The quality indicators of technical, plastometric, petrographic, and granulometric analysis of the investigated coal concentrates are given in Tables 1–3.

Coal concentrates Shchedrukhinskaya and Uskovskaya are characterized by an increased volatile matter (37.5% and 38.3%) with a low value of the content of total sulfur – 0.54% and 0.43%. The components of vitrinite mainly (91.0% and 88.0%) correspond to the stages of metamorphism of DG and GZh coal. This coal can be attributed to the hard group, as the coefficient of Hardgrove grindability index (HGI) is 55 units and 54 units. The mean particle diameter (d_{me}) is 9.67 and 5.33 mm.

Coals rank "Zh" Toms Creek and Carter Roag are characterized by an average total sulfur content of 0.98 and 0.96%, and the vitrinite components are mainly located in the stages of metamorphism of the "DG," "GZhO" and "Zh" ranks.

The petrographic analysis showed that the content of vitrinite is 70.0 and 66.0%, and the sum of the fusinized components is 25.0 and 26.0%, respectively. The mean particle diameter, respectively, is 8.48 mm and 4.89 mm. The values of the Hardgrove grindability index are 68 and 67 units, which classifies these coals as transitional from soft to hard in terms of hardness.

Table 1. Technological properties of coal concentrates Avdeevskii coke plant

Component; country	Coal rank	Proximate analysis, %			Thickness of plastometric layer, mm	Hardgrove grindability index (HGI), units
		A^d	S^d_t	V^{daf}	y	
April						
Shchedrukhinskaya coal, Russia	G	7.5	0.54	37.5	12	55
Toms Creek coal, USA	Zh	7.6	0.98	35.5	18	68
Svyato-Varvarinskaya coal, Ukraine	K	8.7	0.77	27.8	16	82
Section Bochatsky coal, Russia	KO	7.0	0.45	24.8	10	67
August						
Uskovskaya coal, Russia	GZh	7.3	0.43	38.3	17	54
Carter Roag coal, USA	Zh	8.1	0.96	33.7	21	67
Goonyella coal, USA	K	9.1	0.50	26.1	18	72
Berezovskaya coal, Russia	KO	7.7	0.52	25.3	12	62

Table 2. Petrographic characteristics of coal concentrates Avdeevskii coke plant

Component; country	Coal rank	Petrographic composition (without mineral impurities), %					Mean vitrinite reflection coefficient, %	Distribution of vitrinite reflection coefficient, %						
								<0,50	0,50 - 0,79	0,80 - 0,89	0,90 - 1,19	1,20 - 1,49	1,50-1,69	1,70 - 2,59
April														
		Vt	Sv	I	L	∑FC	R_o							0
Shchedrukhinskaya coal, Russia	G	69	1	29	1	30	0.68	3	91	6	0	0	0	
Toms Creek coal, USA	Zh	70	0	25	5	25	0.93	0	25	27	41	7	0	0
Svyato-Varvarinskaya coal, Ukraine	K	88	1	8	3	9	1.16	0	0	0	68	32	0	0
Section Bochatsky coal, Russia	KO	42	2	55	1	57	1.06	0	0	9	82	9	0	0
August														
Uskovskaya coal, Russia	GZh	94	0	5	1	5	0.73	0	88	12	0	0	0	0
Carter Roag coal, USA	Zh	66	0	26	8	26	0.93	0	0	36	64	0	0	0
Goonyella coal, USA	K	79	0	21	0	21	1.13	0	0	0	84	16	0	0
Berezovskaya coal, Russia	KO	45	2	51	2	53	1.04	0	0	3	93	5	0	0

Table 3. Granulometric composition of coal concentrates Avdeevskii coke plant

Component; country	Coal rank	Granulometric composition (%) by class (mm)									Mean particle diameter, mm
		>50	50–25	13–25	6–13	3–6	1–3	0,5–1	<0,5	<3	d_{me}
April											
Shchedrukhinskaya coal, Russia	G	1.9	8.6	11.6	21.6	18.6	17.2	6.7	13.8	37.7	9.67
Toms Creek coal, USA	Zh	0.7	7.8	14.1	18.2	14.5	17.1	8.6	19.0	44.7	8.48
Svyato-Varvarinskaya coal, Ukraine	K	0.0	4.8	11.3	19.0	15.8	17.9	8.1	23.1	49.1	6.49
Section Bochatsky coal, Russia	KO	5.0	18.4	17.0	14.5	12.1	12.8	6.4	13.8	33.0	15.67
August											
Uskovskaya coal, Russia	GZh	0.0	0.0	10.6	28.9	15.5	18.6	6.3	20.1	45.0	5.33
Carter Roag coal, USA	Zh	0.0	3.1	6.5	14.4	18.8	23.1	9.2	24.9	57.2	4.89
Goonyella coal, USA	K	0.0	3.2	7.0	15.3	15.7	18.5	9.3	31.0	58.8	5.21
Berezovskaya coal, Russia	KO	10.0	6.0	10.0	15.1	13.0	14.6	7.8	23.5	45.9	13.7

Table 4. The variation of moisture content of coal concentrates in the process of transportation in condition the raw material base Avdeevskii coke plant

Component; country	Coal rank	Moisture W^r_t, %		ΔW^r_t, %
		After car dumper	Top silo	
April				
Shchedrukhinskaya coal, Russia	G	10.3	10.1	0.2
Toms Creek coal, USA	Zh	7.4	7.1	0.3
Svyato-Varvarinskaya coal, Ukraine	K	9.8	9.6	0.2
Section Bochatsky coal, Russia	KO	8.9	8.7	0.2
Mean loss of moisture	–	–	–	0.2
August				
Uskovskaya coal, Russia	GZh	10.0	9.1	0.9
Carter Roag coal, USA	Zh	7.8	7.0	0.8
Goonyella coal, USA	K	7.8	7.3	0.5
Berezovskaya coal, Russia	KO	10.1	8.7	1.4
Mean loss of moisture	–	–	–	0.9

Coal rank "K" Svyato-Varvarinskaya and Goonyella are petrographically homogeneous: the content of vitrinite is 88.0 and 79.0%, and the sum of fusinized components is 9.0 and 21.0%, respectively. The components of vitrinite mainly correspond to the stages of the metamorphism of "Zh" and "K" coal rank. Coals can be attributed to the soft group since their coefficient of Hardgrove grindability index is 82 and 72 units; the mean particle diameter coals are 6.49 and 5.21 mm.

Coals rank "KO" Bochatsky and Berezovskaya are characterized by a low value of the volatile matter (24.8–25.3%) and a low content of total sulfur (0.45–0.52%). The coals studied are petrographically heterogeneous: the content of vitrinite is (42.0–45.0%), and the content of fusinized components (57.0–53.0%). The components of vitrinite are predominantly concentrated in the middle stage of metamorphism. These coals, along with bituminous coal with a high level of fluidity coal of Toms Creek, are characterized by a transitional level of hardness — the Hardgrove grindability index is 62–67 units. The mean particle diameter coal is 13.70–15.67 mm.

The study to determine the variation in moisture content during the transportation of the above coals was carried out as follows: the conveyor stopped, the coal concentrates from the car dumper to the top of the silo of the closed coal store, and at the same time coal samples (80–100 kg) were taken directly from conveyors.

It should be noted that the weather conditions during the sampling of coal samples differed significantly. In April 2017, the ambient temperature was +4°C, and in August 2017 it rose to +23.5°C. Table 4 shows data of changes moisture content in coal concentrates. Analyzing the data, we can conclude that the loss of moisture in the coal concentrates in the process of their transportation in April amounted to a mean of 0.2%, and in August – 0.9%.

Based on the foregoing, it can be concluded that moisture loss in coal concentrates substantially depends on the ambient temperature: the higher the temperature, the more moisture is lost during transportation of coal concentrates and vice versa. This circumstance must be taken into account when removing the remnants of coal raw materials in the coal preparation department of the coke plant.

Taking into account the present level of coal processing in the coal preparation department (~ 265,000 t/month), the variation in the actual weight of the coal can be in winter time ~530 t/month; in summertime ~2 385 t/month.

To assess the change in humidity during the crushing of coal batch (entering the coke battery 9), samples were taken to determine the working moisture, before crushing, after crushing, and before the coal towers of coke oven batteries. After the selection, coal concentrates were delivered to the control department of the Quality Control Department and immediately disassembled according to the accepted method and transferred to the Central Laboratory of the Plant to determine the moisture in them.

Table 5 shows the variation of moisture content in coal blends (entering the coke battery 9) the coal preparation department PJSC "AKHZ," in the process of their transportation from the silo of closed coal storage to the coal tower of the coke oven battery.

Table 5. The variation of moisture content of coal batches entering the coke battery 9 Avdeevskii coke plant in process its preparation

Battery	Date	Line, load, t/hour		Moisture W^r_t, %			ΔW^r_t, %
		A	B	Calculated before crushing	After crushing	Before coal tower	
9	19.04	8.9/234	8.7/366	8.8/600	8.8	8.8	0.00
9	20.04	8.8/264	8.6/336	8.7/600	8.8	8.7	0.10
mean							0.1
9	28.06	8.5/240	8.3/360	8.38	8.2	7.7	0.68
9	09.08	7.5/228	8.8/372	8.31	8.1	7.6	0.71
mean							0.7

The study was conducted as follows: the conveyor stopped, feeding the coal concentrates from the silos of the closed coal storage to the crushing, and then, taking into account the load on the belt, the mean dynamic moisture value of the entire coal batch was calculated, along with them the conveyor after the crusher and the conveyor also stopped. The coal tower was used to collect coal samples (1 meter) weighing 80–100 kg directly from the conveyors mentioned above.

After the delivery of coal concentrates to the control center of the Quality Control Department, they were promptly disassembled according to the accepted method and transferred to the Central Laboratory of the Plant to determine the working moisture in them.

The results of determining the moisture content of coal batch samples, made in April (ambient temperature + 4°C) showed that the moisture content of the coal batch in the process of its preparation does not change ($\Delta W^r_t = 0.1\%$).

The results of determining the humidity of coal batch samples in the summer showed that the loss of moisture was ~ 0.7%: 0.68% in June and 0.71% in August. The experiment was carried out at mean daily temperatures of 25.5°C and 23.5°C, respectively.

Taking into account the present level of coal processing in the coal preparation department, the variation in the actual weight of the batch can be in winter ~ 265 t/month; in the summer ~ 1 855 t/month.

3. Conclusions

As a result of the actual measurements of the moisture change of incoming coal in the path of the car dumper - silo of the closed coal and coal batch in the path of the crusher - coal tower of coke oven batteries in different temperature conditions, we formulated the following conclusions:

1. Moisture loss in coal concentrates during their transportation significantly depends on the ambient temperature: the higher the temperature, the more moisture is lost, and vice versa. It was established that unloading and transportation of coal to the silo of a closed coal warehouse is accompanied by a loss of ~ 0.9% moisture at an ambient temperature of 23.5°C and ~ 0.2% at a temperature of +4°C.
2. When crushing and transporting the coal batch to the coal tower of a coke oven battery, the variation in its actual weight is ~ 0.1% at an ambient temperature of +4°C and 0.7% at an ambient temperature of 23.5–25.5°C.
3. The results of research should be taken into account when measuring residues of raw materials, materials, and products in warehouses in coal preparation department of coke plants.

Symbols

W^r_t	*moisture content of coal, %;*
A^d	*ash content of coal in the dry state, %;*
St^d	*sulphur of coal in the dry state, %;*
V^{daf}	*volatile matter in the dry ash-free state, %;*
y	*thickness of the plastic layer, mm;*
HGI	*hardgrove grindability index, units;*
Vt	*vitrinite, %;*
Sv	*semivitrinite, %;*
I	*inetinite, %;*
L	*liptinite, %;*
R_0	*mean vitrinite reflection coefficient, %;*
$\sum FC$	*sum of fusinized components, %;*
d_{me}	*mean diameter of coals particles, mm.*

References

[1] Shmeltser EO, Lyalyuk VP, Sokolova VP, Miroshnichenko DV. The using of coal blends with an increased content of coals of the middle stage of metamorphism for the production of the blast-furnace coke. Message 1. Preparation of coal blends. Pet Coal, 2018; 60(4): 605–611.

[2] Lyalyuk VP, Kassim DA, Shmeltser EO, Lyakhova IA, Kormer MV. Improving the Preparation of Coking Batch. Coke and Chemistry, 2018; 61(5): 171–178.
[3] Shmeltser EO, Lyalyuk VP, Sokolova VP, Miroshnichenko DV. Influence of Crushing of Bituminous Batch on Coke Quality. Coke and Chemistry, 2017; 60(12): 470–475.
[4] Desna NA, Miroshnichenko DV. Oxidized coal in coking: A review (Review). Coke and Chemistry, 2011; 54(5): 139–146.
[5] Miroshnichenko DV, Drozdnik ID, Kaftan YS, Ivanova EV, Sirokotyaga KN, Desna NA. Kinetic characteristics of coal oxidation. Coke and chemistry, 2012; 55(3): 87–96.
[6] Miroshnichenko DV, Drozdnik ID, Kaftan YS, Bidolenko NB, Desna NB. Coking of coal batch with different content of oxidized coal. Coke and Chemistry. 2012; 55(5): 155–164.

To whom correspondence should be addressed: Dr. E. O. Shmeltser, Kryvyi Rig Metallurgical Institute, Ukraine National Metallurgical Academy, 50006, Kryvyi Rig, Ukraine, e-mail: shmelka0402@gmail.com

Petroleum and Coal

Article **Open Access**

ESTIMATION OF THE VELOCITIES OF WEATHERED AND CONSOLIDATED LAYERS USING SEISMIC REFRACTION METHOD

*Rasaq Bello[1]*and Robert Brendan Eso[2]*

[1] Department of Physics, Federal University of Kashere, Gombe State, Nigeria
[2] Department of Physics, University of Port Harcourt, Port Harcourt, Nigeria

Received February 2, 2019; Revised April 5, 2019; Accepted May 27, 2019

Abstract

Seismic refraction tomography was carried out in four different sites within University of Port Harcourt to determine the seismic velocities of the weathered and consolidated layers. A total of twenty points were made for both forward and reverse shots using ABEM terralog with 12- channel geophones. The data processing was carried out using ReflexW seismic data processing software. The first arrival times recorded at shot points were plotted against the geophone separations from the shot point to obtain the time distance graphs using Microsoft Excel. The velocities of the different layers were calculated from these plots. The weathered layer velocities range from 900 m/ s to 1300 m/s with an average of 1118.3 m/s for the forward down velocities while the velocities range from 867 m/s to 1200 m/s with an average of 1062.3 m/s for the reverse down velocities. The consolidated layer velocities range from 1592 m/s to 1715 m/s with an average of 11680.5 m/s for the forward up velocities while the velocities range from 1333 m/s to 1964 m/s with an average of 1683.5 m/s for the reverse up velocities. It was observed that these consolidated layers across the study area were sufficiently competent for civil engineering applications judging from their recorded high seismic velocity values.

Keywords: *Geophone; Refraction; Velocity; Tomography; Weathered Layer.*

1. Introduction

Seismic refraction survey is used extensively in engineering geological and geotechnical investigations to determine the overburden and weathered zone thickness, to identify geological anomalies and highly cracked zone, to determine the boundary between rocks of different lithological composition. It is also used to locate aquifers, to search for building materials, to contribute to assess liquefaction and landslides of layers near the surface [1].

Seismic exploration involves the generation, detection, analysis and interpretation of elastic waves in the earth to study the sub-surface properties of the earth. When the seismic wave reaches the interface having higher velocity, it is refracted and travel along the refracted surface. Energy is transmitted back to the surface when the angle of incidence equals the critical angle. At this point, the refracted wave moves along the interface between the two materials. The refracted angle is dependent on layer composition and structure [2].

When the seismic wave is back to the surface, it is discovered by a series of geophones and recorded by a seismograph as shown in Figure 1.

The weathered layer is the shallow subsurface layer composed of unconsolidated materials such as soil, sand and gravel. The delay in travel time experienced during seismic refraction acquisition is as a result of the heterogeneous composition of the subsurface and characterized by low seismic velocity [4].

Characteristics of the weathered layer include low pressure and bulk modulus, lack of cementation and high porosity. These characteristics are responsible for the very low compressional and shear wave velocities occurring in the layer. The interface between the weathered layer and the consolidated layer represents the base of the weathered layer [5].

Investigation of properties of the subsurface could be carried out downhole survey of seismic refraction method. Seismic refraction survey is carried out by recording arrival time and off distance which will be used to determine depth and velocity of the subsurface. This is based on the fact that rays are refracted at boundaries of different properties of formation; the lines of geophone will detect refracted signals which have traveled down the different layers before returning back to the surface [6]. Two most important and commonly used methods of determining the features of low velocity layer are the uphole and downhole seismic refraction methods. The methods can be used to determine thicknesses of layers in vertical direction, depth and near surface velocities. Geology and seismic refraction response of a particular site could be determined once the velocity information is known.

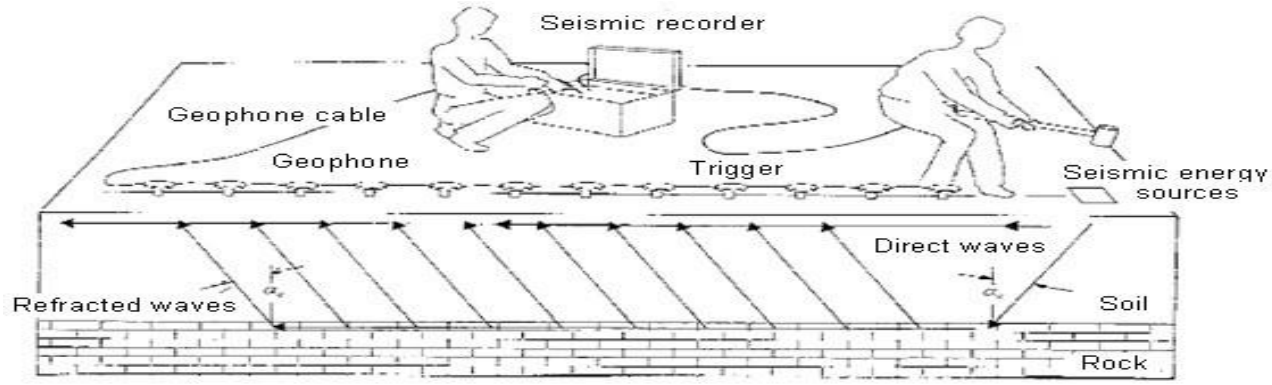

Figure 1: Field layout of seismic refraction [3]

Field data from downhole seismic refraction gives information on travel times of compressional and shear waves from the distance between source and geophone and from source to geophone. In downhole seismic refraction survey, seismic signals are generated from seismic source placed at or near the ground [7].

Lots of civil engineering construction works are going on in the study area which is located within the Niger Delta basin, a prolific oil bearing region. Poor knowledge of weathered layer properties of the study area is responsible for most of the failures recorded in engineering structures [8].

Seismic refraction survey can be used to determine/estimate the velocities of the strata with a view to ascertaining the suitability of these layers for seismic reflection data acquisition and other engineering applications.

The aim of this study was to determine the velocities of weathered and consolidated layers in parts of University of Port Harcourt, Nigeria using a tomography model of seismic refraction method.

1.1. Study area

University of Port Harcourt is located in Choba community in Obio-Akpor local government which is bounded by Port Harcourt (local government area) to the south, Oyigbo to the east, Ikwerre to the north, and Emohua to the west. It is located between latitudes 4°45'N and 4°60'N and longitudes 6°50'E and 8°00'E.

The study area is characterized by high rainfall with little dry season and lies in the tropical wet climate zone. The raining season occurs between April and October, with rainfall ranging between 2000 and 2500 mm with temperature of about 25^{0}C and consistent humidity. Figure 2 shows the map of the study area.

1.2. Geology and relief

University of Port Harcourt has an average elevation generally below 30 metres above sea level and it's regarded as a lowland area. Basement complex and alluvial sedimentary basin characterized the geology of the study area. The vegetation in the area includes raffia palms,

light rainforest and thick mangrove forest. The soil in the area is generally sandy or sandy loamy as a result of the high rainfall prevalent in the area. Leaching of soil in the area is a common occurrence and underlain by a layer of impervious pan.

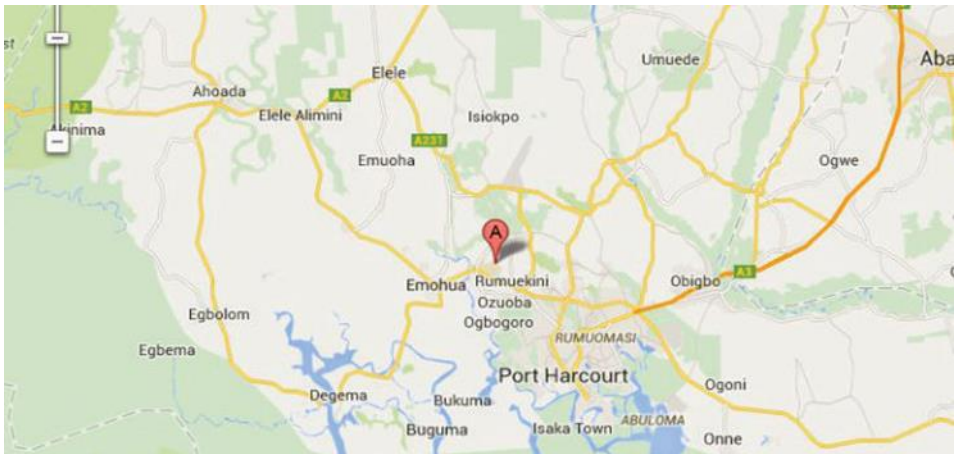

Figure 2. Map of the study area

2. Methodology

A wide variety of seismic geophysical equipment is available and the choice of equipment for a seismic refraction survey should be made in order to meet the objectives of the survey. geophysical equipment used for this seismic refraction measurement includes the seismo-graph, geophones, geophone cable, and energy source and a trigger cable or radio link.

The data for this work were acquired in four different locations with the University Park, University of port Harcourt, Nigeria. The locations are behind the Faculty of Social Sciences (first profile), in the front of the Faculty of Humanities (second profile), behind Faculty of Gas Engineering (third profile), and adjacent to the Faculty of Gas Engineering (fourth profile).

A total of twenty points were made for both forward and reverse shots with a total length of 95 m used for each profile line. In order to reduce random noise, five stacks were made, and the averages were recorded by the seismometer on each shot point.

3. Results and discussion

3.1. Results

The data processing was carried out using ReflexW 2D-data analysis processor software. The data used in this work was acquired from a seismic investigation field for velocity variation of weathered layers (using a 2D Tomography of a seismic refracted method), the signal is a single shot type and the first geophone started from zero point, in Reflex-w software the type of output received is called SEG.

Figure 3 shows the traces of signals at each geophones as received from the refracted incident ray from a single shot point and the signals are accompanied by random noise. For the data to be well processed it will first undergo a filtering process.

Figure 4 shows the data after it has undergone a filtering process which was carried out using a Band pass frequency 1D Filter, but the amplitudes is small and this create troublesome for the data to be well analyse, so the data need to undergo a gaining process.

Figure 5 shows the data after it has undergone a gaining process, now the amplitudes are large and very easy to differentiate. At this point we pick out our various arrival time of signals at each geophone, we do this by picking the point with `x' sign. Gaining means to enlarge our amplitude, and we use the Y gain manual a unit in ReflexW data analysis seismic software, the main objective in gaining data is to pick the 1st arrival time and the reflected ray.

Figure 6 shows that the arrival times have been marked out and the data is set to draw its model (the path of differences). The first arrival times recorded at shot points were plotted

against the geophone separations from the shot point to obtain the time distance graphs using Microsoft Excel to obtain Tables 1 - 4 and Figures 8 – 11.

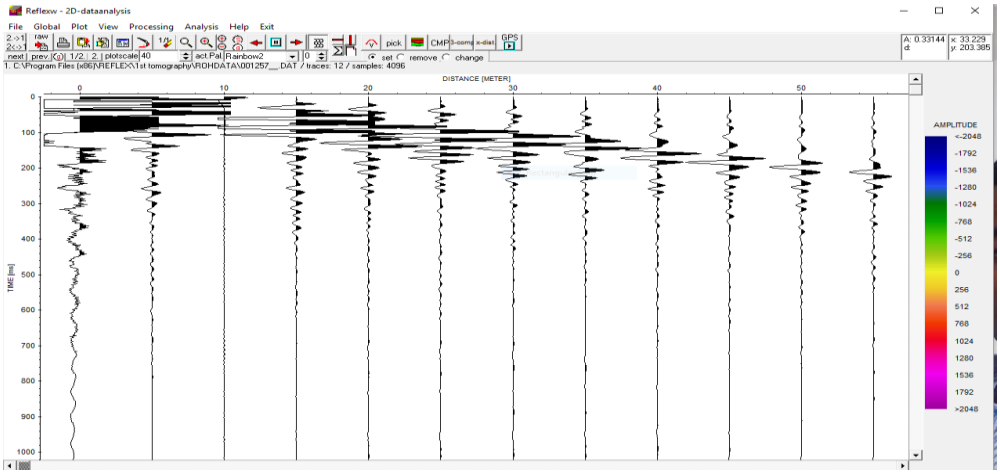

Figure 3. Kicking (traces) before filtering

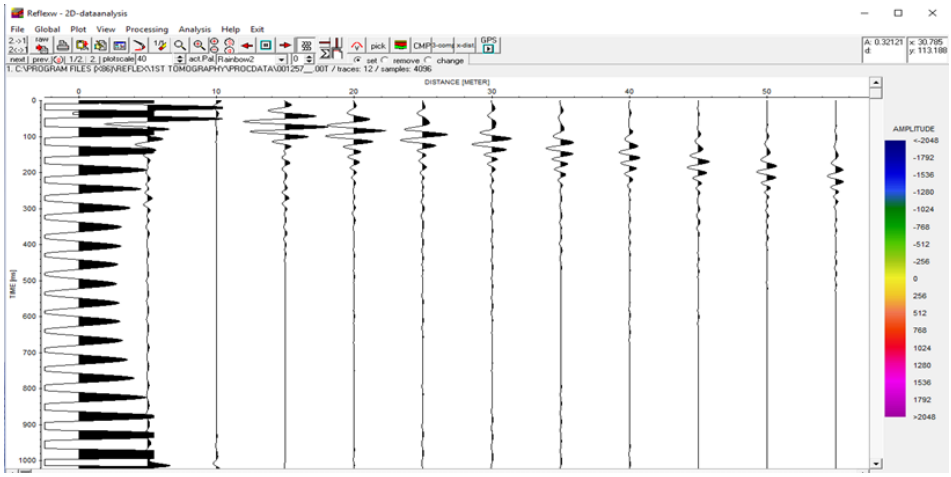

Figure 4. Kicking (traces) after filtering and before gaining

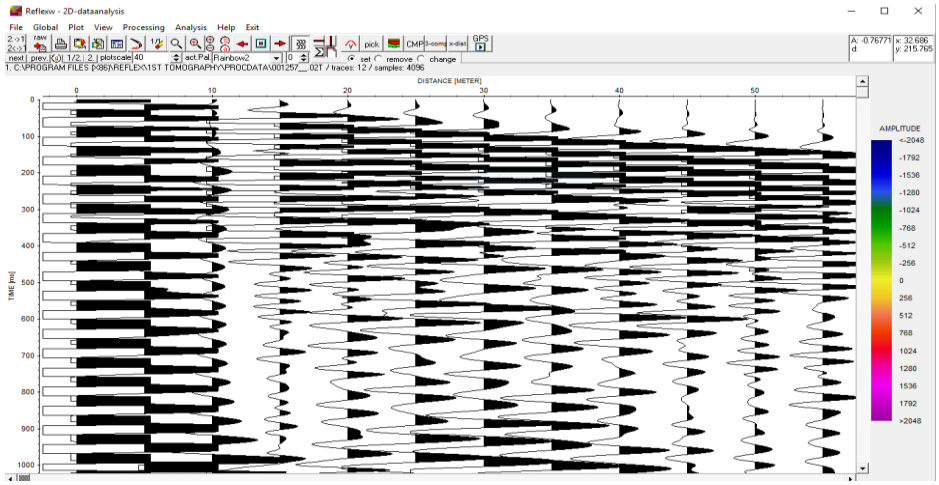

Figure 5. Kicking (traces) after gaining

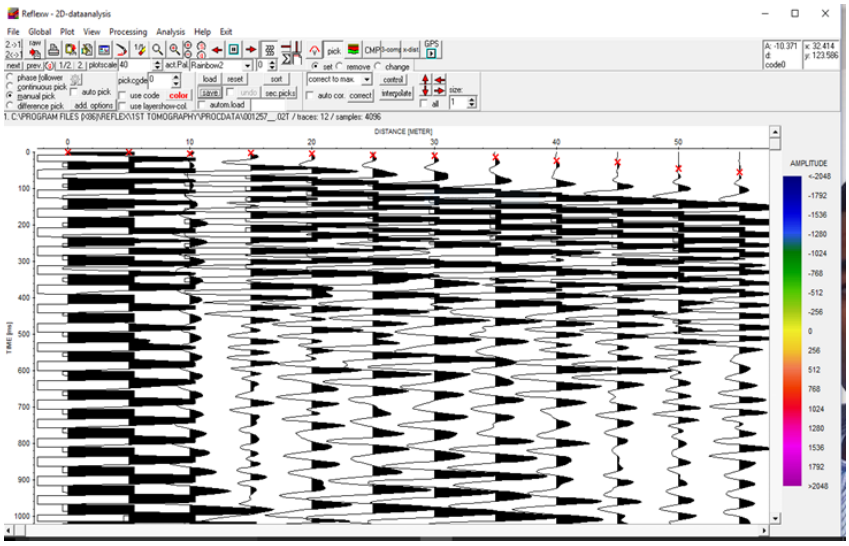

Figure 6. Picking of the first arrival

Table 1. Data for the first forward and reserve time

Distance (m)	Forward time (ms)	Reversed time (ms)
0	5.99	55.9
5	7.98	53.89
10	9.98	39.92
15	15.97	27.95
20	13.97	33.93
25	19.96	33.93
30	19.96	21.96
35	33.93	15.97
40	27.95	11.98
45	39.92	11.98
50	41.92	9.81
55	43.91	5.89

Table 2. Data for the 2nd forward and reserve time

Distance (m)	Forward time (ms)	Reversed time (ms)
0	1.96	43.91
5	2.73	37.93
10	5.99	33.93
15	7.98	43.91
20	11.98	25.95
25	11.96	21.96
30	17.96	13.97
35	19.96	15.79
40	25.95	7.98
45	35.93	7.98
50	37.93	5.99
55	47.91	3.99

Table 3. Data for the 3rd forward and reserve time

Distance (m)	Forward Time (ms)	Reversed Time (ms)
0	0.93	39.92
5	6.52	37.93
10	7.45	35.95
15	11.77	23.95
20	11.8	19.96
25	13.97	15.97
30	15.97	13.97
35	21.96	11.98
40	21.96	19.78
45	25.95	7.98
50	27.93	3.73
55	33.93	1.86

Table 4. Data for the 4th forward and reserve time

Distance (m)	Forward Time (ms)	Reversed Time (ms)
0	0	37.93
5	0.28	33.93
10	2.27	25.95
15	6.43	19.96
20	7.85	19.96
25	13.33	15.97
30	18.06	9.98
35	20.99	9.98
40	23.95	7.98
45	33.93	5.89
50	31.94	1.54
55	39.92	0.77

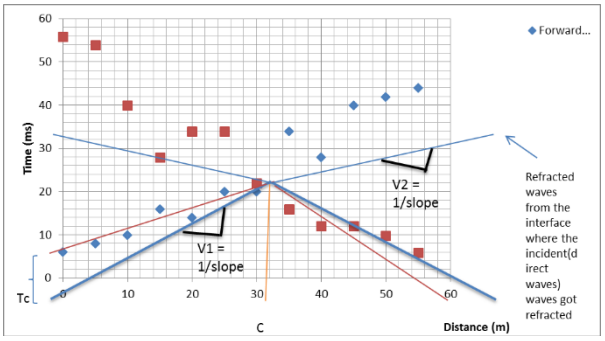

Figure 7. Graph for the first forward and reserve time

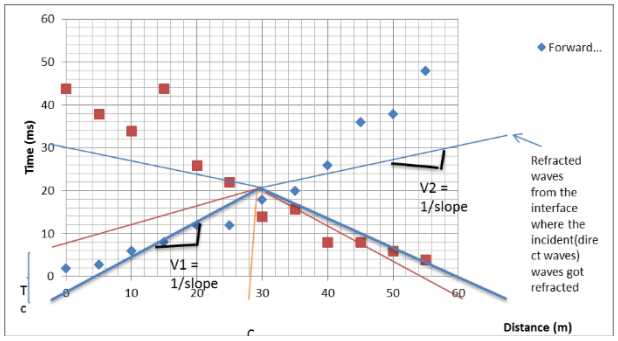

Figure 8. Graph for the 2nd forward and reserve time

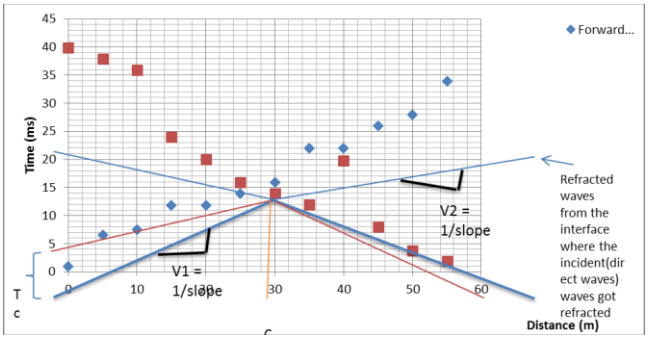

Figure 9 Graph for the 3rd forward and reverse time

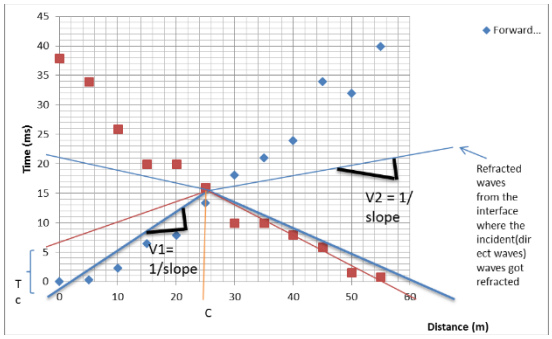

Figure 10. Graph for the 4th forward and reverse time

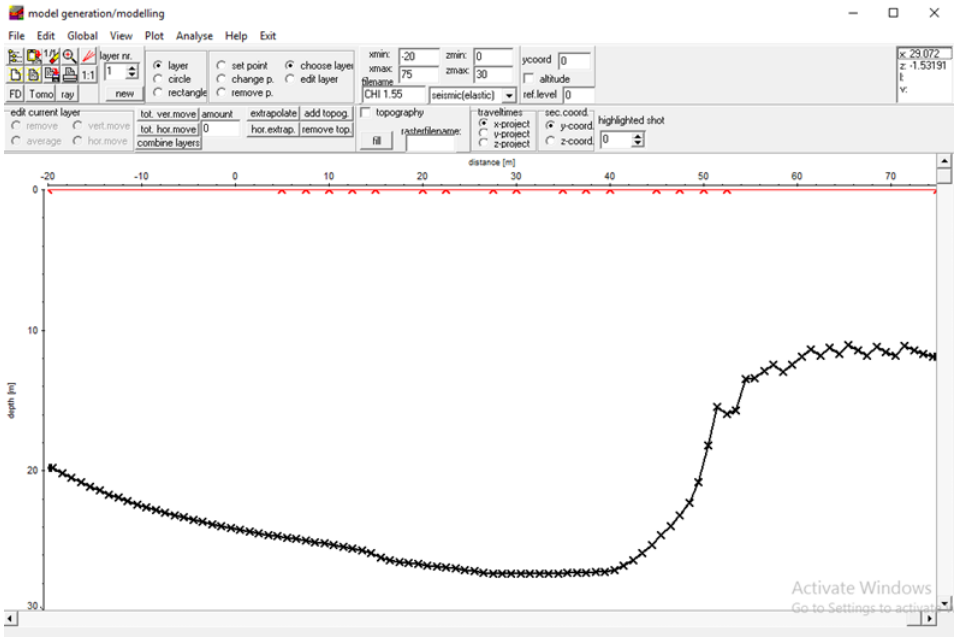

Figure 12. Model

The graphs that were plotted were used to assign layers with the aid of the average travel time from the four charts i.e. Figures 11-12. Figure 11 shows that the model is unparabolic and shows a variation of layers and sign of unconformity. Figure 12 shows the tomographic look of the data, and from it we can predict the various velocities and their variations for each soil layer or soil type.

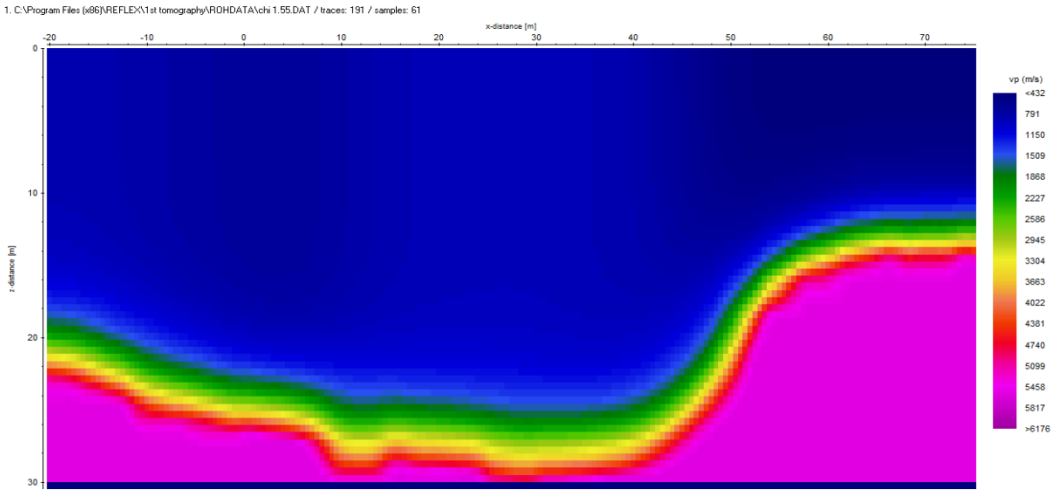

Figure 12. Seismic refraction tomography

The weathered layer velocity can be derived indirectly from surface seismic data and is very essential to geoscientists and environmental engineers [4]. Measurements of arrival times of the seismic pulses to the geophones at various depths give the velocity of the propagation of pulse in the ground. Since the elastic properties of the layer are assumed homogenous generally, the velocity of the ground motion will therefore vary both with depth and horizontal distance. For a source depth of h, an offset of X, the vertical velocity t_v corrected for the source depth is:

$$t_v = \frac{t_s(h-z)}{\left\{\left(\frac{hX-ZX}{h}\right)^2 + (h-Z)^2\right\}^{1/2}} \qquad 1$$

where Z is the respective receiver depths, h is the source depth, X is the offset, t_s is travel time for slant path (the raw time picked from the seismogram). The velocities were computed from the reciprocals of the slopes of the straight-line segments based on the thickness equation 1 [9].

The velocities of the weathered layers for this work were computed from the slopes of four profiles shown in Figures 7 – 10 and presented in Table 5.

Table 5. Table of seismic velocities

	Forward Up Velocity (m/s)	Forward Down Velocity (m/s)	Reverse Up Velocity (m/s)	Reverse Down Velocity (m/s)	Average (m/s)
Profile 1	1645	900	1333	1000	1219.5
Profile 2	1770	1000	1964	867	1400.3
Profile 3	1715	1273	1645	1200	1458.3
Profile 4	1592	1300	1792	1182	1466.5
Average	1680.5	1118.3	1683.5	1062.3	

3.2. Discussion

The velocity determination of weathered layer is bedrock of possibilities in predicting the nature of the earth, in terms of minerals and sustainability. Seismic refraction method in its simplest form had brought a way and easy take in evaluating the content of the Earth's crust, its thickness and permeability conditions. Seismic refraction methods of evaluating the crust (weathered layer) have given a room and possibilities for geoscientist to be fast and accurate to determine or predicting earthquakes and other similar tectonic related hazards.

The near surface geology is comparatively stable and inhomogeneous with moderate velocity contrast. The weathered layer velocities range from 900 m/s to 1300 m/s with an average of 1118.3 m/s for the forward down velocities while the velocities range from 867 m/s to 1200 m/s with an average of 1062.3 m/s for the reverse down velocities. The consolidated layer velocities range from 1592 m/s to 1715 m/s with an average of 11680.5 m/s for the forward up velocities while the velocities range from 1333 m/s to 1964 m/s with an average of 1683.5 m/s for the reverse up velocities. It was observed that these consolidated layers across the study area were sufficiently competent for civil engineering applications judging from their recorded high seismic velocity values.

The values of seismic velocities obtained in this study are in agreement with the results/values obtained by other researchers in the study area [4, 9-11].

Near surface seismic velocity variation gives rise to great chances of encountering inhomogeneity of the weathered zone and poses a problem for a smooth static behavior if seismic reflection survey is to be carried out in the area.

The average consolidated layer velocity of 1680 m/s found in this work falls within the range used for static correction in a reflection survey which is capable of removing it is effect on arrival time. The weathered layers are to a large extent heterogeneous and loose as indicated by the velocities of the layer. Results obtained from this study indicated that static correction will be required in the study area before seismic reflection work is carried out, owing to the high variations in weathered layer seismic velocity.

Results obtained from this study are very important in determining time delays required for static corrections during the processing of seismic reflection data [10-11]. The knowledge of the velocity of the low velocity layer is extremely important in civil engineering works as well as, in groundwater exploration. Civil engineers and construction experts can use the result among other fundamental soil parameters to determine the soil type and position of foundation for structures to be erected [12].

4. Conclusion

Seismic exploration involves the generation, detection, analysis and interpretation of elastic waves in the earth to study the sub-surface properties of the earth. Seismic refraction tomography was carried out in four different sites within the study area to determine the seismic velocities of the weathered and consolidated layers.

Results from the study area revealed that the weathered layer velocities range from 900 m/s to 1300 m/s with an average of 1118.3 m/s for the forward down velocities while the velocities range from 867 m/s to 1200 m/s with an average of 1062.3 m/s for the reverse down velocities. The consolidated layer velocities range from 1592 m/s to 1715 m/s with an average of 11680.5 m/s for the forward up velocities while the velocities range from 1333 m/s to 1964 m/s with an average of 1683.5 m/s for the reverse up velocities.

The values of velocities of weathered and consolidated layers obtained in this work are in agreement with the results obtained by others researchers that have worked in the Niger Delta region of Nigeria where this work was carried out. The high values of seismic velocities of the consolidated layers obtained from this work were adequately sufficient for civil engineering applications.

References

[1] Adewoyin OO, Joshua EO, and Akinyemi ML. Application of Shallow Seismic Refraction Method and Geotechnical Parameters in Site Characterization of a Reclaimed Land. Indian Journal of Science and Technology, 2016; 9(45): 1-7.

[2] Alaminiokuma GI, and Amonieah J. Near Surface Structural model for enhanced Seismic data acquisition and Processing in north-central Niger Delta. Am. J. Sci. Indus. Res., 2012; 3: 252-262.

[3] Pioneer Geophysics Joint Stock Company. www.tpgeo.com.vn

[4] Adeoti KSI, Adesanya O, Olodu U, and Bello MA. Application of Uphole Seismic Refraction Survey for Subsurface Investigation: A Case Study of Liso Field, Niger Delta, Nigeria. World Applied Sciences Journal. 2013; 26 (5): 573-582.

[5] Telford WM, Geldart LP, Sheriff RE, and Keys DA. Applied Geophysics. Cambridge University Press 1976, 3rd Edition, 769pp.
[6] Redpath BB. Seismic Refraction Exploration for Engineering Site Investigations. Technical Report E-73-4, US Army Engineer Waterways Experiment Station 1973, Vicksbury, MS.
[7] Okeke PO, and Ezem LN. Determining weathered layer velocities and depth to Lignite seams of the Anambra Basin, Nigeria by Uphole Seismic Refraction method. Groundwater and Mineral Resources of Nigeria (ed. Charles, O. Ofoegbu). Friedr Vieweg and Sohn Braunschweign/Wiesbaden, 1988.
[8] Uko E D, Tamunobereton-ari I, Omubo-Pepple VB. Comparison of Compressional wave Velocity depth Profiles from Surface and Downhole Detectors in the Near Surface in the Southeast Niger Delta, Nigeria. International Journal of Asian Social Science, 2012; 2(6): 869-880 869.
[9] Uko ET, Emudianughe JE, and Eze CL. (2016). Comparison of the Characteristics of Low Velocity Layer (LVL) in the Mangrove Swamp and in the Upper Flood Plain Environments in the Niger Delta, using Seismic Refraction Methods. Journal of Geology & Geophysics, 2016; 5(4): 248.
[10] Sofolabo AO, Ebeniro JO. Determination of Weathered Layers Characteristics of Field-K, Western Niger Delta, Nigeria Using Uphole Refraction (Borehole) Survey Technique. International Journal of Science and Research, 2017; 6(10): 31-40.
[11] Igboekwe MU, and Ohaegbuchu HE. Investigation into the weathering layer using up-hole method of seismic refraction. Journal of Geology and Mining Research, 2011; 3(3): 73-86.
[12] Nwosu LI, and Emujakporue GO. Seismic Refraction Investigation of Thickness and Velocity of the Weathered Layer in Emuoha Town, Rivers State, Nigeria. IOSR Journal of Applied Geology and Geophysics, 2016; 4(6):52- 57.

To whom correspondence should be addressed: Dr. Rasaq Bello, Department of Physics, Federal University of Kashere, Gombe State, Nigeria

BOOK REVIEW

Martin Bajus

Hydrocarbon Technology - Chemical Processes in Organic Technology and Petrochemistry

Inssued by Slovak University of Technology Bratislava,
in SPEKTRUM-STU, 2019, 1. Edition, 608 pages
e-textbook, price 6 EUR
85-205-2019
ISBN 978-80-227-4897-1

At the begininng of 2019 a new e-textbook on Chemical Processes in Organic Technology and Petrochemistry in the series „Hydrocarbon Technology“, published by the Spektrum – STU at Slovak University of Technology, Faculty of Chemical and Food Technology in Bratislava appeared on the book market. The author of the e-text book is Professor Martin Bajus, a Slovak leading expert in refinery, petrochemical, energy, and recycling technologies. You can get the e-book from bookseller Malé Centrum.

The series „Hydrocarbon technology“ includes four volumes covering following aspects of the technology involved in the oil refinery, petrochemical industry and organic technology:

- Organic technology and petrochemistry; also on CD support (2002),
- Petrochemistry (2017),
- Chemical processes in organic technology and petrochemistry (2019),
- Energetic materials and technologies.

The series is designed for the students and teaching staff at Slovak University of technology, in the Faculty Chemical and Food Technology. The text is the basis for some courses for other it is only supplementary. In all chapters the processes are represented by simplified flow schemes. For clarity these generally do not include process control systems, and valves and pumps are omitted in most cases. It is expected that students after having read the e-textbook, will be able think in “conceptual process design”. The series is designed for the engineers and technicians who will be operating the refineries at the beginning of the 21st century. By the time, solution will necessarily have been found for a member of problems increasingly severe product specifications and, more especially, environmental protection.

The development of the field of hydrocarbon technology has proceeded through a set of remarkable technological advances over nearly two decades. While one of the Twelve Principles of Green Chemistry is devoted to ensuring that all feedstocks for both materials and energy are renewable rather than depleting, it is actually the case that the pursuit of the bio-based energy and material economy will rely on all of the principles of Green Chemistry and Green Engineering. Through the adoption of these design frameworks as a holistic rather system rather than individual criteria, biofuels and biomaterials will be sustainable both for planet as well as for profits.

This e-textbook provides an important review of main processes and technologies that are essential to the future success of clean fuels, biofuels, eco-friendly petrochemicals, elimination of CO_2, reducing methane emissions and using of nanomaterials and the editor and author are to be commended for constructing this high quality collection.
The third volume of the “Hydrocarbon Technology” collection deals with chemical processes for petroleum fractions as produced by separation operations. In addition to scientific disciplines, the control of separation processes also involves the choice of technique (distillation, catalytic distillation, extractive distillation, extraction, adsorption, absorption, percolation, crystallization, etc.) and the choice of technology (mixer-setters types of columns, centrifuges, membranes, etc.). Separation processes would therefore see to play leading role in the future of the hydrocarbon technology. The relevant investments are usually lower than for chemical processes.
Chemical processes have three objectives:

- Improve product quality so as to meet the requirements for the corresponding end use (heat/engines, burners);
- Convert crude oil fractions that cannot directly find an outlet into products better adapted to the market;
- Protect natural environment during product manufacturing and utilization.

Following an introduction which shows the growing importance of chemical processes in organic technology and petrochemistry, this e-textbook presents the fundamentals of the chemical mechanisms at the basis of chemical processes. These disciplines are thermodynamic, chemical kinetics, reactor calculation, and industrial catalyst.
Then the major chemical processes are discussed. The first group of chemical processes is designed to improve the quality of light fractions: catalytic reforming and isomerization. The second group involves the conversion of distillates: catalytic cracking and hydrocacking, along with their related units: alkylation, oligomerization and etherification. The third includes processes for converting residues: visbreaking, coking and hydroconversion with related hydrogen production unit. Lastly, chemical processes which deal with reducing air and water pollution: sweeting of white products and hydrotreating to eliminate sulfur and nitrogen compounds, sour gas treatments to remove hydrogen sulfide, desulfurization of heavy fuel oil combustion off gases and treatments to remove and treatment of process water.

In each of the chapters mentioned above have endeavoured to present both the basis needed to understand the chemical reactions put into practice as well as the technical and economic data required to gauge the impact of processes on refinery operation and on the technology of organic chemical industry.

Obviously. not all process variations can be presented in this e-book. The sole objective here is to give the reader a grasp of the complex world of oil, natural gas, organic chemicals industry product conversion techniques and their role in the chemical industry. Then, at a later date, specialized literature can be approached to get a more thorough understanding of hydrocarbon technology.

I believe that the e-book Hydrocarbon Technology – Chemical Processes in Organic Technology and Petrochemistry will be a welcome study material both for the students of the Faculty of Chemical and Food Technology, STU, but also for other students studying for higher education in the Slovak Republic. As a teacher with long-time practical experience I can recommend this e-textbook as a study material to all students that study chemical technology or similar field of science.

V. Milata